C.R.
NO DAA REQ
210P
1+9

(NASA-CR-176800) MIDDLE ATMOSPHERE PROGRAM. N86-26725
HANDBOOK FOR MAP, VOLUME 19 (International THRU
Council of Scientific Unions) 210 p N86-26734
HC A10/MF A01; also available from SCOSTEP Unclas
CSCL 04A G3/46 43301

Middle Atmosphere Program

HANDBOOK FOR MAP VOLUME 19

Edited by
Richard A. Goldberg

ICSU

International Council of Scientific Unions

SCOSTEP

Scientific Committee on Solar-Terrestrial Physics
K. D. Cole, President
J. G. Roederer, Vice President
C. H. Liu, Scientific Secretary

MAP ORGANIZATION

MIDDLE ATMOSPHERE PROGRAM STEERING COMMITTEE
S. A. Bowhill, SCOSTEP, Chairman
K. Labitzke, COSPAR, Vice Chairman
C. H. Liu, SCOSTEP, Secretary

H. S. Ahluwalia, IUPAP
R. D. Bojkov, WMO
A. D. Danilov, COSPAR
J. C. Gille, COSPAR
I. Hirota, IUGG/IAMAP
A. H. Manson, SCOSTEP
L. R. Megill, IUGG/IAGA
T. Nagata, SCAR
R. G. Roper, IAMAP
P. C. Simon, IAU
J. Taubenheim, IUGG/IAGA
T. E. VanZandt, URSI
R. A. Vincent, URSI

MAP STANDING COMMITTEES
Data-Management -- G. Hartmann and I. Hirota, Co-Chairmen
Dynamics Calendar -- T. E. VanZandt, Chairman
Publications -- C. F. Sechrist, Jr., Chairman

MAP STUDY GROUPS
MSG-5 Ions and Aerosols, F. Arnold and M. P. McCormick, Co-Chairmen
MSG-8 Atmospheric Chemistry, G. Witt, Chairman
MSG-9 Measurement of Middle Atmosphere Parameters by Long Duration Balloon Flights, J. E. Blamont, Chairman

APPROVED MAP PROJECTS

	Coordinator		Coordinator
AMA:	T. Hirasawa	MAC-Epsilon:	E. V. Thrane
ATMAP:	J. M. Forbes	MAC-SINE:	E. V. Thrane
CAMP:	G. Witt	MAE:	R. A. Goldberg
CLIMAT:	J. M. Russell	MASH:	A. O'Neill
DYNAMICS:	K. Labitzke	MSTRAC:	P. K. Rastogi
GLOBMET:	R. G. Roper	NIEO:	S. Kato
GLOBUS:	J. P. Pommereau	OZMAP:	D. F. Heath
GOSSA:	M. P. McCormick	SSIM:	P. C. Simon
GRATMAP:	D. C. Fritts	WINE:	U. von Zahn

MAP REGIONAL CONSULTATIVE GROUP

Europe M. L. Chanin, Chairman

M I D D L E

A T M O S P H E R E

P R O G R A M

HANDBOOK FOR MAP

Volume 19

7608

Edited by

Richard A. Goldberg

NC999967

March 1986

JW839742

Published for the ICSU Scientific Committee on Solar-Terrestrial Physics (SCOSTEP) with financial assistance from the National Aeronautics and Space Administration under P.O. W-15,897 and Unesco Subvention 1986-1987

Copies available from SCOSTEP Secretariat, University of Illinois, 1406 W. Green Street, Urbana, Illinois 61801

FOREWORD

As our knowledge of the middle atmosphere has progressed, it has become increasingly apparent that the early projections of this region as a passive, noninteracting domain were severe oversimplifications of the real case. Results now show the middle atmosphere to be interactive with atmospheric regions both above and below it, with new findings constantly amplifying this point of view. In transmitting, or perhaps even driving such interactions, the middle atmosphere appears to employ both its neutral and charged (or plasma) characteristics.

Rockets have played an important role for study in this region. They provide a unique source of in situ measurements, since much of the upper stratosphere and all of the mesosphere are too high for aircraft or balloon soundings, and too low for direct measurement by orbiting spacecraft. Many of the middle atmospheric parameters, particularly those of the charged particle environment, cannot easily be remotely sensed, thereby making rockets the only platform available for their measurement.

Of course, rockets can only provide an instantaneous snapshot of occurring processes at a single location in time. However, by careful selection of time and event, very meaningful results can be obtained. Rockets also complement measurements attainable from ground and/or orbiting platforms. For example, although comprehensive coverage of global parameters is possible by satellite, one cannot direct the satellite to be at a specific location for a given time to sound, say, an auroral event or a local thunderstorm. The rocket, on the other hand, can be launched from an appropriate site at the exact time necessary to maximize the object investigation. It can also be used to provide ground truth for an orbiter overflight.

This MAP Handbook is concerned with rocket techniques and instrumentation as they are currently employed in the middle atmosphere. It is composed of nine chapters, ~~each~~ written by ~~one or more~~ experts ON ~~who have devoted much of their scientific career to~~ rocket experiments. The emphasis here is on measurement techniques rather than results, although results are incorporated ~~wherever they provide examples which illuminate the measurement features. and subtleties involved.~~ ~~I have attempted to~~ organize the chapters ~~to~~ first cover techniques relating to measurements of neutral dynamics and chemistry, then ~~to cover~~ measurements of the various intermittent and excessive radiation sources which affect the middle atmospheric (particularly electrical) environment, and finally ~~to describe~~ measurements of the plasma environment including electric fields. The weighting toward plasma related parameters is not accidental, but reflects both the historical headstart given by early development of radio wave and probe techniques to measure electron density, and by the relatively limited number of techniques available for neutral atmospheric measurements. This division, of course, is not absolute. The chapter on ion mass spectrometry (Arnold and Viggiano) briefly considers how such devices can be modified to look at neutral constituents. Probe techniques (Thrane, Mitchell) demonstrate that such methods may be applicable to interactive problems between the plasma and neutral environment, e.g., using the plasma as a tracer for neutral turbulence and wave structure. Also, the chapter on electric field measurements (Maynard) shows that such fields may be driven by local neutral wind dynamics. No separate chapter on direct measurement of the solar output is included, although such techniques are mentioned in the chapter on neutral trace constituents (Krueger).

PRECEDING PAGE BLANK NOT FILMED

Clearly, the allotted space does not permit maximum detail on every available technique. Instead, each author has attempted to concentrate on those methods which are most widely used at the present time, with some reference to past results as deemed necessary to put the modern techniques in proper perspective. Hopefully, the discussions provided along with the referenced material will provide the serious reader with adequate information to learn about any reported instrument in detail. For the many techniques, both old and new, which have been overlooked in these discussions, I offer my apologies.

The book has taken more than two years in preparation. Most chapters concentrate on material current to the end of 1984, although a few of the late submissions may be slightly more up-to-date. To all the authors who participated in this work, I offer my sincere thanks. Hopefully, this book will become a reference for future rocket users and illuminate the unique importance of rockerty for middle atmospheric studies.

Richard A. Goldberg
NASA/Goddard Space Flight Center
Electrodynamics Branch
September, 1985

ROCKET TECHNIQUES

TABLE OF CONTENTS

1. ROCKET TECHNIQUES USED TO MEASURE THE NEUTRAL ATMOSPHERE D1-46

p. 20

F. J. Schmidlin

NASA Goddard Space Flight Center
Wallops Flight Facility
Wallops Island, VA 23337

7609

NE157844 N86-26726

ABSTRACT

One important facet of middle atmosphere studies is the role of direct measurements provided by rocket systems. These systems range in size from the small meteorological rocketsonde capable of providing temperature and wind data to the larger sounding rocket designed to carry much larger payloads. This chapter discusses the more common methods of rocket meteorological measurements used today, some of which were first deployed over 25 years ago. The major emphasis is given to that system which produces the most measurements (the small meteorological rocket), the types of sensors, the role and applicability of coordinated launchings such as obtained from the Meteorological Rocket Networks, and, the data quality and uses. The large sounding rockets produce similar data but, because of the cost and complexity involved in launching these bigger vehicles, fewer data are obtained. This does not, however, detract from the value of such data. The observational virtue of rocket data is its vertical height resolution (~~~0.1-0.2 km~~) which added new information on the atmospheric structure in mesoscale and, possibly, microscale dimensions. Rocket exploration of the atmosphere has changed the popular notion that the middle and upper atmosphere is a static, quiet area, to the realization that this region is highly active and dynamic.

INTRODUCTION

Rocket systems ranging in size from small, single-stage meteorological rockets to large, multi-stage sounding rockets, have been used for more than 25 years to investigate the middle atmosphere (~20-100 km). These measurement techniques, while once used extensively are only occasionally used today. The techniques discussed in this chapter, summarized in Table 1, are the pitot probe, acoustic grenade, falling sphere, chemical trail, chaff, and the immersion thermistor, all of which basically provide temperature, density, and wind measurements. Satellite remote sounder instruments also provide atmospheric measurements at a very high sample rate on a global scale. The technological aspects of these satellite instruments, while interesting, are not part of this discussion. Nonetheless, satellite measurements require ground-truth information, often provided by the rocket techniques discussed here (MILLER and FINGER, 1972).

Early observations of the atmosphere were accomplished with instruments carried upward by kites, airplanes, and manned balloons. The kites and airplanes eventually were replaced by balloons capable of carrying small radio transmitters and sensors (called radiosondes) thus permitting measurements to be made to higher altitudes. Improvements in the balloons and radiosondes soon enabled altitudes of 15-20 km to be reached; today altitudes to 30-35 km are routinely sounded from a global network of sites. As these observations were obtained higher in the atmosphere new and important features were discovered. Among the early discoveries was the westerly jet stream occurring in middle latitudes at 8-12 km altitude, and the easterly jet stream occurring near 10°N to 20°N latitude at 30-35 km. These jet streams were basically observed with balloon-borne instruments as was the discovery of the sudden stratospheric warming by SCHERHAG (1952). Stratospheric warmings are wintertime phenomenon and appear strongest near the top of the balloon ascents where large temperature increases of 50°C have been observed to occur within a few days.

Radiosondes were first used to observe another unexpected atmospheric phenomenon, the pronounced quasi-biennial (26 month) oscillation in the equatorial atmosphere (REED, 1965). The 26 month, or quasi-biennial oscillation is most noticeable in the zonal wind which is easterly for one-half the period and westerly for the other half. Radiosonde data show that this oscillation generally occurs above 20 km altitude. Observational data later obtained from rocketsondes showed that the upper bound occurs near 40 km. All of these interesting discoveries using balloon-borne instruments encouraged researchers to extend the measurements to higher altitudes. Their appetites were whetted to learn the origin of these strange phenomena, the dynamics and structure of the higher atmosphere, and the extent and implication of these features.

Early attempts to measure the physical properties of the upper atmosphere with rockets were secondary experiments permitted to be made during tests of large rocket vehicles, such as the captured V-2 rocket at White Sands Proving Grounds during the late 1940s. Development of special rocket systems for determining atmospheric structural parameters soon followed. The capability for making observations of atmospheric features was rapidly being placed on a firm experimental basis. Yet, the few soundings that were possible could not provide an altogether complete picture of atmospheric behavior. The cost and complexity of these large systems inhibited their use in great numbers and created the impetus toward the development of small, low-cost rocket vehicles.

The availability of the less expensive, small meteorological rocketsondes prompted the idea of simultaneous launchings from different locations. Initially, synoptic launchings made within the United States were scheduled only for a few days during the middle of each season. Launch frequency soon increased to three to five times a week from as many as 30 launch sites. The accumulation of these data has resulted in a climatology of the stratosphere and lower mesosphere which has been widely characterized in the development of standard and reference atmospheres.

Table 1 summarizes the large and small systems that have been, or are used extensively. Since the large rocket systems no longer are used to the extent they were a few years ago, they will be discussed at the end of this chapter. The small meteorological rocketsonde is launched routinely from 12 sites at the present time and is increasingly being employed in large research missions by various experimenters. Since meteorological rockets have provided a considerable amount of middle atmosphere data, they will be discussed in some detail.

The improvements made in the Standard Atmosphere during the past 30 years are well illustrated in Figure 1, where models for 45°N are presented. Standard Atmospheres, for periods earlier than 1955, are not shown, but it is now known that those pre-1955 models were quite inaccurate. The 1955 Standard Atmosphere (NACA, 1955), for lack of measurements to higher altitudes, does not extend above 20 km. The temperature data used to construct this atmosphere were obtained primarily from radiosonde observations. With the exception of the profiles of the 1966, January and July atmospheres (COESA, 1966), little change occurred below 50 km between 1955 and 1976. More precise and accurate measurements above 55 km, obtained since 1955, enabled more sensitive models to be produced to higher altitudes. The 1962 and 1976 US Standard Atmospheres (COESA, 1962; 1976) are almost identical; above 52 km some differences are noted. The 1966 Supplemental Atmospheres for January and July clearly bracket the 1955, 1962, and 1976 atmospheres and also point out the cold mesosphere during July and the warmer temperatures during January.

More recently, reference atmospheres have been compiled for 11 US launch sites. Profiles between the surface and 70 km are available for each month, thus, increasing the usefulness of the model. The Wallops Island Range Refer-

TABLE 1. US ROCKET SYSTEMS USED TO MEASURE THE NEUTRAL ATMOSPHERE

Sensor	Technique	Parameters	Capabilities	Peripheral Information*	Used For
Chemical Trail	Photograph Vapor Trail Movement	Winds 90-170 km	High Resolution Night Sounds Remote Site	Large Vehicle and Payload 20K/Sounding Hazardous Material Non-Routine Data Reduction Simple Instrumentation Active	Special Studies
Acoustic Grenade	Detect Sound Arrival at Surface with Microphones	Temp/Density/ Winds 30-90 km	2 km Resolution Day/Night Remote Site	Large Vehicle and Payload Cost 45K/Sounding Non-Routine Data Reduction Simple Instrumentation Inactive	Standard Atmos. Special Studies
Pitot Probe	Senses Ram and Static Pressure	Temp/Density 60-120 km	High Resolution Day/Night Remote Site	Large Vehicle and Payload Cost 60K/Sounding Non-Routine Data Reduction Complex Instrumentation Inactive	Standard Atmos. Special Studies
Instrumented Rigid Sphere	Senses Drag Acceleration	Temp/Density 60-150 km	High Resolution Day/Night	Large Vehicle and Payload 60K/Sounding Non-Routine Reduction Complex Instrumentation Tracking Radar Required Active	Special Studies Reentry Support Standard Atmos.
Inflatable Sphere	Drag Acceleration and Velocity Derived from Precision Radar Track	Temp/Density/ Winds 30-90 km	Moderate Resolution Day/Night	Small Vehicle and Payload 5K/Sounding Standardized Data Reduction No Instrumentation Precision Radar Required Operational	Special Studies Reentry Support Satellite Support Standard Atmos.
Datasonde	Temp Measured by Thermister	Temp/Density/ Winds 20-65 km	Moderate Resolution	Small Vehicle and Payload 5K/Sounding Standardized Data Reduction Instrumentation/Tracking Radars Required Operational	Special Studies Reentry Support Satellite Support Standard Atmos.

*Cost per sounding is in 1984 dollars (US).

ence Atmosphere (RCC-MG, 1983) temperature profile also is shown in Figure 1 and clearly is comparable to the US Standard Atmosphere.

As a further illustration of the usefulness of monthly reference atmosphere data, vertical cross sections of temperature and zonal wind for Wallops Island were constructed. Contours of mean values, as well as the magnitude of the standard deviation are given in Figures 2a and 2b. Given sufficient data, reference atmospheres such as these may be constructed for any location.

SMALL METEOROLOGICAL SYSTEMS

The cost of employing large rocket systems in great numbers for synoptic atmospheric studies, or even for small-scale (space and time) studies of atmospheric structure can be prohibitive. The development, which began in 1959, of small, low-cost rocket vehicles that could lift meteorological instruments to altitudes above 30 km (i.e., above balloon limits) reached a plateau in the early 1970s with the implementation of the Super Loki Datasonde (BOLLERMANN, 1970). Prior to the availability of the Super Loki system, the major small system employed by the rocket ranges was the Arcasonde. This system was sensitive to low level winds that often inhibited its use when surface winds exceeded 15 knots or were gusty. The apogee attained was nominally 60 km where payload ejection occurred. The payload consisted of a bead thermistor that

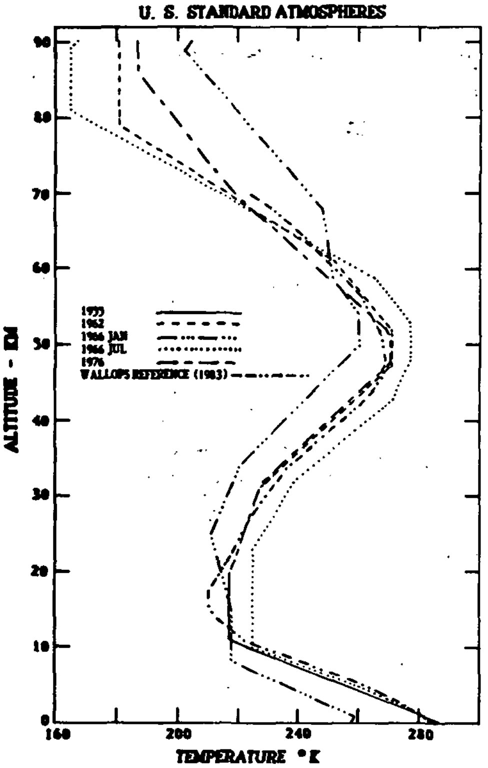

ORIGINAL PAGE IS
OF POOR QUALITY

Figure 1. Standard atmosphere profiles of temperature for 45°N latitude developed since 1955. Radiosonde and rocket measurements provided the major data base. The reference atmosphere shown for Wallops Island, Virginia (38°N) is constructed exclusively from radiosonde and rocket information.

sensed temperature and a transmitter lowered by a parachute. Wind data were obtained by radar tracking the parachute. The Arcas rocket motor was lengthened during the early 1970s to enable it to reach higher altitudes (∿80 km) and was renamed Super Arcas. Although no longer used in the United States for meteorological measurements, the Super Arcas vehicle is capable of carrying other types of measuring devices. A good summary of the Arcasonde technique can be found in BALLARD (1967). The Arcas system has a history of performing well through thousands of launchings; however, its wind sensitivity at launch was an operational liability. A less wind-sensitive vehicle was undergoing development concurrent with the use of the operational Arcas systems. This rocket system, the Loki Datasonde, was the first system to successfully compete with the Arcasonde in terms of operational ease and data comparability.

The small rocketsonde, while telemetering temperature information to a ground receiving site, also must be tracked with radar to determine the payload position with respect to time. From this radar information, atmospheric wind profiles are established. The radars used for this purpose are of variable quality, so that very precise wind information may be obtained only at those launch sites using high precision C-band radars, such as the FPS-16. Because of the need to calculate first and second derivatives in order to properly determine the wind profile, these precision radars are important. However, lesser quality radars can be used with degradation in the precision of the wind measurement.

During the years of the 1960s and 1970s, other countries also were developing and launching small meteorological rocketsondes. These include:

ORIGINAL PAGE IS
OF POOR QUALITY

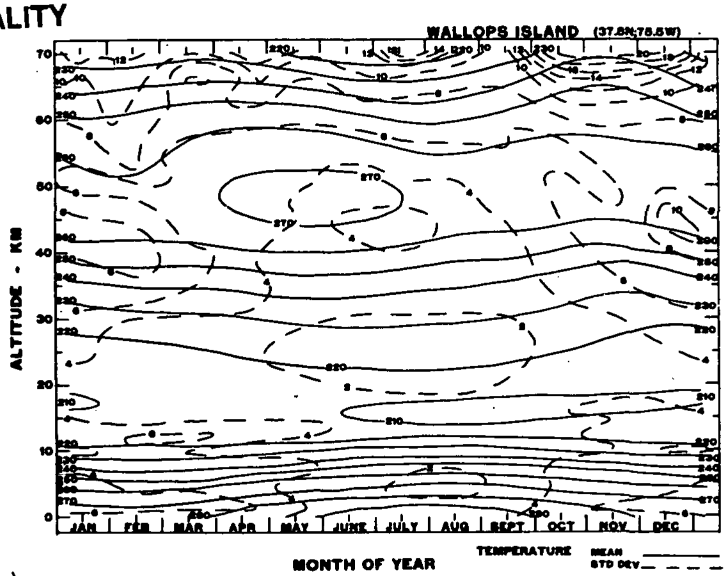

a)

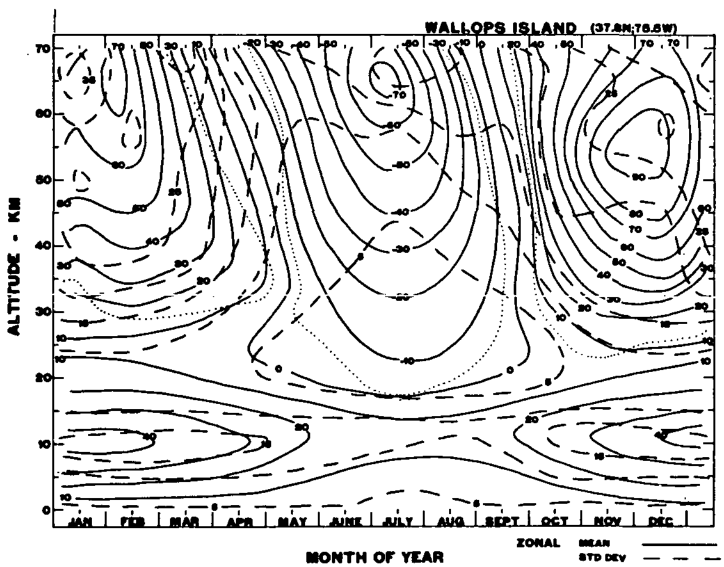

b)

Figure 2. a) Time-height cross section constructed from the Wallops Island, Virginia (38°N) Range Reference Atmosphere (RCC-MG, 1983). Contours for monthly mean temperatures are shown by solid lines and contours of the standard deviation are shown by the dash lines. b) Same as a) except for zonal wind component. The dotted line indicates where the mean wind and standard deviation are the same magnitude.

Japan (MT-135P System). The Japanese MT-135P rocket system is designed to reach ∿60 km altitude where a parachute and transmitter containing a temperature sensor are deployed. The rocket motor is 3.33 meters long and the system, including the payload, weighs approximately 70 kg. The payload, called Echosonde, is a pulse-position-modulation system and contains a temperature sensing device made of a very small-diameter (∿20μ) nickel-iron wire strung on a 10x43 mm frame. Upon receiving a 1673-MHz signal transmitted from the ground equipment, the Echosonde transmitter returns two pulses on a frequency of 1687 MHz. The first pulse retransmitted to the ground equipment is a ranging pulse (i.e., the distance between ground equipment and sonde), the second pulse returned is the temperature information which is determined by its position relative to the first pulse. During the observation, slant range and angular data measured by the ground system are continually recorded from which positional information may be determined. Subsequently, altitude and wind data are derived. The temperature measurements are corrected for aerodynamic heating, radiation, lag, and electrical heating. The total temperature correction at 60 km is approximately 22°C (YATA, 1970). Significant temperatures are selected based on changes in the lapse rate. Wind data are also corrected for fall velocity and ballistic motion effects.

A comparison of wind and temperature data was conducted in 1967, between the MT-135P and the Arcasonde (MILLER et al., 1968). Although a limited sample of measurements was available for study, it was concluded that the data from the MT-135P and Arcasonde were compatible. During 1972, the MT-135P system was also compared with rocketsondes of the United States (Loki-Datasonde) and France (Super Arcas-DMN) as part of the CIMO intercomparison of rocketsondes (LEVITON, 1973).

France (DMN). The French meteorological sounding rocket is comprised of a US manufactured Super Arcas motor and a French designed and fabricated payload called DMN. The French system measures temperatures and winds up to an altitude of 80 km. The DMN rocketsonde payload contains two temperature sensors. One, the prime sensor, is a 5-μ diameter tungsten wire, 2 cm long, coated with gold to prevent oxidation. The time constant of this sensor is approximately one second at 80 km and much faster in the lower altitudes. The tungsten wire is attached to long constantan wires in order to provide thermal isolation from the large mass of the payload body. The second sensor, made of nickel, is plated by vacuum evaporation on a nylon support and anodized with aluminum. The second sensor provides redundancy if the prime sensor fails, and is usable only below 60 km altitude.

The telemetry system converts the resistance measurements of the sensors to frequency variations by means of two converters. These two low frequencies modulate two sub-carriers of 40 MHz and 70 MHz which are demodulated after being received at the telemetry site on the ground. The demodulated signals are then recorded on a multiple track magnetic tape recorder concurrently with radar position data in order to provide profiles of wind and temperature data versus altitude. The sonde was originally fabricated to use 403 MHz and 229.9 MHz for transmitting.

Wind data are corrected to remove ballistic motion and fall velocity effects from the measurements. Temperature measurements are corrected by solving the heat-transfer equation applicable to the wire sensor. The parameters considered are convection, radiation, electrical heating, aerodynamic heating, and conduction. Temperature correction values are of the order of 17-35°C at 70 km and about 5-8°C at 60 km.

The French DMN rocketsonde was compared in 1972 with the US and Japanese rocketsondes at Wallops Island during the first phase of the CIMO Rocketsonde

Intercomparison (LEVITON, 1973), and again in 1973 with rocketsondes from the UK, USA, and USSR at Kourou, French Guiana (FINGER et al., 1975).

A report on the comparison of the temperature measurements resulting from the first part of the CIMO Rocketsonde Intercomparison revealed the Japanese measurements to be generally compatible with those of the United States while some incompatibility between the French and United States temperatures were noted above 45-50 km. Wind comparisons indicated no bias between these systems but the random variation was noted to increase with altitude.

Great Britain (SKUA). The British SKUA is a relatively inexpensive meteorological rocket system intended for routine synoptic studies of the upper atmosphere. This system is no longer launched since Great Britain no longer maintains a routine launch schedule. The SKUA is 2.26 meters long and 0.131 meters in diameter and weighs approximately 78 kg. Apogee is in excess of 70 km with an 8-kg payload. The standard meteorological payload weighs approximately 5 kg and uses a 4.6-meter diameter radar-reflecting parachute. The sonde transmits at a frequency of 28 MHz. The temperature sensor is tungsten wire of 13.5-μ diameter, 772 cm in length, and is supported in "spider web" fashion on a plastic frame spiraled around an 8.9-cm diameter ring.

Temperature data are corrected for aerodynamic heating and radiation. The lag of the sensor is considered negligible since the time constant at 61 km is only 0.9 seconds. The greatest single correction to be applied to the SKUA payload is that caused by solar radiation incident on the sensor which varies according to the solar angle, albedo, and effective area of the sensor receiving radiation at a given time. This is difficult to estimate because of parachute oscillations on the descent. Because of the uncertainty associated with this correction, rocket launchings generally were conducted at night. temperatures from the SKUA payload were found to agree with those from the US and French rocketsondes (FINGER et al., 1975).

USSR (M-100). The Soviet M-100 rocket system is a two-stage, unguided, solid-fuel rocket motor with a payload designed to measure temperature, pressure, and wind. The first-stage rocket motor burns out at about 2-3 km where the second-stage motor ignites and carries the payload to apogee, near 90 km.

The payload contains a parachute and transmitter, as well as the measuring sensors. The nose cone is ejected and the sensors are uncovered during ascent at about 60 km. The parachute is also deployed on the ascent and after passing apogee acts as a stabilizing drag during descent to about 65 km where wind sensing begins. Sensor information is telemetered to a ground site receiver and a transponder is used to determine the payload's position.

Pressure sensing is accomplished by the use of two Pirani gauges and an aneroid, or diaphram device. The pressure gauges are each capable of measuring over two pressure ranges, one between 5.0- to 1.5-mm Hg and 1.5- to 0.5-mm Hg and the other between 0.5- to 0.05-mm Hg and 0.05- to 0.005-mm Hg. The pressure gauge's temperatures are commutated periodically for application of temperature compensation corrections. The aneroid device also is capable of measuring over two ranges of pressure, 5- to 140-mm Hg and 140- to 250-mm Hg. The temperature of the aneroid cell is also measured and commutated periodically.

Two pairs of resistance wire thermometers are used to measure temperature. Each pair is capable of measuring over two temperature ranges. One pair measures between -100°C to 100°C and 0°C to 250°C; the second pair measures between -20°C to 200°C and 90°C to 350°C. The thermometers are mounted on long arms which are folded during launching and are erected perpendicular after

payload ejection in a way that ensures that the air outside the boundary layer is measured. In order to apply conduction corrections, the temperatures of the mounting arms are also measured. Each resistance wire is 40 μ in diameter, made of tungsten, and is 13 cm long. Calibration of the sensors is usually performed within 7 days prior to launch. The information measured by all of the sensors in commutated to the ground site at the rate of 60 pulses per 5 seconds and includes inflight calibration checks, as well as data.

The telemetry and position data received at the ground are put on photographic film in real-time and upon completion of the observation are read off the developed film and plotted on graph paper. The measurements are then processed in two stages. The first stage converts the recorded signals from the sensors into numerical values; the second stage is the calculation, or derivation, of the atmospheric parameters.

The temperature measurements are corrected for aerodynamic heating effects, lag, emissivity, self-heating, conduction, and long- and short-wave radiational heating. The wind data are corrected for fall velocity effects.

The comparison that took place at the Guiana Space Center, Kourou, French Guiana in 1973, was extremely interesting. Temperature differences between measurements of France and the United States and Great Britain and the United States were small up to 55 km during daytime and to almost 70 km during nighttime. Surprisingly (and still unexplained), the differences noted between France and the United States during the comparison in French Guiana were opposite to those observed during the Wallops comparison. A lack of comparability between the temperature measurements of the USSR rocketsonde and the other rocketsondes was found above 45 km. Wind data compared well between France, Great Britain and the United States but, above 40 km the USSR results were considerably different.

During 1977, a bilateral agreement between the United States and USSR led to another comparison at Wallops Island (SCHMIDLIN et al., 1980). The USSR had made changes to the M-100 parachute and the reduction procedures prior to the 1977 test which provided a part of the reason for this test. The conclusion of the test flight data was that better agreement now exists between these two measurements above 40 km, but large differences still exist above 55 km (temperature) and 60 km (wind).

United States. The small meteorological rocketsondes used exclusively at launch sites within the United States since the early 1970s, and more recently at other launch sites with increasing frequency, are the Super Loki Datasonde and Super Loki Sphere. These rocketsondes also have been used in many experimental campaigns, for example, the Energy Budget Campaign which took place during November-December 1980, in Northern Scandinavia (OFFERMANN, 1985), the MAP/WINE Campaign which took place during the winter of 1983-1984 (VON ZAHN, 1983), and during Project Condor in Peru during March 1983 (GOLDBERG, 1984). Other experimental campaigns also have used the Datasonde and Inflatable Sphere and plans have been developed for their future use.

The Super Loki Datasonde provides atmospheric temperatures and winds at measured altitudes while the Super Loki Inflatable Sphere provides atmospheric density and winds. Both systems must be tracked by a ground system, such as radar, in order to define the payloads' position and to enable wind information to be deduced. Datasonde-measured temperatures and winds are available from 70 km down to about 20 km; the lower altitude limit being established by either the payload's battery life or mission requirements. The inflatable sphere dart reaches a nominal altitude of 115 km and, after sphere inflation, provides density data from about 90 km down to 30 km, where the sphere collapses. An advantage of these small US rocket systems is that both use the same rocket motor. Additional information is given in Table 1.

ORIGINAL PAGE IS
OF POOR QUALITY

The Super Loki Datasonde system is basically a small rocket motor with an inert (non-propulsive) Datasonde payload (contained in a dart-type vehicle which has a high ballistic coefficient). The rocket motor is a 10.2-cm diameter high-thrust, internal burning solid propellant unit with a burning time of approximately two seconds. At rocket motor burnout, dart separation occurs due to drag force differential between the larger diameter motor and the smaller diameter dart. A 3.66-meter long helical rail launcher provides support and imparts the spin to the dart vehicle during the launch phase. The dart consists of an ogive, body assembly (dart body), and tail assembly and is coated with an ablative material to reduce the effect of rather severe aerodynamic heating. The dart body contains the decelerator (parachute) and instrument payload. The dart tail contains the delay and ejection system. After separation from the rocket motor, the spin-stabilized dart coasts to apogee where payload ejection occurs at approximately 120 seconds following zero time, or liftoff. The Datasonde instrument transmits temperature data over a carrier frequency of 1680 MHz while descending on the decelerator. (The 403-MHz frequency also has been used successfully.) Figure 3 shows typical dimensions and pre-launch configuration of the Super Loki Datasonde system.

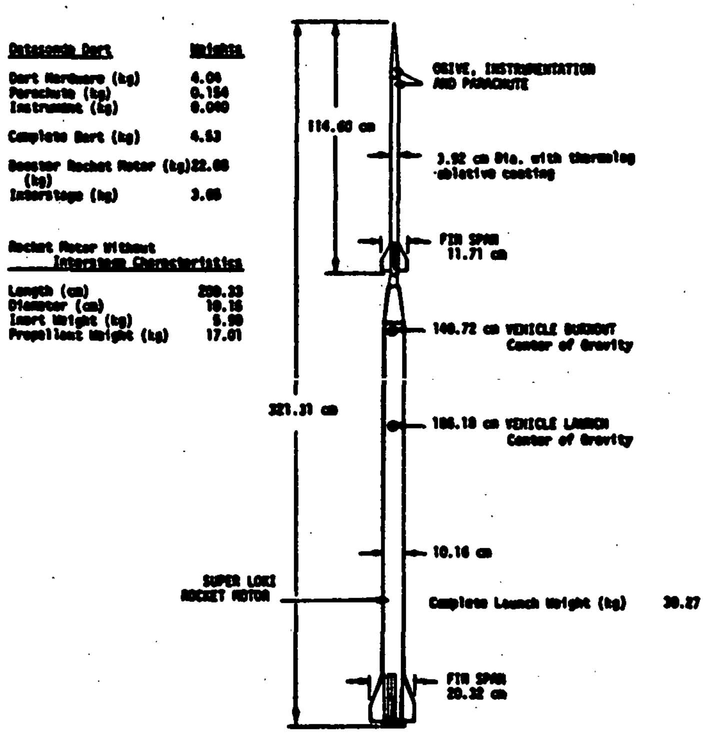

Figure 3. Schematic of the US Super Loki Datasonde. Payload apogee is 80 km from a sea level launch site. High launch velocity makes this system usable during severe surface wind conditions.

The Datasonde decelerator, shown in Figure 4, called a "Starute" also serves as the wind sensor. Portions of the "Starute" have been metalized to facilitate radar tracking. Atmospheric wind data are obtained from the first and second derivatives of the positional data obtained from the tracking radar.

The temperature sensor is a small, aluminized bead thermistor ($\sim$0.25 mm in diameter) whose electrical resistance varies inversely with its temperature. The thermistor is mounted on a mylar loop by means of short lead wires. The mylar loop, shown in Figure 5, is thinly coated with aluminum on the side facing the transmitter and serves to reflect the long-wave radiation from the instrument's body. As the atmospheric temperature varies during the instrument's descent, the varying thermistor resistance controls the modulation rate of the data circuit. The temperature signals are interrupted periodically through electronic switching to permit the transmission of a reference resistance value. This reference frequency is used to monitor changes in the instrument's electronics.

The configuration of the Super Loki Sphere system is similar to that of the Super Loki Datasonde system. The same 10.2-cm diameter rocket motor is used, the dart, however, is slightly smaller in diameter and attaches to the motor adapter in a slightly different manner. The dart reaches a nominal apogee of about 115 km where the sphere is ejected and inflates.

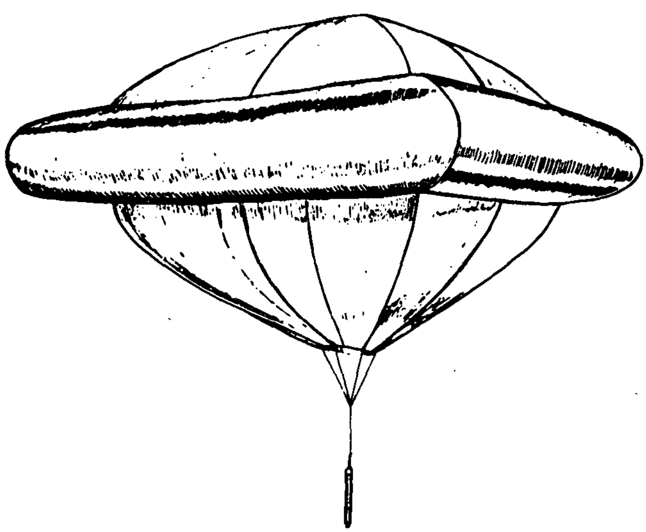

Figure 4. Datasonde payload decelerator and wind sensor. The decelerator is called a "STARUTE" and is very stable during descent. The torus acts to create a flow disturbance which aids stability. Starute inflation is maintained by ram air which enters through a relatively small hole at the bottom.

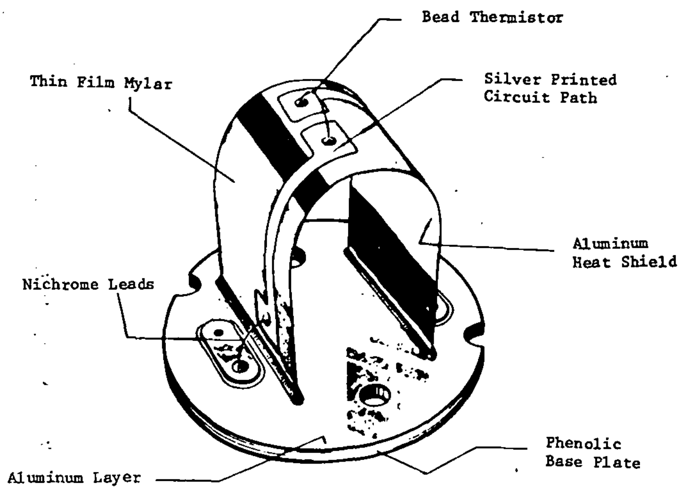

Figure 5. Datasonde thermistor mount. The aluminum-coated mylar mount acts as a heat shield to reflect radiated heat back to the payload body.

The passive inflatable sphere payload is a one-meter diameter inflatable spherical balloon made from ∿0.01-mm thick mylar which is aluminized to enhance radar tracking. A small charge of an inert gas is used to inflate the sphere to a super pressure of about 10-12 mbar, or approximately 32-km altitude. Sphere collapse occurs when the ambient pressure exceeds the sphere's internal pressure.

Tracking of the falling sphere by a high-precision radar is an absolute requirement in order to obtain usable atmospheric density and wind data. Temperature data are obtained from the density data through the application of the perfect gas law.

MEASUREMENT TECHNIQUES

Datasonde Temperature. The temperatures sensed by the Datasonde thermistor are received at the ground where they are time-correlated with radar-derived altitudes. The measured temperatures are those of the thermistor and not those of the atmosphere and must be adjusted to ambient using a detailed correction procedure. The correction method developed by HENRY (1967), accounts for all known external influences and was adapted for use with the Datasonde by KRUMINS and LYONS (1972). The thermistor temperature is adjusted to ambient by applying a heat transfer equation that accounts for aerodynamic heating, emissivity, sensor lag, and radiation. The aerodynamic heating term is proportional to the square of the fall velocity ($\dot{Z}^2$). The Datasonde's fall velocity at 60 km is about 100 mps making the temperature correction nearly 5°K, at twice this fall velocity the correction would be four times larger. The emissivity term is proportional to the fourth power of the thermistor temperature T_t^4, and the lag term is dependent on the actual atmospheric lapse rate. The radiation correction includes short- and long-wave radiation and, for simplicity, is fixed for each altitude. Only the long-wave radiation correction is applied at night. Although the correction terms are small at low altitudes, they increase sharply as 70 km is approached.

ORIGINAL PAGE IS
OF POOR QUALITY

Using the profile of corrected temperatures and the known radar altitudes, pressures may be calculated for the rocket altitudes by integration of the equation of state and hydrostatic equation. Thus, the hypsometric relation

$$P_1 = P_o \cdot \exp[-g\Delta Z/R'\bar{T}]$$

may be solved for each increment of altitude ΔZ, where g is the acceleration of gravity, R' is the specific gas constant for dry air, and $\bar{T}$ is the mean temperature in the interval ΔZ. Density may then be derived from the gas law. The initial pressure P_ρ, required for integration of the hypsometric equation, is normally obtained from a radiosonde observation obtained close in space and time. A 5-6 km overlap of the radiosonde and rocketsonde temperature profiles is desirable so that a suitable initial level may be obtained (usually near 20 km or 50 mbar). Any inaccuracy or profile difference in the overlap region (i.e., in altitude, pressure, or temperature) results in a constant percentage bias in the computed pressures and densities and may be due to errors of the radiosonde or rocketsonde and/or space and time differences between them.

Horizontal Wind. Radar tracking of the Starute or inflatable sphere permits the horizontal winds to be calculated. The wind reduction method is relatively simple and straightforward in that successive position and time differences are used to calculate wind direction and speed. Because of fast descent at higher altitudes, the decelerator responds slowly to horizontal changes in the wind making it necessary to apply corrections. The correction equation for the zonal (east-west) wind

$$W_x = \dot{X} - \frac{(\dot{Z}-W_z)\ (\ddot{X}+C_x-B_x)-g_x}{\ddot{Z} + C_z - B_z - g_z}$$

includes all known effects regardless of their relative magnitude. The equation for calculating the meridional (north-south) wind W_y is identical. Many of the terms in this general equation may be ignored since, for example, the buoyancy force B_z is insignificant for the altitudes over which measurements are made, the vertical coriolis term C_z has little or no effect below 90 km, and the horizontal component of gravity g_x is about 10 percent the magnitude of the error in g_z so that it too may be ignored. With all these assumptions, the zonal wind reduction equation becomes

$$W_x = \dot{X} - \frac{\dot{Z}\ \ddot{X}}{|\ddot{Z}-g|}$$

where $\dot{X}$ and $\ddot{X}$ are the Starute's horizontal velocity and acceleration, and $\dot{Z}$ and $\ddot{Z}$ represents its vertical velocity and acceleration.

It should be noted that the inflatable sphere falls 2-3 times faster than the Starute, consequently its reduced winds are notably smoother, especially at altitudes above 50 km.

Inflatable Sphere Density. In order to obtain density data from the inflatable sphere, a precision tracking radar must be available. Precise calculation of the first and second derivatives of the sensor's measured position is necessary for accurate determination of density. The standard reduction program used in the United States begins the calculation of density ρ, when the vertical acceleration $\ddot{Z}$ of the falling sphere reaches -8 meters/sec^2, usually between 90-100 km (LUERS, 1970). The relation

$$\rho = \frac{2m(\ddot{Z}-g_z-C_z)}{C_d A|V|(\dot{Z}-W_z) + V_b g_z}$$

considers all of the forces acting on the sphere, however, the effects of the coriolis (C_z) and buoyancy ($V_b g_z$) terms may be ignored since they are small. Measurement of the verical winds W_z is not possible with the present system since these are usually 2-4 orders of magnitude smaller than $\dot{Z}$ and are assumed to be equal to zero. Thus, the equation for density may be simplified to

$$\rho = \frac{2m(\ddot{Z}-g_z)}{C_d A|V|\dot{Z}}$$

The terms in this equation are sphere mass m, drag coefficient C_d, sphere cross-sectional area A, and motion of the sphere relative to the air V.

Once the density is obtained, pressure and temperature may be determined. Hence,

$$P(Z) = P_o - \int_{z_1}^{z_2} \rho g dz$$

and

$$T(Z) = \frac{1}{R'} \cdot \frac{P(Z)}{\rho(Z)}$$

The initial pressure P_o, is dependent on a "guess" temperature obtained from the US Standard Atmosphere (COESA, 1976), thus, $P_o = R'T_o\rho(Z_o)$. It follows that the accuracy of the subsequent values of the calculated parameters depends on how close the initial guess temperature is to the actual temperature. Because of this limitation, the temperatures are assumed not to be representative of the actual atmosphere until at least two scale heights (~12 km) below the initial calculations.

DATA QUALITY

Paramount questions of concern often asked are: How good are the measurements? How large are the errors? Measurements made within minutes of each other can be different, often looking as if the measurements were obtained hours, or even days apart. These differences are generally considered to be due to small-scale atmospheric variation, but unless reliable information about the instruments is available the differences observed may be considered due to the instrument.

Temperature. Precision studies of the Datasonde's temperature measurements show that they are repeatable to within 1°K up to 53 km, with a decrease in precision to about 3.8°K at 65 km and 7.5°K at 70 km (SCHMIDLIN, 1981). Other efforts to understand high altitude temperature measurements were made by HOXIT and HENRY (1973), who looked at temperature errors related to altitude and time of day (solar angles), by KRUMINS and LYONS (1972), and by KURMINS (1978), who developed usable optimal corrections for the measurements following theoretical analysis and suggestion by HENRY (1967).

Computation of pressures and densities from the measured temperatures and altitudes depends on an initializing level at the lower end of the rocket-

sonde's temperature profile. The level selected is correlated to a radiosonde observation obtained close to the time of the rocket launch. Experience has shown that the temperature difference between the radiosonde and rocketsonde is usually less than 1°C. It is possible to keep time differences between these instruments to an absolute minimum by exact scheduling; spatial differences, while always a problem, usually are less than 100 km. Radiosonde observation times at rocketsonde sites are controlled so that the balloon-borne instrument, given a nominal ascension rate of 5 mps, reaches the 30-70 mbar layer (∿18-26 km) at approximately the same time that the descending rocketsonde reaches the same layer. Larger differences between the two profiles usually are observed during the winter season because of the stronger temperature gradients that exist. The radiosonde is not an absolute measuring device of pressure and altitude, nevertheless, pressure-heights usually are correct to within 40-50 meters (NESTLER, 1983).

Whenever experimental measurements are in question, knowledge of the precision (or repeatability) of the instruments employed is important. An excellent example of this arises from measurements obtained during the Middle Atmosphere Electrodynamics (MAE-1) program carried out in Northern Norway during October 1980. Two Datasonde temperature profiles, shown in Figure 6, were obtained within the same night and show differences which are much larger than the 1°K rmsd reported in SCHMIDLIN (1981). The question raised, is whether the differences are from a faulty instrument or atmospheric variability. Since this experiment was carried out at a remote location where representative ground tests could not be made, two tests were conducted that still permitted the objectives of MAE-1 to be achieved. The first was to launch one system at the same local time on each of four consecutive nights, and the second was to launch three systems as close together in time as possible. The four successive measurements do not indicate any consistent pattern, and might possibly be representative of the day-to-day variability of the high-latitude atmosphere. The differences observed, while relatively large (the largest 24-hour difference being 9-10°C), were still smaller than those seen in Figure 6. This suggests that one measurement (possibly both) shown in Figure 6 may be unrepresentative, possibly even bad. On the other hand, the three profiles obtained within the 4-hour period also varied considerably, as seen in Figure 7. The conclusion from Figures 6 and 7 suggests that the high-latitude stratosphere and lower mesosphere may be more active than previously had been considered. The profiles seen in Figure 7 suggest that the observation made at 2033 UT is inconsistent with the observations at 2231 UT and 0026 UT. If the plotted profiles are separated by the time difference between the observations as was done in Figure 8, it becomes clear that on this night temperature waves or perturbations existed which appeared to move downward. This then raises an additional question regarding the source of the perturbations.

The validity of Datasonde temperatures is highly dependent on the instrument's calibration. Tests conducted by SCHMIDLIN (Table 1, 1981) indicate that poor calibration should not be a problem. Calibrations from a sample of 18 instruments were checked with positive results, i.e., the calibrations provided by the manufacturer showed no signs of deterioration after 2-3 years. This same paper also points out the Datasonde's capability to obtain temperature measurements with a precision of better than 1°C up to 53 km altitude, and better than 1.6°C up to 60 km. Thus, the variation observed during MAE-1 is believed to occur from natural variability of the atmosphere and not instrument malfunction.

Wind. The quality of the wind information obtained from falling targets depends on radar quality, sample rates, editing and filtering of the raw radar data, and the fall speed of the sensors. Winds obtained from radar tracking of the Starute and inflatable sphere are comparable even though the fall speeds are different. The sphere falls at supersonic velocity above 70 km while the

ORIGINAL PAGE IS
OF POOR QUALITY

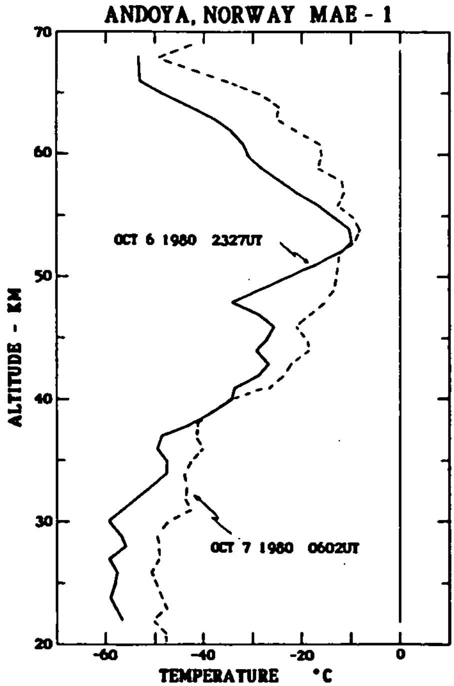

Figure 6. Datasonde temperature profiles obtained during the Middle Atmosphere Electrodynamics (MAE) experiment conducted during October 1980, from Andoya, Norway (70°N). The observed differences between the profiles are larger than those typically observed in mid- to low-latitudes.

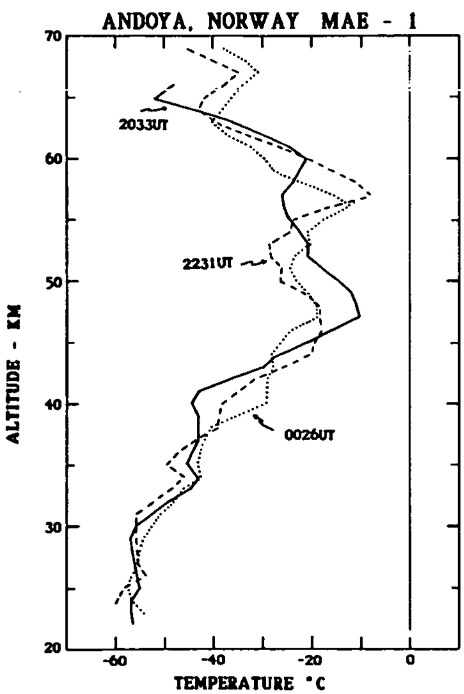

Figure 7. Datasonde temperature profiles obtained over Andoya (70°N) within a few hours of each other during the same night indicate that large variability may be the typical characteristic of the high latitudes.

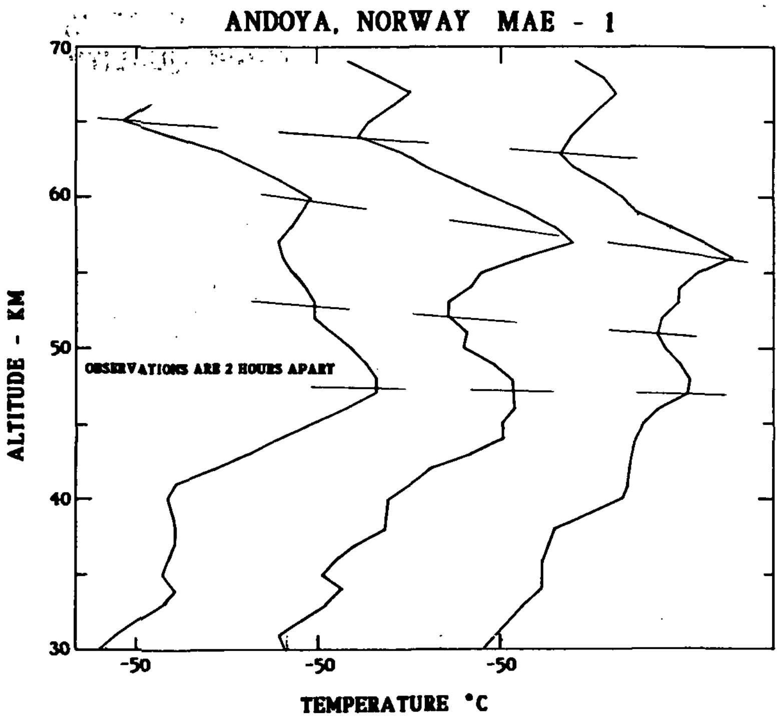

Figure 8. The same temperature profiles shown in Figure 7 but the observations are displayed with two-hour time separations. It appears that downward moving wave structure was present.

Starute does not; for this reason, a discussion of wind data obtained from a sphere may be more interesting.

The primary purpose of the inflatable falling-sphere technique is to provide an inexpensive method for obtaining atmospheric density between 30 and 90 km. However, the sphere's shape also makes it an excellent wind sensor, as well. The inflatable sphere designed to be used in the small meteorological rocket payload body nominally weighs 165 gm. The first and second derivatives of the radar position (x, y, z) information provides fall velocities and accelerations. At the high altitudes reached by the sphere, very little density is present to retard its fall. Thus, because of the high velocities, attained errors in tracking occur which lead to errors in the resulting wind. The magnitude of error is a function of the sphere's fall velocity (BOLLERMANN, 1970; LEVITON, 1962). At fast fall velocities and as the wind shears in the layers increase, the size of the measurement difference between the sensor's horizontal velocity and the actual wind increases. To overcome this situation, corrections often reaching magnitudes of 50-80 mps, are applied to the radar measurements. The size of these corrections can be noted from Figure 9 which shows parachute-derived winds before and after corrections were applied. The corrected wind profiles are compared with chaff-derived winds obtained close in time (BOLLERMANN, 1970) and quite clearly show the success of the corrections being applied to the raw data. The ballistic motion of the rocket

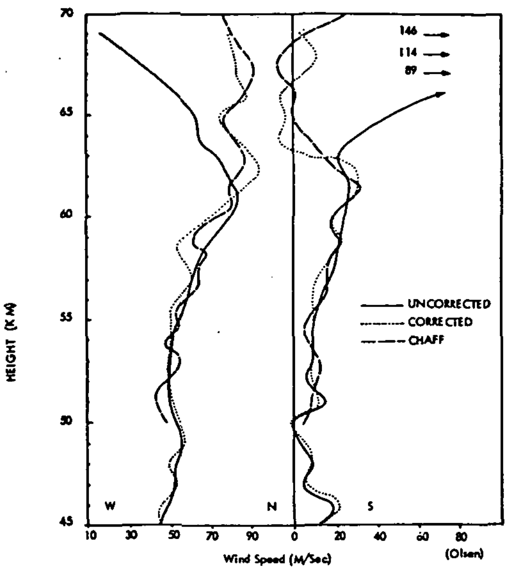

Figure 9. Comparison wind profiles showing uncorrected parachute trajectory, corrected parachute trajectory (wind), and slow falling chaff. The corrected parachute winds show good agreement with the chaff winds.

vehicle is still apparent near the top (above 63 km) of the parachute profile. In general, the faster the wind sensor falls through the atmosphere, the greater the amount of smoothing that must be applied. Thus, in the example shown in Figure 9, perturbations that possibly may be present would not be seen on the corrected wind profile if a fast-falling sphere was used. For some applications, this is not desirable.

Wind measurement resolution may be materially improved by reducing the sensor's fall velocity, especially above 60 km. HYSON (1968) suggested that the sensor's wind response might be expressed in terms of a range constant,

$$h = \tau \dot{Z} = - \frac{2m}{\rho \, C_d \, S}$$

The smaller that h becomes, the better the resolution. In the above relationship, m is the sensor's mass, ρ is atmospheric density, C_d is the sensor's drag coefficient (available from laboratory tests), S the sensor's cross-sectional area, τ is the sensor's time constant, and $\dot{Z}$ the fall velocity.

Examination of this equation shows that the range constant h, can be made smaller by reducing m, by increasing S, or by increasing C_d. However, associated with a change in S would be a corresponding change in C_d, i.e., as S becomes larger, C_d should also become larger. Thus, if S could be made larger without changing m, the effect would be to increase the drag and decrease the fall velocity, thereby reducing h. Larger reductions in h are possible by increasing both S and C_d while decreasing m simultaneously. Figure 10 represents calculations for h at two sphere masses. The smaller values of h(z) obtained for the light sphere indicate that improved wind resolution should be possible.

Two inflatable spheres, which were approximately 50 percent lighter than the standard spheres, were launched from Wallops Island during November 1982. The spheres were lightened by removing the inflation mechanism. Sphere inflation was accomplished solely by entrapped air. During packaging a residual amount of air remains even though a vacuum process is used. The consequence of disabling the inflation mechanism however, caused the spheres to collapse at a

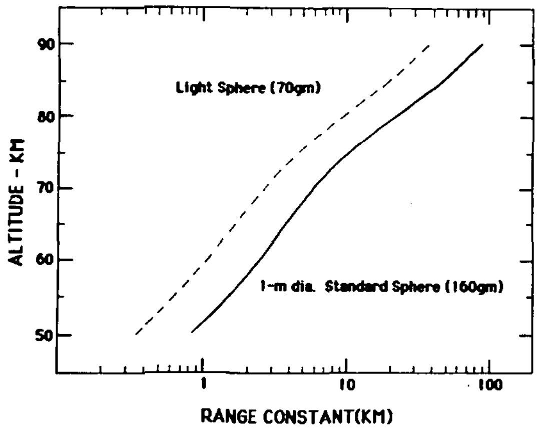

Figure 10. Range constant as an expression of a falling sensor's wind response suggests that a light weight sensor would have a smaller range constant producing better wind resolving capability.

higher altitude than usual (65-70 km vs 30 km). Nonetheless, our concern in this test was only the high altitude winds. Figure 11 characterizes some improvements realized from this modification. First, the wind perturbations seen with the lighter sphere are clearly of a larger magnitude than those obtained with the standard sphere, for example, the wind shear in direction near 68 km. As a result of this test, lightened spheres were used during an electrodynamics experiment that took place in Peru during March 1983.

These wind profiles reveal considerably more structure than would have been obtained if standard weight spheres were used. The perturbations in the zonal wind (u-component), seen in Figure 12, are consistent over time and also are noted to change magnitude with altitude. The striking feature of these data was the very pronounced wind change near 50 km. Below 50 km, the zonal (E-W) wind component was easterly (negative directed) and westerly (positively directed) above. The lower altitude winds were found to be consistent with the easterly phase of the quasi-biennial oscillation while the semiannual and annual phase of the zonal wind above 40 km appear to dominate (ANGELL and KORSHOVER, 1970). Thus, it seems that strong wind shear separates the region below 50 km from the region above. Wind shears of up to 0.025 s^{-1} were found in the nearly 6-km deep layer surrounding 50 km. The layer also was noted to oscillate vertically during the one-day observational period. Concurrent with the vertical distribution of the zonal wind, the meridional (N-S) wind com-

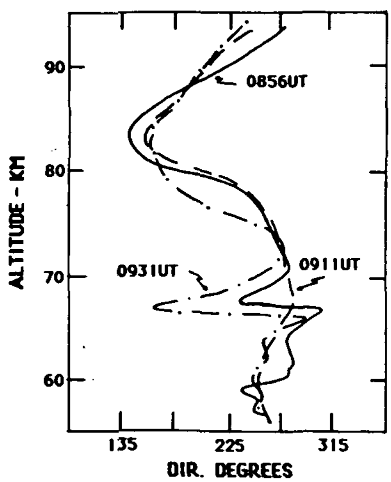

Figure 11. Two light spheres (∿85 gm each), launched at 0856UT and 0931UT, show signigicantly better response to a shear in wind direction than the normal weight (∿160 gm) sphere (0911UT).

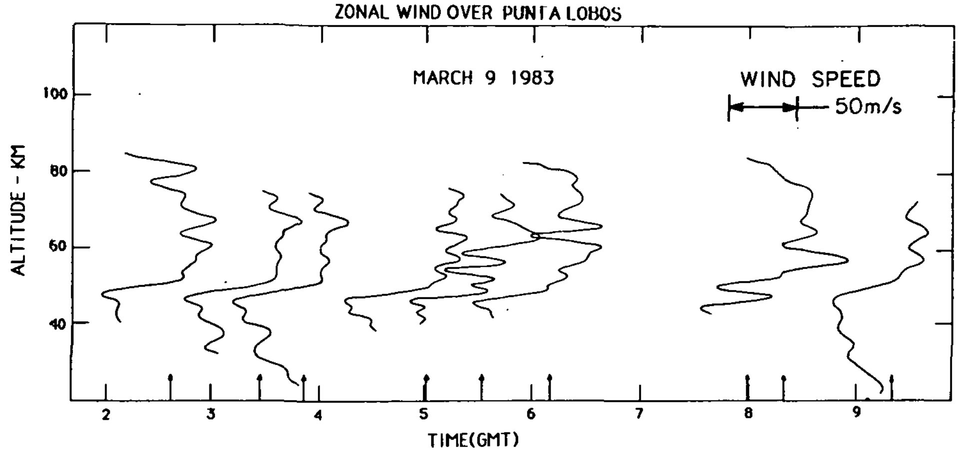

Figure 12. Light weight spheres used during an experiment conducted from Punta Lobos, Peru (~12°S) show enhanced structure of the middle atmosphere. The arrows mark launch timer and zero wind speed. The perturbations shown here might possibly have not been observed if normal weight spheres were used.

ponent was essentially nil below 50 km and directed away from the equator or from the north (negatively directed) above 54 km. It is apparent that two or possibly three circulation regimes overlap in the vertical. This application of the inflatable sphere is a good example of the small meteorological rocket capability for measuring winds to 85-90 km.

Density. The basic measurement made with the sphere is atmospheric density. The quality of the density data is highly dependent on the reliability of positive sphere inflation and its integrity to remain pressurized until its designed collapse altitude of approximately 12 mbars (~30 km) is reached. In addition to sphere reliability, a computer reduction program is required that is specifically designed to produce density from the radar position of the sphere (LUERS, 1970). This program calculates altitude, density, wind, temperature, and pressure at each second of the radar data. The rms noise error in density, temperature, pressure, and winds also are calculated in this program. The sources which produce significant density errors are: 1) random error due to radar noise, 2) bias error introduced by the improper choice of smoothing function, 3) error in initial guess temperature, 4) drag coefficient errors, and 5) vertical winds.

The random error resulting from radar noise is quite large immediately after sphere apogee. Estimates of this error given by LUERS (1970) is eight percent at 95 km decreasing to two percent near 70 km. Below 60 km, a two percent noise error is maintained by gradually expanding the smoothing interval during data reduction.

It is known that a bias error in density occurs when the smoothing function does not fit true perturbations in the position coordinates. Although efforts are made to remove all known bias, some remains, usually this residual bias is one percent or less.

Calculation of density requires that a guess of the temperature be made at the first point being reduced. This first guess temperature comes from the 1976 US Standard Atmosphere tabulations (COESA, 1976). The uncertainty of this first guess temperature (vs true temperature) introduces density errors in succeeding computations that decrease with altitude. The error usually does not extend over more than two scale heights (approximately 12 km) below the first point selected for reduction. A ten percent error in the initial guess temperature translates to about a three percent error in the density data and is usually negligible by 85 km.

Errors in determining the drag coefficient affect the density accuracy in two ways. An error in drag coefficient produces errors in density directly since it is used in the equation to produce density. Errors in density caused by errors in the drag coefficient feed back into producing errors in the calculated Reynolds and Mach numbers used in a table of lookup values to determine the next drag coefficient; hence, density calculations ultimately are derived using the wrong region of the drag table. The drag coefficient is based upon the ballistic sphere measurements of BAILEY and HIATT (1972). These investigators quote a maximum error of two percent over the observational range. In any case, below 90 km altitude, the error in density due to error in the drag table is normally less than one percent.

Finally, errors in density due to vertical winds are very probably present and would vary within a single observation and even between observations. This variation is dependent on the extent of the vertical wind (i.e., magnitude and direction). The effect of the vertical wind is largest at the lower altitudes because the sphere is falling more slowly and is smallest at the top of the trajectory since $\dot{Z}$ is considerably larger than any vertical wind. In general, above 70 km, the density error due to a one-meter-per-second vertical wind is less than one-half percent.

LARGE ROCKET SYSTEMS

Large rocket vehicles generally are designed to carry several experiments to measure related parameters and, in some cases, unrelated parameters. For example, several disciplines of interest which have been studied using large rocket systems are: a) meteorology, b) solar activity, c) airglow, d) Aurora, e) geomagnetism, f) cosmic rays, and g) ionospheric physics. While all these disciplines are very interesting, this chapter only discusses measurements of the neutral atmosphere, i.e., those instruments capable of meteorological measurements such as: chemical trails; acoustic grenades; pitot probes; and, rigid spheres. The sensors employed, parameters measured, cost, and other information are given in Table 1.

Chemical Trails. Chemical releases from rocket vehicles have been made for experimental purposes since 1954. The experiment is relatively simple to perform requiring rocket-borne storage and release capability for the chemical agent employed, and ground-based photographic recording to capture the movement with time of the trail generated by the release of the chemical. Compared to other techniques, chemical trail releases are relatively inexpensive and easy to perform; however, the materials used to generate the trail tend to be hazardous. Time of day is a necessary limitation, since most chemical trails must be sunlit while the viewing equipment is in darkness. The photographic technique provides the capability to study the wind structure over large height intervals with high accuracy. Horizontal winds are determined by noting changes which occur in the trail over fixed time intervals. It also is possible to measure small vertical structure and its time duration and other characteristics to obtain information about diffusive mixing and turbulence. The continual photographic process and nearly instantaneous (less than a few

minutes) release of the chemical trail makes this technique highly suitable for those purposes. The wind accuracy that has been quoted for typical time intervals of about 100 seconds is 1 meter per second near 100 km (BEDINGER and KNAFLISH, 1965).

A recent utilization of the chemical trail method during the Energy Budget Campaign (REES et al., 1981) provided details of the neutral wind between 80-180 km. The trails were synchronously photographed from two of three sites, the third site not being able to see the trail because of cloud cover. The wind data were obtained by triangulation of the trail as it was distorted by the ambient wind. A comparison of high level winds obtained from the various techniques used in the Energy Budget Campaign has been given by SCHMIDLIN et al. (1985). The reported winds between 70 and 100 km are shown here in Figure 13.

Acoustic Grenades. The operation and performance of the acoustic grenade technique is well documented (NORDBERG and SMITH, 1964; STROUD et al., 1955; NORDBERG et al., 1965) so requires only a brief discussion. The acoustic grenade technique ejects explosive charges of various weights (1-, 2-, and 3-pound charges) at 2- to 4-km altitude intervals (4- to 6-km intervals in the earlier versions of the system). The position and time of each explosion is determined either by a precision radar or a Doppler tracking system, or both when possible. An infrared photocell carried on the rocket vehicle detects the

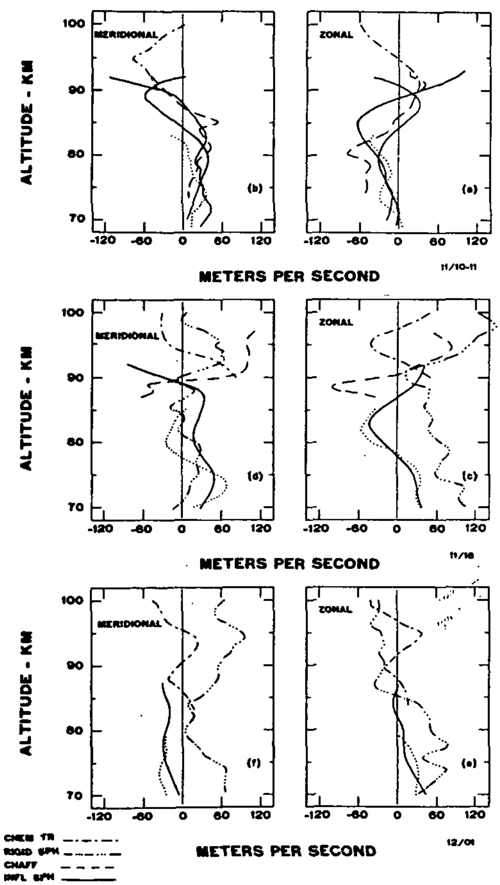

Figure 13. (a-f) Comparison of wind profiles obtained with the chemical trail, rigid accelerometer sphere, chaff, inflatable sphere, and Starute techniques. Zonal and meridional component winds are shown separately for the nights of November 10 and 16, 1980, and the night of December 1, 1980, (after SCHMIDLIN et al., 1985).

ORIGINAL PAGE IS OF POOR QUALITY

explosions' flash. The times of the explosions are telemetered to the ground receiving site. A ground-based array of microphones is necessary in order to detect and record the sound waves arriving from each explosion. Measured parameters include the times and positions of the grenade explosions and the times and angles of arrival of the sound wave at each microphone.

The error inherent in the acoustic grenade technique was reported by RAMSDALE (1968) as due to the uncertainty of reading the times the sound waves crossed each microphone and the deviation of the layered model atmosphere from the true atmosphere. Ramsdale did not include error estimates for pressures and densities since these quantities depend on independent measurements from a different source whose uncertainties were not considered. The majority of the experimental errors was determined to come from the ability to determine the acoustic arrival angles at the individual ground-based microphones (SMITH et al., 1968). It was further determined that the results were sensitive to the geometry of the microphone array. Figure 14, from SMITH et al. (1968) indicates the improvement in estimating the temperatures at Wallops Island (38°N, 75°W) after the basic size of the microphone array was enlarged. Errors in pressures and densities are also influenced by the initial level data which comes from another source, such as a radiosonde. The percent error in temperature has been given as less than 3 percent for most acoustic grenade soundings so that the major source of error in determining pressures and densities is the error deriving from the measured radiosonde pressures (RAMSDALE, 1974).

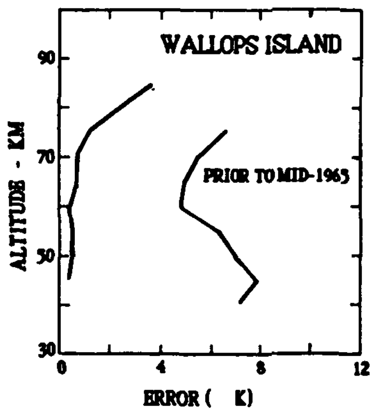

Figure 14. Temperature error arising from the acoustic grenade technique prior to 1965, and after enlarging the ground-based microphone array (after SMITH et al., 1965).

A series of grenade soundings made during September 1971 (SMITH et al., 1974) provided a useful and interesting set of measurements from Kourou, French Guiana (~6°N). These soundings revealed a very structured tropical mesosphere and is a clear example of the density change occurring with time. Figure 15, taken from SCHMIDLIN (1985), shows the observed density at 90 km to change by 30 percent or more within a few hours. These same data were subjected to harmonic analysis by COLE and KANTOR (1975). At 70 km and below, the diurnal range of density varies 7 to 8 percent while at 80 km the variation is 23 percent and larger.

The grenade technique, although simple in principle and noted for providing highly reliable measurements, requires precise measurements and complex processing. Because of the high cost of even a single launch the grenade technique is no longer used.

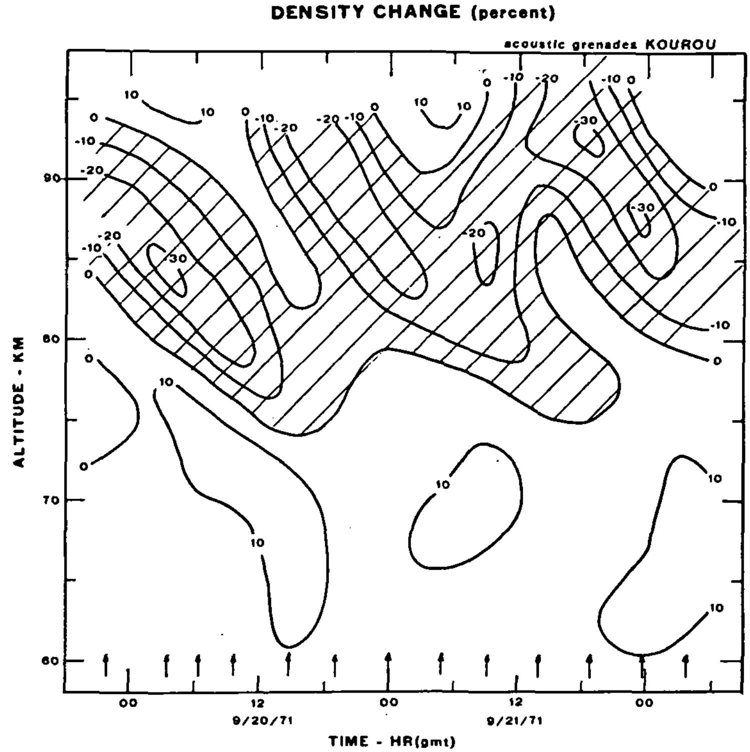

Figure 15. Time-height cross section of acoustic grenade derived temperatures over Kourou, French Guiana. Diurnal changes near 90 km are the order of 30 percent or larger (after SCHMIDLIN, 1985).

Pitot Probe. Atmospheric density profiles can be determined from the measurement of ram pressure at the nose of a rapidly ascending sounding rocket. As early as 1952, this technique was used; however, the rockets and instrumentation were large, complex, and costly. Gauges, used to measure the stagnation (impact) and static pressures, are either of the ionization or hot-filament type. The measured pressures are telemetered to ground receiving and recording equipment. The measurements are most valid when the vehicle is moving at speeds between MACH 3 and MACH 7, requiring that the rocket trajectory be accurately determined. Precision radar or Doppler velocity tracking needs to be employed to obtain an accurate trajectory between 50 and 120 km, the altitude range of this technique.

A detailed description of the pitot probe concept would require considerably more space than is available in this chapter. However, the procedure adopted to derive density profiles follows that of AINSWORTH et al. (1961), and is based upon the supersonic normal shock wave relationships. The expression derived for ambient density results from simplifying assumptions of Ainsworth et al., for vehicle velocity, angle of attack, and the effect of atmospheric winds upon the measured impact pressure. This expression is

$$\rho_1 = P_{o_2} \cdot m^{1/2} \cdot (2\pi RT_{o_2})^{-1/2} \cdot (V \cos \alpha)^{-1}$$

where ρ_1 is ambient density, P_{o_2} is isentropic stagnation pressure, T_{o_2} is gas temperature, m is mean molecular mass of the gas, R is universal gas constant, α is angle of attack, and V is free stream velocity normal to the pitot orifice.

A number of factors must be considered in order to use the above simplified expression to compute density with a reasonable degree of accuracy. These factors are vehicle speed, angle of attack, the effect of atmospheric winds, outgassing effects, transducer error, heating effects, viscous effects due to tube shape and Reynolds number, and impact pressure deficiency. In general, the rocket-borne pitot-probe technique is expected to have density errors of less than ±1 percent below 84 km and of about ±4 percent between 84 and 100 km. A detailed discussion of this technique also may be found in HORVATH (1972).

Rigid Accelerometer Sphere. The rigid accelerometer (instrumented) sphere uses a three-axis piezoelectric accelerometer which provides high resolution measurements (PHILBRICK et al., 1978). The improved measurements range over a larger altitude interval than was possible with earlier versions of the rigid sphere technique. Atmospheric density is determined from the magnitude of the drag acceleration vector which is collinear and oppositely directed to the velocity vector. The drag coefficients for conditions below 90 km were obtained from the wind tunnel tests of BAILEY and HIATT (1971). The error in the drag coefficient in the continuum flow regime below 90 km is about ±3 percent while errors in mass, area, and velocity are all less than 1 percent. Errors in density are expected to be less than 10 percent. Temperature is obtained by integrating down the density profile.

The accelerometer sphere determination of the wind relies on different methods, depending on whether the analysis is performed on up-leg and down-leg motion of the cross-track trajectory or is performed on the in-track trajectory. Each method has different errors, with errors from the cross-track analysis the smallest. Any differences observed between up-leg and down-leg analysis is assumed to come from the temporal and/or spatial changes in the wind field. In-track winds can be determined by assuming spatial uniformity and only by a closed solution when both up-leg and down-leg data are available. Figure 13 shows an example of accelerometer sphere winds with winds from other techniques used in the Energy Budget Campaign.

SUMMARY

The history of rocket development for scientific purposes has been varied and interesting. Tests of the V-2 rocket, which permitted some of the first experiments in the atmosphere to be conducted, provided impetus for the development of special rocket systems designed expressly for atmospheric studies. This led to organized campaigns comprising a number of different instruments whose purpose was to take an occasional "snapshot" of the atmosphere. The scientific community soon realized that more than an occasional look was required and designed their requirements around a synoptic schedule of rocket launchings. During this same period, smaller launch vehicles were developed which became known (generically) as small meteorological rockets. Both passive and active measurements were possible with these systems. A passive system employs wind sensors such as chaff, weighted parachutes, and inflatable spheres that must be tracked by a ground-based system, such as radar. The sphere also provides density measurements. The active sensing systems employ transmitters that send sensor information to a ground receiving station, and also are tracked from the ground. Since the early 1960s, the small meteorological rocket has provided the bulk of the middle atmosphere meteorological measurements available today.

Turning to large rocket systems, chemical release trails, used since 1954, are a relatively simple technique. However, this technique requires clear skies because of the ground-based photography required and must observe the time of day limitation, i.e., the chemical trail must be sunlit while the photographic equipment is in darkness. This system provides detailed wind structure to altitudes above 100 km. The chemical trail technique is still available and used today.

The acoustic grenade technique, although no longer used, has provided numerous profiles of temperature and wind to 90 km and higher from a number of locations. An array of sensitive microphones are needed to detect and record the arriving sound waves from the exploded grenades. The experimental limitation requires that the surface winds be light so as not to create unwanted noise at the microphones. The grenade technique, although simple in character, provided highly reliable measurements. The large cost of this technique is one major factor inhibiting its use today.

Similarly, the pitot-probe technique, which reportedly has measurement errors of less than four percent, is no longer used. This system required complex tracking and recording equipment; but state-of-the-art improvements to the flight and ground systems indicate that the pitot probe can be made adaptable for use with the small meteorological rocket.

One system still used experimentally is the rigid accelerometer sphere. However, because of its high cost and complex data retrieval technique, this system is being phased out. The singular advantage of this system is its capability to provide density measurements to about 150 km.

The use of the small meteorological rocket weighing less than 40-50 kg and capable of providing measurements between 20-90 km reached a peak in the early 1970s. The small systems, once launched synoptically from as many as 30 sites at one time are now launched from only 12 United States sites. The launch frequency has also decreased from 3-5 launchings per week to 1-3 per week. Nonetheless, the meteorological rocket has provided considerable information on atmospheric behavior that has proven valuable to many groups. The basic atmospheric model used in the design of the Space Shuttle, especially the wind parameters, was generated from data obtained from routine and special balloon- and rocket-borne sensing instruments. Many experimental designs of aerospace systems are based on existing rocket data. And most importantly, in recent time, the small rocketsonde has proven itself capable of providing ground truth information for the calibration and verification of satellite remote measurements. This effort started in 1970, with hopes that satellite instruments with their capability for worldwide coverage would replace most if not all _in situ_ measuring devices. It has been recognized that the _in situ_ meteorological measurements are invaluable for this purpose and future remote sensing missions already are requesting that calibration information be made available from balloons and rocketsondes. Although the future requirements seem clear, there has been no thought given to improving the measurement capability, e.g., precision and altitude measuring capabiltiy. Although the Datasonde system provides excellent temperature data to 52-55 km and good temperatures to 60-65 km with reliable wind data to 70 km, it appears that current and future users would like to obtain measurements to 85-100 km, e.g., the Upper Atmosphere Research Satellite (UARS) program planned for 1989. Only by beginning within a reasonable time prior to the launch of the first UARS mission can the needed enhancements be made to our present stable of instruments.

REFERENCES

Ainsworth, J. E., D. F. Fox, and H. E. LaGow (1961), Measurements of upper-atmosphere structure by means of the pitot-static tube, NASA TN D-670.

Angell, J. K., and J. Korshover (1970), Quasi-biennial, annual, and semiannual zonal wind and temperature amplitudes and phases in the stratosphere of the northern hemisphere, J. Geophys. Res., 75, 543-550.

Bailey, A. B., and J. Hiatt (1971), Free-flight measurements of sphere drag at subsonic, transonic, supersonic, and hypersonic speeds for continuum, transition, and near-free-molecular flow conditions, Von Karmon Gas Dynamics Facility, Arnold Engineering Development Center, AFSC, Arnold AFS, Tennessee, Report AEDC-TR-70-291, March.

Ballard, H. N. (1967), A guide to stratospheric temperature and wind measurements, In COSPAR Technique Manual Series, available from COSPAR Secretariat, Paris, France, 117 pages.

Bedinger, J. F., and H. Knaflish (1965), Small scale structure observed in vapor trails around 100 km, Presentation, Second Conf. on Direct Aeronomic Measurements in the Lower Ionosphere, Univ. Illinois, September 1965.

Bollermann, G. (1970), A study of 30 km to 200 km meteorological rocket sounding systems, Contractor Report NASA CR-1529.

COESA (1962), U. S. Standard Atmosphere, 1962, US Government Printing Office, Washington, DC.

COESA (1966), U. S. Atmosphere Supplements, 1966, US Government Printing Office, Washington, DC.

COESA (1976), U. S. Standard Atmosphere, 1976, US Government Printing Office, Washington, DC.

Cole, A. E. and A. J. Kantor (1975), Tropical atmospheres 0 to 90 km, Air Force Cambridge Research Laboratories (currently Air Force Geophysics Laboratory), Rep. AFCRL-TR-75-0527, 31 pages.

Finger, F. G., M. E. Gelman, F. J. Schmidlin, R. Leviton, and B. W. Kennedy (1975), Compatability of meteorological rocketsonde data as indicated by international comparisons tests, J. Atmos. Sci., 32, 1705-1714.

Goldberg, R. A. (1984), Middle atmospheric electrodynamic studies during Project Condor, Overview, Proc. Seventh Int. Symp. on Equatorial Aeronomy, Hong Kong, 1984.

Henry, R. M. (1967), Corrections for meteorological rocket temperature soundings on an individual basis, Paper presented at the Conf. on High Altitude Meteorology and Space Weather, Am. Meteorol. Soc., Houston, Texas, March 1967.

Horvath, J. J. (1972), Pitot measurements on Sparrow Arcas vehicles, Final Report, Univ. Michigan to AFCRL-69-0241, Rep. No. 07301-1-F, Contract No. AFC 19/628/-5069.

Hoxit, R., and R. M. Henry (1973), Diurnal and annual temperature variations in the 30-60 km region as indicated by statistical analysis of rocketsonde temperature data, J. Atmos. Sci., 30, 922-933.

Hyson (1968), Windfinding data from radar tracking of high altitude sensors, Q. J. Royal Meteorol. Soc., 94, 592-597.

Krumins, M. V., and W. C. Lyons (1972), Corrections for upper atmosphere temperatures using a thin-film mount, NOLTR-72-152, Naval Ord. Lab., White Oak, Silver Spring, MD.

Krumins, M. V. (1978), A study of corrections for the loop-mounted sensor, Ph.D. Thesis, Univ. Maryland, College Park, MD.

Leviton, R. (1962), A detailed wind sounding technique, Proc. National Symposium on Winds for Aerospace Vehicle Design, AF Surveys in Geophysics, No. 140, AFCRL.

Leviton, R. (1973), International Meteorological Rocket Comparison Programme, WMO Bulletin, January 1973, 13-15.

Luers, J. K. (1970), A method of computing winds, density, temperature, pressure, and their associated errors from the high altitude robin sphere using an optimum filter, Final Contract Rep. prepared for Air Force Cambridge Research Laboratories, Bedford, MA, AFCRL-70-0366, 80 pages.

Meteorology Group, Range Commanders Council (1983), Wallops Island, Virginia, Range Reference Atmosphere, 0-70 km altitude, RCC-MG Document 364-83, 206 pages, (available from Secretariat, Range Commanders Council, WSMR, New Mexico, 88002).

Miller, A. J., H. M. Woolf, and F. G. Finger (1968), Small-scale wind and temperature structure as evidenced by meteorological rocket systems, J. Appl. Meteorol., 7, 390-399.

Miller, A. J., and F. G. Finger (1972), Results of a rocket nimbus sounder comparison experiment, NASA Contractor Rep. CR-62081, 26 pages.

National Advisory Committee for Aeronautics (1955), Standard Atmosphere - tables and data for altitudes to 65000 feet, NACA Rep. 1235, US Government Printing Office, Washington, DC.

Nestler, M. S. (1983), A comparative study of measurements from radiosondes, rocketsondes, and satellites, Final Rep. Contract NAS6-2726, The Pennsylvania State University, NASA CR-168343, 98 pages.

Nordberg, W., and W. Smith (1964), The Rocket-Grenade Experiment, NASA Tech. Note NASA TN D-2107, 32 pages.

Nordberg, W., L. Katchen, J. Theon, and W. S. Smith (1965), Rocket observations of the structure of the mesosphere, J. Atmos. Sci., 22, 611-622.

Offermann, D. (1985), The Energy Budget Campaign 1980, Introductory Review, J. Atmos. Terr. Phys., 47, to be published MS166.

Philbrick, C. R., A. C. Faire, D. H. Fryklund (1978), Measurements of atmospheric density at Kwajalein Atoll, 18 May, 1977, Air Force Geophysics Laboratory Report AFGL-TR-78-0058, 113 pages.

Ramsdale, D. J. (1968), Error propagation in the Rocket-Grenade Experiment, Progress Rep. NASA Contract NAS5-9583, Globe Exploration Co., El Paso, TX, 44 pages.

Ramsdale, D. J. (1974), Final Rep., Acoustic Grenade Sounding Program, NASA Contract NAS5-11576, Gus Manufacturing, Inc., El Paso, TX, 82 pages.

Reed, R. J. (1965), The quasi-biennial oscillation of the atmosphere between 30 and 50 km over Ascension Island, J. Atmos. Sci., 22, 331-333.

Rees, D., M. Carlson, N. C. Maynard, and K. U. Kaila (1981), Neutral wind and electric field measurements in the upper mesosphere and lower thermosphere by chemical trail and rocket probe techniques, in Sounding Rocket Program Aeronomy Project: Energy Budget Campaign 1980 Experiment Summary, edited by D. Offermann and E. V. Thrane, BMFT-Forschungsbericht W81-052, 362-367.

Scherhag, R. (1952), Die Explosionsartigen Stratospharenerwarmungen des Spatwinters 1951-1952 (The Explosive-Type Stratospheric Warming of Late Winter, 1951-52), Ber. Deut. Wetlerd, 6, 51-63.

Schmidlin, F. J., J. R. Duke, A. I. Ivanovsky, and Y. M. Chernyshenko (1980), Results of the August 1977 Soviet and American Meteorological Rocketsonde Intercomparison held at Wallops Island, Virginia, NASA Reference Publication 1053, National Aeronautics and Space Administration, Scientific and Technical Information Office, Washington, DC 20546, 193 pages.

Schmidlin, F. J. (1981), Repeatability and measurement uncertainty of the United States meteorological rocketsonde, J. Geophys. Res., 86, 9599-9603.

Schmidlin, F. J., M. Carlson, D. Rees, D. Offermann, C. R. Philbrick, and H. U. Widdel (1985), Wind structure and variability in the middle atmosphere during the November 1980 Energy Budget Campaign, J. Atmos. Terr. Phys., 47, in press.

Schmidlin, F. J. (1984), Intercomparisons of temperature, density, and wind measurements from in situ and satellite techniques, Adv. Space Res., 4, No. 6, 101-110.

Smith, W. S., L. B. Katchen, and J. S. Theon (1968), Grenade experiments in a program of synoptic meteorological measurements, in Meteorological Monographs, 9, No. 31, Meteorological Investigations of the Upper Atmosphere, edited by R. S. Quiroz, 170-175.

Smith, W. S., J. S. Theon, D. U. Wright, D. J. Ramsdale, and J. J. Horvath (1974), *Measurements of the structure and circulation of the stratosphere and mesosphere, 1971-1972*, NASA Tech. Rep. NASA TR R-416, 93 pages.

Stroud, W. G., E. A. Terhune, J. H. Venner, J. R. Walsh, and S. Weiland (1955), Instrumentation of the rocket-grenade experiment for measuring atmospheric temperatures and winds, Rev. Sci. Inst., 26, 427-432.

von Zahn, U. (1983), The Project "Winter in Northern Europe" of the Middle Atmosphere Program (MAP/WINE). *Campaign Handbook, University of Bonn* Report: Bonn-EP-83-1, Bonn, FRG, 207 pages.

Yata, A. (1970), Correction for the temperature data obtained by MT-135 system, Geophysical Magazine, 35, No. 1, Published by Japan Meteorological Agency, Tokyo.

N86-26727 D2-46 p.27 7610 NC999967

2. ROCKET TECHNIQUES FOR MEASUREMENT OF OZONE AND RELATED NEUTRAL MINOR CONSTITUENTS

A. J. Krueger

Planetary Atmospheres Branch
NASA/Goddard Space Flight Center
Greenbelt, MD 20771

ABSTRACT

Rockets are the only vehicles for direct measurement of the neutral composition of the stratosphere and mesosphere above balloon altitudes (35-40 km). Instrumentation ~~has been~~ were developed for routine measurements of ozone using either UV absorption, chemiluminescence, or airglow techniques, and for nitric oxide using chemiluminescence.

Other species which ~~have been~~ were measured are nitrogen dioxide, water vapor, hydroxyl, and atomic oxygen. Ozone ~~has been~~ were measured about 400 times, nitric oxide about 10 times, and the remaining species only one or two times.

I. INTRODUCTION

Rockets have played a key role in the development of knowledge of the physical state and composition of the stratosphere and mesosphere. Two thirds of the stratosphere and all of the mesosphere are above the reach of routine sounding balloons and only rarely do research balloons reach the stratopause. In the age of satellites, rocket instruments serve an important purpose in establishing absolute concentrations of constituents, determining vertical structure in distributions (particularly necessary for satellite remote sensing techniques with non-unique results, such as the Nimbus-Solar Backscatter Ultraviolet method for ozone measurements), and providing information on temporal variations that are not easily separable from spatial variations on satellites. Furthermore, constituents without spectral emissions or absorptions in otherwise transparent spectral regions must be measured directly with rocket instruments.

In this chapter the types of rocket techniques for measurement of neutral constituent vertical distributions are discussed. The techniques are illustrated by specific instruments where possible, and the scope is limited to those devices which measure during flight. For example, cryogenic air samplers are also of considerable value but are not treated here because the measurements are done in the laboratory after the flight.

II. ROCKET-BORNE OZONE MEASUREMENT METHODS

Rockets have been used for direct soundings of the ozone distribution from the lower stratosphere to the middle mesosphere since the latter 1940s. However, few soundings were conducted until the 1960s when low-cost meteorological sounding rockets became available. By 1984, approximately 400 rocket ozone soundings had been obtained. Of these, 80 percent used meteorological rockets. These soundings are of value for determining profile changes with latitude and season, for estimating the existence of small-scale structure in the profiles, and for observing diurnal and other short-term changes in ozone. Because the atmospheric variability must be characterized before a constituent is considered understood, the use of inexpensive rockets is mandated in the current age. This limits the instruments in size and weight, as well as in cost.

II.1 Overview of Developed Techniques

In this section, the ozone sounding techniques are reviewed. The methods are presented here; in Section II.2 their limitations are discussed; and the error sources are given in Section II.3. The techniques are considered in detail in Section II.4.

Three basic methods have been used for rocket soundings of ozone in the stratosphere and mesosphere. The methods can be classified as follows:

- o UV absorption
  - side-looking photometers
  - flux photometers
- o chemiluminescence
- o O_2 ($^1\Delta_g$) airglow

The UV absorption techniques are most commonly used and involve measurement of the attenuation of sunlight (or moonlight) in the ultraviolet absorption bands of ozone as a function of height. Two distinctly different approaches have been developed. The first uses side-looking photometers for which the field-of-view is swept in azimuth (and across the solar disc) by the spin of the rocket. This type of sensor has been developed and flown on large rockets in Australia (CARVER et al., 1972; LEAN, 1983), England (MILLER and RYDER, 1973), India (SUBBARAYA and LAL, 1978), Japan (TOHMATSU et al., 1974), Sweden (GRAHN and WITT, 1974), and the United States (WEEKS et al., 1972). In some cases (e.g., TISONE, 1972) an attitude control system has been used to point the photometer at the sun.

The second UV absorption technique involves measurement of the vertical flux of sunlight on a horizontal diffuser plate as the instrument descends on a parachute after deployment from the rocket at apogee. Flux instruments have been developed for meteorological sounding rockets in Australia (SISSONS, 1974) and the United States (KRUEGER, 1973). Both absorption techniques determine ozone number density as a function of geometric height.

Chemiluminescence sensors measure ozone through luminescence of a dye upon contact with the ozone as an air sample is drawn. These meteorological rocket instruments are designed to operate from a parachute similar to the UV flux instruments. The method measures ozone mixing ratio vs geometric height. HILSENRATH et al. (1969) and RANDAWA (1967) in the United States have made soundings with this technique.

The $O_2(^1\Delta_g)$ airglow sensor type is indirect, using measurements of the 1.27 m decay emission of the $O_2(^1\Delta_g)$ metastable excited state to infer ozone densities. This state is produced during photolysis of ozone by sunlight at wavelengths shorter than 310 nm. The measurements are obtained from an ascending rocket using an upward-pointed photometer. To derive the ozone density it is necessary to calculate the ozone photolysis rate and account for the loss of photons by collisional deactivation of the $O_2(^1\Delta_g)$. Most soundings of this type have been made by W. J. F. Evans (AES, Canada) and E. J. Llewellyn (Univ. of Saskatchewan) and associates in Canada.

II.2 Functional Limitations of the Techniques

The basic ozone sounding techniques have operational characteristics which limit their usefulness to certain altitude ranges, times of day, and latitudes. These limitations are summarized in Table 1. The side-pointed photometers are limited in lower altitudes by constraints on release of covers in the vehicle skin required for aerodynamic reasons and sensor protection at lower altitudes.

TABLE 1

Rocket ozone sensor characteristics

Sensor Type	Altitude Range, km	Solar Zenith Angle Limit	Height Resolution km	Estimates of Precision, %
UV Absorption (side pointed)	30-75	45°-96°	1-2	6-10%
UV Absorption (vertical flux)	15-60	15°-80°	0.5-2	3%
Chemiluminescent	30-65	none	0.5-1.5	6%
Oxygen ($^1\Delta_g$) Airglow	50-100	45°-96°	3.5	10-20%

The upper altitude is determined (aside from vehicle performance limits) by the minimum ozone optical depth that can be measured given the signal-to-noise ratio of the sensor. Observing times are limited by the lowest solar zenith angle that can be acquired with the field-of-view and by the highest solar zenith angle where the sun or moon is not occulted by the horizon or clouds. These limiting zenith angles typically are 45 to 96 degrees.

The UV flux instruments have an upper altitude limit controlled by parachute stability. This depends on the air density and ejection conditions. The lower limit is determined by error growth where either the solar flux is very small or the absorption per unit height becomes small. Limits on solar zenith angle are fixed by parachute obscuration for zenith sun and by signal levels as the zenith angle approaches the plane of the diffuser.

The chemiluminescence instrument is not restricted in time of day and has an upper altitude limit determined by parachute stability and a lower limit of approximately 30 km determined by the calibration equipment.

The $O_2(^1\Delta_g)$ sensor is of particular value for mesospheric ozone determinations. It is limited to daytime operation and has height limits which depend on vehicle performance or on signal-to-noise ratios at the top of the profile, and, at the bottom of the profile, on collisional deactivation of the state rather than radiation.

II.3 General Sources of Error

<u>In situ</u> sounding instruments are carried through the atmosphere along some trajectory which generally is a simple function of altitude. Each height is sampled just once and the sounding corresponds to a time series of sampled data. Unless duplicate instruments are carried on the same vehicle, the sounding can never be exactly repeated to test for errors since the atmosphere changes continuously.

In side-looking photometers the principal sources of random errors are solar aspect errors, electronic noise and telemetry errors. Solar aspect errors result in signal errors due to variations of the photometer response as a function of angle of incidence. In addition, the center wavelength of interference filters in the photometer depends on the angle of incidence. Thus, aspect errors also lead to random calibration errors. The effects of elec-

tronic noise depend on ozone optical depth, τ, being a minimum over the range $0.1 < \tau < 3$. This range of τ takes place in a 15-20 km height span for a single wavelength, and multiple wavelength channels are required for a complete ozone profile. The product of ozone density uncertainty and height resolution is proportional to the signal-to-noise ratio. Experimenters generally choose 1 or 2 km height resolution.

Solar aspect errors, filter wavelength calibration errors, ozone effective absorption coefficient errors, light leaks, electronic bias and nonlinearity, radiometric bias from extraneous sources (e.g., cloud reflections), and optical path errors are sources of altitude-dependent biases. Estimates of precision and total bias in ozone density from a side-pointed photometer are 6-10 percent and 6 percent, respectively (WEEKS et al., 1972) for 1 km resolution data.

The flux photometer has similar sources of error, except that in the Super Loki optical ozonesonde, solar aspect errors are removed by use of electronic compensation within the instrument. This, and increased measurement time in the stratosphere during parachute descent, results in a decrease in random ozone errors to about 3 percent at 2 km height resolution (KRUEGER, 1984). Altitude-dependent biases in this instrument estimated from data discrepancies at altitudes where two channels overlap, are 3-7 percent and depend on wavelength-dependent ozone cross section data errors. Wavelength-independent biases in laboratory measurements of ozone cross sections would have a common effect on all instruments using the same source of laboratory data.

Sources of random errors in the chemiluminescence technique are electronic noise, air pressure and temperature measurement errors, and telemetry errors. Bias errors originate during payload calibration, and from inlet duct ozone losses, and residual nonlinearities in the chemiluminescence process (HILSENRATH and KIRSCHNER, 1980).

The principal sources of error for the $O_2(^1\Delta_g)$ technique are attitude errors, photometer noise, and uncertainties in conversion of $O_2(^1\Delta_g)$ emission rates to ozone densities. The conversion errors depend on errors in air density and the rate coefficient for collisional deactivation, the photolysis rate of ozone and on corrections for departure from photochemical equilibrium (particularly for large zenith angle conditions). The ozone errors in the $O_2(^1\Delta_g)$ measurement process are 10-20 percent at a height resolution of 3.5 km (LLEWELLYN and WITT, 1977).

II.4 Instrumentation and Sample Results

II.4.1 Side-looking UV photometers. The first successful rocket measurements of ozone made use of spectrographs to measure the changes in extinction of sunlight over the near ultraviolet wavelengths absorbed by ozone as the rocket ascended (JOHNSON et al., 1952). Lacking a solar pointing system, the spectrometers were equipped with wide field-of-view optical systems designed to overcome the attitude variations of the rocket. Having proved that ozone was the dominant absorber by these experiments, spectrometers are rarely used today. This technique (simplified by use of optical filters) has been a favorite for occasional ozone sounding because of its straightforward implementation on ballistic, spin-stabilized vehicles and attitude-controlled platforms. The general configuration consists of a photodetector, a filter or dispersive device, and an optical or aperture system to define the field of view. In its simplest form, the side-looking photometer contains a photomultiplier tube with a filter covering the photocathode, directed to an aperture in the skin of the rocket, together with a high voltage power supply and signal conditioning electronics. Lenses or mirrors are employed to either increase or decrease the field of view. On a ballistic flight, the optical axis is set at an angle to the vehicle axis such that the rocket spin sweeps

the field of view across the sun. This angle is typically adjusted for the different solar zenith angle conditions and flight trajectory of individual flights. Generally, several photometers with different wavelength settings are flown simultaneously to increase the altitude range of the measurements.

The principle of this technique and of the flux photometer method described in the next section is based on the Beer-Lambert Law of absorption, which applies to the Hartley and Huggins absorption bands of ozone; that is,

$$I = I_o e^{-\alpha u}$$

where I = the light intensity after passing through a column of absorber u, with an absorption coefficient α, for a given source intensity I_o. This method could make use of a local light source passing through a column of air within the instrument but this becomes impractical above about 40 km because kilometer path lengths are required to measure the low ozone densities. Instead, an extraterrestrial light source (the sun or moon) is used and the signal is dependent on the integral amount of ozone above the instrument. The technique is, in fact, the same as used with the Dobson Spectrophotometer for measurement of total ozone from the ground.

A key feature of rocket applications of this technique is that a laboratory absolute radiometric calibration is irrelevant since the instrument response to the extraterrestrial solar flux, I_o, is directly measured at apogee. This is an important aspect because the uncertainty of laboratory irradiance standards far exceeds the accuracy required in the determination of I_o. Furthermore, by solving for the ozone density rather than its integral amount, even the extraterrestrial flux response is extraneous to the measurement, as shown in Section II.4.2.

The absorption coefficient for ozone is a strong function of wavelength in the near ultraviolet, varying by a factor of 100 between 310 and 255 nm. By selection of the wavelength, it is possible to choose the altitude region for the measurement for a given solar zenith angle. Mesospheric ozone measurements use channels near 255 nm while lower stratosphere data are obtained from wavelengths near 305 nm. The altitude range for each channel is determined by the signal-to-noise ratio of the photometer, and is typically 10 - 15 km. The vertical resolution of the ozone distribution is also a function of the signal-to-noise ratio although this factor is frequently obscured by data-smoothing and curve-fitting procedures used with noisy data.

The simple photometer is well suited for use on a pointed platform but requires information about aspect angles when used on a spinning rocket. This is because the flux of light at the photodetector varies with the cosine of the angle of incidence, but equally important, the transmission and center wavelength of an interference filter depend on the angle of incidence. An example of the variations of signal due to aspect angle changes is shown in Figure 1 from LEAN (1983). The maximum signal current on each revolution of the rocket occurs as the photometer field of view sweeps past the moon (the data came from a nighttime experiment) in each of three wavelength channels. During the rocket ascent from 30 to 60 km the signals increase almost monotonically due to the decreased integral ozone. The rate of increase varies with wavelength because of differing ozone absorption coefficients. Above about 60 km, the ozone optical depth is very small at all wavelengths so that the signal changes are due only to lunar aspect angle changes as shown at the bottom of the chart. The same modulations are hidden at lower altitudes by the large slope of the curve due to the exponential decrease of ozone density with height. If uncorrected, these modulations would produce errors that are orders of magnitude greater than the ozone densities in the mesosphere. However, with

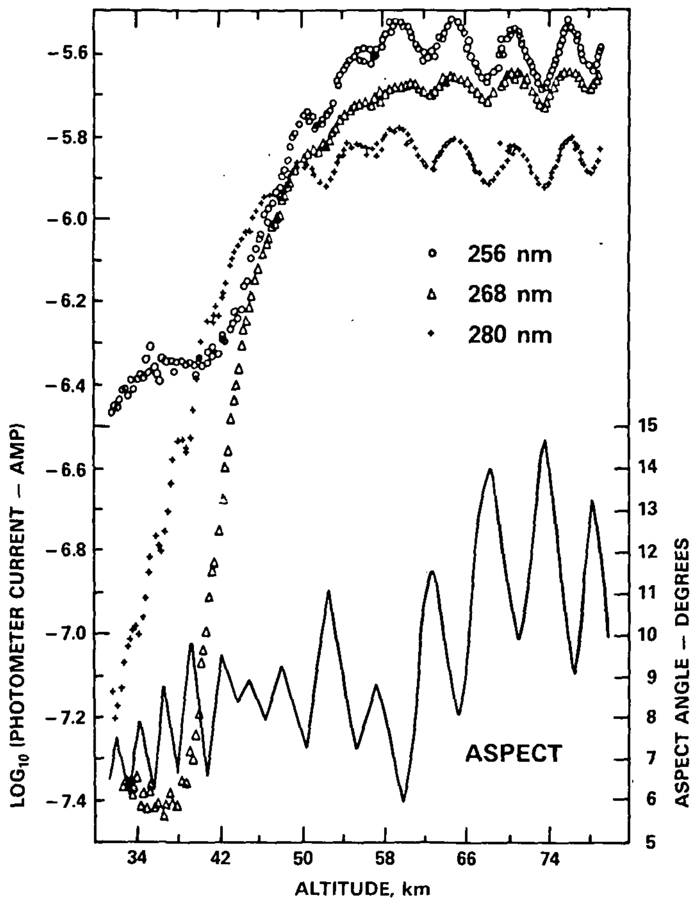

Figure 1. Example of raw telemetry data from a side-looking UV photometer from LEAN (1982). The dominant increase in signals between 30 and 50 km is due to the decrease in ozone. Superimposed are modulations due to aspect angle variations shown by the solid line, which would produce large errors in computed ozone densities if not corrected.

accurate aspect data and a good calibration of the photometers for aspect sensitivity, it is possible to correct the irradiance data and obtain valid ozone data.

An example of the configuration of a side-looking photometer is shown in Figure 2. This diagram, from SCHLYTER and WITT (1982), portrays the typical components used but with certain improvements. G. Witt employs a single photodetector with a mirror array that collects light through several ports, each with its own filter set and lens, on the sides of the rocket. Since the sun illuminates only one port at a time, the individual channels are sequenced by the spin of the rocket. This design eliminates inter-channel drifts of detector sensitivity as sources of bias in ozone measurements.

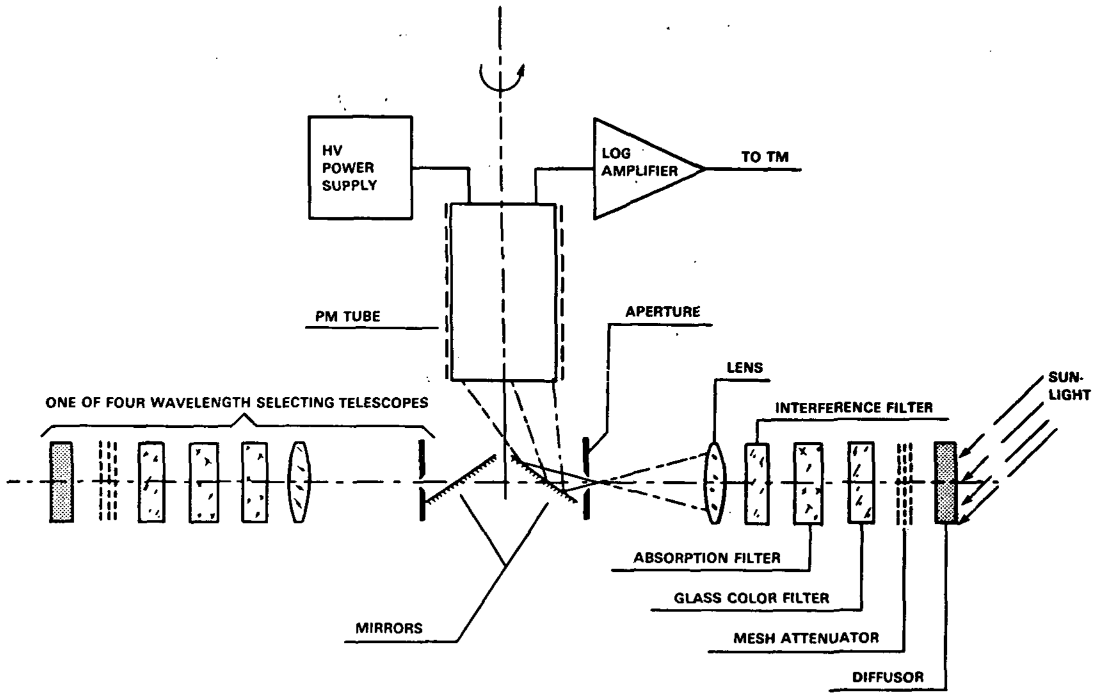

Figure 2. Schematic diagram of a side-pointed UV ozone photometer indicating typical components. In this adaptation by SCHLYTER and WITT (1982) several channels are fed to a single photodetector and the angle of incidence of light at the interference filters is controlled by a lens and diffuser plates at the optical entrance.

Another aspect of this design is the use of a diffuser plate as the first optical element to eliminate the wavelength dependence on aspect angle in simple ozone photometers. The use of a diffuser plate in the Witt instrument assures that the angle of incidence at the filter remains constant so that the optical properties remain constant during the flight. However, it is still necessary to account for the solar aspect angle because of a cosine-law response of the diffuser. This can be accomplished with a non-absorbed reference channel. The greatest problem with a side-looking diffuser plate is that the horizon is always within the field of view and reflections from clouds seriously complicate the signal analysis at the longer wavelengths.

A different approach is used in Japan by T. Ogawa and T. Watanabe (pvt. comm., 1980) of the University of Tokyo. Their instrument contains a single axis tracking system to maintain the photometer axis at the elevation angle of the sun. The maximum signal then is always at a zero angle of incidence and aspect angle corrections are unnecessary. Furthermore, the photometer field of view can be limited to exclude horizon light.

The side-looking photometer approach has been used successfully for many years. It is particularly suited for measurements at high solar zenith angles, including sunrise and sunset when the highest altitude measurements are pos-

sible because of the long path through the atmosphere. Because of the physical size of the photometers, the method is limited to the larger rockets and has not been employed on meteorological sounding rockets. An example of flight results is given in Figure 3 from WEEKS et al. (1972).

II.4.2 UV flux photometers. The ROCOZ optical ozonesonde developed for the Super Loki rocket is a miniaturized four-band filter wheel photometer which measures the relative vertical flux of sunlight as a function of height. Ozone densities are calculated from the height gradient of the signals. The filter wavelengths are selected in the UV Hartley and Huggins bands to provide measurements between 17 and 60 km. This instrument is a second generation ozonesonde which was developed during the mid-1970s at the Goddard Space Flight Center (KRUEGER, 1984) to replace the Arcas rocket ROCOZ instrument originally designed and tested in 1962-1965 (KRUEGER and MCBRIDE, 1968), and is now commercially produced by the Sen Tran Company, Santa Barbara, California.

The ROCOZ instruments are designed to function during descent after deployment on a decelerator. In general, the output of a vertically pointed photometer depends on solar zenith angle and deviations of the photometer axis from the vertical due to pendulation. In the Arcas instrument, the instrument response was made independent of the attitude angle by use of a spherical

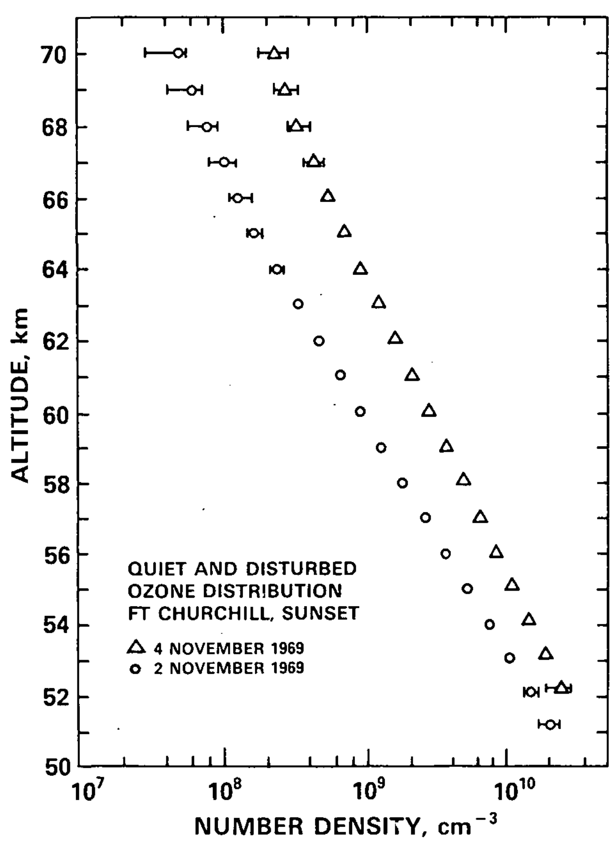

Figure 3. Example of ozone distributions obtained with side-pointed photometers by WEEKS et al. (1972).

transmission diffuser at the optical entrance, similar to the method of the Paetzold balloon ozonesonde (KULCKE and PAETZOLD, 1957). In the Super Loki instrument, the sphere was replaced with a transmission diffuser plate. The variation of sensor response due to angle of incidence of sunlight on the diffuser plate is corrected electronically.

The optical design of the Super Loki instrument is shown in Figure 4. Sunlight is diffusely transmitted through the diffuser plate shown at the left in the diagram. The diffuser assembly consists of a stack of three quartz plates which have been ground on both sides. The light from the diffuser is divided into two components by a quartz plate beam splitter. The main fraction of the light passes directly into the ozone photometer which consists of a filter wheel containing four UV interference filters, a broad-band UV filter, a lens and a UV enhanced silicon photodiode. The 5 percent of the diffuse light reflected by the beam splitter is directed to a second photometer which is matched to the characteristics of the UV photometer except for spectral response. The lenses in the photometers allow only rays within nine degrees of normal incidence to be accepted by the photodiodes.

The filter wheel is rotated continuously by a dc motor at approximately 60 rpm. Both photometers are sampled exactly at the time that each filter is aligned with the UV optical axis. The timing is controlled by a LED-photodiode sensor triggered by reflective spots on the filter wheel. The ratio of the signals from the matched photometers is independent of attitude angle of the instrument and of the solar zenith angle.

The interference filters are selected to cover the altitude range of 20 to 60 km with some redundant data at intermediate heights. Table 2 is a list of typical properties of filters used in flights before 1982. The column labeled "half width" denotes the full width at the 50 percent of peak transmission points. The altitude range indicates the limits where the ozone optical depth is between 0.10 and 2.0 for moderate solar zenith angle conditions. The filter at 257 nm is particularly valuable because it is at the center of the Hartley band where an error in filter wavelength causes no error in ozone absorption coefficient.

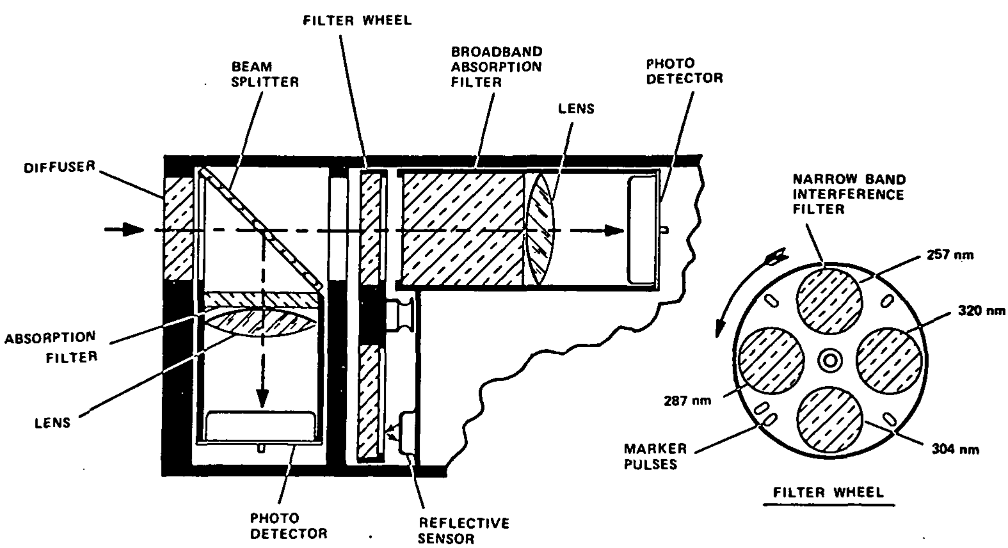

Figure 4. The optical design of a vertical flux photometer for the Super Loki - Dart rocket (KRUEGER, 1984).

TABLE 2

Optical filter characteristics

Center Wavelength, nm	Half-width, nm	Altitude Range, km
320	3	Reference
304	3	20-35
287	3	33-45
257	10	42-57

The broad-band filter has a transmission band from 240 and 340 nm and blocks the visible wavelengths with a transmission less than 10^{-7}.

The instrument is operated as a dropsonde carried by a Starute decelerator after deployment near 70 km from a Super Loki-Dart vehicle (Figure 5-right side). The Super Loki booster is identical to that used for meteorological soundings throughout the US.

The assembled payload (Figure 5-left side) consists of a telemetry and power module at the forward end of the Dart, the ozone sensor, a spool for a 10 m lanyard required to prevent shading of the optics during flight, and the

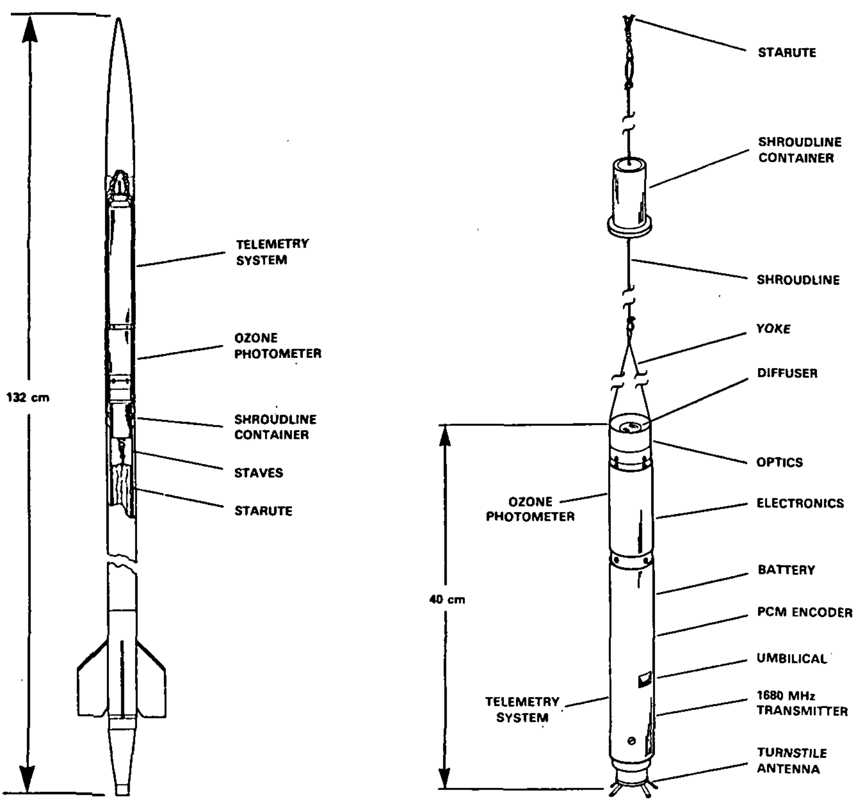

Figure 5. The flight configuration of a Super Loki optical ozonesonde; (left) - installed in Dart vehicle for upflight, (right) - as suspended from the decelerator after deployment from Dart at apogee.

Starute decelerator. The instrument weight is 1 kg and the assemble Dart weight is 7.7 kg.

II.4.3 Processing of UV absorption data. The analysis of data from the UV absorption methods depends on the instrument peculiarities, but the theoretical basis is the same for all.

Ozone densities are determined by a finite difference method derived from Beer's law:

$$I_\lambda = I_{o\lambda}\, e^{-\alpha_\lambda u - \beta_\lambda m}$$

where I_λ is the incident direct sunlight at wavelength, λ, at any level, $I_{o\lambda}$ is the extraterrestrial solar flux, α_λ is the ozone absorption coefficient, u is the slant path integral ozone amount above the observing level, β_λ is the Rayleigh scattering coefficient and m is the integral amount of air along the slant path. The finite difference equation is formed from the logarithmic derivatives,

$$\frac{d \ln I_\lambda}{dh} = -\left(\alpha_\lambda + u \frac{d\alpha}{du}\right) \frac{du}{dh} - \beta_\lambda \frac{dm}{dh}$$

where minor terms have been ignored. This expression can be solved for the change in slant path ozone per unit height:

$$\frac{du}{dh} = \frac{-1}{\left(\alpha_\lambda + u \frac{d\alpha}{du}\right)} \left(\frac{d \ln I_\lambda}{dh} + \beta_\lambda \frac{dm}{dh}\right)$$

Because finite bandwidth filters are employed, the ozone absorption coefficient must be replaced by effective absorption coefficients for each of the j filters defined as follows:

$$\alpha_j(u,m) = -\frac{1}{u} \ln \frac{\int I_{o\lambda} P_\lambda F_{j\lambda} T_\lambda e^{-\alpha_\lambda u - \beta_\lambda m} d\lambda}{\int I_{o\lambda} P_\lambda F_{j\lambda} T_\lambda e^{-\beta_\lambda m} d\lambda}$$

here P_λ is the photodetector response, $F_{j\lambda}$ is the spectral transmission of the j^{th} filter, and T_λ is the spectral transmission of the diffuser plate.

An effective Rayleigh scattering coefficient is also computed for each filter and can be specified as a constant.

$$\beta_j\ (u,m) = B_{oj}$$

Various data smoothing methods are used by different experimenters and the quantitative nature of the derived ozone distribution depends on the smoothing. Least squares curve fitting over the complete extinction curve produces ozone profiles which depend on the selected functional form, have biases which grow large at the upper and lower altitude limits, and are sensitive to flight data quality and outliers. Manual data smoothing has ill-defined spectral properties but generally avoids biases at the end points. The ROCOZ processing algorithm fits a low-order polynomial to the data points in the vicinity of each height level, detects outliers by their deviation from the fitted curve, and refits the curve to find the central point. This procedure is then repeated at each one-kilometer height level, and a finite difference scheme is used to compute ozone densities.

The number of ROCOZ measurements per unit height varies considerably with altitude with a fixed sampling rate of approximately one sample per UV channel

per second coupled with a descent rate which decreases by a factor of two for each 10 km altitude change. This yields about 11 samples/m at 50 km and 50 samples/km at 30 km. An example of raw data from a ROCOZ flight is shown in Figure 6. Under most conditions, the random errors in the data are due to angle compensation errors which are on the order of 0.4%. Telemetry quantization errors are distinguishable by the steps in the curve at the later times and lower altitudes. Common mode errors and drift in the UV photometer are removed by ratioing the three short wave UV samples to the 320 nm reference channel. This also removes any low frequency changes in the compensation photometer from the UV data.

The ozone densities are computed independently for each of the three active channels over the optical depth range from 0.1 to 2. To produce a single ozone profile the results are merged using the uncertainties as weighting factors in the regions of overlap. The bias between results in the overlap regions provides an internal test for validity of the filter calibration and instrument performance. An example of repeatability between ROCOZ instruments is shown in Figure 7. The two soundings were made 15 minutes apart from Wallops Flight Center (KRUEGER, 1984).

II.4.4 Chemiluminescent detectors. The chemiluminescent technique for ozone detection was first described by BERONOSE and RENE (1959) in which organic dyes impregnated on paper discs were shown to luminesce upon exposure to ozone. This process appeared to be quantitative and REGENER (1964) adapted the method for balloon ozone soundings because its high sensitivity permitted measurements of the low ozone concentrations found in the troposphere. The competitive balloon ozone sensors were 1) an electrochemical cell using potassium iodide in an aqueous solution through which ambient air was pumped and 2) an optical

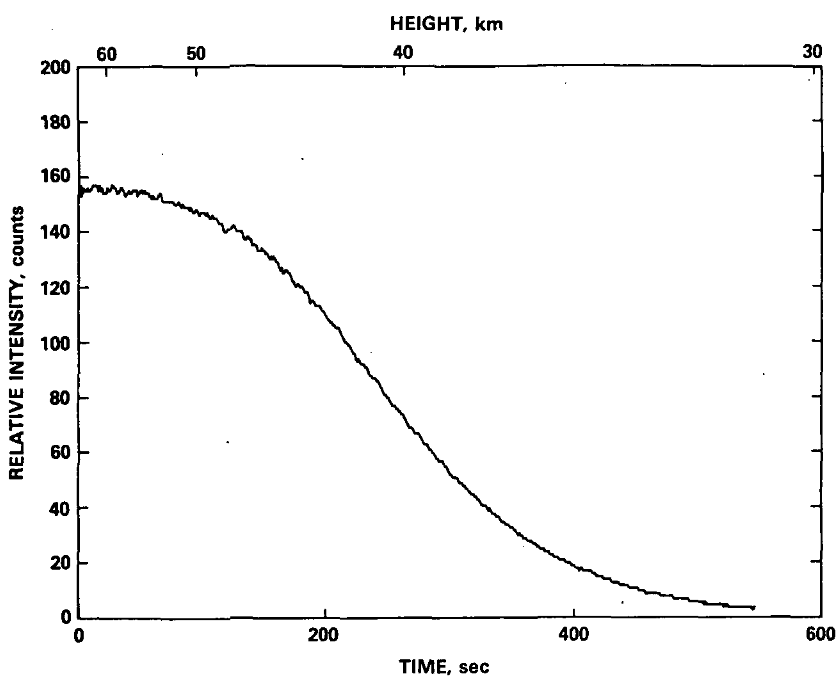

Figure 6. Example of raw telemetry data from a Super Loki optical ozonesonde for a channel centered at 288 nm. The signal decreases with time as the instrument descends.

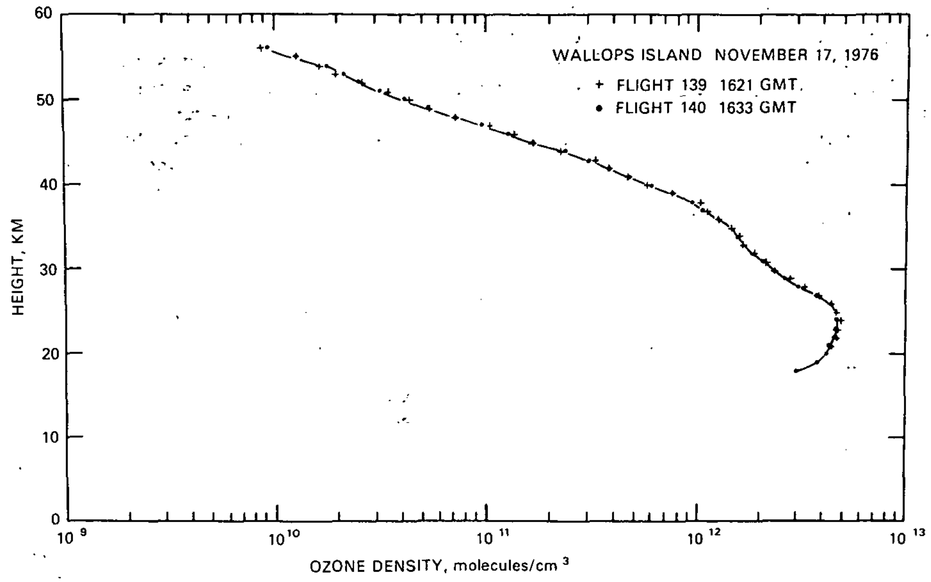

Figure 7. Results from nearly coincident flights of Super Loki ozonesondes at Wallops Island (KRUEGER, 1984).

sonde similar to the UV flux photometer described above. The apparent simplicity, ruggedness, and sensitivity for resolving the detailed vertical structure were qualities that led the US Air Force to further develop the chemiluminescence instrument for routine sounding purposes during the 1960s. Subsequently, HILSENRATH, et al. (1969) and RANDHAWA (1967) developed rocketsondes based on the technique. None of the instruments are in current use. The production version balloon-borne instruments developed instabilities and nonlinearities. The Randhawa instrument similarly appeared to be unstable, particularly at the high altitudes reached by rockets where the ozone densities were very low. The Hilsenrath instrument was used until recently, and by meticulous attention to instrument calibration and calibration stability, the problems appeared to be overcome. This instrument design is reported in the next section.

The physical mechanisms in chemiluminescence with ozone are not well understood. However, the process has been characterized in laboratory studies. Certain dyes, such as the rhodamine-B used by Hilsenrath, produce light when exposed to ozone or atomic oxygen, but are insensitive to other minor atmospheric constituents (eg., NO_2, SO_2, H_2O_2, H_2O, NO). The oxyluminescence is temperature sensitive and appears to have some synergistic effects with water vapor and ammonia. The efficiency, stability, and response time are also dependent on the method of preparation and deposition on a substrate so that each of these factors was examined to produce a suitable sensor. For example, Hilsenrath found that the addition of gallic acid increased the stability and response time of rhodamine-B. Because the absolute luminescent efficiency of the dyes is not predictable, the instrument response is determined in laboratory calibrations.

The chemiluminescence instruments require that a known air sample be drawn as the instrument descends on a parachute. The method employed by both Hilsenrath and Randawa involves a chamber which is evacuated during the ascent,

then backfills as the external air pressure increases during the descent. The air flow rate past the detector is proportional to the pressure change in the chamber. This method is indicated in Figure 8, illustrating the components of the Hilsenrath instrument. Air is drawn through a light trap and across the chemiluminescent disk as it flows into the ballast chamber. The light is detected with a photomultiplier tube after passing through a chopper wheel used to suppress the dark current. A calibration light source periodically is turned on to establish the detector response. The temperature and pressure of the ballast chamber are monitored during the flight.

The expression for the chemiluminescent response is given by:

$$L = KC_oF(1 - e^{-q/F}),$$

where L = luminescent light level, K = photon production efficiency and instrument calibration constant, C_o = ozone concentration, F = flow rate, and q = detector cell efficiency. At low flow rates this reduces to:

$$L = K\ C_o\ F,$$

and the luminescence is proportional to ozone concentration and flow rate. The flow rate is derived from the ballast chamber temperature, T, and pressure, p, resulting in the expression:

$$L = (K'r_3/T)\ (dp/dt),$$

where r_3 is the ozone mixing ratio, and dp/dt is the rate of change of pressure in the ballast chamber. The calibration constant, K', is determined when the instrument is evacuated and attached to a source of ozone using an appara-

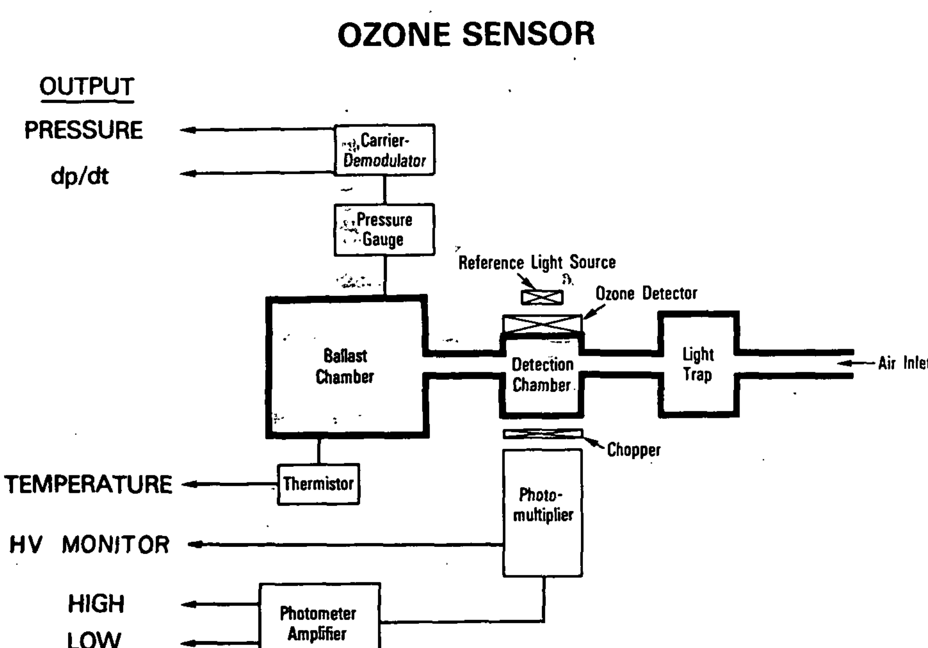

Figure 8. Principal components of a chemiluminescence ozonesonde for the Super Arcas rocket (HILSENRATH and KIRSCHNER, 1980).

tus which simulates the descent pressure profile. It has been found that preconditioning with ozone is necessary to stabilize the instrument response. This involves passivation with high ozone concentrations and cycling through the range of operating pressures and flow rates.

An example of the repeatability between instruments (HILSENRATH and KIRSHNER, 1980) is shown in Figure 9. The two flights were launched 13 minutes apart from Wallops Island, Va. It is noted that the system appears to produce data of good quality throughout the upper stratosphere and into the mesosphere to approximately 65 km. In comparisons with other instruments, particularly the Super Loki optical ozonesonde, good agreement (10%) is usually found from 30 to 55 km, but the chemiluminescence instrument results appear to be significantly larger below 30 km.

One of the most important virtues of the chemiluminescence technique is the ability to observe day or night with the same precision of measurement. HILSENRATH (1971) obtained a determination of the diurnal variation of ozone and confirmed that the theoretically predicted odd oxygen partitioning between ozone and atomic oxygen was correct in the mesosphere.

II.4.4 Singlet delta oxygen emission photometer. When ozone is photodissociated in the Hartley bands, oxygen molecules are produced in a metastable excited state, $O_2(^1\Delta_g)$, with a radiative lifetime of 2.7 x 10^3 seconds. Unless the molecules are collisionally deactivated they decay to the ground state by emission of radiation in the region of 1.27 μm. EVANS et al. (1968) first exploited this effect to infer the distribution of ozone by measuring the change with height of the $O_2(^1\Delta_g)$ emissions with a photometer on a rocket.

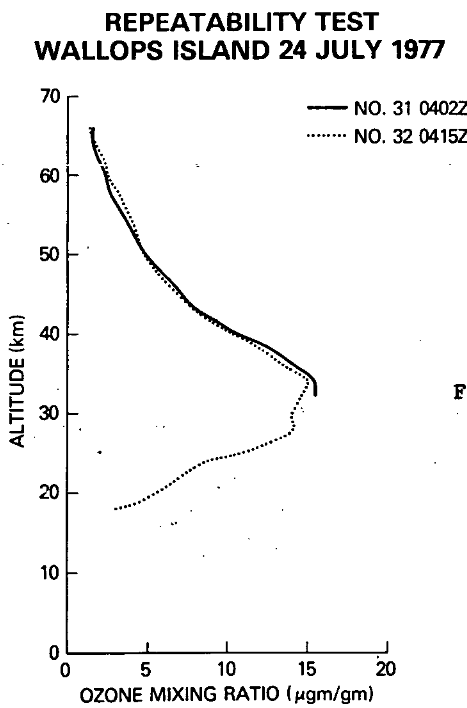

Figure 9. Results from nearly coincident flights of chemiluminescence ozonesondes at Wallops Island (HILSENRATH and KIRSHNER, 1980).

The processes can be described by the excited state production equation:

$$O_3 + h\nu \xrightarrow{J_3} O\,(^1D) + O_2\,(^1\Delta_g),\ \lambda < 310\ \text{nm},$$

where J_3 is the ozone photolysis rate, and the loss reactions:

$$O_2(^1\Delta_g) \xrightarrow{K_r} O_2 + h\nu\ (1.27\,\mu\text{m})$$

for radiation at the rate K_r (sec^{-1}), and,

$$O_2(^1\Delta_g) + M \xrightarrow{K_c} O_2 + M$$

the non-radiation transition at the rate K_c, $\text{cm}^3\,\text{sec}^{-1}$. The last expression, which represents collisional deactivation, depends on air density [M], and dominates over the emission below the stratopause. This effect controls the lower altitude limit for the technique. The rate equation for $O_2(^1\Delta_g)$ is of the form:

$$dn^*/dt = J_3\,[O_3] - (K_r + K_c\,[M])\,n^*$$

where n^* is the density of $O_2(^1\Delta_g)$. Under mid-day conditions, the production rate can equal the loss rate and a particularly simple (steady-state) relation is found between the ozone density $[O_3]$ and n^*, namely:

$$[O_3] = (K_r + K_c\,[M])\,n^*/J_3.$$

The accuracy of the technique depends on the accuracy of J_3, which must be iteratively computed from solar flux and ozone cross section data and an initial guess for the ozone distribution, and on the accuracy of the collisional deactivation rate coefficient and of the air density, which must be independently determined. These factors introduce more uncertainty in the ozone results than present in the other techniques, as was indicated in Table II-1.

The photometer flown by EVANS et al. (1968) consists of a baffled port through the side of the rocket, a folded optical path into a sealed chamber containing a chopper, beamsplitter, and two PbS detectors with filters to isolate the 1.27 μm band emissions and to measure the background light due to Rayleigh and aerosol scattering. The design is illustrated in Figure 10 as implemented for an Aerobee 150 rocket. The background channel was found to be unnecessary (WOOD et al., 1970) and the instrument was subsequently redesigned at the University of Saskatchewan (EVANS and LLEWELLYN, 1971; SOLHEIM, 1979) and flown to measure night airglow from the limb as well as for day and twilight ozone soundings. The new design uses a light baffle to limit the field of view, a narrow band interference filter to define the 1.27 μm band, an objective lens to focus the light on a lead sulfide detector, a tuning fork chopper, and a broad band filter. For daytime ozone measurements, the instrument is pointed along the spin axis of the rocket and data are taken after the nose tip is ejected above 40 km. An example of the ozone distribution obtained by this method is given in Figure 11.

III. ROCKET-BORNE INSTRUMENTS FOR OTHER MINOR CONSTITUENTS

III.1 Nitrogen Radicals

The odd nitrogen radicals ($NO_x = NO + NO_2$) account for most of the odd oxygen destruction in the stratosphere and participate in the chemical pro-

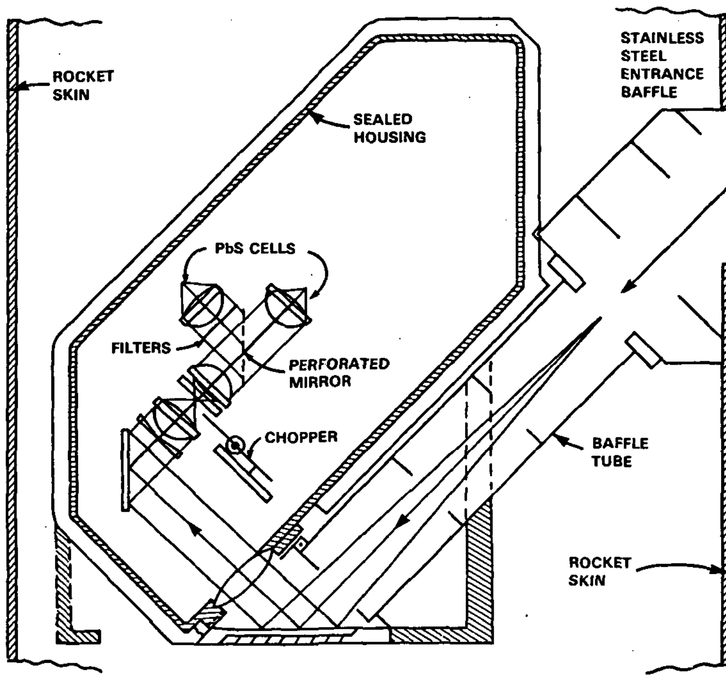

Figure 10. Design of an oxygen airglow photometer for ozone measurements (EVANS et al., 1968).

cesses throughout the middle atmosphere. The NO_x species have two source regions in the atmosphere, being produced at thermospheric altitudes from energetic particle and ion processes and, at stratospheric altitudes, from nitrous oxide reacting with excited oxygen atoms. Rocket techniques are not well developed to measure these radicals although a clear need exists for in situ data. Most of the existing observations are from occasional research soundings.

III.1.1 Nitric oxide. The means for measurement of stratospheric and mesospheric nitric oxide have developed independently from different disciplines and, at this time have not been combined. We first discuss the methods for measurement of mesospheric NO that were developed for purposes of aeronomy.

The nitric oxide in the mesosphere is quite evident in airglow spectra taken from high altitudes due to resonance scattering of sunlight in the ultraviolet gamma bands of NO near 215 nm (BARTH, 1964). Several rocket soundings were made by the University of Colorado using spectrometers to observe the spectral radiance of the zenith sky as a function of altitude. MEIRA (1971) showed that by accounting for the Rayleigh scattered component in the radiance, ozone absorption, and polarization sensitivity of the spectrometer, it was possible to obtain quantitative NO profile information.

Probably the most recent development in instrumentation to measure the nitric oxide vertical distribution in the mesosphere by rockets is by the Geophysics Research Laboratory of the University of Tokyo. TOHMATSU and IWAGAMI (1976) designed a radiometer which discriminates the NO gamma-band emissions from the background Rayleigh scattered continuum by a gas correlation

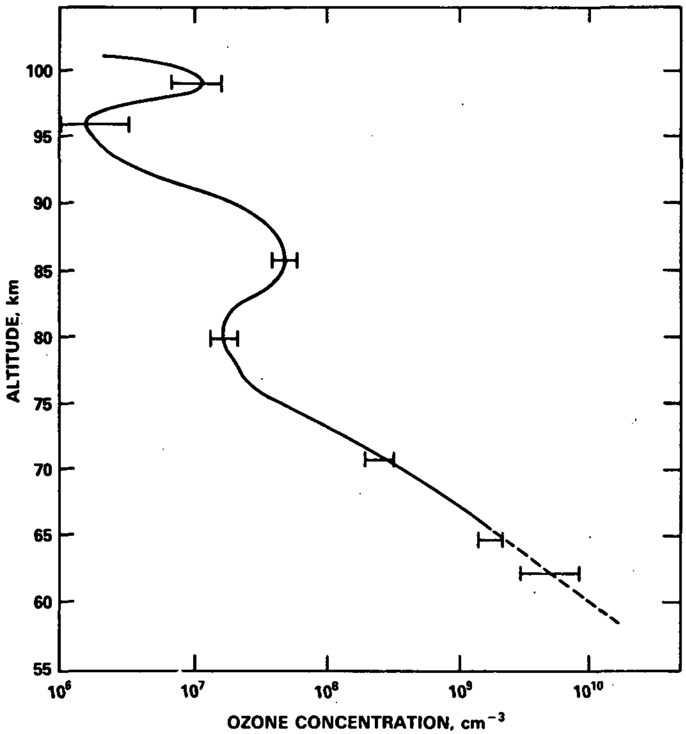

Figure 11. The ozone distribution obtained from conversion of O_2('Δg) emission measurements (LLEWELLYN and WITT, 1977).

technique. A photometer whose spectral response is limited to the vicinity of 215 nm by an interference filter is fitted with a collimator and a device for alternately exchanging two optical cells in the optical path. One cell is filled with nitric oxide gas while the other is evacuated. The NO-filled cell selectively absorbs the resonantly scattered light from the atmospheric nitric oxide while the other cell passes all the light. The difference between the signals from the two cells thus, is proportional to the atmospheric nitric oxide within the field of view. The instrument calibration is based on the Rayleigh scattered intensity which can be computed for the air pressure distribution.

Results from several flights of this instrument have been reported. Figure 12 illustrates the signals observed as a function of height for a rocket flight from Syowa Station, Antarctica in August, 1977, as reported by IWAGAMI and OGAWA (1980). The apparent emission rates measured through the nitric oxide filled cell (S_{NO}) and the blank cell (S_{BL}) are shown for both ascent and descent. In this and the prior flights, a constant background signal, presumably due to instrumental stray light, was observed in addition to the Rayleigh and resonance scattered intensity. The measured nitric oxide profiles are shown in Figure 13 where prior results from flights of the sensor at Thumba, India, and Uchinoura, Japan, are also indicated.

The resonance scattering technique fails at lower altitudes due to the large Rayleigh scattering background, but the correlation technique appears to be very promising for resolving questions about transport of thermospheric

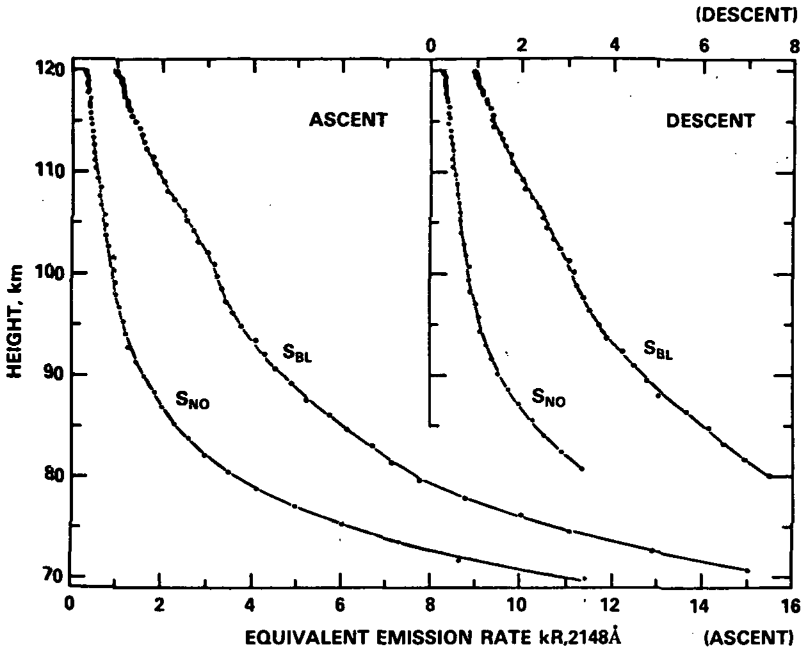

Figure 12. Resonance scatter apparent emission rates for a NO-filled cell (S_{NO}) and a blank cell (S_{BL}) from IWAGAMI and OGAWA (1980) gas correlation instrument at 214.8 nm (1 nm = 10Å).

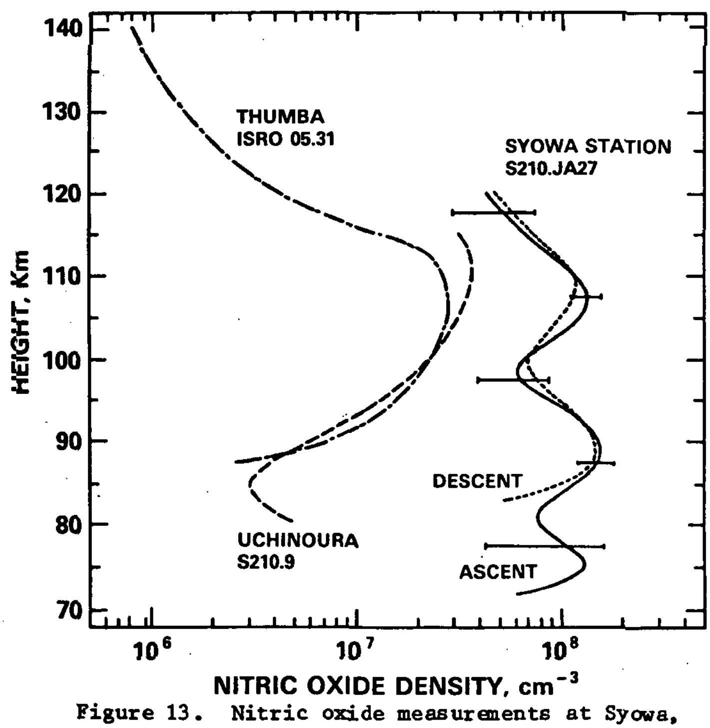

Figure 13. Nitric oxide measurements at Syowa, Uchinoura, and Thumba using the NO gas correlation instrument (IWAGAMI and OGAWA, 1980).

nitric oxide to the stratosphere. The technique for measurement of nitric oxide in the stratosphere is described in the following.

Nitric oxide is found in the stratosphere in concentrations of less than about 30 ppbv. Measurements of this constituent with an accuracy of 1 - 3 ppbv are required to establish the completeness of photochemical models and to determine whether thermospheric NO_x is contributed to the budget of stratospheric odd nitrogen. Because of the low concentrations, many of the conventional measurement methods are ruled out. An indirect method that can be employed on balloons and rockets is based upon the reaction of nitric oxide with ozone to form nitrogen dioxide in an electronic exited state. These molecules decay to the ground state emitting photons in the red and infrared spectral regions. HORVATH and MASON (1978) of the University of Michigan have developed this technique for sounding rocket use as a dropsonde. In the parachute-borne instrument, ambient air is drawn by a cryogenic pump into a reaction chamber where it is mixed with ozone that is carried with the instrument. The resulting chemiluminescent emissions are detected with a photomultiplier tube.

The reactions taking place in the instrument are as follows:

(1) $NO + O_3 \longrightarrow NO_2^* + O_2$

(2) $NO + O_3 \longrightarrow NO_2 + O_2$

(3) $NO_2^* \longrightarrow NO_2 + h\nu$

(4) $NO_2^* + M \longrightarrow NO_2 + M$

When nitric oxide reacts with ozone, either excited or ground state NO_2 is produced depending on whether path 1 or path 2 is followed. The reaction rates favor the production of the ground state molecule about 96% of the time. The excited NO_2^* can decay by reaction 3 to produce a photon, or by reaction 4 in which the photon is lost by collisional deactivation. The signal detected by the photomultiplier thus, is a due to a small fraction of the nitric oxide molecules that are present. Since the reaction rates are not known with high accuracy and the detection efficiency depends on a number of empirically determined factors, the instrument is calibrated before flight in the laboratory with a known source of nitric oxide.

The apparatus that was designed for deployment with an Orion rocket (HORVATH et al., 1983) is illustrated in Figure 14. The instrument is 115 cm long and weighs 9.5 kg. The reaction chamber, located near the center of the instrument, is supplied with ambient air through an inlet tube extending to the forward end for an uncontaminated sample. Ozone is supplied to the reaction chamber from a storage chamber filled with a 5% ozonated-oxygen mixture prepared before launch with an ozone generator. A liquid nitrogen cryogenic pump, located at the top of the instrument, provides the pressure differential to obtain sample flow rates over the range of 0.2 to 12 cm3/sec S.T.P. between 50 and 35 km. The reaction chamber pressure is measured with a mechanical pressure transducer and the temperature is measured at several locations with thermistors. The conductance of the inlet duct is measured in the laboratory for a range of pressures corresponding to flight conditions.

This instrument and its developmental precursor have been flown on nine occasions between 1976 and 1981, primarily at Wallops Island, Virginia. An example of recent flight results and the repeatability between soundings (HORVATH et al., 1983) is shown in Figure 15. The two soundings were taken 50 minutes apart near local noon on July 23, 1981, at Wallops Island. The error bars indicate the uncertainty in the measurements due to pulse counting statis-

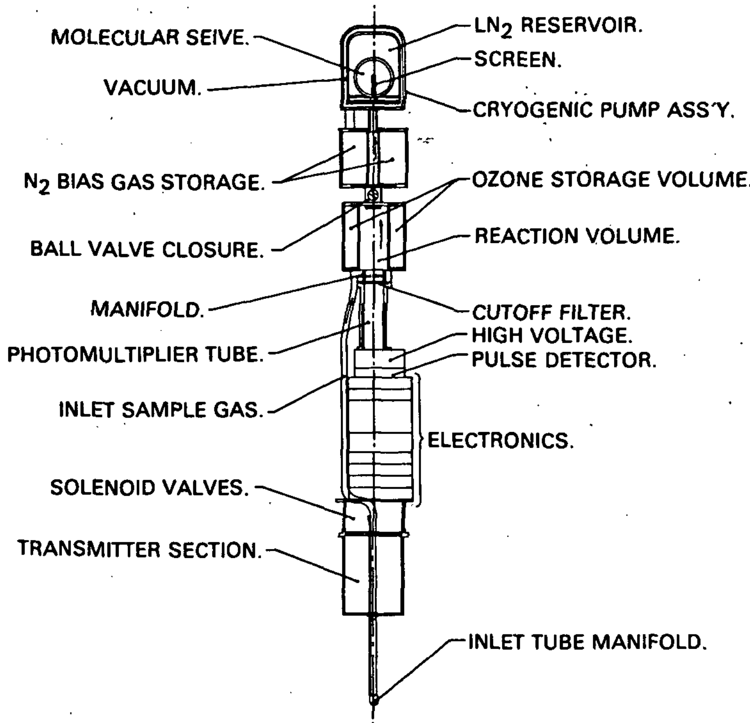

Figure 14. Schematic of a chemiluminescence instrument to measure nitric oxide (HORVATH et al., 1983).

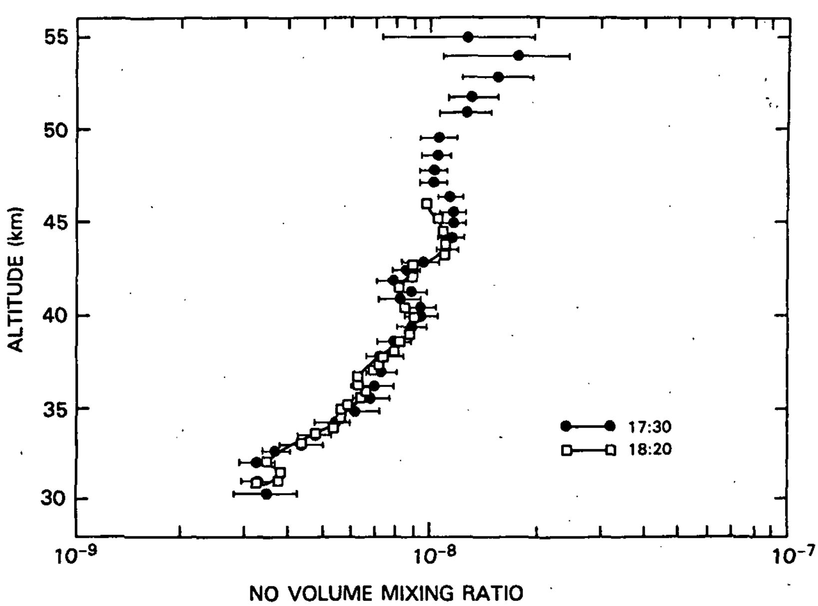

Figure 15. Results from nearly coincident flights of chemiluminescence nitric oxide instruments at Wallops Island (HORVATH et al., 1983).

tical errors and the errors in flow rate and air and ozone densities. The two profiles generally agree within the measurement errors of about 10% and in addition produce evidence for some structure in the nitric oxide distribution on the day of the flights.

These rocket measurements of nitric oxide have not been directly intercompared with other techniques at this time. The same chemiluminescence technique has been employed on balloons although the instruments differ in many operational details. In general the results from the balloon soundings are higher by about a factor of two than the rocket results. At the present time photochemical models of the stratosphere give little guidance in choosing between the two sets of results.

III.1.2 Nitrogen dioxide. Absorption bands of NO_2 in the 400 nm region have been applied to its measurement from the ground and from balloons and rockets. With low abundances of NO_2 the measurements are enhanced if long paths such as limb occultation paths are used. The Solar Irradiance Photometer (SIP) instrument developed by Georg Witt of the Department of Meteorology, University of Stockholm (see Figure 2), was modified to observe the atmospheric NO_2 absorption (GRAHN and WITT, 1974) and flown from the Guiana Space Center, French Guiana, in March 1974. One channel was dedicated to NO_2 using an 8-nm-wide filter centered on the 409-nm absorption peak of nitrogen dioxide. The remaining channels were used to measure the distribution of ozone and for a nonabsorbed reference signal to measure attitude-dependent signal variations.

The experiment produced measurements of nitrogen dioxide density from 21 to 35 km, as shown in Figure 16.

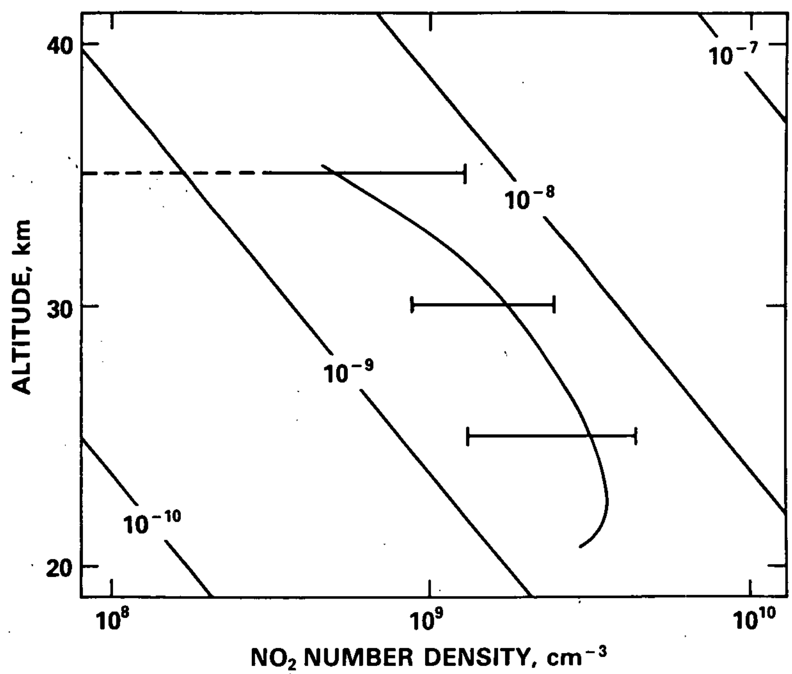

Figure 16. The number density distribution of nitrogen dioxide obtained by rocket at Guiana Space Center in March 1974 (SCHLYTER and WITT, 1982). Error bars are one-sigma uncertainty; diagonal lines are volume mixing ratio isolines.

III.2 Atomic Oxygen

A silver film sensor for atomic oxygen was developed by HENDERSON and SCHIFF (1970). The technique made use of the change in conductivity of a submicron film as the silver is converted to silver oxide on exposure to atomic oxygen. A series of four sounding rocket flights was conducted to evaluate the technique (HENDERSON, 1974). The method has produced results in the 90 to 120 km altitude region which are in general agreement with mass spectrometer observations which overlap at the higher altitudes. The lower altitude limit for the silver film technique appears to be constrained by aerodynamic heating which would destroy the film. In the Henderson experiments, the rocket apogees were near 130 km so that the films were deployed at 90 km.

III.3 Hydrogen Compounds and Radicals

III.3.1 Water vapor. Water vapor is an active constituent of the stratosphere because odd hydrogen radicals, important to the ozone chemistry, are readily formed. Water vapor has been measured from rockets using long path absorption of sunlight in the 2.7 μm spectral region (EVANS, 1974; DEJONCKHEERE, 1975) and by thermal infrared emission (ROGERS et al., 1977). A major problem with the measurement of stratospheric water vapor concentrations (particularly from balloons) is that the sample of air is easily contaminated by water carried on the equipment itself. By the use of rockets, it is anticipated that rapid ventilation of the equipment combined with an external measurement technique will alleviate this problem.

The long-path absorption instrument designed by EVANS (1974) consists of a two-channel radiometer, each channel using a lead sulfide detector and a thin film interference filter. One filter includes the water vapor absorption band centered at 2.7 μm while the other is a reference filter near 2.4 μm. The instrument is flown with the sun on the horizon as the spinning rocket sweeps the field of view in azimuth. The amplitude of the waveform on each rotation is a measure of the absorption. The calibration of the instrument is based on the effective absorption coefficient weighted by the filter spectral response, which is computed similar to that for ozone soundings. However, the line characteristics of infrared spectra require special treatment compared with the continuous absorption spectra in the ultraviolet for ozone or water vapor.

O'BRIEN and EVANS (1981) reported on flights of this instrument at Cape Perry, Canada, and Kiruna, Sweden. The two flights indicate a general increase in the water vapor mixing ratio from about 1 ppm at the tropopause to 8 ppm at 55 km with an estimated uncertainty of 1.5 to 2 ppmv. This general behavior with altitude is as expected from the oxidation of methane in the upper stratosphere.

The second type of technique is based on the thermal emission of water vapor. At the present time, data from a general purpose infrared spectrometer have been applied to the water vapor measurement problem. ROGERS et al. (1977) analyzed emission spectra from the mesosphere using a rocket-borne cryogenic spectrometer to scan the region from 7 to 24 μm in a flight from the Poker Flat Research Range in Alaska in March 1973. The radiances on the long wavelength wing of the 6.3 μm band of water were found to be consistent with a mixing ratio of 3.5 $\pm$ 2.2 ppmv between 49 and 70 km. The prospects for developing this technique for more routine use are not known.

III.3.2 Hydrogen radicals. Although odd hydrogen reactions are believed to control the abundance of odd oxygen in the mesosphere, the mixing ratios of the hydroxyl and hydroperoxyl radicals are generally less than 1 ppbv. At stratospheric altitudes the mixing ratios are lower by a factor of ten than in the

mesosphere, and the problems of measurement are severe. Two rocket flights have been made to measure mesospheric hydroxyl, but HO_2 has not been measured above 40 km. The technique used for the hydroxyl measurements makes use of resonance fluorescence emissions at 306.4 nm in the near ultraviolet spectral region. ANDERSON (1971) conducted both soundings using an Ebert-Fastie spectrometer to scan the spectral region containing an OH line as the spinning rocket ascended through the mesosphere. The atmospheric radiance at this wavelength region is dominated by Rayleigh scattered light so that the problem is to separate the resonance scattered light from the background. On the first flight on June 28, 1969, data were taken between 60 and 108 km at evening twilight. The hydroxyl emissions could not be clearly resolved in the presence of large modulations due to the polarization of the Rayleigh scattered light and interference between the rocket roll rate and the spectrometer scan rate. It was possible, however, to compute an upper limit to the hydroxyl densities.

A second sounding was made on April 22, 1971, from White Sands, New Mexico, in which advantage was taken of the polarization of Rayleigh scattered light to discriminate the OH emissions from the background. In this case, the spectrometer field of view was directed to the zenith shortly before sunset so that the view angle is perpendicular to the incident sunlight. The results of this flight are shown in Figure 17. Hydroxyl densities between 45 and 70 km were determined to be about 3×10^6 cm^{-3} with little variation with altitude and with an uncertainty of $\pm$ 120%.

IV. SUMMARY

In this chapter, an attempt has been made to survey the techniques that have been devised to measure the neutral composition of the middle atmosphere from rockets. Although the effort has certainly not uncovered all of the methods that have been attempted, and perhaps has entirely missed some ingeneous techniques, it is apparent that rockets have not been heavily employed for composition soundings. The following constituents have been measured directly

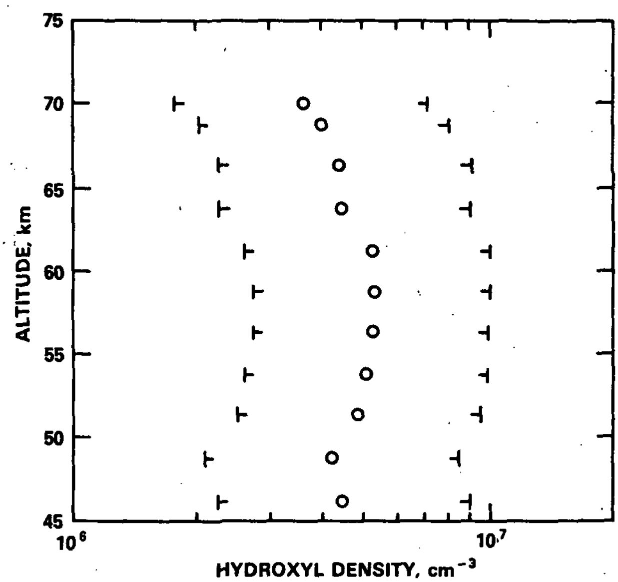

Figure 17. The vertical distribution of hydroxyl measured at White Sands, New Mexico, on April 22, 1971 (ANDERSON, 1971).

with rockets, in some cases, only one time:

- Ozone
- Nitric oxide
- Nitrogen dioxide
- Water vapor
- Hydroxyl
- Atomic oxygen

While ozone has been sounded by rockets about 400 times, and nitric oxide about 10 times, the other constituents have only one or two measurements. A few additional data points for neutral constituents will be added if grab samples flights are included. Since it might be expected that a dozen or more flights are needed before the instrument and the technique begin to be understood by the experimenter, it would seem that rocket exploration of the neutral composition of the middle atmosphere is still in its infancy. Furthermore, the first completely valid sounding constitutes a zeroth order understanding of the geophysical behavior of the constituent.

Measurements of the neutral composition of the middle atmosphere are necessary to complete our understanding of the chemical and physical processes that control ozone. Rockets offer the only realistic possibility for direct measurements over the entire stratosphere and mesosphere. Yet, the only type of sensor for which substantial efforts have been employed is the ozone sensor. All other developments have been either individual one-time research efforts or very limited research campaigns. Large rockets, with their supporting equipment, can be quite expensive. Meteorological sounding rockets are inexpensive but the payload volume is small and considerable ingenuity is required to design composition measuring instruments. However, it is clear that these rockets are under-utilized in the current age when electronic components no longer require significant volume and measurements can indeed be very sophisticated. A hope is that MAP will encourage the development of new rocket techniques, and that the existence of these techniques will bring funding support to this fertile field.

REFERENCES

Anderson, J. G. (1971), Rocket measurement of OH in the mesosphere, J. Geophys. Res., 76, 7820-7824.

Beronose, H. J., and M. G. Rene (1959), Oxyluminescence of a few fluorescent compounds of ozone, Ozone Chemistry and Technology, Advan. Chem. Series, 21, 7-12.

Carver, J. H., B. H. Horton, and R. S. O'Brien (1972), Ozone determinations by lunar rocket photometry, Planet. Space Sci., 20, 217-223.

DeJonckheere, C. G. (1975), A measurement of the mixing ratio of water vapor from 15 to 45 km, Q. J. R. Meteorol. Soc., 101, 217-226.

Evans, W. F. J., D. M. Hunten, E. J. Llewellyn, and A. Vallance Jones (1968), Altitude profile of the infrared atmospheric system of oxygen in the dayglow, J. Geophys. Res., 73, 2885-2896.

Evans, W. F. J., and E. J. Llewellyn (1971), ISAS Report, University of Saskatchewan.

Evans, W. F. J. (1974), Rocket measurements of water vapor in the stratosphere, Proceedings of the International Conference on Structure, Composition and General Circulation of the Upper and Lower Atmospheres and Possible Anthropogenic Perturbations, IAMAP, Melbourne, January 14-25.

Evans, W. F. J., E. J. Llewellyn, and A. Vallance Jones (1972), Altitude distribution of the $O2('\Delta g)$ nightglow emission, J. Geophys. Res., 77, 4899-4901.

Grahn, S., and G. Witt (1974), High-latitude ozone soundings with a rocket-borne multi-wavelength solar irradiance photometer, Rep. AP-16, Inst. of Meteorol., Univ. of Stockholm.
Henderson, W. R. (1974), Atomic oxygen profile measurements, J. Geophys. Res., 79, 3819-3825.
Henderson, W. R., and H. I. Schiff (1970), A simple sensor for the measurement of atomic oxygen height profiles in the upper atmosphere, Planet. Space Sci., 18, 1527.
Hilsenrath, E. (1971), Ozone measurements in the mesosphere and stratosphere during two significant geophysical events, J. Atmos. Sci., 28, 295-297.
Hilsenrath, E., L. Seiden, and P. Goodman (1969), An ozone measurement in the mesosphere and stratosphere by means of a rocketsonde, J. Geophys. Res., 74, 6873-6880.
Hilsenrath, E., and P. T. Kirshner (1980), Recent assessment of the performance and accuracy of a chemiluminescent rocketsonde for upper atmospheric ozone measurements, Rev. Sci. Instrum., 51, 1381-1389.
Horvath, J. J., and C. J. Mason (1978), Nitric oxide mixing ratios near the stratopause measured by a rocket-borne chemiluminescent detector, Geophys. Res. Lett., 5, 1023-1026.
Horvath, J. J., J. E. Frederick, N. Orsini, and A. R. Douglass (1983), Nitric oxide in the upper stratosphere: measurements and geophysical interpretation, J. Geophys. Res., 88, 10809-10817.
Iwagami, N., and T. Ogawa (1980), An Antarctic NO density profile deduced from the Gamma band airglow, Planet. Space Sci., 28, 867-873.
Johnson, F. S., J. D. Purcell, R. Tousey, and K. Watanabe (1952), Direct measurements of the vertical distribution of atmospheric ozone to 79 kilometers altitude, J. Geophys. Res., 57, 157-176.
Krueger, A. J. (1973), The mean ozone distribution from several series of rocket soundings to 52 km at latitudes from 25 S to 64 N, Pure Appl. Geophys., 81, 1272-1280.
Krueger, A. J. (1984), Inference of photochemical trace gas variations from direct measurements of ozone in the middle atmosphere, Ph.D. Dissertation, Colorado State University.
Krueger, A. J., and W. R. McBride (1968), Rocket ozonesonde (ROCOZ) - Design and development, NWC TP4512, Naval Weapons Center, China Lake, Calif.
Kulcke, W., and H. K. Paetzold, Uber eine Raiosonde zuer Bestimmumg der vertikalen Ozonverteilung, Ann. Meteorol., 8, 47-53.
Lean, J. L. (1974), UV rocket spectroscopy measurement of the nighttime ozone distribution, J. Geophys. Res. 88, 1468-1474.
Llewellyn, E. J., and G. Witt (1977), The measurement of ozone concentrations at high latitude during the twilight, Planet. Space Sci., 25, 165-172.
Mason, C. J., and J. J. Horvath (1976), The direct measurement of nitric oxide concentration in the upper atmosphere by a rocket-borne chemiluminescent detector, Geophys. Res. Lett., 391-394.
Meira, L. G. (1971), Rocket measurements of upper atmospheric nitric oxide and their consequences to the lower ionosphere, J. Geophys. Res., 76, 202-212.
Miller, D. E., and P. Ryder (1973), Measurement of the ozone concentration from 55 to 95 km at sunset, Planet. Space Sci., 21, 963-970.
O'Brien, R. S., and W. F. J. Evans (1981), Rocket measurements of the distribution of water vapor in the stratosphere at high latitudes, J. Geophys. Res., 86, 12101-12107.
Randhawa, J. S. (1967), Ozonesonde for rocket flight, Nature, 213, 53-54.
Regener, V. H. (1964), Measurement of atmospheric ozone with the chemiluminescent method, J. Geophys. Res., 69, 3795-3800.
Rogers, J. W., A. T. Stair, T. C. Degges, C. L. Wyatt, and D. J. Baker (1977), Rocket-borne measurements of mesospheric H_2O in the auroral zone, Geophys. Res. Lett., 4, 366-368.

Schlyter, P., and G. Witt (1982), A rocket-borne photometric measurement of O_3 and NO_2 in the equatorial stratosphere, J. Geophys. Res., 87, 7228-7234.

Sissons, N. V. (1968), Ozone measuring techniques and their assessment for W. R. E. dropsonde use, Australian Defence Scientific Service, Weapons Research Establishment, Tech. Note SAD 196, December.

Solheim, G. H. (1979), M. Sc. Thesis, Univ. of Saskatchewan.

Subbaraya, B. H., and Shyam Lal (1978), Space Research, 19, COSPAR, Innsbruck, Austria.

Tisone, G. C. (1972), Measurements of the absorption of solar radiation by O_2 and O_3 in the 2150-A region, J. Geophys. Res., 77, 2971-2974.

Tohmatsu, T., T. Ogawa, and T. Watanabe (1973), Photoabsorption of the upper atmosphere in the middle ultraviolet region, COSPAR, Konstanz.

Tohmatsu, T., and N. Iwagami (1976), Measurement of nitric oxide abundance in equatorial upper atmosphere, J. Geomag. Geoelectr., 28, 343-358.

Weeks, L. H., R. S. Cuikay, and J. R. Corbin (1972), Ozone measurements in the mesosphere during the solar proton event of 2 Nov. 69, J. Atmos. Sci., 29, 1138-1142.

Wood, H. C., W. F. J. Evans, E. J. Llewellyn, and A. Vallance Jones (1970), Summer daytime height profiles of O_2 ($^1\Delta$) concentration at Fort Churchill, Can. J. Phys., 48, 862-867.

D-3 46 R3R 7611

N86-26728

DM025X15

3. MEASUREMENTS OF X-RAY ENERGY DEPOSITION IN THE MIDDLE ATMOSPHERE

J. R. Barcus

Department of Physics
University of Denver
Denver, Colorado 80208

ABSTRACT

Rocket techniques as applied to measurements in the middle atmosphere of X-rays in the 5-100 keV range are presented. Different types of detectors and payloads are compared in regard to their capabilities and limitations. Assessment of the energy deposition by X-rays is examined by methods involving in situ measurements and/or model-dependent calculations. Recent results illustrate the role of X-rays as an important source of ionization in the middle atmosphere at all latitudes, with the greatest range of effects taking place at high magnetic latitudes.

INTRODUCTION

The purpose of this chapter is to present some details of rocket techniques and measurements which are aimed at assessing the role of extraterrestrial X-rays for energy deposition in the middle atmosphere (∿30-90 km). The importance of energy deposition by X-ray radiation in comparison with other sources has not been a subject of general agreement. To a certain extent, this has come about from drawing conclusions based on results of computed depositions using source functions and/or model parameters that were uncertain or nontypical. In situ measurements by rocket-borne experiments covering a wide range of disturbance conditions has served to improve our understanding of these problems.

Perturbations of the quiescent state of ionization are thought to be important for a number of studies, including those concerned with minor constituents, aerosols, and global electrodynamics, where ionization rates form the starting point for all investigations of ultimate interest. A review of the several energy inputs to the middle atmosphere has been given recently by ROSENBERG and LANZEROTTI (1979). This valuable work has examined most of the conventional sources of ionization due to energetic charged particles and electromagnetic radiation, both of transient event types and for the quasi-steady background. Their review considered data gathered from ground-based as well as spacecraft experiments and also included results of model calculations.

Here we are concerned primarily with rocket techniques and some illustrative results as they pertain to the energy deposition by X-rays (∿ few keV to ∿ 100 keV) in the middle atmosphere. These results are compared with other known sources occurring at the same time and place. The organization of the paper is as follows: first are discussed some basic characteristics of the detectors and a description of typical rocket instruments; then the penetration of X-rays in the terrestrial atmosphere is examined together with the methods of assessing the energy deposition; the paper concludes with a presentation of some illustrative results obtained at different latitudes as they relate to the importance of X-rays as a competitive source of ionization in the middle atmosphere.

DETECTORS

A variety of conventional instruments is available for X-ray measurements from rockets transiting the atmosphere as well as during overflights conducting

ORIGINAL PAGE IS
OF POOR QUALITY

mapping surveys at high altitude. Among others, these instruments include ionization chambers, Geiger counters, proportional counters, and scintillation and semiconductor detectors. Despite comparable efficiency and superior energy resolution, semiconductor detectors have not seen much use for low-energy X-ray measurements in the atmosphere. The major drawbacks for high purity germanium and lithium-drifted silicon relative to other detectors are the need for cryogenic support, including the preamplifier, and the cost. Two materials that can be operated at room temperature are cadmium telluride (CdTe) and mercuric iodide (HgI_2); they have considerable efficiency because of their high atomic number, but poorer energy resolution than germanium because of the larger energy needed to produce an electron-hole pair.

By far, the detectors most commonly employed for rocket work have been the proportional counter and, increasingly in recent years, the scintillator. These instruments may be operated (indeed usually are) with passive and/or active collimation, in configurations employing coincidence/anticoincidence so as to reduce background and/or to identify specific events. A brief account follows covering some of the capabilities and limitations of these detectors, information needed for proper interpretation and use of the experimental results are presented later. This abbreviated examination is far from complete, and the reader who is interested in further information on scintillation detectors and proportional counters should consult reference works such as BIRKS (1964) and CURRAN and WILSON(1965). Also, a very readable account of the fundamentals and design of pulse amplifiers can be found in a series of articles by FAIRSTEIN and HAHN (1965, 1966).

Proportional Counters. A cross section of a typical gas-filled counter is shown in Figure 1. The anode A is a small tungsten wire ($\lesssim$ 1 mm) mounted coaxially with the cathode C. High tension (1200-2400 volts, depending upon the construction) is applied between C and A. The entrance window is preferable on the side, as shown, eliminating dead space. The window can be of mica with its inner surface thinly coated with a metal to maintain a uniform electrical field; alternatively, the window can be of thin beryllium. Another, usually larger, exit window is placed opposite the entrance, thus preventing those photons which pass unabsorbed through the gas from striking the thick cathode walls and causing spurious pulses. Since the gas-absorption path is small, a gas having a high absorption coefficient must be used to obtain a reasonable quantum-counting efficiency. Noble gases such as argon, xenon, and krypton at a few ten's of cm Hg pressure are common.

The operating voltage is below the Geiger threshold so that, upon photoelectric conversion, the discharge is limited to the region where absorption occurred. The resulting charge amplification is only the order of 10^4 so

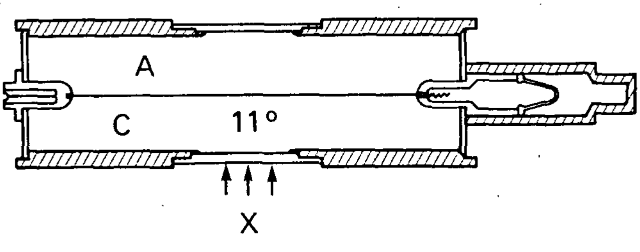

Figure 1. Cross section of a proportional counter. X-rays are shown entering by a side window (W) placed in the cathode (C) housing. The coaxial anode (A) collector is operated at high voltage.

that a high-gain linear amplifier is necessary to bring the resultant pulses to an amplitude useful for pulse-height analysis.

A pure gas counter has a long lifetime but suffers from the phenomenon of after-pulsing, causing false counts. Addition of a small amount (∿10%) of a quench gas (large organic molecules, such as methane) is common. Such counters have a useful lifetime of $\sim 10^9$ counts.

As with the scintillator and solid-state detectors, the proportional counter has the advantages of good pulse-height linearity with X-ray energy and short pulse times ($\lesssim$ μsec) so that operation at high counting rates is possible.

Table 1 lists some typical parameters for counters commercially available. Special designs have been implemented by numerous research groups.

TABLE 1

PROPORTIONAL COUNTER SPECIFICATIONS

Window					
Typo	end window	end window	side window	side window	side window
Thickness (mg/cm^2 or in.)	.002	.002	3 - 4	.010	.010
Dimensions (in.)	1/4 dia.	1/2 dia.	.817 X .25	1.0 dia.	1.0 dia.
Material	Beryllium	Beryllium	Mica	Beryllium	Beryllium
Wall Material	Cr Fe	Cr Fe	Cr Fe	Cr Fe	Cr Fe
Tube Dimensions					
Inside diameter (in.)	1/2	1/2	25/32	1 7/8	1 7/8
Path length (in.)	1/2	1/2	13/16	2	2
Max. diameter (in.)	11/16	11/16	1	2	2
Max. overall length (in.)	1 7/8	1 7/8	4 3/8	8 1/8	8 1/8
Gas filling	Ar	Ar	Xe	Kr	Xe
Gas pressure (cm Hg)	12	72	34	72	72
Operating voltage, V_b (V.)	1250-1500	1250-1500	1700-2000	1700-2200	1800-2400
Max. resolution (Fe-K) (%)	25	25	20	18	18
Tube Capacitance (pF)	3	3	4.5	8	8
Weight (g)	25	25	135	420	420

Scintillation Detectors. The two elements of the detector are a fluorescent crystal and a photomultiplier tube (Figure 2). The most widely used crystal is thallium activated sodium-iodide, [NaI(Tl)]. Sodium iodide is hygroscopic and must be hermetically sealed. Many other medium- to high-Z inorganic crystals are available, and some of these are listed, together with their important properties, in Table 2. As the table shows, none of these materials excels in light output compared to NaI. Also, there are many organic scintillators, both solid and liquid, but these are relatively less efficient than the inorganics for X-ray detection. The entrance window is commonly beryllium (∿0.1 mm) which will transmit X-rays down to a few keV (Figure 3). The quantum counting efficiency is dependent on X-ray absorption in the crystal (see Figure 4 and the further discussion following this section). The principal fluorescent decay time in NaI is only 230 nanoseconds, so that linearity to high counting rates is possible. The radial sensitivity can be made practically constant with suitably designed systems of optical-coupling to the photomultiplier; thus, the size of the crystal can be chosen to implement rather large detectors. Also, it is possible to obtain scintillation crystals in a wide variety of geometric forms and thicknesses. It is essential that the photomultiplier have low-noise characteristics ($\lesssim$ 0.5 keV equivalent). The charge pulse delivered by a photomultiplier is generally larger than that from

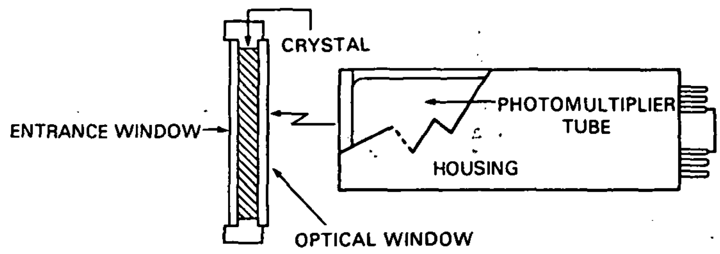

Figure 2. Cross section of a scintillation detector. The exploded view shows the crystal hermetically sealed between the entrance and optical windows.

TABLE 2

PROPERTIES OF SCINTILLATION PHOSPHORS

Material	Wavelength of Maximum Emission (nm)	Decay Constant (μS)	Scintillation Cutoff Wavelength (nm)	Index of Refraction	Density (g/cc)	Hygro-scopic	Scintillation Conversion Efficiency (%)*
NaI(TI)	410	.23	320	1.85	3.67	Yes	100
CaF_2(Eu)	435	.9	405	1.44	3.19	No	50
CsI(Na)	420	.63	300	1.84	4.51	Yes	85
CsI(TI)	565	1.0	330	1.80	4.51	No	45
^{6}LiI(Eu)	470-485	1.4	450	1.96	4.08	Yes	35
TICI(Be,I)	465	0.2	390	2.4	7.00	No	2.5
CsF	390	.005	220	1.48	4.11	Yes	5
BaF_2	325	.63	134	1.49	4.88	No	10
$Bi_4Ge_3O_{12}$	480	.30	350	2.15	7.13	No	8
KI(TI)	426	.24/2.5	325	1.71	3.13	Yes	24
$CaWO_4$	430	.5-20	300	1.92	6.12	No	50
$CdWO_4$	530	.5-20	450	2.2	7.90	No	65
Plastics	350-450	.002-.020	Varies	Varies	1.06	No	5
Liquids	350-450	.002-.008	Varies	Varies	0.86	No	5

*Referenced to NaI

a proportional counter converting the same energy; however, linear amplifiers having moderate gain are still required before presentation of the pulses to the analyzer.

Quantum Counting Efficiency. The efficiency of a detector may be calculated from known absorption coefficients, $Eff(E) = f_T(E)\ f_A(E)$, where f_T is the fraction of the incident photons of energy E transmitted by the window (see Figure 3) and f_A is the fraction absorbed in the active portion of the detector. The intrinsic f_A of a NaI detector is essentially equal to $1-\exp\ (-\ \mu(E)/L)$, where $\mu(E)$ is the absorption coefficient and L is the thickness of the crystal. This relationship assumes that only photoelectric absorption determines f_A. Examination of Figure 4 for NaI shows that this is valid for 'thin' crystals, working at low energy where Compton scattering in the crystal detector is much less probable than photoelectric absorption. However, for some detector configurations, limited angular and radial sensitivity as well as escape peaks (see following) may considerably reduce Eff, and should be allowed for. In any case, Eff always varies to some extent with energy, falling off at high energy because of lower absorption in the active

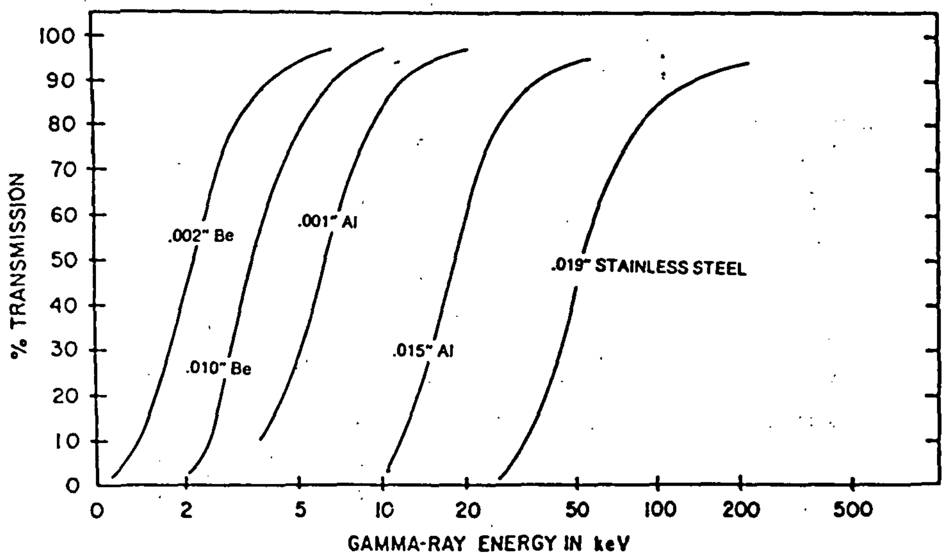

Figure 3. Photon transmission through beryllium and aluminum entrance windows and a stainless steel housing of typical thicknesses.

volume and also at low energy because of higher absorption in the window. Also, there may be abrupt changes in Eff at absorption edges, for example at the iodine K-edge in the NaI scintillator. The energy dependence of Eff is shown in Figure 5 for four common detectors compared to double-coated X-ray film. Here one can see that the scintillation detector (1 mm thick) has the highest and most uniform Eff in the X-ray regime of interest for the middle atmosphere. Figure 6 is a similar presentation for a Ge semiconductor detector, yielding an efficiency comparable to a scintillator.

Pulse Amplitude Distribution. For proportional, scintillation, and semiconductor detectors a principal advantage is that the pulse amplitudes are proportional to the X-ray energy converted in the active volume. Thus, electronic methods may be used not only to study the spectral content of the incident radiation, but also to reject unwanted signals. The inherent energy resolution of proportional and scintillation detectors for 5-100 keV X-rays is rather poor, considerably less than that attainable with semiconductor detectors. Consider monochromatic radiation (E) incident on the detector. The resulting pulse amplitude distribution is not a narrow line but rather a broad peak, normally characterized by its width W at half-maximum. This distribution is the end result of a chain of probabilistic processes, beginning with the conversion of absorbed energy into quanta or elementary charges in the active volume. The ratio W/E is a measure of the energy resolution: the smaller the ratio the better the resolution. Well constructed proportional counters give $W/E \sim 0.2$ at ~ 6 keV, whereas equally well produced scintillators with a 'good' photomultiplier tube can do no better than ~ 0.4 at the same energy; however, semiconductor detectors are about an order of magnitude better, capable of $W/E \sim 0.03$ in the same energy range (Figures 7 and 8).

Escape Peaks. The pulse amplitude distribution may contain two (or more) peaks even when monochromatic X-rays are incident. Absorption of the X-ray may cause fluoresence in the gas or crystal. If this radiation is

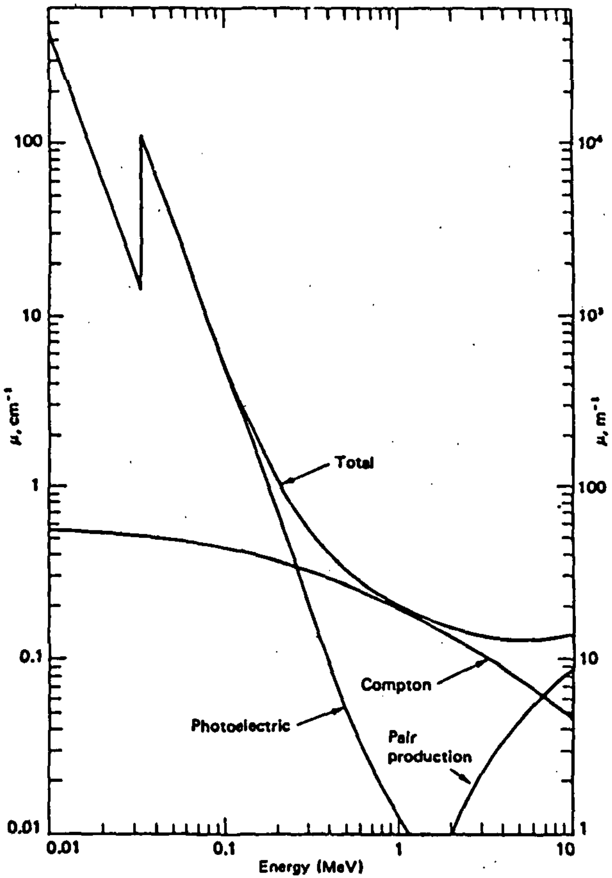

Figure 4. Photon absorption coefficients for sodium-iodide.

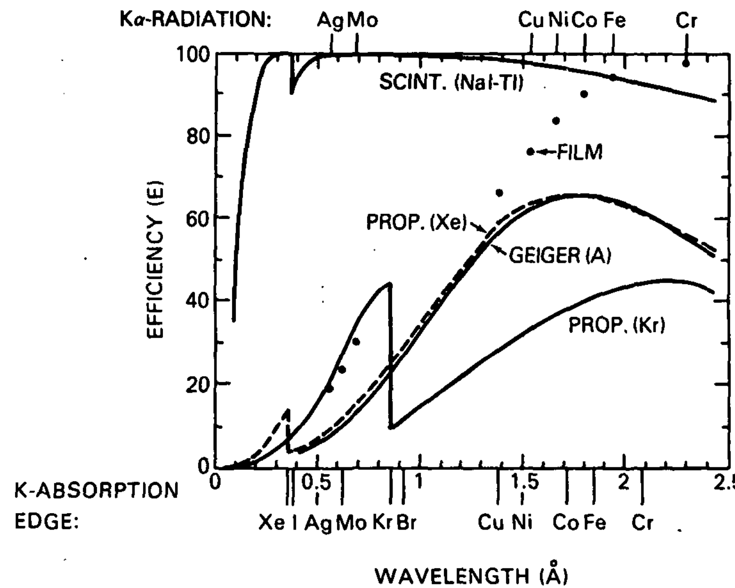

Figure 5. Wavelength dependence of the quantum counting efficiency for a scintillation detector (1 mm thick NaI), proportional counter, and Geiger counter, compared to X-ray film (1 A = 12.4 keV).

ORIGINAL PAGE IS OF POOR QUALITY

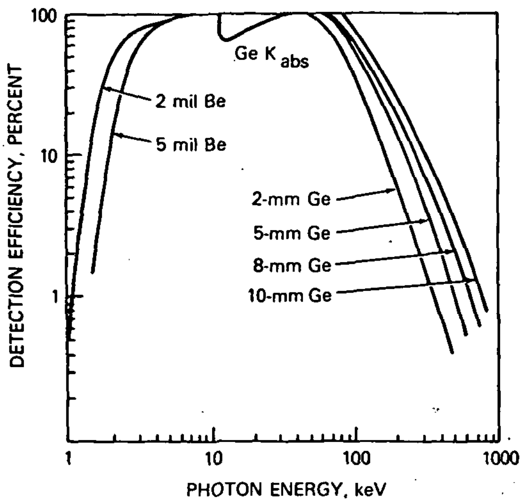

Figure 6. Efficiency of a hyperpure germanium detector for various thicknesses.

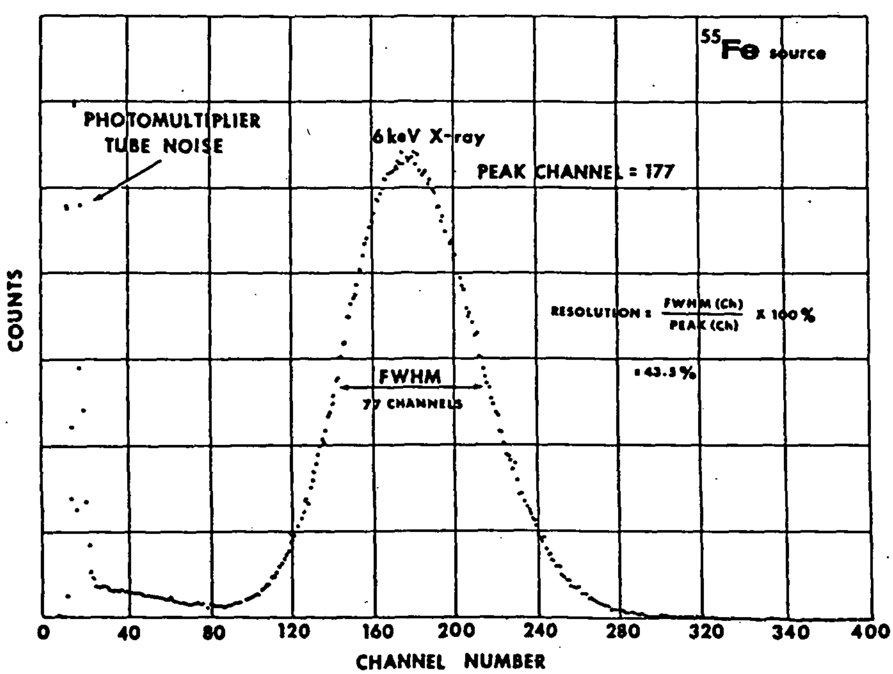

Figure 7. Energy resolution for a NaI scintillator at 5.9 keV (source Harshaw Chemical Co.).

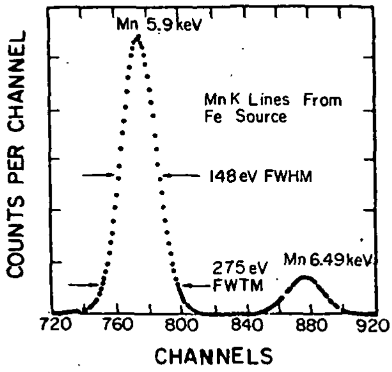

Figure 8. Energy resolution for a Si(Li) solid-state detector at 5.9 keV (source Ortec Inc.).

reabsorbed in the active volume only one pulse, of average amplitude A, proportional to E is formed; thus, $A = K E$, where K is some constant. The distribution of such pulses forms the 'photopeak'. However, if the gas or crystal has a low absorption coefficient for its own fluorescent radiation, some quanta, of energy e, may escape from the active volume (the actual number depending on the geometry, among other factors). The average amplitude of the pulses, thus produced is only $a = K(E-e)$. The distribution of these pulses forms the 'escape peak.' For Kα emission is NaI, as an example, one has e = 28.5 keV; thus, some incident X-rays at 33.5 keV actually appear in the distribution at 5.0 keV.

Spectrum Unfolding. Raw experimental data seldom gives the answer to the problem that is the objective of the measurement. As shown in the preceding discussion, for example, the measured energy spectrum can never be a faithful replica of the source spectrum because of inherent imperfections associated with the detection technique (e.g., efficiency, line shape, escape peaks, etc.). When the imperfections are reasonably well known, a better approximation to the source spectrum can be obtained by "unfolding" the measurements. To illustrate the most simple example, consider the case where the data have been purged of any contamination (e.g., noise, background, other extraneous signals). Then, if M_i is the result of measuring the number of events with energy falling in the bin, E_i to E_{i+1}, M_i is related to the source spectrum $S(E')$ by

$$M_i = \int_{E_i}^{E_{i+1}} dE \int_0^{\infty} R(E,E')\ S(E')\ dE'$$

where $R(E,E')\,dE$ is the response function of the detector, that is, the probability that a source photon of energy E' will be recorded as having an energy between E and E+dE.

The method of solution for S(E') varies from application to application; however, many of these methods are based on the transformation to a matrix equation. The integral over E' is replaced by a sum of integrals over N energy intervals $\Delta E_j = E_{j+1} - E_j$, and the source spectrum is approximated by $S(E') = S_j/\Delta E_j$.

The result is

$$M_i = \sum_{j=1}^{N} R_{ij} S_j$$

where

$$R_{ij} = (\Delta E_j)^{-1} \int_{E_i}^{E_{i+1}} dE \int_{E_j}^{E_{j+1}} R(E,E')\ dE'$$

Written more concisely in matrix notation,

$$\underline{M} = \underline{R} \cdot \underline{S},$$

with the formal solution

$$\underline{S} = \underline{R}^{-1} \cdot \underline{M},$$

where $\underline{R}^{-1}$ is the inverse matrix of $\underline{R}$.

When the spectrum is slowly varying (as is usually the case for X-rays in the atmosphere), the often difficult inversion process may be avoided. One scheme uses an iteration method which starts with the measured spectrum as a first guess for the source spectrum. Thus, $S_K^{(1)} = M_k$,

so that $M_i^{(1)} = \sum R_{ik} S_k^{(1)}$, with the resulting error $M_i - M_i^{(1)}$.

The next iteration uses $S_k^{(2)} = S_k^{(1)} + [M_k - M_k^{(1)}]$,

so that $M_i^{(2)} = \sum R_{ik} S_k^{(2)}$, with the resulting error $M_i - M_i^{(2)}$.

The iteration proceeds in like manner until the error $M_i - M_i^{(n)}$ is acceptably small. This method often converges in a few iterations.

In some cases, purely analytic procedures have produced equally good results in unfolding spectra (TSOULFANIDIS et al., 1969).

Contamination by Energetic Electrons. Many rocket measurements of X-rays in the middle atmosphere have been made at high latitudes where a relativistic electron precipitation from the magnetosphere is common. If the X-ray detector is not provided with some type of electron rejection, energetic electrons, which are present at altitudes as low as 50 km, will penetrate the entrance window and deposit varying amounts of energy in the active medium (e.g., scintillation crystal or absorption gas) as well as produce local bremsstrahlung by impact on the detector and surrounding payload structure. It is necessary to remove such effects from the raw observations in order to arrive at the true X-ray flux in the atmosphere. Moreover, evaluation of the energetic electron flux is useful in its own right, both as an important source of ionization in the middle atmosphere and also as a means of obtaining additional data relevant to energetic magnetospheric processes.

Taking as an example a typical detector consisting of a 1 mm (367 mg/cm^2) thick NaI(Tl) crystal fitted with a 0.005-in (23.5 mg/cm^2) beryllium window, some semi-quantitative features of energetic electron penetration can be gained by considering Figure 9. Here are shown the residual energy losses in the NaI crystal for electrons with energy 100 keV to 300 keV incident on the beryllium entrance window at 0°, 45°, and 60°. The energy thresholds for penetration are ∿120 keV, ∿147 keV, and ∿182 keV at the incidence angles of 0°, 45°, and 60°, respectively. Above the threshold, the energy loss rises rapidly, then approaches an approximately linear relationship with incident electron energy until the range of the electron exceeds the combined thickness

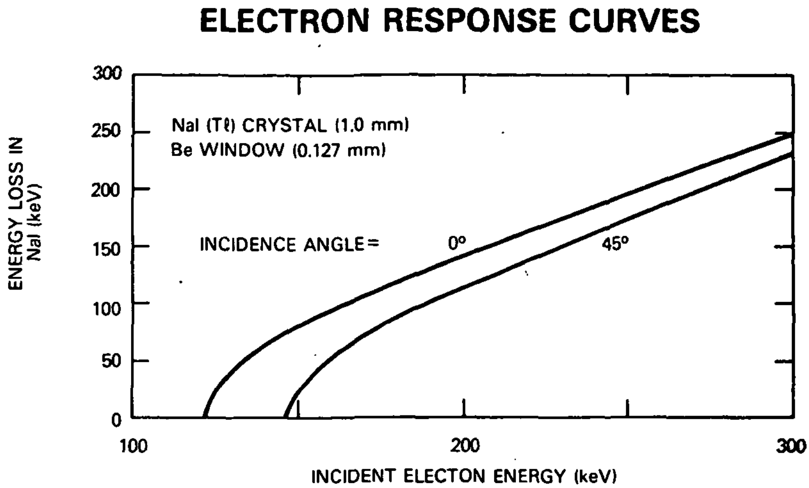

Figure 9. Energy loss in a NaI crystal 1 mm thick due to electron penetration of the 0.005-in beryllium entrance window.

of the window and crystal. For the combination considered here, the maximum energy loss is $\sim$650 keV for electrons of $\sim$700 keV at normal incidence. At greater energies, the energy loss falls off (and the pulse height distribution becomes double-valued) until the region of minimum ionization ($\gtrsim$ a few MeV in NaI) is reached, where the energy loss due to collisions attains a broad minimum of about 1.14 MeV/gm/cm^2. However, at these energies, radiation by electrons in the detector has become a significant factor, and this eventually becomes the dominant mechanism of energy loss at still greater energies.

Many of the X-ray detectors in use are of the wide-angle variety, with acceptance cones extending to 45° or more. Thus, for the typical wide-angle detector considered here, if pulse-height discriminators are set to record X-rays of, say, $\geq$5 keV and $\geq$100 keV, energy losses at these levels could be due to penetrating electrons with energies $\gtrsim$ 120-180 keV and $\gtrsim$ 170-223 keV, respectively. In principle, more refined estimates may be extracted from the data by unfolding the observations with an appropriate response function, including both angular and energy effects, once any genuine X-ray contribution has been removed. In the absence of strong temporal variations in the radiation encountered, the presence of energetic electrons is easily recognized by the character of the atmospheric absorption of the radiation, as revealed in the altitude profiles of intensity at various energies.

Similar estimates for other combinations of window and crystal thicknesses may be made using the energy-loss and range functions for beryllium and sodium-iodide given in Figures 10 and 11, respectively.

ROCKET INSTRUMENTS

Examples of proportional counter instruments which have been used for X-ray measurements in the auroral zone at energies of 1-10 keV are those of WILSON et al. (1969) and ULWICK et al. (1967). The instrument of Wilson et al. employed identical, back-to-back counters of large area ($\sim$40 cm^2) equipped with grid collimators having narrow fields of view ($\sim$0.1 steradians). Except for the entrances, the counter assembly was encased in a plastic

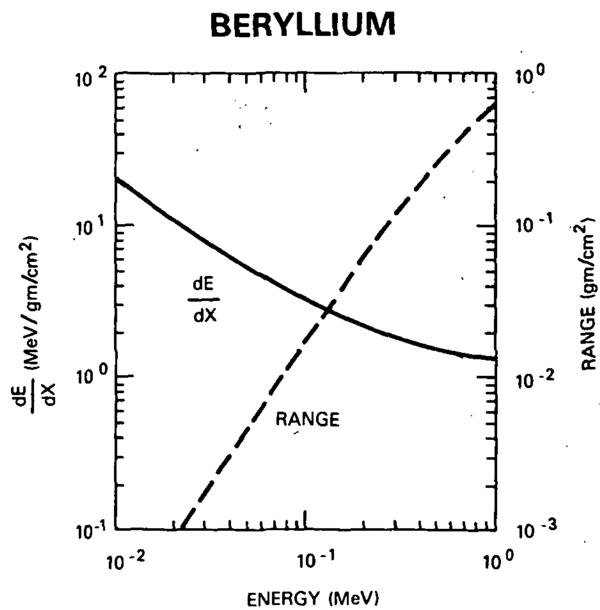

Figure 10. Collisional energy-loss and range functions for electrons in beryllium (PAGES et al., 1972).

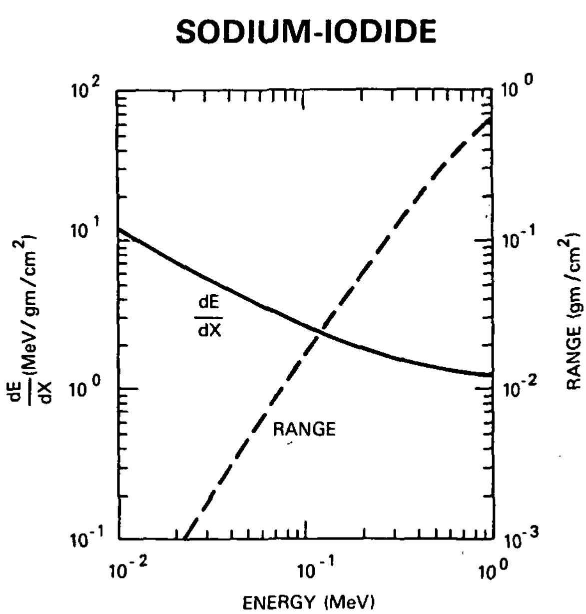

Figure 11. Collisional energy-loss and range functions for electrons in sodium-iodide (PAGES et al., 1972).

scintillator, which was used to reduce background. This instrument was originally intended for astronomical studies, observing by chance on one occasion the X-ray emission from an auroral arc.

Pursuing a variety of purposes, several groups have used NaI scintillation detectors in and above the atmosphere for X-ray measurements from rockets at energies ranging from a few keV to over 100 keV (AARSNES et al., 1976; BARCUS et al., 1979, 1981, 1984; BERING et al., 1980; GOLDBERG et al., 1977, 1982, 1983, 1984; KODAMA and OGUTI, 1976; VIJ et al., 1975, 1980; and others). These instruments are quite similar in many respects, differing in one or more of the following features: mounting, collimation, entrance windows, size and thickness of the NaI crystal, provision for charged particle rejection, and the type and complexity of the pulse-height analysis performed. A brief description of some of these instruments will serve to illustrate their essential features.

The payload used by Kodama and Oguti (Figure 12) consisted of a pair of NaI scintillators (25.4 mm diameter x 2 mm thickness) mounted at 45 and 135 degrees with respect to the rocket axis. Attached to each was a grid-type collimator providing an acceptance cone of about 17 degrees full width. The energy range was set for 4-40 keV energy losses by operating two threshold discriminators in anti-coincidence as shown. The experiment was intended to map auroral X-rays from both below and above the bremsstrahlung production layer (~100 km).

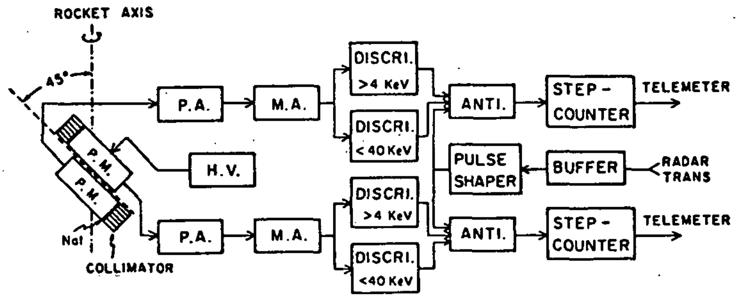

Figure 12. Schematic of the X-ray payload of KODAMA and OGUTI (1976).

Similar experiments (Figure 13) have been carried out by other groups. These incorporated multichannel analyzers (four to eight energy bins) having millisecond resolution and used passively collimated detectors which were also protected against electron contamination by magnets (Figure 14).

Greater energy resolution has been employed in the experiments of BERING et al. (1980) where the energy range 9.5 to 95 keV was examined by a 15-channel analyzer providing four spectra per second. Still greater energy resolution has been utilized in the system of VIJ et al. (1980) in which individual pulses were stretched in time and then telemetered to an analyzer on the ground (Figure 15a). A sample spectrum, covering the range 10-110 keV and acquired over a 10-second interval near 50 km, is shown in Figure 15b; the energy resolution achieved is about a kilovolt. The true spectrum must be mathematically unfolded using appropriate energy-dependent efficiency and resolution functions.

ORIGINAL PAGE IS
OF POOR QUALITY

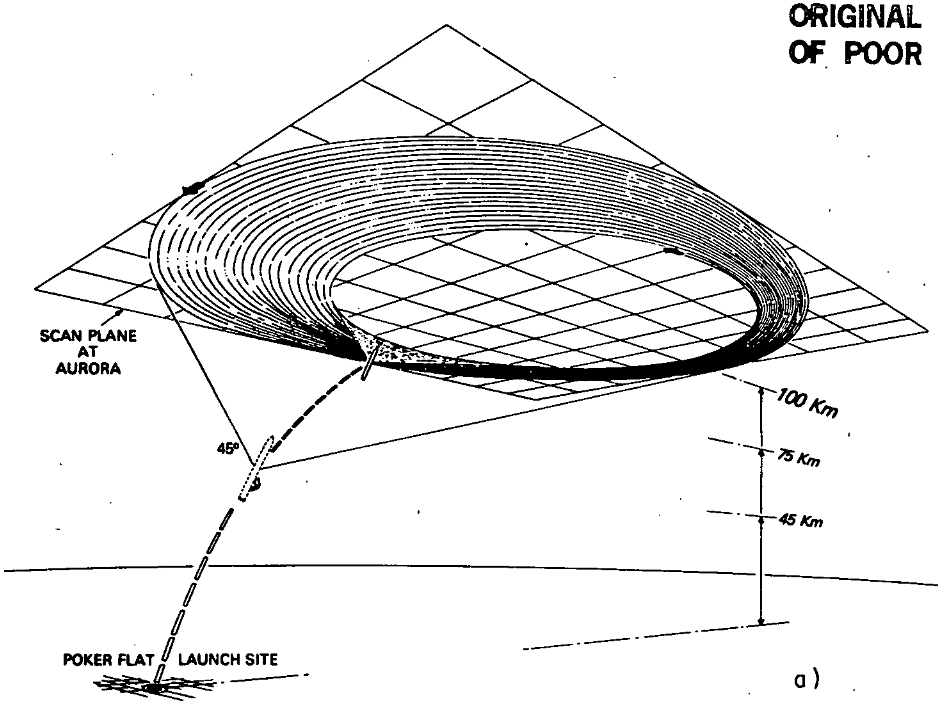

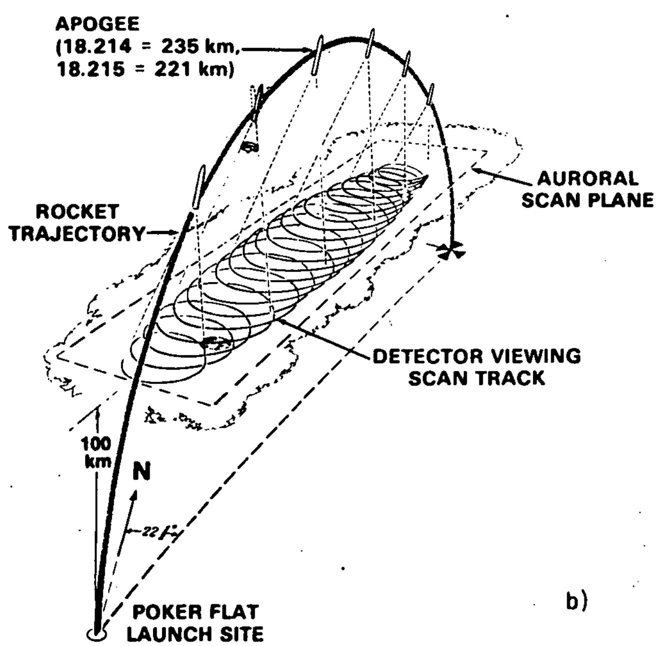

Figure 13. Conceptual depiction of mapping auroral X-ray emission by rocket experiments
(a) From below the production layer and
(b) From above.

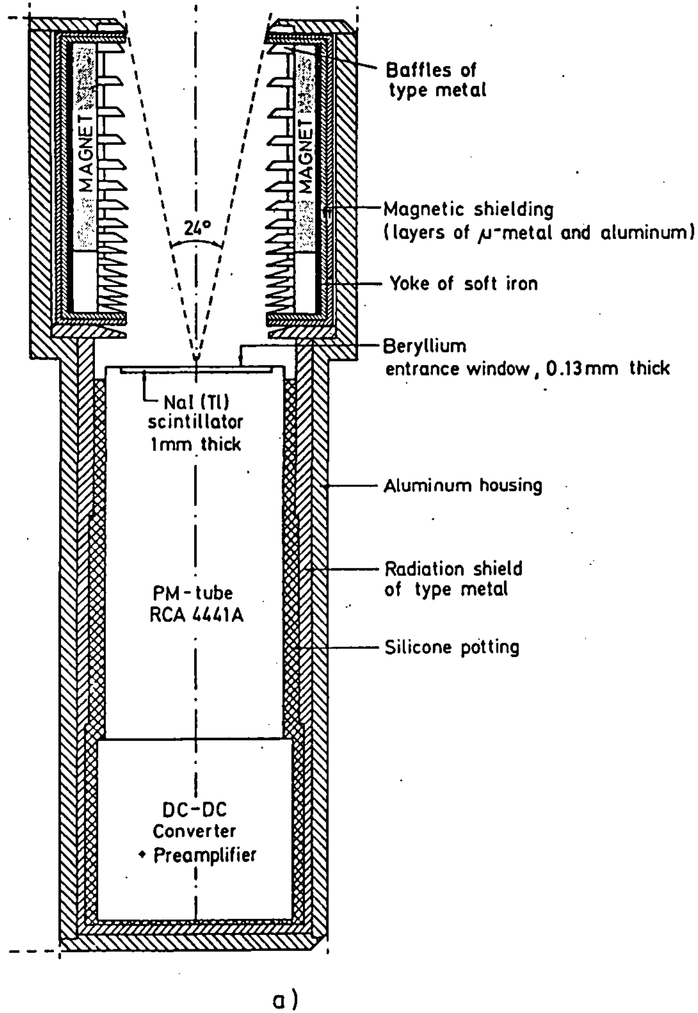

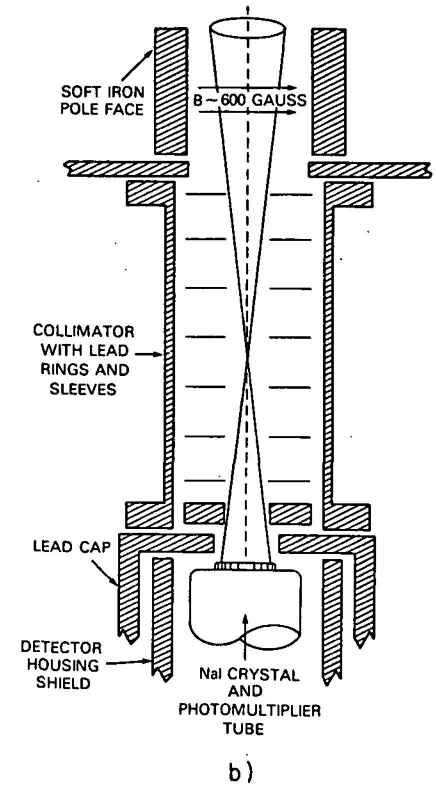

Figure 14. X-ray detectors equipped with broom-magnet protection against energetic electrons entering the instrument through the viewing aperture.
(a) The instrument used by AARSNES et al. (1976), and
(b) The instrument used by GOLDBERG et al. (1982).

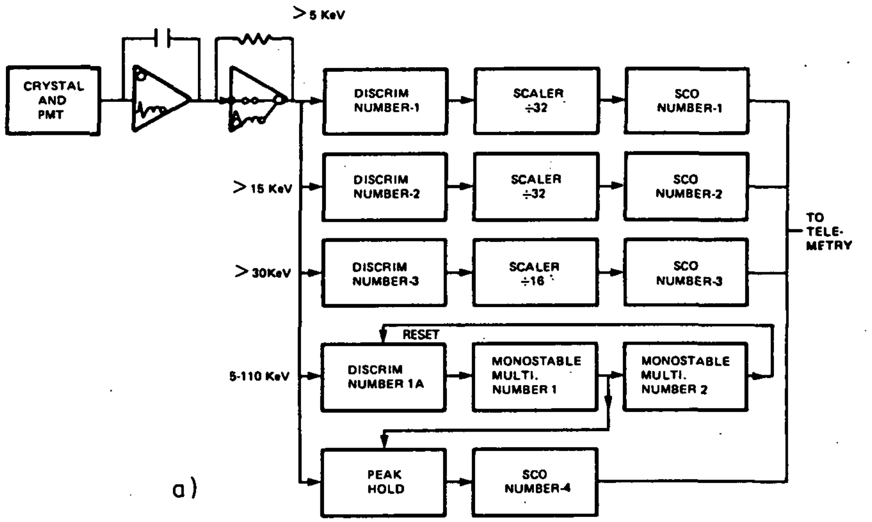

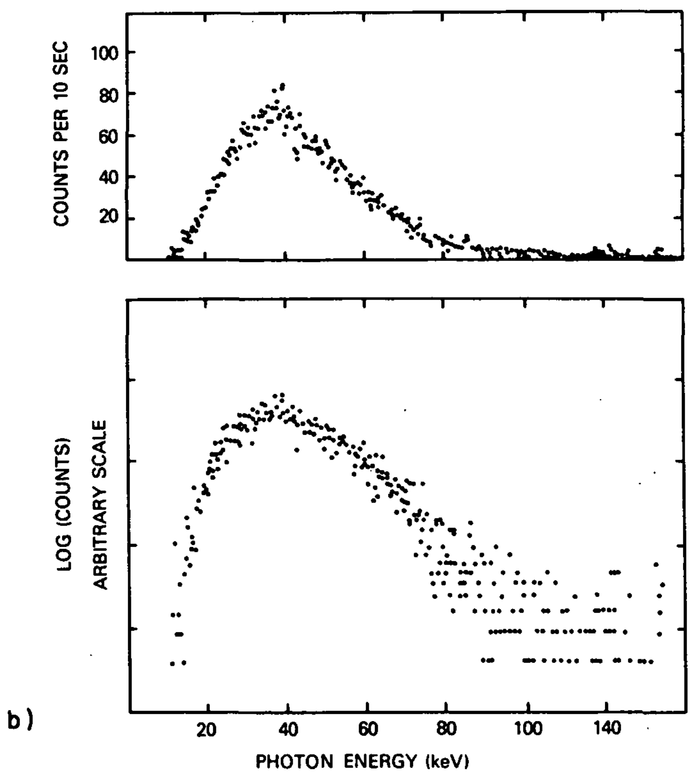

Figure 15. (a) Schematic of the X-ray payload of VIJ et al. (1980), (b) Auroral X-ray energy spectrum (linear and logarithmic plots) obtained at ∿50 km altitude with the instrument shown in (a).

The question of how much energy resolution is needed depends on the nature of the experiment. For example, in the experiment of Vij et al., it was necessary to locate the peak of the X-ray distribution as a function of atmospheric depth; for this purpose, high-resolution was required and unfolding is justified. In contrast, for studies of the energy deposition, low-resolution measurements provide data which are quite adequate to yield excellent results.

PENETRATION OF X-RAYS IN THE ATMOSPHERE

The altitudes to which X-rays of a given energy will penetrate the atmosphere are compared with the range of electrons and protons in Figure 16. For X-rays, the curve gives the depth at which 50% of the initial energy in a vertically incident beam remains. In contrast to the continuous slowing down which is characteristic of charged particles, photon interactions are probabilistic and involve large fractional energy transfers. Thus, the height profiles of energy deposition for X-rays in the atmosphere are more spread out than those for charged particles, and the photon range is correspondingly less well defined.

By way of illustration, Figure 17 shows a result obtained with the instrument of Kodama and Oguti (Figure 12) which was used, in part, to examine the absorption of bremsstrahlung X-rays in the atmosphere. The figure demonstrates the expectation that X-rays of a few keV are effectively absorbed in the upper mesosphere, whereas X-rays of a few ten's of keV will easily penetrate to stratospheric depths. In examining this figure, one should not be misled by the large increase in counting rate seen at high altitude on both up- and downleg passes. Since the detector was unguarded against charged particles, the counting rates at high altitude are probably contaminated to some extent by locally produced bremsstrahlung as well as energetic electron penetration of the entrance window.

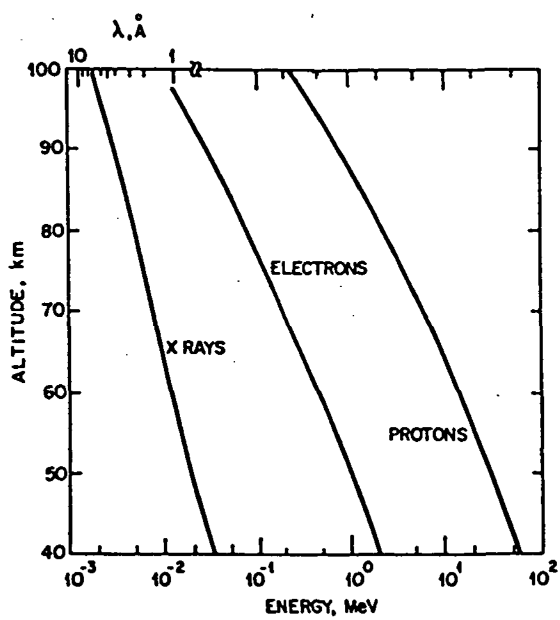

Figure 16. Penetration depths in the atmosphere for X-rays, electrons, and protons. For X-rays, the curve gives the height for 50% transmission (adapted from ROSENBERG and LANZEROTTI, 1979).

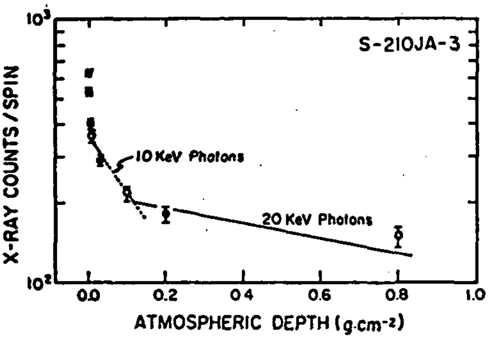

Figure 17. Measurements of the absorption of bremsstrahlung X-rays in the atmosphere by the instrument shown in Figure 12. The solid and open circles are for ascent and descent of the rocket, respectively (from KODAMA and OGUTI, 1976).

Relativistic electrons are present in the high latitude atmosphere much of the time during significant magnetospheric activity. Whether or not they constitute a serious factor in affecting unguarded X-ray detectors depends on a number of factors involving the instrument design as well as the relative intensity of the low-energy bremsstrahlung flux in comparison with that of relativistic electrons. Since these later factors are quite variable and in any case beyond the experimenter's control, it would appear prudent to always include in the rocket's complement of instruments some kind of energetic electron detector.

That energetic electron effects can be identified easily when the rocket also carries an electron detector is demonstrated in Figure 18. Here are shown the raw counting rates of an unguarded NaI scintillator (Ch. 1: 5-10 keV; Ch. 2: 10-20 keV; Ch. 3: 20-40 keV; Ch. 4: >40 keV) together with one channel of a semiconductor electron detector (S1-2: >162 keV) during the upleg portion of a rocket launched into post-breakup auroral activity at Andoya, Norway (69° N) on October 7, 1980. These were two instruments of a large complement carried on rockets involved in a study of the electrodynamics of the middle atmosphere at high latitude (MAYNARD et al., 1984). The X-ray and electron detectors were exposed at approximately 52 seconds after lift-off (altitude = 45 km). Energetic electron bursts are evident in Figure 18 at about 77 seconds (73 km), 87 seconds (82 km), and 97 seconds (90 km). Contamination of the X-ray detector is seen most clearly in the integral channel, E >40 keV, and represents large energy losses in the NaI crystal due to electrons (E $\gtrsim$160 keV) which have penetrated the entrance window. Although the differential X-ray channels appear relatively less affected, particularly at lower energies, the response in the range 5-40 keV is nevertheless seen to be significant. With the verification provided by the electron detector, the contamination is more easily identified, and the X-ray data can be corrected and gainfully used.

Figure 19 illustrates a comparison of the height profiles of the bremsstrahlung fluxes in the energy range 5-10 keV with nominal background rates encountered in the middle atmosphere at high latitudes. The auroral event probed by this flight was by all accounts ordinary. The figure illustrates the ample X-ray signal usually available, so that background corrections are scarcely required except at the lower altitudes. When background corrections are necessary, it is best to make them empirically by means of control measurements with the same or, in so far as possible, similar instruments and payload configurations (as was done for data shown in Figure 19). Relying solely on calculated background corrections has been known to cause a lot of grief and needless speculation.

Background is principally composed of three parts: galactic X-rays from isotropic and discrete sources, atmospheric X-rays produced by the cosmic ray flux, and energy losses in the detector due to a variety of cosmic ray inter-

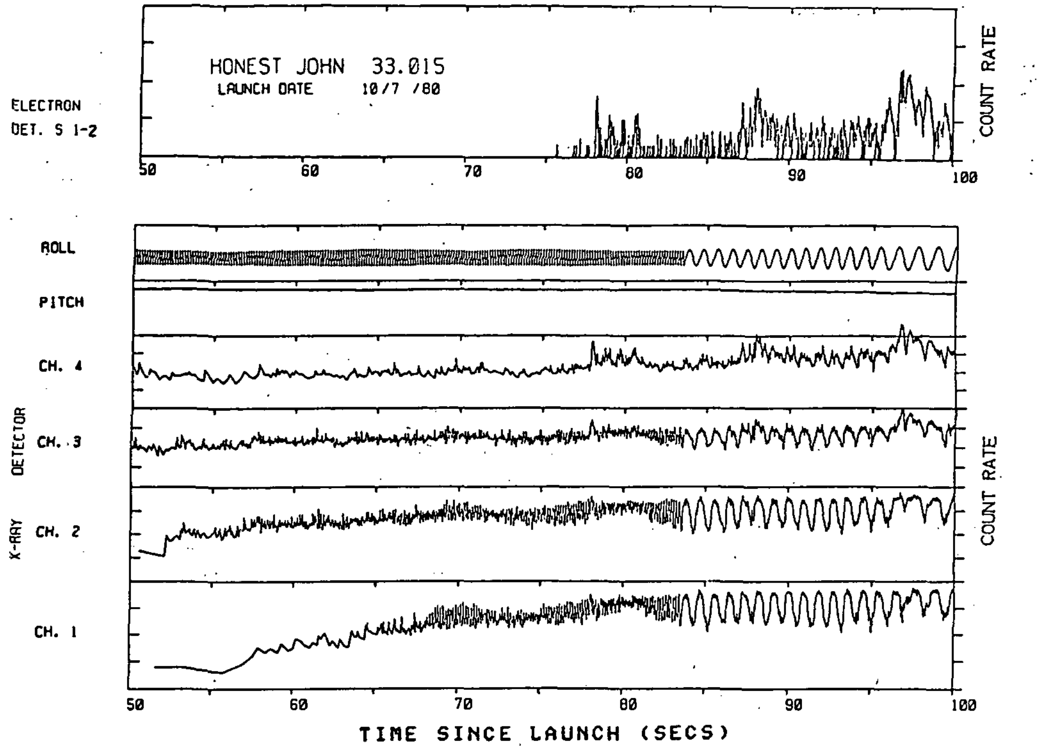

Figure 18. An example of the contamination of an unprotected X-ray detector by energetic electrons penetrating into the mesosphere at high magnetic latitudes. The rocket is at 73 km altitude at 77 seconds after liftoff. Shown for the X-ray detector are count rates for energy losses 5-10, 10-20, 20-40, and >40 keV in Channels 1, 2, 3, and 4, respectively; the upper panel is a similar presentation for Channel S1-2 (>162 keV) of the solid-state electron detector (courtesy F. Soraas, U. of Bergen). The count rate scales for all channels are logarithmic, each spanning 10^0 to 10^4 counts/second.

actions in and around the instrument. The first and second contributions constitute an irreducible background level against which all other sources must be observed. The third contribution, which by no means is insignificant in some instruments, can be reduced by clever design and/or the application of active anti-coincidence techniques (PETERSON et al., 1973). For the purpose here, the second and third can be taken together and will be referred to as the cosmic ray background. Thus, in the instrument used to make the measurements shown in Figure 19, the relative importance of the sources of background for 5-10 keV X-rays in the upper mesosphere stand in the ratio ∿5:1 for galactic X-rays to cosmic rays. At the equator, where the cosmic ray contribution is reduced, the corresponding ratio is ∿20:1. At much higher photon energies the cosmic ray contribution begins to dominate considerations of detector background as the energy spectrum for galactic X-rays falls off rapidly with increasing energy above ∿20 keV (BOLDT et al., 1969). The exact factors are very much instrument-dependent.

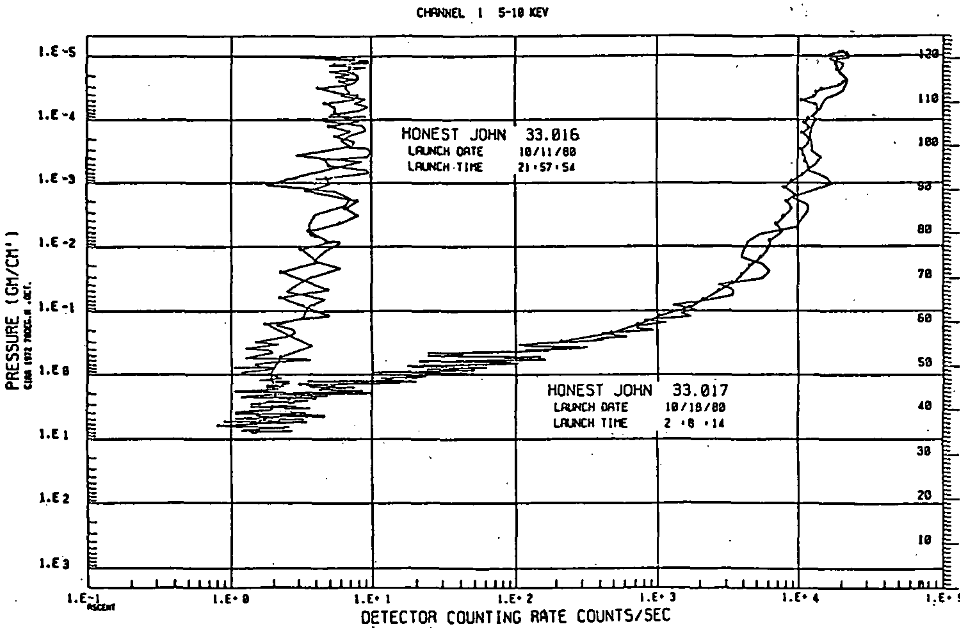

Figure 19. Height profile of 5-10 keV bremsstrahlung X-rays in the middle atmosphere measured by 33.017 during an auroral disturbance compared to cosmic background sources measured by 33.016 during a period of geomagnetic quiet.

ENERGY DEPOSITION BY X-RAYS

There are basically two approaches to the problem of evaluating the energy deposition by X-rays in the atmosphere. One is based on the availability of measurements of X-rays in the atmosphere, whereas the other relies on theoretical computations based on assumed or, perhaps, partially known source functions at the top of the atmosphere. If the measurements are sparse or incomplete in some respect, then a combination of the methods has been used.

The number of ion-pairs formed by a photon of energy E traversing unit path in air at height H is given by $\tau(E)\ M(E)\ N(H)$, where $\tau(E)$ is the absorption cross section, M(E) is the ionization efficiency, and N(H) is the number density at height H. The number of ion-pairs formed in unit volume per unit time at a height H is given by

$$q(H) = \int \int \tau(E)\ M(E)\ N(H)\ \Phi\ (E,\ \theta,\ \phi,\ H)\ dE\ d\Omega$$

where $\Phi(E, \theta, \phi, H)$ is the differential photon flux crossing unit area per second, having directions of incidence lying in unit solid angle centered about a direction fixed by local zenith and azimuth angles θ and ϕ. Thus, if $\Phi(E, \theta, \phi, H)$ is known by measurement, the determination of the local ionization produced is straightforward. Most often, however, even if measured, $\Phi(E, \theta, \phi, H)$ will have been observed only over limited portions of the ranges of the respective variables. In some cases this is not very damaging, as for example in examining the deposition from extraterrestrial low-energy sources where a knowledge of the complete angular distribution is hardly necessary since scattering is not very important. In other cases, involving

say high-energy electron bremsstrahlung which can be quite variable in space and time and also involves considerable energy degradation in scattering processes, knowledge of the angular distribution may be more essential. Figure 20 illustrates some features of the angular distribution for widespread electron bremsstrahlung observed for 20-40 keV photons at ∿60 km (BARCUS et al., 1985). In this instance, the backscattered flux is small, and the dominant, downward flux is nearly isotropic; thus, a reasonable estimate of the energy deposition can be derived from the zenith measurement alone. Nature is not often this accommodating, and it is frequently necessary to deal with results averaged over 'lumpy' distributions in space, time, angle, and energy.

There have been numerous model-dependent calculations of the ionization produced in the middle atmosphere by a variety of photon sources, including quiescent solar EUV and X-rays, scattered Lyman α and β, solar flare enhancements, cosmic X-rays, and bremsstrahlung X-rays from precipitating magnetospheric electrons. The relative importance of any source of ionization for the middle atmosphere is often gauged by comparison with that due to Lyman α above ∿75 km and galactic cosmic rays below, as these are considered to be the major persistent contributors. Figure 21 shows the height profiles of ionization for these two sources for a range of latitudes and solar conditions; the different production rates shown for Lyman α below about 85 km reflect different assumptions about the concentration of nitric oxide. The curves also show the overall latitude effect for cosmic rays and the solar cycle modulation, which becomes particularly large at polar latitudes.

The production and propagation of bremsstrahlung X-rays in the atmosphere has attracted the attention of several authors (REES, 1964; KAMIYAMA, 1966; BAILEY, 1968; PILKINGTON and ANGER, 1971; BERGER and SELTZER et al., 1973; BERGER et al., 1974; NEWKIRK et al., 1974; LUHMANN, 1976; WALT et al., 1979).

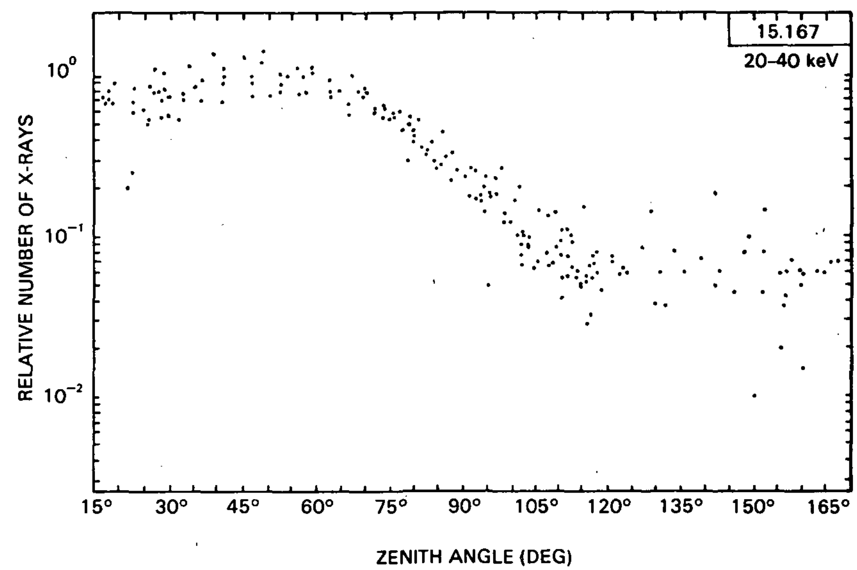

Figure 20. Angular distribution of bremsstrahlung X-rays (20-40 keV) observed at 60 km altitude. At lower energies, the ratio of X-ray intensities arriving from the zenith (0°) and nadir (180°) is greater, otherwise the behavior is similar (from BARCUS et al., 1984).

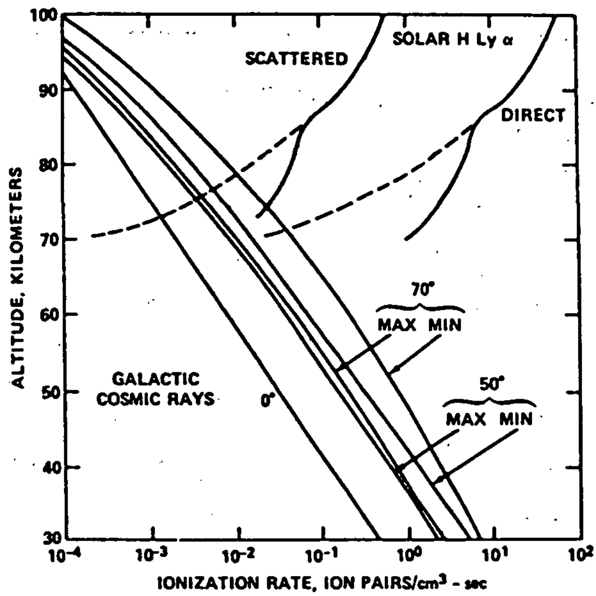

Figure 21. Altitude dependence of ionization rate due to galactic cosmic rays and solar Lyman α (adapted from ROSENBERG and LANZEROTTI, 1979).

The problem can be stated thus: given the energy, angle, and spatial distribution of electrons entering the atmosphere, what is the resulting flux of photons $\Phi(E, \theta, \phi, x, y, z)$? From this result, the energy deposition can be evaluated as already discussed. The methods of computation have been quite varied, as have the specifications of the precipitating electrons and the treatment of photon scattering. Consequently, the results differ on certain details. Typical of the results for energy deposition are the height profiles produced by Berger et al. (1974) which are reproduced in Figure 22. The curves, which are for widespread, isotropic electron precipitation characterized by different e-folding energies (E_o), show that for a wide range of precipitation energies most of the energy deposited by bremsstrahlung X-rays will lie between approximately 20 and 80 km.

AIKIN and MAIER (1963) recognized that, because of the large collisional input by parent electrons at high altitude and the increasingly strong ionization by cosmic rays at low altitude, the bremsstrahlung contribution would likely be of importance only for a smaller range of intermediate heights than indicated above. Figure 23 shows their result, produced for an electron spectrum $1.6 \times 10^{12} E^{-5.2}$ electrons per cm^2-sec-keV-ster. These results suggested that ionization by bremsstrahlung would play a significant role from 50 to 70 km.

SOME EXPERIMENTAL RESULTS

Turning now to some illustrative results of recent measurements, we attempt to give further perspective to the relative importance for the middle atmosphere of energy deposition by X-rays in comparison to other sources of ionization. Many of these results have been taken from our own work for which a greater familiarity with the instruments and prevailing geophysical circumstances is possible. The discussion is organized by latitude, proceeding from high to low.

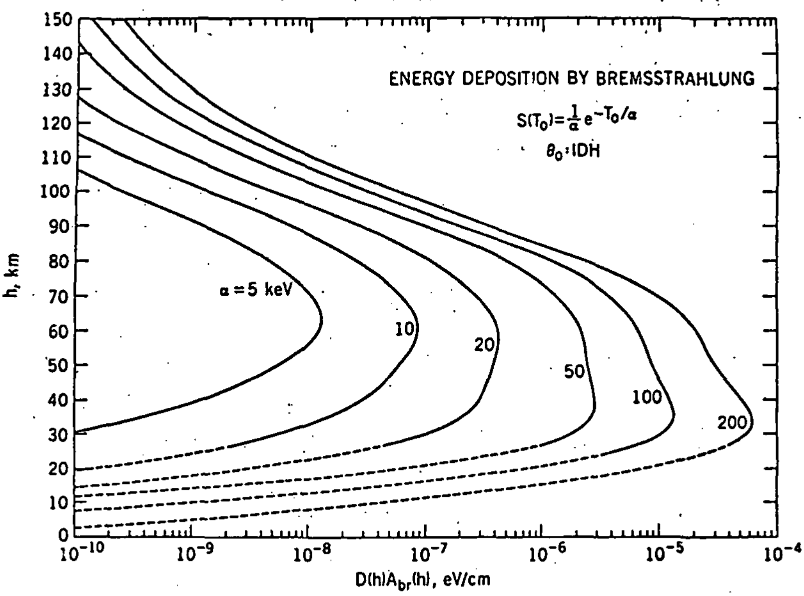

Figure 22. Altitude profile of energy deposition by electron-produced bremsstrahlung in the atmosphere for the case of wide-area precipitation of an electron flux incident isotropically over the downward hemisphere with an exponential spectrum. Results are normalized to one incident electron/cm^2 (from BERGER et al., 1974).

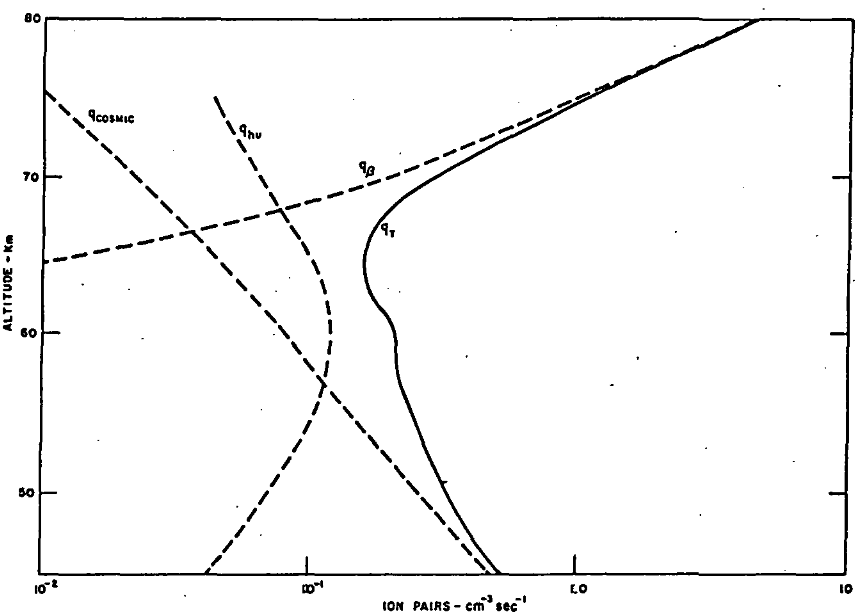

Figure 23. Comparison between the rates of ionization by cosmic rays, auroral electrons, and bremsstrahlung for an electron spectrum represented as 1.6 x 10^{12} $E^{-5.2}$ electrons per cm^2-sec-keV-ster (from AIKIN and MAIER, 1963).

<u>High Latitude</u>. One of the most spectacular phenomena occurring at high latitude is the aurora. Ever since MEREDITH et al. (1955) first showed that there was an associated flux of photons in the energy range 10-100 keV, there have been numerous attempts to assess the ionization effect of this radiation at and below ionospheric heights. Mention has already been made that a wide range of conditions is likely to occur. For some of these, X-rays should be an important energy source in the middle atmosphere and for others, not.

Figure 24 illustrates a situation frequently observed at auroral latitudes. The figure shows the height profiles of ion production by simultaneously measured fluxes of energetic electrons and bremsstrahlung X-rays compared to ionization by cosmic rays (GOLDBERG et al., 1984). The precipitating electron spectrum for this event was best described by a multi-component exponential form

$$J(E) = \sum_i A_i \exp(-E/E_{oi})$$

with the following parameters

E(keV)	$A(cm^{-2}\text{-}sec^{-1}keV^{-1}\text{-}ster^{-1})$	E_o(keV)
15-69	1.5 x 10(8)	5
70-800	2.5 x 10(2)	150
800-1500	1.2 x 10(1)	350

The curve labeled electrons shows the very large collisional ionization produced by the soft component (E_o = 5 keV) at high altitude (H >90 km) and a secondary bulge of ionization at 60-80 km due to the high energy components (E_o >150 keV). The majority of the measured bremsstrahlung X-rays (5-40 keV) were produced by the soft electron component. In this instance, the ionization by X-rays is seen to be significant only in a rather narrow range of altitudes around 40-50 km. By way of contrast, Figure 25a illustrates the case where relativistic electrons were less of a factor, so that here low-energy X-rays are seen to be important over a greater range of altitudes. The opposite case is shown in Figure 25b, where the ionization by X-rays is practically negligible at all altitudes. Thus, as magnetospheric processes alter the

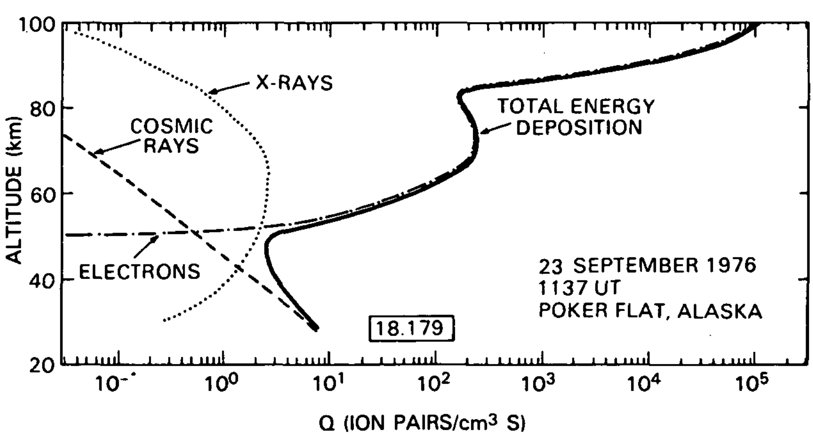

Figure 24. Ionization profile for an auroral event. The X-ray, electron (>15 keV), cosmic ray background, and combined total ionization are presented (from GOLDBERG et al., 1984a).

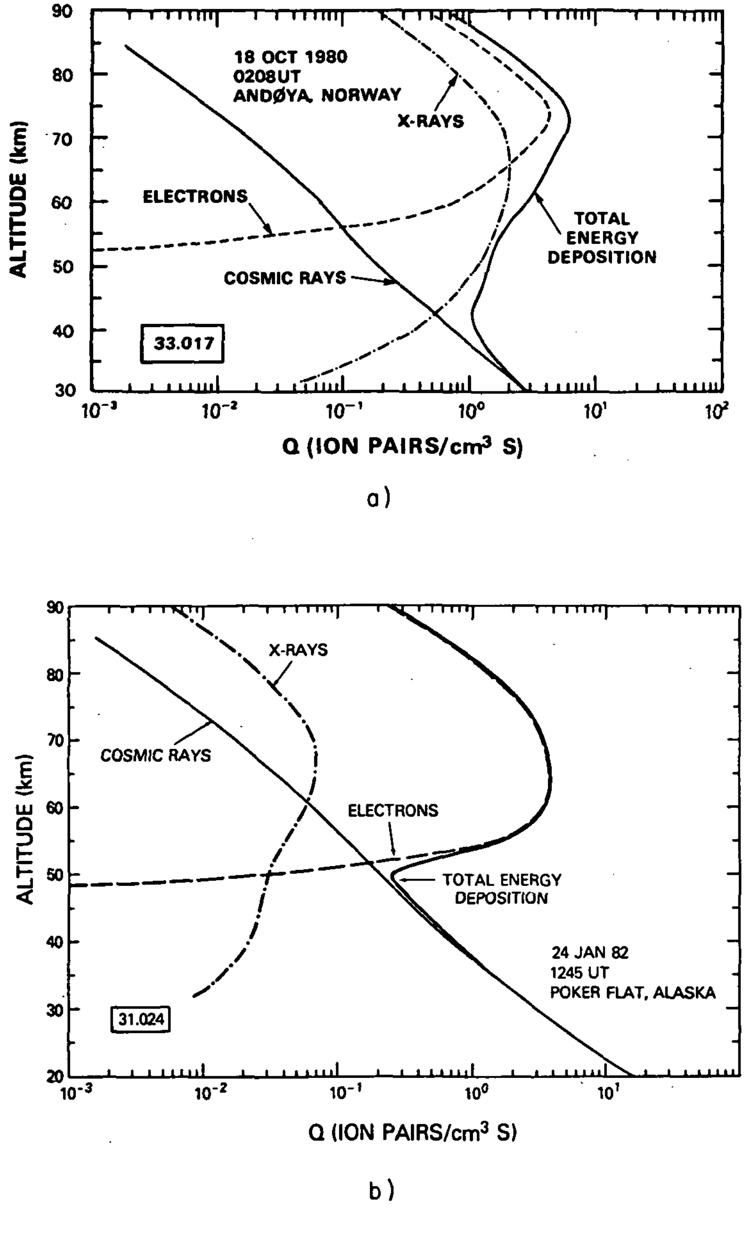

Figure 25. (a) Similar to Figure 24, but illustrating an event in which the ionization by bremsstrahlung X-rays dominates over a greater range of altitudes. Here the curve labeled Electrons includes only the high energy (E>100 keV) contribution (GOLDBERG et al., 1984a). (b) Similar to (a) but illustrating an event in which the energy deposition by bremsstrahlung is negligible at all altitudes (from GOLDBERG et al., 1984a).

intensity and spectral character of the precipitated electrons, so also is altered the possible heights where X-rays may be significant contributors to the energy input.

Middle Latitudes. Here, energy deposition by X-rays in the middle atmosphere is likely to be important only for solar flare activity. The electron precipitation normally occurring at midlatitudes is not as strong at the high latitudes (PAULIKAS, 1975), and the associated bremsstrahlung is correspondingly weak and usually not competitive with other sources. As for the ionization, the results of LARSEN et al. (1976), shown in Figure 26, are probably typical. Occasionally, intense, soft electron precipitation does occur at midlatitudes during great magnetic storms, so that during such periods X-rays can be an important source of ionization.

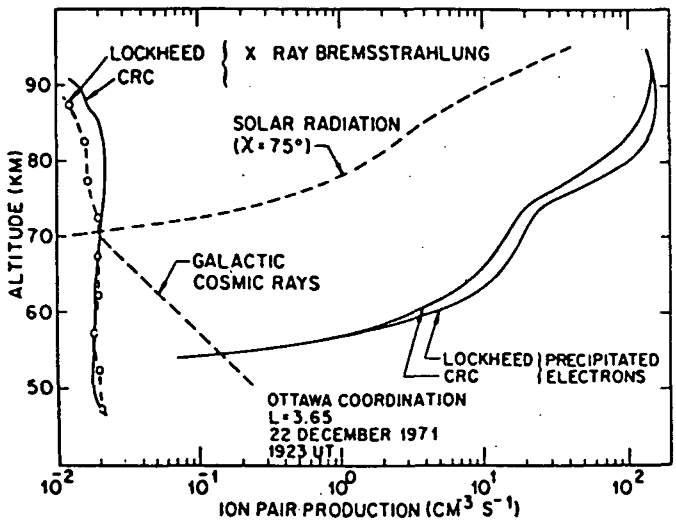

Figure 26. Comparison of ion production rates over Ottawa (L = 3.65) computed from a satellite-measured electron spectrum when an isotropic pitch angle distribution is assumed (from LARSEN et al., 1976).

Experiments examining the possible stimulation of energetic electron precipitation via natural or man-made injections of very low frequency (VLF) electromagnetic waves into the magnetosphere have produced mixed results (ROSENBERG et al., 1971; RYCROFT, 1973; VAMPOLA and KUCK, 1978; BERING et al., 1980; DOOLITTLE and CARPENTER, 1983; IMHOF et al., 1983; GOLDBERG et al., 1983). The probable existence of interaction between VLF waves and energetic electrons in the magnetosphere by means of Doppler-shifted cyclotron resonance has been recognized for some time (DOWDEN, 1962; DUNGEY, 1963; BRICE, 1963). The measurements presently in hand indicate the electron flux (>10 keV) effectively scattered into the loss cone is relatively small ($<10^4$ cm^{-2} str^{-1} sec^{-1}), spatially limited, and often burst-like; thus, the attendant bremsstrahlung radiation, when averaged over space and time, is probably insignificant as a source of energy deposition for the middle atmosphere. More important, perhaps, are the possibilities for active, transient sources of ionization induced by ULF/VLF interactions for specific kinds of aeronomical studies.

Low Latitude. Here the nighttime contribution by discrete cosmic X-rays in competition with scattered Lyman α and cosmic rays has been the sub-

ject of considerable controversy (MITRA and RAMANAMURTY, 1972 and other references cited therein; RIZZO PIAZZA et al., 1983). Rocket measurements at the magnetic equator reported by GOLDBERG et al. (1977) demonstrated an effect on electrical conductivity at 60-65 km altitude which was attributed to measured X-rays from Sco X-1. The experiment has been repeated with a number of improvements (GOLDBERG et al., 1985). For the X-ray measurements, the improvements included greater sensitivity, better energy resolution, and provision for unambiguous aspect. Among other instrumentation, NASA rockets 31.032 and 31.033 carried two separate NaI scintillation detectors for measuring X-rays in the range 5-80 keV. The detectors were identical except for look directions and collimation. One (X-1) was mounted at 45 degrees with respect to the rocket axis and was fitted with a collimator whose field of view was narrow in azimuth but broad in zenith. This detector was exposed at low altitude during upleg and its response together with the gyro output was used to identify the presence of discrete sources. The other (X-2), a wide angle detector, was mounted on-axis, looking vertically upward when the payload was deployed on a parachute at apogee (∿85 km). This detector was used to make a more precise measurement of the X-ray spectra encountered. A schematic of the payload, in the configuration for parachute descent is shown in Figure 27. The portion of the celestial sphere scanned by 31.033, included Sco X-1, but did not for 31.032. The latter rocket was intended as a control measurement, having been launched some 5.5 hours earlier on the same night. Figure 28 shows the count-rate vs time plots for 5-10 keV on each flight. As expected, an enhanced flux of X-rays was observed by 31.033. The radiation levels encountered by 31.032 were representative of the isotropic galactic X-ray flux and cosmic ray induced background. The shaded region in the figure marks the enhanced flux due to Sco X-1. The large variations in the counting rate seen at high altitude (∿150 seconds after lift-off) are due to variable payload orientation immediately following deployment.

Figure 29 provides additional evidence that the source is Sco X-1. Shown here are the results of a superimposed epoch analysis of the forward (X-1) detector of 31.033 during upleg. These data have been binned (100 intervals of 3.6 degrees) for each spin of the rocket (∿5.4 rps) from 80 to 128 seconds in-

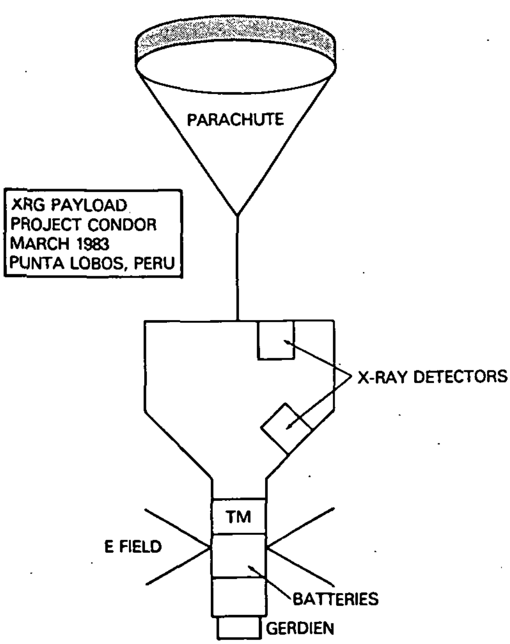

Figure 27. Schematic representation of the XRG payload used to investigate the response of the equatorial middle atmosphere to Sco X-1 (from GOLDBERG et al., 1984b).

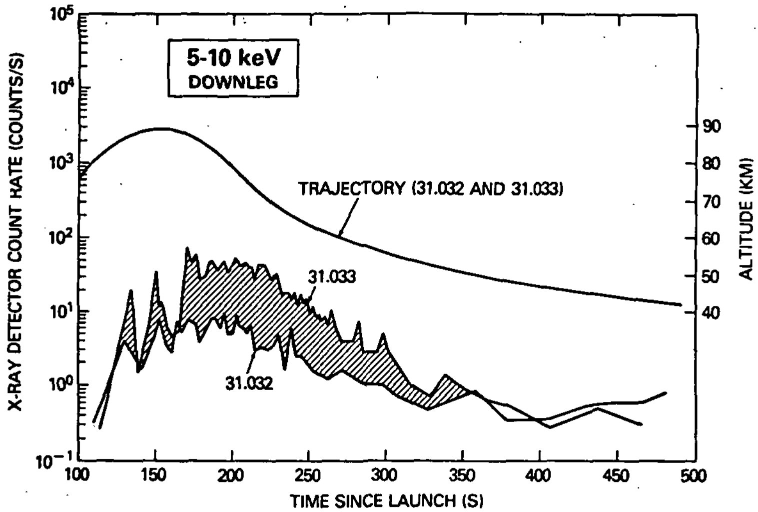

Figure 28. Time history of 5-10 keV X-ray detector count rates during downleg for both 31.032 and 31.033. The nearly identical trajectory for each flight is also shown. The large intensity variations centered about 150 seconds are due to variations in the payload orientations following deployment (from GOLDBERG et al., 1984b).

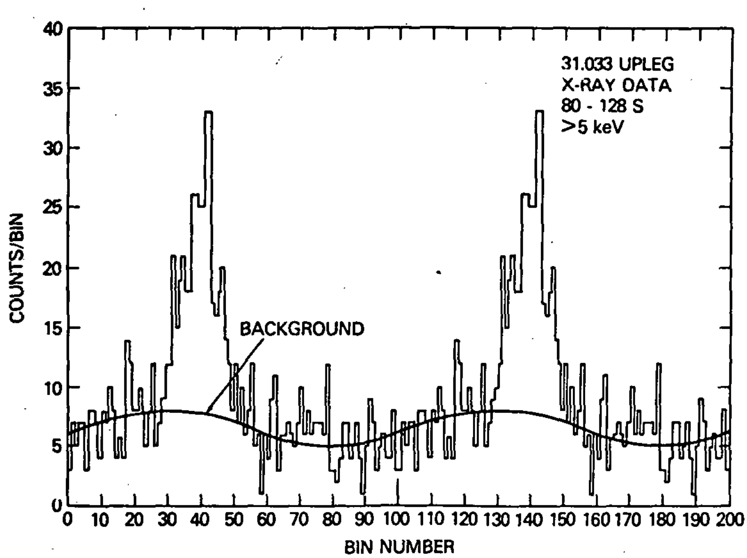

Figure 29. Superposed epoch analysis of >5 keV upleg data (80 to 128 seconds) for 31.033. The 100 bin pattern is repeated for clarity (from GOLDBERG et al., 1984b).

to the flight. The figure shows the result for >5 keV (the pattern is repeated for clarity). The peak centered at bin 42 (and repeated at bin 142) demonstrates the existence of a discrete source, which is consistent with Sco X-1 based on the known aspect of the rocket. No comparable source was revealed by similar analysis of the upleg data from 31.032 when Sco X-1 was below the horizon.

Evaluating the excess flux at the highest altitudes attained, it is found that the X-ray spectrum in the range 5-80 keV can be approximated by $dN/dE = 6.18 \times 10^3 E^{-3.56}$ photons/cm^2-sec-keV. Using this spectrum, the ionization due to Sco X-1 has been calculated for various zenith angles, and these results are shown in Figure 30. At the time of measurement, the source was at a zenith angle of about 20°. The consequences of this additional input of energy on local electrical parameters is being studied using these and other data acquired from the rocket experiments.

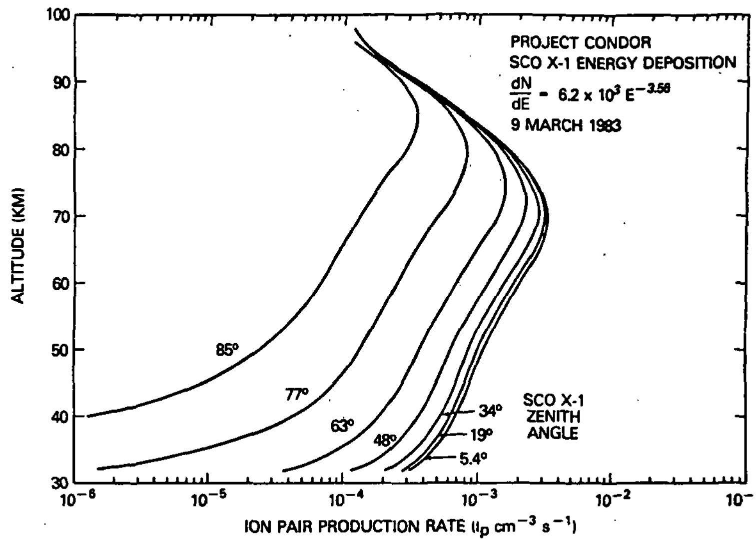

Figure 30. Ionization curves for various zenith angles of Sco X-1 using the X-ray data from 31.033. Each curve represents a one-hour separation. The measurements of 31.033 were obtained when Sco X-1 was at a zenith angle of 20° (from GOLDBERG et al., 1984b).

SUMMARY

Scintillation phosphors are the most commonly used detector element for rocket measurements in the middle atmosphere of X-rays having energy the order of 5-100 keV. Presently, sodium-iodide is the unchallenged favorite, largely due to its high luminous conversion coefficient compared to all others. At the lower energies, proportional counters have better energy resolution than scintillators, but poorer efficiency, and have been employed mainly for measurements in the 1-10 keV range. Semiconductors are capable of comparable efficiency as scintillators and much the better energy resolution. However, Ge and Si detectors (and their preamplifiers as well) require cooling to liquid nitrogen temperature, and the total systems are presently about an order of magnitude more expensive than scintillators, factors which no doubt have discouraged their use. Newer types of high-Z semiconductor detectors, such as

CdTe and HgI_2 which can operate at room temperature, should see considerable use in the future, as large-area detectors of these materials become available.

Energy deposition by X-rays in the middle atmosphere has been found to be important at all latitudes, significant sources ranging from the intense bremsstrahlung by magnetospheric electrons at high latitudes, to discrete galactic X-ray sources at low latitude where the cosmic ray ionization in the mesosphere is least. Solar flare X-rays are effective, although transient, contributors at all latitudes. Naturally occurring precipitation of magnetospheric electrons at midlatitudes is common, but except during great magnetic storms does not lead to bremsstrahlung fluxes capable of significant energy deposition in the middle atmosphere. Attempts to precipitate intense fluxes of magnetospheric electrons by means of wave-particle interactions induced by injection of very-low frequency waves have seen only modest success, leading thus far to an insignificant deposition of energy in the middle atmosphere by bremsstrahlung.

Measurements have confirmed that the relatively energetic, intense bremsstrahlung which occurs at high latitudes is capable of competing with the cosmic ray ionization in the upper stratosphere. However, measurements have also shown that because of the persistent and effective ionization produced by relativistic electrons, X-rays are often less of an important factor in the mesosphere than believed previously.

Within the polar cap there remain other possibilities for measurable energy deposition by photons in the middle atmosphere. During solar particle events there are two sources which could be important. First, it is well known that nuclear gamma-rays are produced by solar proton interactions in the terrestrial atmosphere (BROWN and D'ARCY, 1959; BHAVSAR, 1962; HOFMANN and WINCKLER, 1963; BARCUS, 1969). Nuclear reaction cross sections for gamma-ray production by proton impact are highly energy dependent, being maximum around 10 MeV for protons on O^{16} and N^{14} (RAMATY et al., 1979). Apart from the early phase, the solar proton spectrum is most intense at low energy; thus, gamma-ray production during these events takes place mainly high in the atmosphere at altitudes corresponding to the depth of penetration for low energy solar protons. Nuclear gamma-rays are typically in the MeV energy range and can readily penetrate to stratospheric depths. Moderate nuclear gamma-ray fluxes, the order of $10^2/cm^2$-sec, can produce ionization rates comparable with that due to cosmic rays in the upper stratosphere. Second, solar electrons also have access to the polar caps (VAMPOLA, 1969; EVANS and STONE, 1972; LANZEROTTI and MACLENNAN, 1972), and for some events have arrived with intensities (at >100 keV) similar to or exceeding, auroral zone precipitation. Collisional ionization by energetic solar electrons in the mesosphere is certain to be of importance, and the associated bremsstrahlung could be effective as well. Because of the large area and time duration covered by solar particle events, the integrated effects of nuclear gamma-rays and electron bremsstrahlung in the middle atmosphere could be significant and merit further examination.

REFERENCES

Aarsnes, K., S. Njaastad, T. Ryngoye, J. Stadsnes, and F. Soraas (1976), Description of the UB-Experiment in the Polar 5 rocket, U. of Bergen Tech. Rep., Bergen, Norway.

Aikin, A. C., and E. J. Maier (1963), The effect of auroral bremsstrahlung on the lower ionosphere, NASA Tech. Note TN D-2096.

Bailey, D. K. (1968), Some quantitative aspects of electron precipitation in and near the auroral zone, Rev. Geophys., 6, 289.

Barcus, J. R. (1969), Diurnal variation in low-energy cosmic-ray cutoffs, Planet. Space Sci., 17, 1173.

Barcus, J. R., R. A. Goldberg, E. R. Hilsenrath, and J. D. Mitchell (1979), Middle atmosphere response to measured relativistic electrons, Proc. of the XVII IUGG Symposium, Canberra, Australia, available from NCAR, Boulder, CO.

Barcus, J. R., R. A. Goldberg, and L. H. Gesell (1981), X-ray scanning of overhead aurora from rockets, J. Atmos. Terr. Phys., 43, 1003.

Barcus, J. R., R. W. Fathauer, and R. A. Goldberg (1985), Measurements of the angular distribution of auroral bremsstrahlung in the middle atmosphere, J. Atmos. Terr. Phys., 47, in press.

Berger, M. J., and S. M. Seltzer (1972), Bremsstrahlung in the atmosphere, J. Atmos. Terr. Phys., 34, 85.

Berger, M. J., S. M. Seltzer, and K. Maeda (1974), Some new results on electron transport in the atmosphere, J. Atmos. Terr. Phys., 36, 591.

Bering, E. A., T. J. Rosenberg, J. R. Benbrook, D. Detrick, D. L. Mathews, M. J. Rycroft, M. A. Saunders, and W. R. Sheldon (1980a), Electric fields, electron precipitation, and VLF radiation during a simultaneous magnetospheric substorm and atmospheric thunderstorm, J. Geophys. Res., 85, 55.

Bering, E. A., J. R. Benbrook, E. G. Stansbery, W. R. Sheldon, and J. L. Roeder (1980b), The results from the X-ray experiment of Project Trigger, J. Geophys. Res., 85, 5079.

Bhavsar, P. D. (1962), Gamma rays from the solar-cosmic-ray-produced nuclear reactions in the Earth's atmosphere and lower limit on the energy of solar protons observed at Minneapolis, J. Geophys. Res., 67, 2627.

Birks, J. B. (1964), The Theory and Practice of Scintillation Counting, Pergamon Press, Macmillan Co., London.

Boldt, E. A., U. D. Desai, S. S. Holt, and P. J. Serlemitsos (1969), 2-20 keV X-ray sky background, Nature, 224, 677.

Brice, N. (1963), An explanation of triggered very low frequency emissions, J. Geophys. Res., 68, 4626.

Brown, R. R., and R. G. D'Arcy (1959), Observations of the solar flare radiation at high latitudes during the period July 10-17, 1959, Phys. Rev. Lett., 3, 390.

Curran, S. C., and H. G. Wilson (1965), Proportional counters and pulse ionization chambers, in Alpha-, Beta-, and Gamma-Ray Spectroscopy, edited by K. Siegbahn, North-Holland Pub., Amsterdam.

Doolittle, J. H., and D. L. Carpenter (1983), Photometric evidence of electron precipitation induced by first hop whistlers, Geophys. Res. Lett., 10, 611.

Dowden, R. L. (1962), Doppler-shifted cyclotron radiation from electrons: A theory of very low frequency emissions from the exosphere, J. Geophys. Res., 67, 1745.

Dungey, J. W. (1963), Loss of Van Allen electrons due to whistlers, Planet. Space. Sci., 11, 591.

Evans, L. C., and E. L. Stone (1972), Electron polar cap and the boundary of open geomagnetic field lines, J. Geophys. Res., 77, 5580.

Fairstein, E., and J. Hahn (1966), Nuclear pulse amplifiers--Fundamentals and design practice, Part I: Nucleonics, 23, No. 7, 56, 1965; Part II: Nucleonics, 23, No. 9, 81, 1965; Part III: Nucleonics, 23, No. 11, 50, 1965; Part IV: Nucleonics, 24, No. 1, 54, 1966; Part V: Nucleonics, 24, No. 3, 68, 1966.

Goldberg, R. A., W. H. Jones, P. R. Williamson, J. R. Barcus, and L. C. Hale (1977), Equatorial X-rays and their effect on the lower ionosphere, J. Atmos. Terr. Phys., 39, 1017.

Goldberg, R. A., J. R. Barcus, L. A. Treinish, and R. R. Vondrak (1982), Mapping of auroral X-rays from rocket overflights, J. Geophys. Res., 87, 2509.

Goldberg, R. A., S. A. Curtis, J. R. Barcus, C. L. Siefring, and M. C. Kelley (1983), Controlled stimulation of magnetospheric electrons by radiowaves: Experimental model for lightning effects, Science, 219, 1324.

Goldberg, R. A., C. H. Jackman, J. R. Barcus, and F. Soraas (1984), Nighttime auroral energy deposition in the middle atmosphere, J. Geophys. Res., 89, 5581.

Goldberg, R. A., J. R. Barcus, and J. D. Mitchell (1985), Response of the equatorial middle atmosphere to Sco X-1, J. Atmos. Terr. Phys., 47, in press.

Hofmann, D. J., and J. R. Winckler (1963), Simultaneous balloon observations at Fort Churchill and Minneapolis during the solar cosmic ray events of July 1961, J. Geophys. Res., 68, 2067.

Imhof, W. L., J. B. Reagan, H. D. Voss, E. E. Gaines, D. W. Datlowe, J. Mobilia, R. A. Helliwell, U. S. Inan, J. Katsufrakis, and R. C. Joiner (1983a), Direct observation of radiation belt electrons precipitated by controlled injection of VLF signals from a ground-based transmitter, Geophys. Res. Lett., 10, 361.

Imhof, W. L., J. B. Reagan, H. D. Voss, E. E. Gaines, D. W. Datlowe, J. Mobilia, R. A. Helliwell, U. S. Inan, J. Katsufrakis, and R. C. Joiner (1983b), The modulated precipitation of radiation belt electrons by controlled signals from VLF transmitters, Geophys. Res. Lett., 10, 615.

Kamiyama, H. (1966), Flux of bremsstrahlung photons caused by energetic electrons precipitating into the upper atmosphere, Rep. Ionosphere Space Res. Japan, 20, 374.

Kodama, M., and T. Oguti (1976), Spatial distribution of auroral zone X-rays as viewed from rockets, Mem. Nat'l. Inst. Polar Res., A14.

Lanzerotti, L. J., and C. G. Maclennan (1972), Relative importance of solar electrons, protons, and alphs in the November 1969 PCA event, Proc. COSPAR Symposium on Solar Particle Event of November 1969, edited by J. C. Ulwick, AFCRL-72-0474, Hanscom Field, Bedford, MA.

Larsen, T. R., J. B. Reagan, W. L. Imhof, L. E. Montbriand, and J. S. Belrose (1976), A coordinated study of energetic electron precipitation and D region electron concentrations over Ottawa during disturbed conditions, J. Geophys. Res., 81, 2200.

Luhmann, J. G. (1976), Auroral bremsstrahlung spectra in the atmosphere, J. Atmos. Terr. Phys., 39, 595.

Maynard, N. C., L. C. Hale, J. D. Mitchell, F. J. Schmidlin, R. A. Goldberg, J. R. Barcus, F. Soraas, and C. L. Croskey (1984), Electrical structure in the high-latitude middle atmosphere, J. Atmos. Terr. Phys., 46, 807.

Meredith, L. H., M. B. Gottlieb, and J. A. VanAllen (1955), Direct detection of soft radiation above 50 kilometers in the auroral zone, Phys. Rev., 97, 201.

Mitra, A. P., and Y. V. Ramanamurty (1972), Ionization contribution by cosmic X-rays, COSPAR Symposium on D- and E-Region Ion Chemistry, Aeronomy Rep., #48, U. of Illinois, Urbana.

Newkirk, L. L., W. E. Francis, and M. Walt (1974), Bremgat--A code for the generation and transport of bremsstrahlung through the atmosphere, Rep. LMSC/D407007, Lockheed Palo Alto Res. Lab., Palo Alto, CA.

Pages, L., E. Bertel, H. Joffre, and L. Sklavenitis (1972), Energy loss, range, and bremsstrahlung yield for 10 keV to 100 MeV electrons in various elements and compounds, Atomic Data, 4, 1.

Paulikas, G. A. (1975), Precipitation of particles at low and middle latitudes, Rev. Geophys., 13, 709.

Peterson, L. E., R. M. Pelling, and J. L. Matteson (1972), Techniques in balloon X-ray astronomy, Space Sci. Rev., 13, 320.

Pilkington, G. R., and C. D. Anger (1971), A Monte-Carlo analysis of the passage of auroral X-rays through the atmosphere, Planet. Space Sci., 19, 1069.

Ramaty, R., B. Kozlovsky, and R. E. Lingenfelter (1979), Nuclear gamma-rays from energetic particle reactions, Ap. J. (Supplement Series), 40, 487.

Rees, M. H. (1964), Ionization in the Earth's atmosphere by aurorally associated bremsstrahlung X-rays, Planet. Space Sci., 12, 1893.

Rizzo Piazza, L., P. Kaufmann, and P. Ramirez Pardo (1983), VLF ionosonde and long-distance propagation produced by galactic Cen X-4 X-ray burst in May 1979, J. Atmos. Terr. Phys., 45, 121.

Rosenberg, T. J., R. A. Helliwell, and J. P. Katsufrakis (1971), Electron precipitation associated with discrete very low frequency emissions, J. Geophys. Res., 76, 8445.

Rosenberg, T. J., and L. J. Lanzerotti (1979), Direct energy inputs to the middle atmosphere, in Middle Atmosphere Electrodynamics, edited by N. C. Maynard, NASA CP-2090.

Rycroft, M. J. (1973), Enhanced energetic electron intensities at 100 km altitude and a whistler propagation through the plasmasphere, Planet. Space Sci., 21, 239.

Seltzer, M. J., and S. M. Berger (1974), Bremsstrahlung in the atmosphere at satellite altitudes, J. Atmos. Terr. Phys., 36, 2383.

Tsoulfanidis, N., B. W. Wehring, and M. E. Wyman (1969), The use of an analytical response function for unfolding Beta spectra, Nucl. Instr. Meth., 73, 98.

Ulwick, J. C., W. Pfister and K. D. Baker (1967), Rocket measurements of bremsstrahlung X-rays and related parameters during auroral absorption events, in Space Research VII, Amsterdam: North-Holland Pub.

Vampola, A. L. (1969), Energetic electrons at latitudes above the outer zone cutoff, J. Geophys. Res., 74, 1254.

Vampola, A. L., and G. A. Kuck (1978), Induced precipitation of inner zone electrons: 1. Observations, J. Geophys. Res., 83, 2543.

Vij, K. K., Venkatesen, W. R. Sheldon, J. R. Benbrook, and B. A. Whalen (1975), Simultaneous investigation of parent electrons and bremsstrahlung X-rays by rocket-borne detectors, J. Geophys. Res., 80, 2869.

Vij. K. K., J. S. Vogel, and D. Venkatesen (1980), Auroral X-ray observations at 60-30 km altitudes, J. Geophys. Res., 85, 5096.

Walt, M., L. L. Newkirk, and W. E. Francis (1979), Bremsstrahlung produced by precipitating electrons, J. Geophys. Res., 84, 967.

Wilson, B. G., A. J. Baxter, and D. W. Green (1969), Low energy bremsstrahlung spectra from a stable auroral arc, Can. J. Phys., 47, 2427.

 Dy-46

N86-26729

P-14

4. DETECTORS FOR MEASURING ENERGETIC CHARGED PARTICLES IN ROCKETS

7612

F. Soraas

Department of Physics
University of Bergen
Bergen, Norway

BN209651

ABSTRACT

The physical principles of electron and ion detection are discussed.

A detector model is developed and different charged particle detectors are surveyed. It is shown how the energy and pitch angle distribution of the energetic particles can be measured. Examples of rocket instruments for charge particle measurements are shown.

INTRODUCTION

The hot plasma population of the magnetosphere plays a central role in the coupling of energy, mass and momentum within the earth's atmosphere-ionosphere-magnetosphere system. The electrical energy is transferred between the magnetosphere and the ionosphere by field-aligned currents which are largely carried by the hot plasmas in the energy range from a few eV to several tens of keV. The direct coupling of energy from the magnetosphere to the ionosphere and atmosphere is dominated by the precipitation of hot plasmas caused by particle acceleration and wave-particle interaction. These precipitating particles collide with the atmospheric atoms and molecules and gradually lose their energy to the neutrals.

The population of energetic charged particles in the magnetosphere is governed by a great number of processes. All these processes print their mark on this population. Thus, by examining the distribution function of the particles, it is possible to gain some insight on the fundamental processes taking place in the magnetosphere. How are the particles accelerated, where are their sources, and in what way are they lost?

The role of incident electrons on creating the nighttime polar ionosphere is well known. In particular, it has been determined that the E-region ionization associated with auroral activity results from energetic (keV) electrons streaming into the upper atmosphere. More energetic electrons are responsible for ionization and excitation in the D region. The problem of computing the altitude profile of the ionization and excitation produced by a given energy distribution of the incoming electrons has been considered by many authors (REES 1963, BANKS et al., 1974). From the distribution function of the electrons the energy flux and the field-aligned current carried by the incoming electrons can be computed.

Fast precipitating protons produce ionization and excitation in much the same way as electrons. However, because of the large mass of the protons, they will hardly suffer any noticeable deflections through collisions with the atmospheric atoms. Therefore, as a first approximation we assume that the angle between the local geomagnetic field vector and the velocity vector of the proton remains constant as the protons are gradually slowed down. The auroral protons with energies up to tens of keV will influence the upper atmosphere mainly in the E region. More energetic protons associated with solar flares can affect the atmosphere all the way down to 40 km altitude.

A detailed knowledge of the distribution function is thus necessary when we want to evaluate the effect of the precipitating particles on the ionosphere and upper atmosphere.

PARTICLE DETECTION

We will first see how the intensity, the energy, and pitch angle distribution of the energetic particles can be measured and how the distribution function can be evaluated. After this, we will show examples on rocket instruments for measuring charged particles.

A detection system. A detection system can be considered to consist of two parts, a detector and a measuring instrument. The interaction of the radiation takes place in the detector. The measuring instrument takes the output of the detector and performs the functions required to accomplish the measurements.

Figure 1 shows a block diagram of a typical detector system. The different types of detectors can be characterized by the nature of the interaction of the radiation with the detector. Several types operate by the ionization which is produced in them by the charged particles. These detectors include ionization chambers, proportional counters, Geiger-Muller counters, semiconductor radiation detectors, cloud chambers, and spark chambers. In certain detectors, excitation and sometimes molecular dissociation also play important roles. These phenomena, in combination with ionization, produce the luminescence involved in scintillation detectors and the latent images in photographic emulsions.

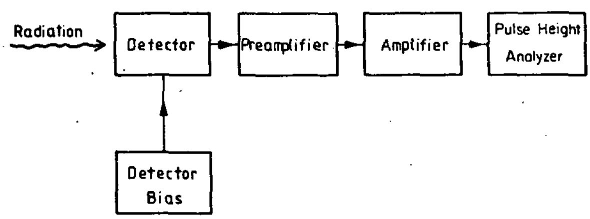

Figure 1. Block diagram of a typical detector system.

The operation of any radiation detector depends on the manner in which the radiation to be detected interacts with the material of the detector itself. An understanding of the response of a specific type of detector must therefore be based on the fundamental mechanisms by which radiations interact and lose their energy in matter.

Interaction of heavy charged particles. Heavy charged particles, protons and heavier particles, interact with matter primarily through coulomb forces between their positive charge and the negative charge of the orbital electrons within the absorber atoms. Upon entering any absorbing medium, the charged particle immediately interacts with many electrons. The electron in the absorbing medium feels an impulse from the attractive coulomb force. This impulse may be sufficient to either raise the electron to a higher lying shell within the absorber atom (excitation) or to completely remove the electron from the atom (ionization). The energy that is transferred to the electron must come at the expense of the charged particle penetrating the medium, and its velocity is therefore decreased.

C-2

The paths taken by heavy charged particles in their slowing down process tend to be quite straight because the particle is not greatly deflected by any one encounter. Heavy charged particles are therefore characterized by a definite range in a given absorber material. The range represents a distance beyond which no particles will penetrate.

The products of these collisions in the absorber are either excited atoms or ion pairs. Each ion pair is made up of a free electron and a positive ion, which may be used as the basis of detector response.

Interaction of fast electrons. When compared with heavy charged particles, fast electrons lose energy at a lower rate and follow a much more complicated path through absorbing materials. Large deviations in the electron path are possible because the fast electron mass is equal to that of the orbital electrons in the absorbing atoms, and a much larger fraction of its energy can be lost in a single collision. This means that there is a large spread in the range of electrons in an absorber. Even small values of the absorber thickness lead to the loss of some electrons from the detected beam because scattering of the electron effectively removes it from the flux striking the detector.

The fact that electrons often undergo large-angle deflections along their track leads to the phenomenon of backscattering. An electron entering one surface of an absorber may undergo sufficient deflection so that it leaves the absorber from the same surface through which it entered. These backscattered electrons do not deposit all of their energy in the absorbing medium. Electrons that backscatter in the detector "window" or dead layer will escape detection entirely.

A detector model. We begin with a simplified detector which is subject to some type of radiation. In order for the detector to respond at all, the radiation must undergo interaction through one of the mechanisms mentioned.

The net result of the radiation interaction in a wide category of detectors is the appearance of a given amount of electric charge Q within the detector active volume. This charge must be collected to form the basic electrical signal. Typically, collection of the charge is accomplished through an electric field within the detector which causes the positive and negative charges created by the radiation to flow in opposite directions. The time required to fully collect the charge varies greatly from one detector to another. For example, in ion chambers the collection time can be as long as a few milliseconds, whereas in semiconductor diode detectors the time is a few nanoseconds. These times reflect both the mobility of the charge carriers within the detector active volume and the average distance which must be traveled before arrival at the collection electrodes.

SURVEY OF DETECTOR TYPES

Gas-filled detectors. Three of the oldest but still very useful radiation-detector types are the ionization chamber, the proportional counter, and the Geiger-Muller (G-M) tube. Each of these detector types employs gas-filled chambers. The difference in the three systems can be explained through the use of Figure 2. We will discuss this system in some detail as a basis for other detection systems. The system shown consists of a gas-filled chamber with a central electrode insulated from the chamber walls. A voltage is applied between the wall and the central electrode through the resistor R shunted by the capacitor C.

Assume that the passage of an ionizing particle releases N_1 ion pairs within the chamber. The positive and negative charges within the chamber move toward the chamber wall and central electrode, respectively, because of the

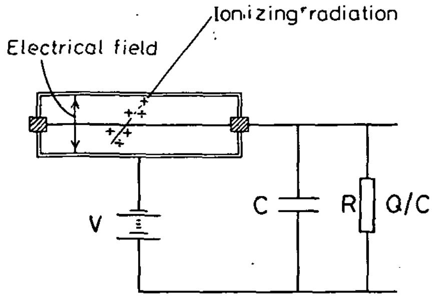

Figure 2. Gas-filled chamber. Used to explain the operation of different detectors.

direction of the electric field. The charge Q appearing on the capacitor per particle as a function of V is given by curve 1 (2 MeV) in Figure 3. For a particle producing a larger number of ion pairs N_2 curve 2 (3 MeV) is obtained.

These curves can be divided into four main regions depending on the applied voltage. In region I, there is a competition between the loss of ion pairs by recombination and the removal of charge by collection on the electrodes. With increasing field the drift velocity of the ions increases; therefore, the time available for recombination decreases, and the fraction of the charge which is collected becomes larger. It is not suitable to operate a detector in region I.

In region II, the recombination loss is negligible, and the charge collected is

$$Q_1 = N_1 \cdot e \quad \text{and} \quad Q_2 = N_2 \cdot e$$

$$\Delta V_1 = \frac{N_{1e}}{C} \quad \text{and} \quad \Delta V_2 = \frac{N_{2e}}{C}$$

This region is referred to as the saturation region or the ionization-chamber region. The charge Q collected by the detector is proportional to the number of electron-ion pairs created in the absorbing medium.

In region III, the collected charge is increased by a factor M through gas multiplication. The electrons which are released in the primary ionization are accelerated sufficiently to produce additional ionization and thus add to the

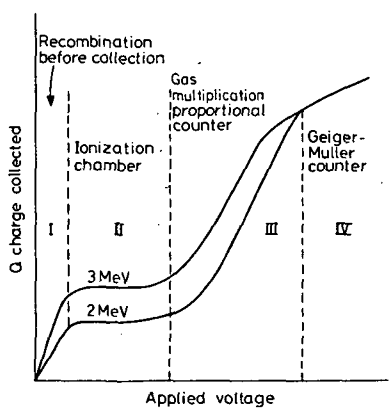

Figure 3. Charge Q appearing on the capacitor per particle as a function of voltage.

collected charge. At the onset of region III, the multiplication M for a given applied voltage is independent of the initial ionization, thus preserving the proportionality of pulse sizes. This strict proportionality breaks down with increase in applied voltage until, at the upper limit of region III, the pulse size is independent of the initial ionization. This region, in which gas multiplication is employed while at the same time a dependence of the collected charge on the initial ionization remains, is known commonly as the proportional region.

In region IV, the charge collected is independent of the ionization.

Ionization-chamber detectors. An ionization-chamber detector can take many forms. However, a typical form consists of a cylindrical, conducting chamber containing a central conducting electrode located on the axis of the chamber and insulated from it, as in Figure 2. The proper voltage is maintained between the wall of the chamber and the central electrode to operate it in region II of Figure 3.

Ionization chambers are used to some extent for detection of all types of particles. An example of pulse-type operation is the measurement of the specific ionization and energy of highly ionizing particles such as alpha particles. In this application, the ionization-chamber detector is used in conjunction with electronic equipment for pulse-height analysis. In mean-level operation either the current is measured, yielding a quantity proportional to the rate of arrival of charged particles, or the charge released in the chamber over a time is determined, yielding a quantity related to the total radiation incident on the chamber during the period of the measurement.

Semiconductor radiation detectors. There is a very important type of detector that is commonly referred to as the semiconductor radiation detector, after the fact that it is the properties of semiconductor materials that make these detectors possible. This detector can also be thought of operating in region II of Figure 3.

In its simplest analogy, the surface barrier detector is an ionization chamber where the usual gas has been replaced by a semiconducting solid, here being silicon. When a charged particle enters the detector, it creates free electron-hole pairs by loosing energy at a rate of 3.6 electron volts per electron-hole pair. This rate of charge carrier formation has been found to be independent of energy and ionization density over a very wide range of particle energies. Therefore, the detector response is linear with energy over a very wide range, provided the sensitive depth of the detector exceeds the range of the particle, and provided also that the electric field in the sensitive region is sufficiently large to separate the charge carriers before they recombine.

Among the advantages of the semiconductor detectors are the following:

a. For a given amount of energy lost by the ionizing particle, approximately 10 times as many free charge carriers are created in silicon as compared with gas, thus improving the counting statistics.
b. Since both the electrons and holes are very mobile and collection distances are short, it is possible to achieve relatively short collection times (of the order of a few nanoseconds).
c. Also, they possess small size, low bias voltage, and negligible power consumption.

The most severe limiting factor for rocket applications of semiconductor detectors is their sensitivity to direct sunlight.

In Figure 4, an instrument schematic (4a) and the energy response of a 300 μm thick detector (4b) are shown. The detector response is linear for protons with energies less than 5.6 MeV, for α-particles less than 22 MeV, and for electrons with energies less than 300 keV. For particles above these energies the output pulse will decrease with increasing particle energy. The probability of X-ray interaction in silicon is quite low due to the low atomic number Z = 14.

The semiconductor radiation detector is very important for pulse-type operation and is rapidly becoming the most versatile type of ionization-radiation detector.

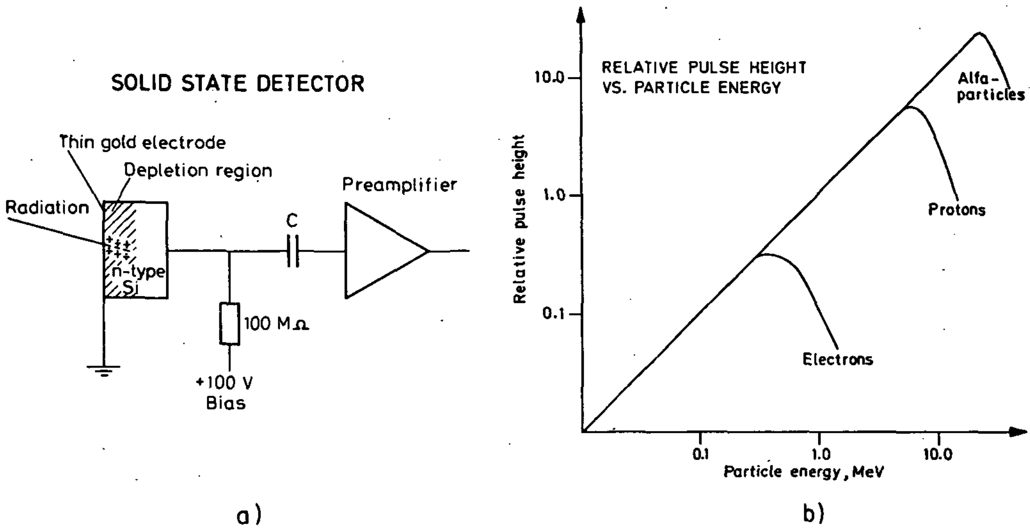

Figure 4. (a) Solid-state detector. (b) Detector response for α, protons and electrons.

Proportional counters. In proportional counters the voltage applied between the collector electrode and the chamber wall is such that the detector is operated in region III of Figure 3. Gas-multiplication factors as high as 10^5 or 10^6 are sometimes employed. The most common applications of proportional counters employ pulse type operation. Use is made of the fact that a gain in pulse size is achieved while the dependence of pulse size on the primary ionization is preserved.

Scintillation detectors. When ionizing particles pass through certain substances, ionized and/or excited states are produced which, during the return to the normal states, produce light emission or scintillations. In the modern scintillation detector, this light is normally picked up by a photomultiplier tube, and the resulting pulse of current out of the photomultiplier indicates the passage of the ionizing particles through the scintillator. Under proper conditions, the resulting charge is proportional to the energy lost by the ionizing particle in the crystals. Thus, as in the cases of the proportional counter and the pulse ionization chamber, this detector can be used to measure the energy distribution of particles in addition to counting them.

The widespread use of scintillation counting in radiation detection and spectroscopy depends on a device to convert the extremely weak light output of

a scintillation pulse into a corresponding electrical signal. The photomultiplier (PM) tube accomplishes this task converting light signals that typically consist of no more than a few hundred photons into a usable current pulse without adding a large amount of random noise to the signal. Most photomultipliers perform this charge amplification in a very linear manner, producing an output pulse that remains proportional to the number of original photoelectrons.

Electron channel multipliers. Another type of specialized electron multiplier is the continuous channel, illustrated in Figure 5. This device is extremely simple, consisting of a hollow glass tube whose inner surface acts as a secondary electron emitter. A potential difference is applied across the length of the tube, thereby attracting electrons from the entrance end to the exit end. Electrons entering the tube will eventually strike the wall giving rise to a pulse of secondary electrons. These will be further accelerated along the length of the tube until they, in turn, also strike the wall giving rise to further secondaries. The device acts much like a photomultiplier tube with continuous dynodes available along its entire length. The number of times an entering electron and its subsequent secondary strike the wall is an accident of past orientation and individual trajectories, and will vary considerably for different entering electrons. When operated at high voltages, the electron gain may be large enough so that the resulting space charge near the exit of the channel limits the total charge per pulse to about 10^6 or 10^7 electrons at saturation.

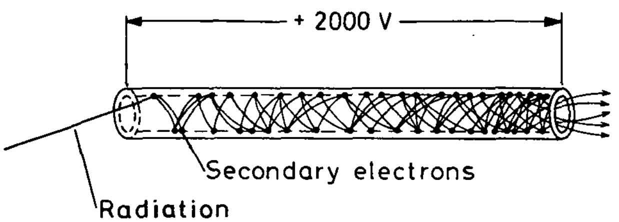

Figure 5. Electron multiplier.

Channel multipliers must be shaped to prevent feedback problems that can arise when positive ions occasionally formed within the channel are accelerated in the reverse direction from the electrons. By forming the channel as a curve, these ions can be made to strike a wall before their energy is high enough to create secondary electrons.

Clusters of many thousands of tubes can be fabricated to form a "microchannel plate". Each channel is of very small diameter (typically 15-50 μm), and acts as an independent electron multiplier.

Geiger-Muller tubes. Gas-type detectors operating in region IV of Figure 3 are known as Geiger-Muller (G-M) tubes. These detectors can be used for counting any type of radiation which will produce ionization within the tube, no matter how small the amount of ionization. The G-M tube is widely used for counting electrons, gamma rays, and X-rays. It is ideally suited for these radiations since their small specific ionization makes them hard to detect otherwise. Alpha particles and highly ionizing particles are sometimes detected by G-M tubes. However, because of the short range of these particles, either tubes with thin windows are required or the source of radiation must be placed inside the tube. Because the pulse sizes in the G-M tube are independent of

the primary ionization, this factor cannot be used as a measure of particle energy, nor is it possible to discriminate between different types of particles by means of the sensitivity of the electronic circuit.

INSTRUMENTATION

Before discussing the instrumentations using the different types of radiation detectors, we will first outline some general properties which apply to all types of detectors: such as efficiency, energy resolution, maximum count rate, etc.

Pulse height spectra. When operating a radiation detector in region II and III of Figure 3, each individual pulse amplitude carries important information about the recorded particle. If we examine a large number of such pulses coming from a detector, their amplitudes will not all be the same. Variations may be due either to differences in the radiation energy or to fluctuations in the response of the detector to monoenergetic radiation. The pulse amplitude distribution is a fundamental property of the detector output which is used to deduce information about the incident radiation or the operation of the detector itself.

The most common way of displaying pulse amplitude information is through the differential pulse height distribution. Figure 6 gives a pulse height distribution. The abscissa is a linear pulse amplitude scale which runs from zero to a value larger than the amplitude of any pulse observed from the source. The ordinate is the differential number dN of pulses observed with an amplitude within the differential amplitude increment dH, divided by that increment, or dN/dH.

Figure 6. Differential pulse height distribution.

Statistics of detection systems. The measurement of charged particles involves phenomena which are statistical in nature. The understanding of these statistical effects is important both from the standpoint of the design of experiments and in the interpretation of the results. By use of statistical analysis, estimates can be made of the accuracy of the measurements, and procedures can be devised which will minimize errors due to the random nature of the process. In addition, the apparatus can be tested for fluctuation due to causes other than statistical by comparison of the actual distribution in measurements with that predicted by statistical law.

Particle distributions. So far, we have been concerned with observations of energetic charged particles. We can measure their energy, their count rate, their time of arrival and their intensity in a specific direction of space. In order to develop the subject in a more quantitative fashion, one has to introduce the concept of directional flux. The count rate of a particle detector is given by

$$R = G \int_0^\infty n(E)\, j\,(E, \theta) \cdot dE \cdot dQ$$

where E is the energy of the particle being detected and dQ is the solid angle covered by the detector in a direction θ with the magnetic field. Furthermore, G is the geometric factor and $\eta(E)$ is the detection efficiency.

A radiation detector will give rise to an output pulse for each charged particle which interacts with it. The interaction will take place immediately upon entry of the particle into the active volume. The particle need only travel a sufficient distance so that the resulting pulse is large enough to be seen above the noise in the detector system for the event to be recorded. Under these conditions the detector is said to have a counting efficiency of 100 per cent. Particles with so low an energy that they tend to be buried in the noise will not be counted with 100 per cent efficiency. For sufficiently low energies the efficiency will drop to zero, as can also be the case for particles with very high energies. The latter can pass through the detector as a minimum ionization particle leaving too little energy in the detector for the signal to be detected above the noise level. As a result, the detector is able to record particles in a specific energy band with a varying efficiency.

We define $j\ (E, \theta)$ for a given class of particles and energy as the number of particles coming from a given direction per unit time, unit solid angle in direction θ, and unit energy, on a surface of unit area oriented perpendicularly to their direction of incidence. Then

$$dN = j\ (E, \theta)\ dS \cdot dQ \cdot dE\ dt$$

dN is the number of particles impinging on the area dS during the time dt. The particles have energies in the interval E to E + dE and their direction of incidence lies in the solid angle dQ.

In practice, every detector must have a finite active area, be sensitive to particles in a given energy range and cover a finite solid angle.

We will now define some often useful quantities concerning particle measurements. The omnidirectional flux J is defined by

$$J\ (E) = \int_{4\pi} j\ (E, \theta)\ dQ$$

This represents the total number of particles coming from all directions per unit time onto a sphere of unit area cross section. The quantities

$$j\ (>E, \theta) = \int_E^\infty j\ (E, \theta)\ dE$$

and

$$J\ (>E) = \int_E^\infty J\ (E)\ dE$$

are called, respectively, directional and omnidirectional integral fluxes. An isotropic flux is one for which the number of incoming particles is independent of the direction.

ROCKET INSTRUMENTATION

To obtain complete experimental information about the precipitation of energetic particles into the atmosphere, it is necessary to determine $j(E, \theta, t)$, the directional particle flux, E the particle energy, θ the pitch angle between the particle trajectory and the local geomagnetic field vector and t the time.

Information about the distribution function of the particles in the 100 eV to 30 keV range can best be obtained by using channel electron multipliers as particle detectors. Information about the distribution function of particles above this energy range is best obtained by solid-state detectors. In the low energy range, information about the energy distribution of the particles is obtained by electrostatic analyzers and in the high energy range by analyzing the amount of charge liberated in the solid-state detector by the incoming particle. A collimator is used to define the angular range analyzed. It can be equipped with a grid having a low voltage in order to get rid of unwanted particles in the thermal energy range. A detector using an electrostatic analyzer covers a fairly narrow angular range. A wider angle range can be covered by means of the payload spin and through the use of several detectors. A solid-state detector can cover a larger angular width as it is not limited by the acceptance angle of the electrostatic analyzer. In this case, the particle intensity is averaged over the angular width of the detector. It is typical of experiments on sounding rockets to have high time resolution and therefore a high spatial resolution. Figure 7 shows the pitch angle scan of a detector mounted an angle α with the rocket axis during a rocket spin-period. The angle between the rocket axis and the magnetic field is θ.

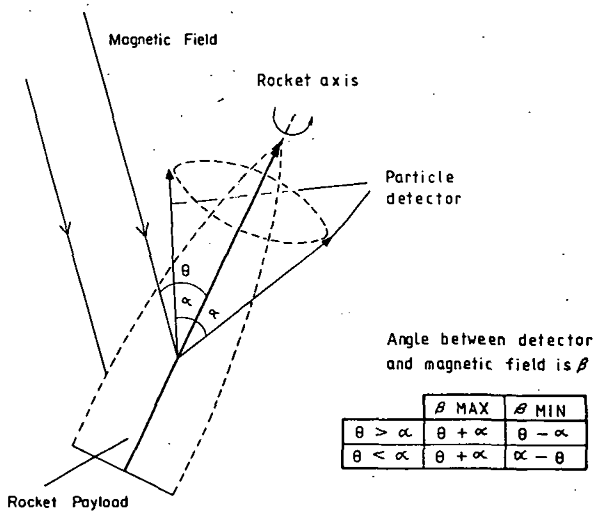

	β MAX	β MIN
$\theta > \alpha$	$\theta + \alpha$	$\theta - \alpha$
$\theta < \alpha$	$\theta + \alpha$	$\alpha - \theta$

Figure 7. The dependence of the detector pitch angle scan on the angle between the magnetic field and the rocket axis (θ) and the angle between the detector looking direction and the rocket axis (α).

Instruments using electrostatic analyzers must sweep the voltage on the analyzer plates fast in order to get good time and energy resolution. This is necessary in order to identify microstructures or to obtain accurate altitude resolution. The technique for energy determination in the solid-state detector makes it normally possible to obtain higher time resolution with this kind of detector.

In the next section, we describe some typical rocket instruments for measuring electrons and positive ions in the energy range less than a keV to several hundred keV.

An electron-ion spectrometer using channel electron multipliers. The particle experiment described here is designed to achieve good energy and angular resolution, with fast time resolution for the measurement of both particle species (electrons and protons). These requirements are met by a spherical electrostatic analyzer system followed by continuous channel electron multipliers. The block diagram in Figure 8 shows the design of the experiment for measuring electrons with three sensors mounted at 30°, 90°, and 150° with respect to the payload axis, with the high voltage power supplies for the acceleration potential of the electron multipliers and for the analyzer deflection voltage. Furthermore, it shows the interface to the telemetry encoder containing the measurement mode control unit and the pulse counters which receive the uniform pulses from the preamplifiers located at the sensor boxes.

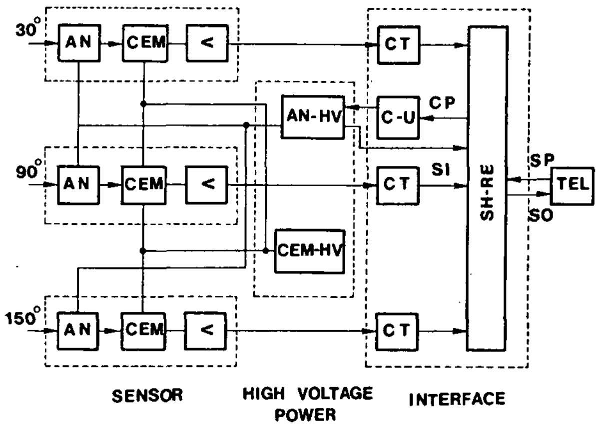

AN ... Energy analyzer
CEM ... Channel electron multiplier
AN-HV ... Analyzer-high voltage
CEM-HV... Multiplier-high voltage
CT ... Counter (12 bit)
CU ... Control program unit
CP ... Control pulses
SH-RE ... Shift registers
SI ... Steps indicator
SP ... Shift pulses
SD ... Science data
TEL ... Telemetry

Figure 8. Block diagram of an electron-ion spectrometer.

Table 1 describes characteristics of the instrument. The instrument is capable of measuring both particle species, electrons or protons, dependent on the polarity of the deflection plates. The measurements of proton fluxes which are usually one order of magnitude lower than the electron flux intensities, required analyzer deflection plates with a large geometric factor. When applying them to measure electrons it has the advantage of a wide dynamical range. For a full description of this instrument, see URBAN (1981).

An instrument for measuring electrons and protons with energies above 20 keV. Figure 9 shows a block diagram of a typical solid-state detector instrument as employed by the University of Bergen. One detector counts protons and

Table 1: Characteristics of the electron-ion spectrometer

Energy range E	keV	0.1 to 25
Resolution ΔE/E	%	7.5
Geometric factor G	cm^2 sr	4 x 10^{-3}
Sampling time	ms	32
Time for one spectrum	ms	576
Maximum count rates	cts s^{-1}	2.5 x 10^5
Pitch angle resolution at 2.6 Hz payload spin	deg	7.4°
Telemetry capacity for one sensor	kbit s^{-1}	0.73

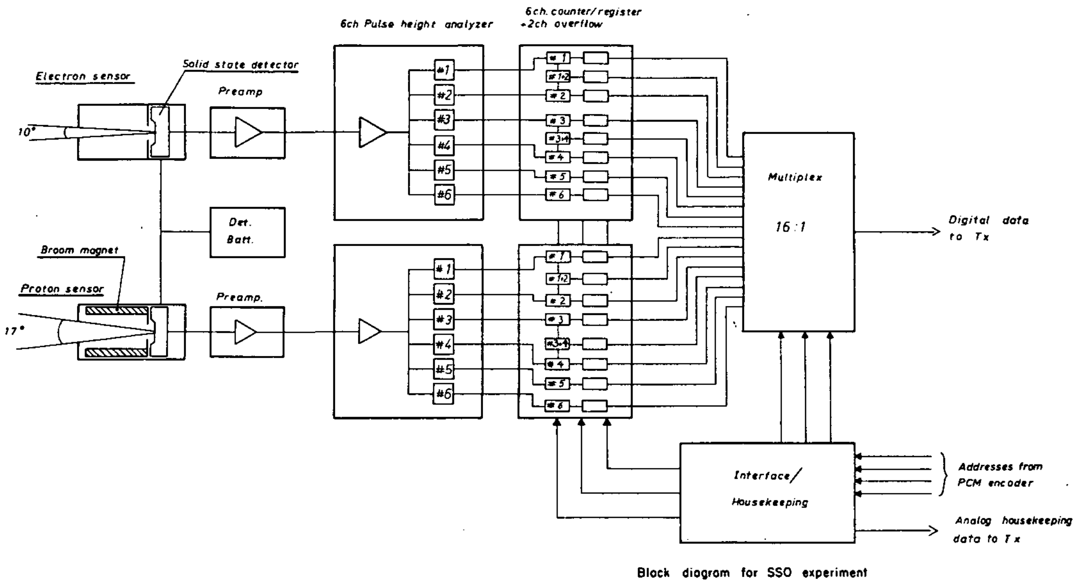

Figure 9. Block diagram for an instrument measuring electrons and protons above 20 keV.

the other detector counts electrons. The experiment is built on a module system in order to make integration and replacement easier. Mechanically the instrument consists of three units: 1) the proton sensor, 2) the electron sensor, and 3) the logical unit.

The electron sensor and the proton sensor are identical except for a broom magnet that is mounted in the collimator of the proton sensor to exclude electrons below a few hundred keV. The proton sensor will thus only count protons and heavier particles, whereas the electron detector will, in addition to these, count electrons.

The two detectors are mounted parallel with each other, thus they are at all times measuring particles which have the same direction in space. It is thus possible to correct the electron counts for the proton contribution by subtracting the counts observed in the proton detector making due corrections for the different geometric factors.

The sensor unit contains a solid-state surface barrier detector, a charge sensitive preamplifier, and a voltage amplifier. The detector and the amplifiers are built close together and well shielded in a compact unit. This gives good signal-to-noise ratio and high immunity against pick-up noise. The output impedance is low and the sensor unit can be separated from the logical unit containing the pulse-height analyzer and all additional electronics. This makes the integration of the rocket payload easier.

Particles entering the detector give rise to small pulses that are amplified by a charge sensitive preamplifier. The pulse amplitude is proportional to the energy absorbed in the detector. From the charge sensitive amplifier the pulses are fed to the pulse height analyzer, having 6 differential energy levels. On each energy level, the sampling time is chosen to be 8 ms, thus, a six point energy spectrum for both electrons and protons can be obtained every 8 ms.

The pulses from the discriminators are fed to a 6-channel counter/register. The two highest energy channels have 8-bit registers while the four lowest channels have 12-bit registers. The data are transferred to the rocket telemetry system via a 16:1 multiplexer. The interface and housekeeping data are also mixed into the telemetry stream.

Finally, Figure 10 shows a schematic for a typical PCM-format on a rocket. Only those words used by the particle experiment are shown. The electron and proton data are transmitted in words 64 and 65. The format consists of 32 frames so that the information sent from the experiment repeats 4 times during a format. Frames 6 and 7 are used to send the four most significant bits for the four lowest energy channels. In word 4, the data from the rocket aspect magnetometer is transmitted. This information is needed when one wants to obtain the pitch angle distribution of the measured particles.

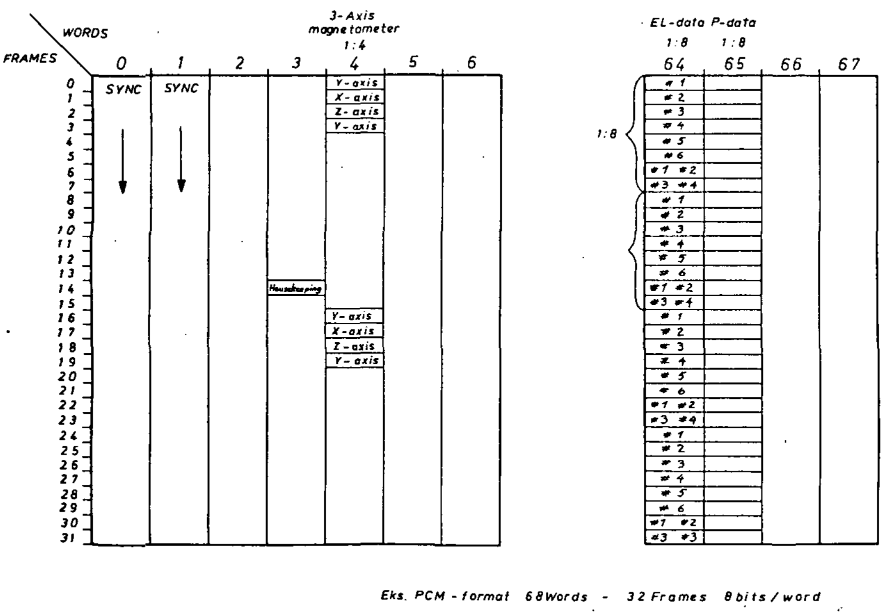

Figure 10. A typical telemetry format for a rocket payload.

ORIGINAL PAGE IS
OF POOR QUALITY

REFERENCES

Banks, P. M., C. R. Chappell, and A. F. Nagy (1974), A new model for the interaction of auroral electrons with the atmosphere; spectral degradation, backscatter, optical emission and ionization, J. Geophys. Res., 79, 1459.

Barthe, H., F. Cotin, and H. Reme (1981), Electron spectrometers for the study of artificially injected particles during the Araks experiments, Space Sci. Instrum., 5, 177-187.

Knoll, G. F. (1979), Radiation Detection and Measurements, John Wiley & Sons.

Price, W. J. (1964), Nuclear Radiation Detection, McGraw-Hill Book Company.

Rees, M. H. (1963), Auroral ionization and excitation by incident energetic electrons, Planet. Space Sci., 11, 1209.

Urban, A. (1981), A low energy particle spectrometer with a large geometric factor, Sounding Rocket Program Aeronomy Project: Energy Budget Campaign 1980, Experiment Summary, BMFT-FB-W81-052.

 D5-46

369

N86-26730

5. REVIEW OF ROCKET-BORNE ION MASS SPECTROMETRY IN THE MIDDLE ATMOSPHERE

F. Arnold and A. A. Viggiano*

7613 MN009167

Max-Planck-Institut for Kernphysik
P. O. Box 103980, D-6900 Heidelberg, F. R. Germany

*Permanent address: Air Force Geophysics Laboratory
Hanscom AFB, MA 01731, USA

ABSTRACT

Experimental methods employed in middle atmosphere rocket-borne ion mass spectrometry are reviewed with an emphasis on recent developments. Interest is also focussed on milestones in instrumental developments and related progress in the exploration of the middle atmosphere ionized component. Attention is also drawn to interesting applications of in situ ion composition measurements in the middle atmosphere, particularly the detection of neutral trace gases and microaerosols using passive chemical ionization mass spectrometry. Finally, future trends in rocket-borne ion mass spectrometry are assessed.

1. INTRODUCTION

The aim of this chapter is to review rocket-borne ion mass spectrometry in the middle atmosphere with particular emphasis on experimental methods, pioneering experiments, and recent developments. Results of ion composition measurements are discussed mostly for illustrative purposes and the interest is focussed on milestones in the exploration of the middle atmosphere's ionized component.

Ion mass spectrometry has played and is still playing an important role in middle atmosphere research. It greatly contributes to the exploration of atmospheric ions and their chemistry and still represents the only method which allows identification of the chemical nature of atmospheric ions. However, ion mass spectrometry yields new and interesting information not only on ions, but also on electrically charged microaerosols or microclusters and, perhaps most important, also on neutral trace gases. Certain neutral trace gases, which react with atmospheric ions, can be inferred from the measured ion composition. The strength of this indirect method, termed passive chemical ionization mass spectrometry (PACIMS), lies in its enormous sensitivity being due to the high efficiency on ion-molecule reactions. This results from the long-range charge-dipole or charge-induced dipole attraction. In favorable cases, PACIMS may reach a detection limit of only 100 molecules or atoms per cm^3. Various neutral trace gas species have been detected by PACIMS in the middle atmosphere, which has markedly contributed to our understanding of trace gas cycles and budgets in this part of the atmosphere. A most striking example is the detection of sulfuric acid vapor in the stratosphere by PACIMS (ARNOLD and HENSCHEN, 1978; ARNOLD and FABIAN, 1980). This trace gas gives rise to the formation of the stratospheric aerosol layer, which at least temporarily influences the earth's radiation budget, and thereby has an impact on climate. Other interesting examples for PACIMS are the detection of meteoric metal atoms (NARCISI and BAILEY, 1965) and of chlorine (ARNOLD et al., 1971) which catalytically destroys stratospheric ozone.

Ion mass spectrometers for atmospheric studies were originally used in the upper atmosphere at altitudes far above 100 km, where the gas pressure is sufficiently low (lower than 0.0001 torr) to allow a mass spectrometer to be operated without additional pumping. Upon re-entry into the denser atmospheric layers, such unpumped rocket-borne ion mass spectrometers yielded the first ion mass spectra of the uppermost part of the middle atmosphere.

Further progress, however, had to await the advent of pumped mass spectrometers which could be operated at the high gas pressures prevailing in the middle atmosphere. Thus, middle atmosphere ion mass spectrometry was largely dependent on progress in pump technology and also on high sensitivity ion detection systems which make mass spectrometers sufficiently sensitive to detection at very low total ion concentrations, with 100-10,000 cm^{-3} being typical of most parts of the middle atmosphere.

The first ion mass spectrometer equipped with a compact high speed cryopump was built by the group of Narcisi at the AFGL (Air Force Geophysics Laboratory; formerly Air Force Cambridge Research Laboratory) and successfully flown on a rocket on October 31, 1963 (NARCISI et al., 1965). This pioneering experiment opened a new area of atmospheric research. In the meantime, various research groups including those at NASA Goddard Space Flight Center, Greenbelt, Maryland (NASA), at the Max-Planck-Institut for Kernphysik, Heidelberg (MPIK), and at the University of Bern (UB) joined the AFGL group in this difficult field of research and contributed to make rocket-borne ion mass spectrometry a vivid and productive area of research up to the present time.

More recently, sampling of middle atmospheric ions was greatly extended by balloon (ARNOLD et al., 1978; ARIJS et al., 1979), aircraft (HEITMANN and ARNOLD, 1983), and most recently also by parachute-borne drop-sonde ion mass spectrometry (PFEILSTICKER and ARNOLD, 1984). Thus, atmospheric ion mass spectrometry now covers the entire range of the middle atmosphere (10-100 km) and even major parts of the troposphere (Figure 1). These recent extensions have revealed new aspects and possibilities of atmospheric ion research, some of them also stimulating new interest in the upper parts of the middle atmosphere, which can be probed only by using rocket-borne ion mass spectrometers. A striking manifestation of this renewed interest is the development of a novel parachute-borne drop-sonde mass spectrometer payload which is carried by a single-stage rocket to 60-70 km. Recently, this "dropmas" payload was flown for the first time by the MPIK group (PFEILSTICKER and ARNOLD, 1984) with great success.

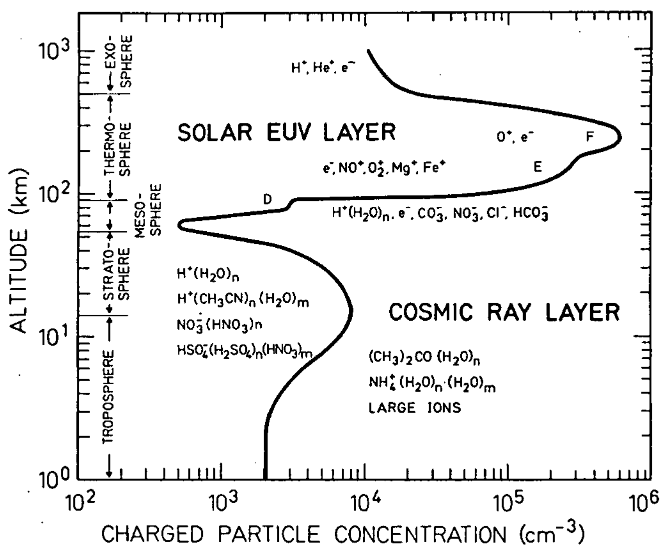

Figure 1. Schematic representation of the atmospheric ionized component.

In view of the renewed interest in rocket-borne ion mass spectrometry, it seems appropriate to review the present status of this field, the aim of this chapter. Earlier, reviews of middle atmospheric ion mass spectrometry include NARCISI (1973), ARNOLD and KRANKOWSKY (1977), and ARNOLD (1980).

2. EXPERIMENTAL METHOD

2.1 General Operating Principles

Experimental conditions dictating the design of a rocket-borne ion mass spectrometer for middle atmosphere studies are mainly the relatively low total ion concentrations (100-10,000 cm^{-3}, see Figure 1), high gas pressure (0.0002-200 torr) and the specific circumstances of a rocket flight, particularly high velocity, high acceleration, and orientation.

Since the atmospheric gas pressure largely exceeds the critical pressure (about 0.0001 torr) in which a mass spectrometer can be operated, additional pumping is required. At gas pressures above the critical value a mass spectrometer starts to suffer for several reasons. First of all, ions undergo scattering by gas molecules which gives rise not only to a loss of transmission and thereby sensitivity for ion detection, but also leads to ion fractionation. The latter is due to the fact that ions with different size have different collision cross sections and thus, undergo scattering with different efficiency. Scattering may also lead to a degradation of mass peak shape and mass resolution. Taking a typical ion path length inside the mass analyzer of 10 cm (approximate size of the mass analyzer) and a typical collision cross section of 4×10^{-15} cm^2, it turns out that for a gas pressure of 3×10^{-4} torr, 50 percent of the ions entering the analyzer have already suffered from collisions.

Another important effect of a high gas pressure inside the instrument is perturbation of the multiplier used for ion detection. The maximum pressure which can be tolerated depends on the type of multiplier and on the mode of operation of the multiplier used. Today, usually channel electron multipliers (CEM) are used which have maximum operational pressures of about 0.0001 torr. At higher pressures, ion-feedback occurs resulting in degradation of the inner CEM surface and other perturbations.

Therefore, only pumped ion mass spectrometers work properly under middle atmospheric conditions. A middle atmosphere ion mass spectrometer consists of three major elements, a mass analyzer (MS), an ion detection system (usually a CEM) and a pump (P), which are housed in a vacuum tank (Figure 2). Ions and atmospheric gases enter the instrument through a small inlet hole, which is drilled into an electrically insulated sampling or draw-in electrode. The size of the inlet hole which controls the flux of ions and neutrals into the instrument is dictated by the pumping efficiency and the ambient atmospheric gas pressure. Since the sensitivity for ion detection is approximately proportional to the incoming ion flux, the size of the inlet hole should ideally be as large as possible, which means large enough to have a gas pressure of 0.0001 torr inside the instrument. However, in practice this is not possible since the ambient atmospheric gas pressure varies strongly with altitude while the speed of the pump remains essentially constant. This requires a compromise for the choice of the size of the inlet hole, depending on the altitude range and corresponding range of ambient pressures to be probed.

The most critical requirement is a pump with a speed as large as possible which immediately leads to sorption and condensation pumps. These are the most efficient pumps for short term applications, they do not require electric power nor sophisticated mechanisms which would likely be affected by the enormous

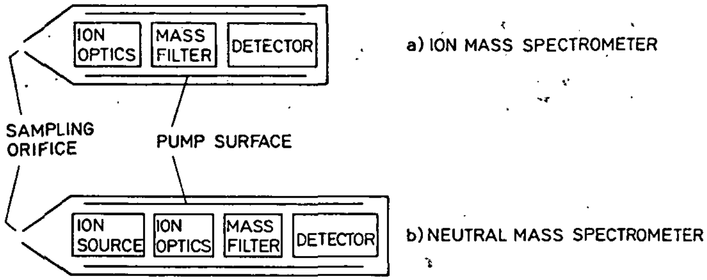

Figure 2. Schematic representation of a rocket-borne ion mass spectrometer for middle atmosphere studies.

mechanical stress during rocket-motor operation (acceleration up to 40-60 G depending on the type of rocket), and they can be built rather compactly. Among the sorption pumps, cryopumps are most efficient but also most delicate to handle. Such pumps, despite their small size required, may provide pumping speeds of the order of 1000 l s^{-1} which allows one to use an inlet hole diameter of about 0.1 cm at 70-80 km. Various types of sorption pumps including titanium sublimation and sorption pumps and cryopumps with liquid nitrogen-cooled zeolithe, and liquid helium- and liquid neon-cooled metal surfaces have been used, as will be discussed in the following section. In fact, progress in the area of small and compact cryopumps has, to a large extent, determined the advance of rocket-borne ion mass spectrometry.

Of great importance for the operation of a middle atmospheric ion mass spectrometer, is the focussing and injection of ions into the mass analyzer. After entering through the inlet hole, the ions are carried by the gas jet which forms behind the inlet hole. If no electric fields are present, the ion density distribution resembles the distribution of gas molecules in the jet, implying a dramatic reduction of the ion flux density along the jet axis. In this case, only a minor fraction of the inflowing ions would reach the small entrance aperture of the mass analyzer, usually placed on axis with the inlet hole. Therefore, ion focussing must be employed in order to guide as many of the inflowing ions as possible into the mass analyzer.

2.2 Ion Sampling

The circumstances of a rocket flight, in particular the high velocity and the varying rocket orientation, are also very important for the design of the ion mass spectrometer. First of all, the high velocity dictates very frequent sampling which means a fast scanning of the mass range. Taking a typical velocity of 1 km s^{-1}, a scan time of one second is required to obtain an altitude resolution of 1 km. Meeting this requirement is not trivial since middle atmosphere ions can reach very large mass numbers (up to about 500 amu) requiring a large mass range and consequently a large scan speed per mass. Taking a total mass range of 500 amu (atomic mass units), the scan time per mass is 2 ms. Since more than 2 values are usually required to characterize a mass peak, the electronics of the ion detection system has to be sufficiently fast to handle at least 1 ms signals. This can best be achieved by a pulse counting technique which provides single ion detection and was for the first time used in rocket-borne ion mass spectrometry by the MPIK group (ARNOLD et al., 1971).

Another quite different effect of the large supersonic rocket velocity (1000 m per second corresponding to about Mach 3), is the formation of a shock wave in front of the rocket resulting in substantial dissociation of weakly bonded cluster ions and also a reduction of ion sampling efficiency due to flow disturbances. In order to overcome these problems, the MPIK group (ARNOLD et al., 1977) introduced a double-cone sampling electrode, which practically attaches the shock wave and thereby allows one to sample ions from the undisturbed region upstream of the shock wave. This technique has led to major progress and is also used by the AFGL and UB groups (see next section).

Ion fragmentation can be induced not only by a shock wave, but also by electric fields used for ion sampling and focussing. First of all, a draw-in potential is usually applied to the sampling electrode in order to prevent repulsion of ions of a given polarity due to an electric charge-up of the rocket payload which usually occurs during the flight. Such a charge-up may result from unequal currents of atmospheric positive and negative charges hitting the rocket, as is for example, the case in the region above about 75 km where free electrons are prominent. Due to their much larger thermal velocity compared to positive ions, they impact with the rocket much more often than positive ions leading to a negative charge-up. Photoelectron emission is another cause of charge-up. Usually, electric charge-up is weak (a few volts at most) and thus, may be compensated for by a correspondingly small draw-in potential of opposite polarity. However, since the diameter of the sampling electrode is much smaller than the payload diameter, electric field lines originating from the charged-up payload may occupy the region in front of the sampling electrodes and thereby reduce the ion current flowing to the sampling electrode. Therefore, a sufficiently large draw-in potential has to be chosen in order to ensure efficient ion sampling. Draw-in potentials up to 10 V have been used.

Electric fields are also used for the extraction of ions from the gas jet formed behind the inlet hole and for focussing of the extracted ions on the entrance of the mass analyzer. Ion extraction is necessary since otherwise, ions would be carried by the gas jet resulting in a dramatic reduction of the ion flux density along the jet-axis. Therefore, the ions must be decoupled from the gas jet before they have travelled too far from the jet-axis. After extraction, ions are then focussed on the entrance of the mass analyzer in the x-y plane (perpendicular to the jet axis) where decoupling of ions from the jet occurs. The typical extension of the ion swarm in the x-y plane is already much larger than the diameter of the inlet hole. Therefore, focussing has to be employed in order to inject the ions into the mass analyzer.

Electric fields employed in the regions in front and behind the inlet hole (where ions undergo collisions with gas molecules) may lead to cluster ion fragmentation. This process is caused by collisions of electric field-accelerated ions with gas molecules and, therefore, occurs only in front of the sampling electrode and in the region just behind the inlet hole where a gas jet is formed. Since the gas is rarefied very quickly along the jet axis, the ion fragmentation region extends only over a distance of about 1-2 cm behind the inlet hole. The critical parameter controlling electric field-induced collisional cluster ion fragmentation is E/P (E = electric field strength, P = gas pressure). Usually, the cluster ions are internally excited by collisions with collision energies lower than the cluster ion band energy. Multiple collisions may ultimately lead to dissociation.

Laboratory simulation studies of cluster ion fragmentation in front of and behind the inlet hole were performed by the MPIK group (ARNOLD et al., 1977; BOHRINGER and ARNOLD, 1979). They revealed that even in front of the sampling electrode, where E/P is usually low, ion fragmentation can be quite efficient

(Figure 3). Depending on altitude, even low sampling electrode potentials of only a few volts can lead to substantial fragmentation due to multiple collision excitation. This finding has led to a reduction of sampling electrode potentials in flight experiments.

The gas pressure distribution in the region of the gas jet behind the inlet hole was probed by ARNOLD et al. (1977) using a miniaturized ionization gauge. It was found that the aperture plate of the mass spectrometer (acting as an obstacle in the jet) gave rise to a marked pressure increase in the region between sampling electrode and mass analyzer (Figure 4). This, in turn, leads to a reduction of transmission and thereby, sensitivity, and also to increased ion fragmentation. In order to overcome these problems, the MPIK group has introduced a novel technique, namely freezing-out of the gas jet (ARNOLD et al., 1977; see also next section) by which any pressure increase in front of the mass analyzer could be voided (Figure 4).

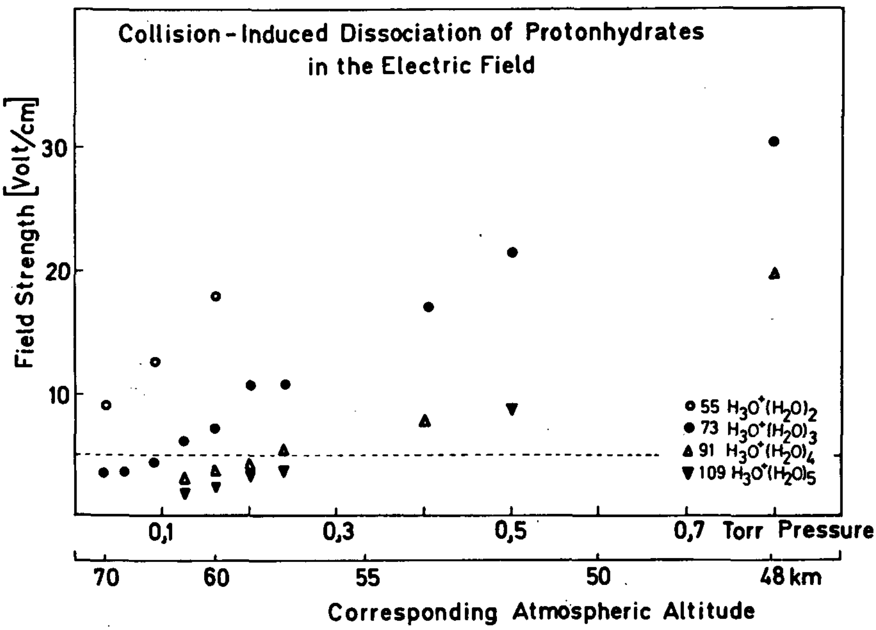

Figure 3. Laboratory studies of electric field-induced cluster ion fragmentation in a drift cell showing calculated critical field strength for cluster ion dissociation in the atmosphere (from BOHRINGER and ARNOLD, 1979).

Another important characteristic of a ballistic rocket flight is payload orientation, which influences the sensitivity of the ion mass spectrometer. Since rockets are usually spin-stabilized and launched at an elevation angle of about 70-80 degrees, the angle of attack α (angle between the fixed rocket axis and the velocity vector) changes during ascent from 0 to 70 degrees. During descent α becomes even larger than 90 degrees. Furthermore, large α's may also be caused by coning of the spin-stabilized rocket. Finally, during descent, when the rocket dives into denser atmospheric regions, rocket flip-over occurs due to aerodynamic forces acting on the rocket fins. Consequently, α decreases again during descent. A schematic representation of angle of

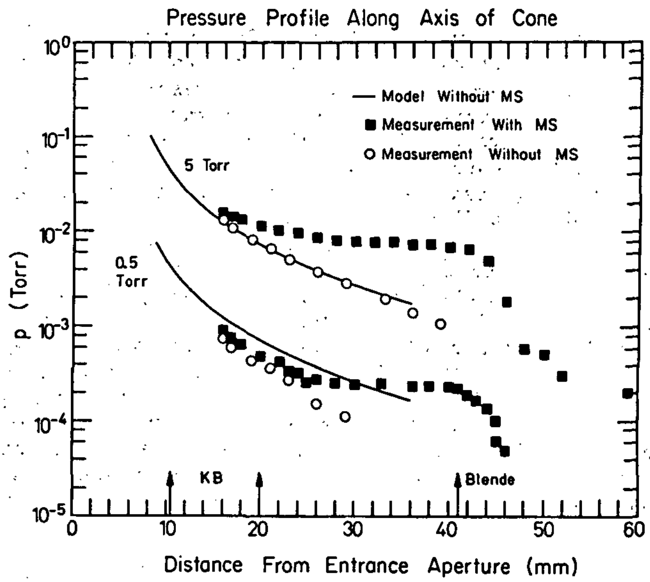

Figure 4. Laboratory diagnosis of the gas distribution behind the inlet hole of middle atmosphere mass spectrometer (from ARNOLD et al., 1977).

attack variations during a typical ballistic rocket flight is shown in Figure 5. The angle of attack α influences both the ion sampling efficiency and the focussing of ions into the mass analyzer and thereby affects the instrument's sensitivity. Furthermore, an increasing α also leads to increasing mass discrimination since the reduction of sensitivity is ion mass dependent. Finally, shock wave-induced cluster ion fragmentation may occur at large α even if a sampling cone is used since ions have to pass the shock waves created by the vacuum housing of the instrument or even the payload body.

As a consequence, reliable measurements on ballistic rockets can be made only for small α which implies that only the ascent part of the flight, except for the uppermost 10-20 km, is useful. Thus, a rocket apogee height of 110-120 km has to be chosen if measurements up to 100 km are intended. Unfortunately, this implies increased shock wave effects due to the higher velocity. Evidently, for a given rocket trajectory there exists only a relatively limited height range within which the experimental conditions are favorable. This forces the experimenter to set clear priorities as to the atmospheric layer to be investigated. For example, if the region 80-100 km has highest priority, an apogee height of 110-120 km has to be chosen. In contrast, if the mesosphere 55-85 km has highest priority, the apogee height should not exceed 95-105 km in order to reduce shock wave effects.

The above discussion clearly demonstrates the limitations of ballistic rockets as carriers of middle atmosphe.ic ion mass spectrometers. In order to overcome these difficulties, the MPIK group, as mentioned above, has recently developed a parachute-borne drop-sonde mass spectrometer payload which is always oriented in the flight direction (α remains below about 30 degrees) and travels at subsonic velocities (see following section).

2.3 Mass Analyzers

The mass analyzer is usually the least unique element of the rocket-borne

Quadrupole mass spectrometry was an adaption from particle accelerator techniques. As early as 1952, it was found at Brookhaven (COURANT et al., 1952) that the focussing of a beam of protons to be accelerated in the "cosmotron" could be remarkably improved by using alternating quadrupole fields. Magnetic fields were arranged around the accelerator so as to squeeze the beam first in one direction and then perpendicular to that direction. This "strong focussing, alternating gradient" principle had, in fact, been proposed several years earlier by Christofilos, an electrical engineer in Greece, but his proposal was overlooked until after its independent discovery at Brookhaven. From the equations of ion motion, it was apparent that alternating electric quadrupole fields could also be used for focussing (BLEWETT, 1952). It was soon recognized that the focussing could be made mass selective so that an RF electric field applied to a single set of electrodes would be appropriate for low energy ions. Building on these ideas, Paul and his colleagues at the University of Bonn (PAUL and RAETHER, 1955) recognized that the strong focussing, alternating gradient principle could be applied to mass spectrometry. This group pioneered the development of the quadrupole mass filter through most of the 1950s. As a result, commercial instruments became available during the early 1960s, and today they constitute a large fraction of the mass analyzer market.

The mass filter consists of four parallel rods, which ideally should be hyperbolic in cross section, but in practice usually contains circular rods to approximate the ideal hyperbolic shape. The best approximation is obtained for $r_{rod} = 1.148\ r_o$ where r_o is the minimum distance from the axis to a rod, and r_{rod} is the rod radius. A dc voltage U and an RF voltage $V \cos \omega t$ are applied between opposite pairs of rods. The x direction is taken here as being through the centers of the pair of rods for which the dc voltage is positive with respect to the other pair.

Ions injected into one end of the instrument are acted upon in the x and y direction by the field, but experience no field in the z direction along the axis of the instrument. For a given set of conditions of voltage, rod separation, and frequency, an ion species must have "bounded" oscillatory trajectories in the x and y directions, staying within the electrodes until they emerge out of the far end. Ions of other charge-to-mass ratios are filtered out in the x or y directions since their amplitudes in the x-y plane of their oscillations quickly increase exponentially with time to values exceeding r_o. Consequently, these ions either impinge on the electrodes or escape between the rods to the tube envelope.

The voltage applied to the rods, $\phi_o = (U + V \cos \omega t)$, gives rise to a potential field in the vicinity of the z axis of the form $\phi = (U + V \cos \omega t)(x^2-y^2)r_o^{-2}$. In the y direction, the dc field has a defocussing effect whereas it has a focussing effect in the x direction. The equations of motion for ions are:

$$\begin{aligned} m\ddot{x} + 2e\,(U + V \cos \omega t)\, x r_o^{-2} &= 0 \\ m\ddot{y} - 2e\,(U + V \cos \omega t)\, y r_o^{-2} &= 0 \\ m\ddot{z} &= 0 \end{aligned}$$

of which the first two are known as the Mathieu differential equations. They describe oscillations of the ions under the action of a periodic force. The third of the above equations is trivial, simply implying that ions injected in the z direction move at a constant velocity. Usually ion injection into the quadrupole is achieved by applying an additional draw-in potential, the so-called "field axis potential", to all 4 rods. When U is set equal to zero, the mass filter works in the so-called "total throughput" or "integral" mode which allows all ions to be transmitted whose mass is larger than a lower mass boundary, which is determined by V, r, r_o, and ω.

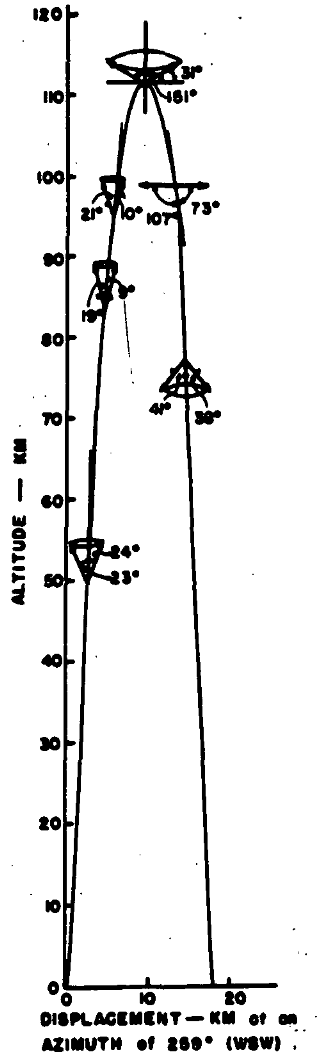

Figure 5. Schematic representation of the angle of attack variation during a typical ballistic rocket flight (from NARCISI and BAILEY, 1965).

ion mass spectrometer probe. Apart from its particular rigid and compact size construction, it is usually more or less of the standard design used for common laboratory work.

To date, two types of mass analyzers, the quadrupole mass filter and the single-focussing magnetic sector instrument, have been used for rocket-borne ion mass spectrometry in the middle atmosphere. The mass filter has been employed by the AFGL, NASA, and MPIK groups, while the magnetic instrument has been used only by one group, namely the UB group. By far, most of the rocket-borne ion composition measurements made to date in the middle atmosphere were due to the use of mass filters. It is the development of the mass filter which has stimulated middle atmospheric ion research. Therefore, and also because only the magnetic sector instrument and not the mass filter is described in the standard textbooks on experimental physics, the latter will be described in somewhat greater detail.

Having described the principle of operation of the mass filter, we shall now discuss its properties with particular emphasis placed upon applications in rocket-borne ion composition measurements under middle atmosphere conditions.

The mass resolution power increases with increasing U/V becoming maximum for a limiting value of U/V being about 0.16784. It also increases with an increasing number of RF oscillations, n, an ion experiences while traversing the quadrupole. This number n is, in turn, determined by the length l of the quadrupole, the RF frequency and the injection velocity in the z direction. Experimental studies have revealed that n and the mass resolution m/Δm are related by $n \approx 3.5(m/\Delta m)^{1/2}$ for mass resolution settings around 100 (PAUL et al., 1958). This sets an upper limit to the injection voltage as

$$U_i^{max} \approx 4.2 \times 10^2 \omega_{MHz}^2 l^2 \; M \; \Delta m / \; m \; (\text{volt})$$

where l is the length of the quadrupole field and M is the ion mass in atomic mass units (amu). An increase of the mass resolution power by an increase of ω is, of course, limited by the electric power consumption, P, being proportional to ω^5,

$$P = 6.5 \; 10^{-4} C^2 Q^{-1} M^2 \omega_{MHz}^5 r_o^4 \text{cm (watt)},$$

where C is the capacitance in picofarads and Q is the figure of merit of the power supply.

The mass range of the mass filter is determined by the ranges of U and V (whose ratios remain constant for a particular mass resolution setting), r_o and ω. The relations of the ion mass m and the above quantities are

$$V = 7.219 \; m_{amu} \omega_{MHz}^2 r_o^2 \text{cm}^2 (\text{volt})$$

$$U = 1.212 \; m_{amu} \omega_{MHz}^2 r_o^2 \text{cm}^2 (\text{volt})$$

Thus, an increase of the mass range can be achieved either by increasing U and/or by decreasing ω or r_o. An increase of U is limited by technical problems including also problems with RF arcing under typical operational conditions in the middle atmosphere. Hence, an increase of the mass range beyond a certain limit can be achieved only by a decrease of ω and r_o. Unfortunately, however, this reduces the mass resolution power since a reduction of ω reduces n and a reduction of r_o requires higher precision of fabrication of the quadrupole and makes ion injection more difficult. Furthermore, a decrease of r_o reduces the ion acceptance area of the quadrupole and thereby, sensitivity.

Finally, conditions for ion injection into the quadrupole will be addressed. The maximum amplitudes of ion oscillation in the x-y plane (x_M, y_M) depend not only on U, V, ω, and r_o but also on the initial conditions of the ion motion which, in turn, are sensitively determined by the ion injection conditions. Since the mass filtering effect of the instrument is due to making the amplitudes of oscillation of unwanted ions larger than r_o, the mass resolution power is larger for maximum amplitudes approaching r_o. Consequently, a larger mass resolution setting makes the instrument potentially more unstable with regard to departures from ideal injection conditions (in z direction and injection point exactly on z axis). For injection parallel to the z axis with coordinates x_o and y_o of the injection point in the x-y plane at z=0 (front end of quadrupole) the risk of ion loss due to collisions with the rods increases with increasing mass resolution power (larger amplitude of oscillation) and with increasing x_o and y_o. Therefore, only a certain fraction of the total field cross section πr_o^2 can be used for ion

injection, depending on the mass resolution setting. Maximum amplitudes x_M and y_M, and coordinates of the ion injection point x_o and y_o are related to the mass resolution power by

$$x_M/x_o,\ y_M/y_o < 1.8\ (m/\Delta m)^{1/2}$$

Thus, the maximum amplitude increases only as the square root of the mass resolution. For $x_M=y_M=r_o$ one obtains a crude estimate of the diameter D of the effective area in the x-y plane at z_o which provides a high ion transmission (close to 100 percent)

$$D \approx r_o (m/\Delta m)^{1/2}$$

For ion injection within an angle β with respect to the z axis (at x_o=y_o=0), the ion transmission of the quadrupole again decreases with increasing mass resolution setting. Here, the critical parameters are the radial ion velocities $\dot{x}_M$ and $\dot{y}_M$. These should fulfill the requirement

$$\dot{x}_M,\ \dot{y}_M < 0.16\ r_o\ (\Delta m/m)^{1/2}$$

Another important aspect of the ion injection energy is that it is not critical provided that M remains sufficiently large. The latter requirement can be easily met by properly adjusting 1 and ω.

Having discussed the operational principles and properties of the mass filter, we now turn to a discussion of consequences for rocket-borne application in the middle atmosphere.

The most important properties making the mass filter an almost ideal tool for rocket-borne ion mass spectrometry in the middle atmosphere are the uncritical ion injection conditions. These allow for a high overall ion transmission (between inlet hole and multiplier) even for unfavorable rocket orientations. When only moderate mass resolution is required (peak width 1 amu at 50 percent amplitude), just sufficient to separate adjacent mass peaks of comparable amplitude, the mass filter offers a relatively large acceptance area, which may be a major fraction of the quadrupole field cross section πr_o^2. Since the ions enter the probe through a small inlet hole (typical diameter: 0.1 cm), one can obtain a large overall ion transmission with a moderate size quadrupole, say, with r_o equal to 0.5 cm. This is true even if some broadening of the ion swarm occurs to collision-controlled ion motions in the gas jet behind the inlet hole. Usually, most ions can be electrically extracted from the gas jet before their x- and y-coordinates have become larger than about 0.1 cm.

Other favorable properties of the mass filter for rocket-borne application are its rigid and compact size construction and its flexibility as far as modes of operation are concerned. Various modes of operation can, in principle, be used in a single rocket flight including positive and negative ion detection, variable mass resolution and sensitivity settings, variable ion injection energy and the total throughput mode. Switching from one mode to another involves only switching of electrical potentials which can be accomplished within 10 ms of the above modes, the total throughput or integral mode is particularly interesting since it provides a very large overall ion transmission and thereby, a high sensitivity. Laboratory simulation experiments of the MPIK group have shown that for an ambient atmospheric gas pressure of 1 mb, corresponding to an altitude around 50 km, an overall transmission of 50 percent can be achieved.

Thus, the mass filter appears to be particularly well suited for rocket-borne ion composition studies in the middle atmosphere where ion concentrations are low and therefore require a large sensitivity.

The other type of mass analyzer used for rocket-borne ion studies in the middle atmosphere, the single focussing magnetic sector instrument, will now be briefly reviewed. *This analyzer employs the impulse-selective deflection of* ions by a sector magnet (for example, a 90° sector). The ions are injected through a narrow entrance slit (typical width: 0.01 cm) which is placed in front of the sector magnet. In the magnetic field region, the ion trajectories are circular with a radius r which is related to the ion mass m, the magnetic field strength H, and the injection voltage V by

$$\frac{m}{e} = H^2r^2/2V$$

A mass spectrum can be obtained in several ways. A fixed detector, usually a multiplier with an entrance slit can be placed at the rear end of the sector magnet and then either H or V can be swept to produce the mass spectrum. The rocket-borne ion instrument of the UB group (ZBINDEN et al., 1975) employs a U-sweep from about 180-2000 V with a fixed magnetic field strength H of 4500 Gauss. The strength of the magnetic instrument lies in its very high mass resolution power being far greater than that of a quadrupole mass filter. However, severe shortcomings, in particular for middle atmospheric ion studies, are a relatively low ion transmission of the mass analyzer especially at higher mass numbers, and even more severe, a much lower overall transmission. The latter is mostly due to the inefficient focussing of ions extracted from the gas jet behind the inlet hole on the narrow entrance slit (typical width: 0.01 cm) of the mass analyzer. Usually, the focussing efficiency is only around 2 to 6 percent. Furthermore, the magnetic instrument is rather sensitive to oblique ion injection. Another shortcoming is the upper limitation of the mass range, presently around 250 amu.

In view of the relatively low sensitivity, the high resolution power of the magnetic sector instrument pays off only for special applications. A very attractive application is the isotope studies, which usually require the separation of minor ion peaks adjacent to major peaks.

In summary, therefore, it appears that the quadrupole mass filter is superior for moderate and low mass resolution ion studies, especially when high sensitivity and high mass range are required. In contrast, the magnetic sector instrument is superior as mass resolution is concerned. Thus, the two types of mass analyzers complement each other and combined measurements using both types of mass analyzers provide a broader data base. Such combined flights of an MPIK mass filter and a UB magnetic sector instrument have been made on numerous occasions.

2.4 High Speed Pumping Systems

The high speed pump represents perhaps the most unique element of the rocket-borne ion mass spectometer probe. Its design is to a large extent dictated by the specific experimental circumstances, particularly the ion and gas sampling configuration. Ideally, the inflowing gas should be removed in front of the mass analyzer and only ions should have access to the mass analyzer. In practice, however, such differential pumping involving two chambers does not necessarily represent the most favorable solution. Therefore, all instruments flown to date have employed only a single chamber for the pump, mass analyzer, and multiplier.

A simplified view of this single chamber configuration would be a cylindrical chamber whose walls act as a pump and into which ions and gas enter

through a small inlet hole drilled into the top plate of the cylinder. Behind the inlet hole a gas jet is formed which usually does not significantly interact with "background" gas molecules since the mean free path length of "background" molecules must be larger than the length of the cylinder. This requirement is imperative in order to avoid ion scattering in the mass analyzer, whose size is almost as large as that of the cylinder. The ideal situation would be a free jet expansion through the inlet hole with a unit pumping efficiency (the probability of sticking by a gas molecule upon wall collision is one) of the inner walls of the cylinder. In this case, the gas density distribution inside the cylinder would be highly nonuniform. Also, the velocity distribution of gas molecules would be highly non-Maxwellian. Alternatively, for a sticking probability much lower than one, a "background" gas pressure builds up which may become large enough to reduce the mean free path for gas molecules to a value lower than the length of the cylinder. Here, the gas jet interacts with the background gas rather than with surfaces. As a consequence, the "background" gas distribution becomes more or less Maxwellian with a shape determined by the wall temperature. However, since ion scattering by molecules must be avoided, only the first of the above scenarios is of primary interest here. Here, the size of the inlet hole has to be adjusted to the ambient atmospheric gas pressure and the speed of the pump such that the "background" gas pressure remains sufficiently low to ensure that the mean free path remains larger than the length of the cylinder.

In practice, the mass analyzer and eventually also the ion optical elements are positioned on-axis with the gas jet and are more or less close to the inlet hole. Thus, the gas jet is scattered by non-pumping surfaces before gas molecules ultimately arrive at pump surfaces. Consequently, the gas density distribution inside the cylinder is modified especially along the cylinders' z-axis, which usually is identical to the z-axis of the ion optics and/or the mass analyzer. For the specific configuration described above, the efficiency of the pumping system is not simply determined by the conventionally defined pumping speed. Instead, the geometry of the instrument and of the ion optical elements and the mass analyzer are all important. This is more thoroughly discussed below in connection with practical examples.

To date, five different types of high speed pumping systems have been used for middle atmosphere rocket-borne ion mass spectrometry including cryo sorption, titanium-film sorption, and cryo condensation pumps.

The first pumping system, introduced by the AFGL group in 1963 (NARCISI and BAILEY, 1965), was a liquid nitrogen-cooled zeolithe pump (Figure 6). It consisted of 7 concentric stainless steel cones with a total surface area of about 2,000 cm^2 onto which zeolithe material was bonded. Zeolithe is a crystalline aluminosilicate containing crystal water. It is composed of SiO_4- and AlO_4-tetraeders which form a polyeders having a cavity at its center. Cavities of individual polyeders are linked with each other by pores having typical sizes of 0.5-1 nm. By out-baking of the zeolithe, the crystal water can be driven out and thereby the pore system can be activated for the adsorption of gas molecules having diameters around 0.2-0.4 nm. Usually, the zeolithe material used for adsorption pumps is composed of small spherules (diameter: 0.3 cm) or cylinders (length: 0.15 cm) which are bonded together by about 20 percent bonding material. As a consequence, the effective heat conductance is relatively low, about 10 W m^{-1} $^{\circ}K^{-1}$.

The sticking probability p of N_2 and O_2 molecules hitting the zeolithe is about 0.6 for freshly activated zeolithe kept at a temperature of 77 $^{\circ}$K (liquid N_2 temperature). However, p decreases distinctly as the mass of adsorbed gas increases. This is due to coverage of the surface of the sorbant by gas molecules and the increase of the effective temperature of the pump surface due to the reduction of the heat conductance. The sticking probabilities

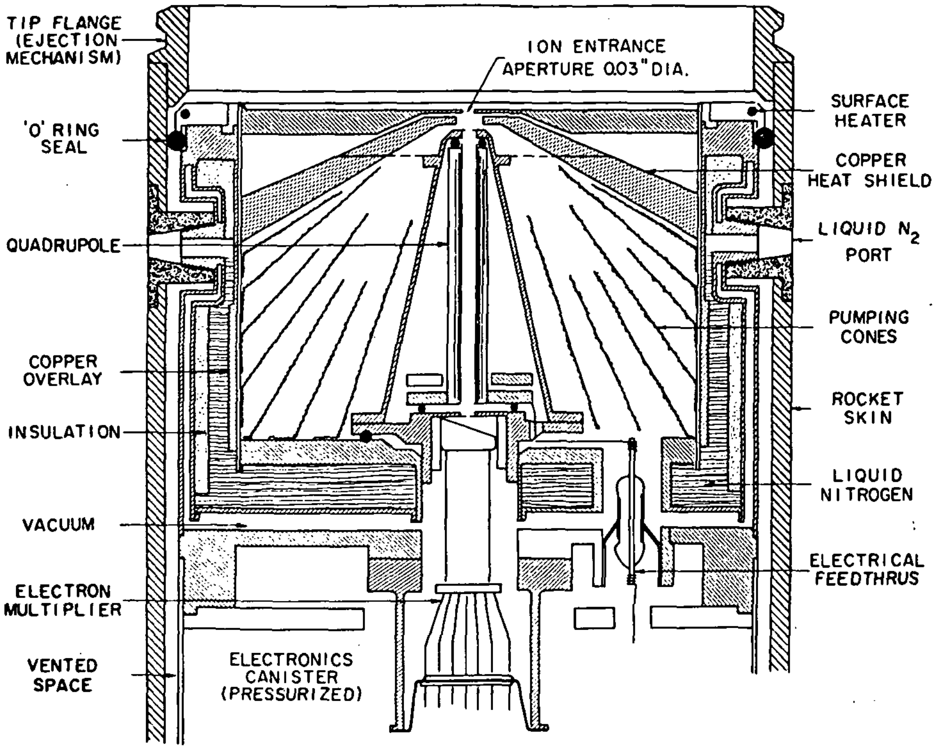

Figure 6. *First pumped rocket-borne ion mass spectrometer as used by the AFGL group in 1963 (from NARCISI and BAILEY, 1965).*

of He, Ne, and H_2 are very much lower than those of N_2 and O_2. However, these gases have low abundances only in the upper part of the middle atmosphere and therefore, they do not build up critical partial pressures inside the instrument during the short time span of a rocket flight.

Another important characteristic of the cryosorption pump is its pumping capacity, C. Usually, C is around 4×10^{24} molecules per kg (of sorbant material) for N_2 gas and for zeolithe at 77 °K. During a typical ballistic rocket flight with an inlet hole of 0.01 cm in diameter the integral number of inflowing molecules above 60 km is on the order of 10^{22}. Thus, the minimum zeolithe mass required is of the order of a few g. The standing time of the pump which is determined by the evaporation rate of the liquid nitrogen is about 5 hours.

Now we will discuss more thoroughly the problem of pumping efficiency using this first rocket-borne pumped ion mass spectrometer as an illustrative example. As can be seen from Figure 6, the gas jet which is formed behind the inlet hole mostly impacts on the front end of the housing of the quadrupole mass filter used for the mass analyzer. Thus, relatively high gas densities build up in the region between the inlet hole and the quadrupole housing. Most of the gas leaves this region sideways via the slit between the quadrupole housing and the copper heat shield. Another fraction of the gas leaves the high pressure region via the entrance aperture (diameter: 0.1 cm) of the quadrupole and flows into the most critical part of the instrument, namely the

mass analyzer. As already mentioned above, the high gas pressure building up in front of the mass analyzer causes several problems including a reduction of transmission and thereby sensitivity as well as collisional breakup of cluster ions. These perturbations become particularly severe at lower heights or higher ambient gas pressures. Another shortcoming of the zeolithe pump is the risk of contamination of the mass analyzer and the multiplier by zeolithe particles which may eventually disintegrate from the pump surface.

The second high speed pumping system, developed and first flown in 1968, is the titanium sublimation pump of the NASA group (GOLDBERG and BLUMLE, 1970). It (Figure 7) consisted of a chamber surrounding a quadrupole mass filter, which was protected by a series of optical baffles in order to reduce the risk of contamination of the mass analyzer and multiplier by titanium vapour deposition. The pumping effect of a titanium sublimation pump relies on the absorption of chemically active gases by the titanium film via chemisorption, formation of chemical compounds, and diffusion. At a temperature of the Ti-film of 293 K, the sticking probabilities for N_2 and O_2 are large whereas, He, Ne, H_2 and even the relatively abundant argon (volume mixing ratio: 0.01) are practically not pumped. The pumping capacities C for N_2 and O_2 are about $4x10^{24}$ and $8x10^{24}$ molecules per kg titanium film.

As with the zeolithe pump, the sticking probability p decreases distinctly with increasing gas load of the Ti-film. To remove atmospheric argon which is not pumped by the Ti-sublimation pump, the latter was supported by an ion getter pump. In order to ensure a high pumping efficiency of the titanium film, the film had to be deposited within about 1-4 hours before rocket launch, which was accomplished by electrical heating of titanium filaments mounted inside the pump chamber.

An advantage of this pump is its simplicity, in particular, the absence of a liquid coolant which is usually difficult to handle in a rocket-borne instrument. Shortcomings include a relatively low pumping efficiency and the

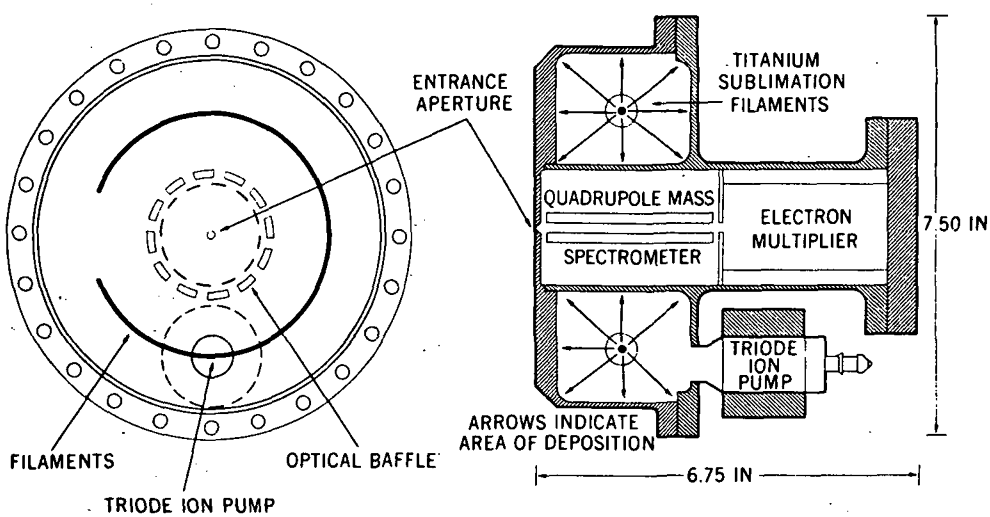

Schematic of the basic spectrometer plus the vacuum housing and pumps.

Figure 7. Pumped rocket-borne ion mass spectrometer as used by the NASA group (from GOLDBERG and BLUMLE, 1970).

risk of titanium contamination of the mass analyzer and the multiplier. Evidently, the series of optical baffles employed to protect the mass analyzer and multiplier from titanium contamination severely reduce the access of the inflowing gas to the pump chamber. Thus, most gas molecules undergo multiple scattering by nonpumping surfaces before they reach the pump chamber which gives rise to a relatively high gas density in the quadrupole chamber. Furthermore, the entrance aperture plate of the quadrupole placed very close to the inlet hole acts as an obstacle to the gas jet leading to the buildup of a relatively high gas density in this critical region. In summary, it appears that the NASA instrument is most suited for studies of the uppermost part of the middle atmosphere where the atmospheric gas pressure is not too high.

A third pumping system was introduced by the MPIK group and flown in 1969 (ARNOLD et al., 1971; 1977); it is a pure cryo-condensation pump cooled by liquid helium. A further improved version of this pump flown in 1972 (ARNOLD et al., 1977), is shown in Figure 8. Here a basically different approach was taken. The pump surface is fabricated of gold-plated copper to increase heat conduction. No baffles are used offering maximum access of the inflowing gas to pump surfaces. Due to the extremely low temperature of the coolant (4.2°K), all gases except for He and H_2 are pumped practically with unit sticking probability. The ultra-rare atmospheric gases He and H_2 are sufficiently well pumped by cryo trapping in the condensate matrix composed of mainly N_2 and O_2. Cryo trapping represents no problem for the short time of a rocket flight. Due to its small size and low mass (6 kg), the standing time of the helium pump is only about 20 minutes requiring liquid helium filling to be completed within 10 minutes prior to launch.

Most importantly, the MPIK pump freezes out most of the gas jet using a laminated cold surface placed in front of the mass analyzer. Upon extraction from the gas jet, ions are focussed onto a central hole (diameter: 0.5 cm) drilled into the cold surface. Because of the very efficient pumping, a large inlet hole can be used resulting in a large sensitivity. Alternatively, when using an inlet hole with a diameter of merely 0.1 cm, ion composition measurements can be extended to lower altitudes than was possible with previous instruments. In fact, the first rocket flight of the modified pump in 1972, led to a major breakthrough, namely an extension of ion composition measurements downwards in altitude to 35 km, compared to about 60-70 km reached in previous experiments.

A fourth type of pump, which was flown in 1971, by the UB group (ZBINDEN et al., 1975) (Figure 9) is also a liquid helium-cooled cryopump but without a cold surface for direct freezing out of the gas jet. Instead, the rather large and massive pump (22 kg) is built around a complex ion optical system employed for the focussing of incoming ions onto the entrance aperture of a magnetic sector mass analyzer. Due to its large size, this pump has a standing time of 4 hours which is a major advantage over the small MPIK helium pump. However, a shortcoming of the bigger UB pump is that it requires the use of larger rockets.

A fifth type of pump introduced in 1978, by the MPIK group (ARNOLD et al., 1982; ARNOLD and VIGGIANO, 1982) is a liquid neon-cooled cryopump. It was developed by the MPIK group building on the experience with their balloon-borne ion mass spectrometer (ARNOLD et al., 1980). The liquid neon pump offers nearly the same high efficiency for removal of N_2 and O_2 as the liquid helium pump. For He, H_2, and Ne, the pumping efficiency is much less but cryo trapping at the temperature of liquid neon (27°K) is still sufficient for the short time span of a rocket flight. The use of liquid neon offers major advantages as far as the standing time and the behavior of the liquid coolant under flight conditions are concerned. This is due to its large latent heat of vaporization of 87.2 kJ per kg for helium. Considering the specific

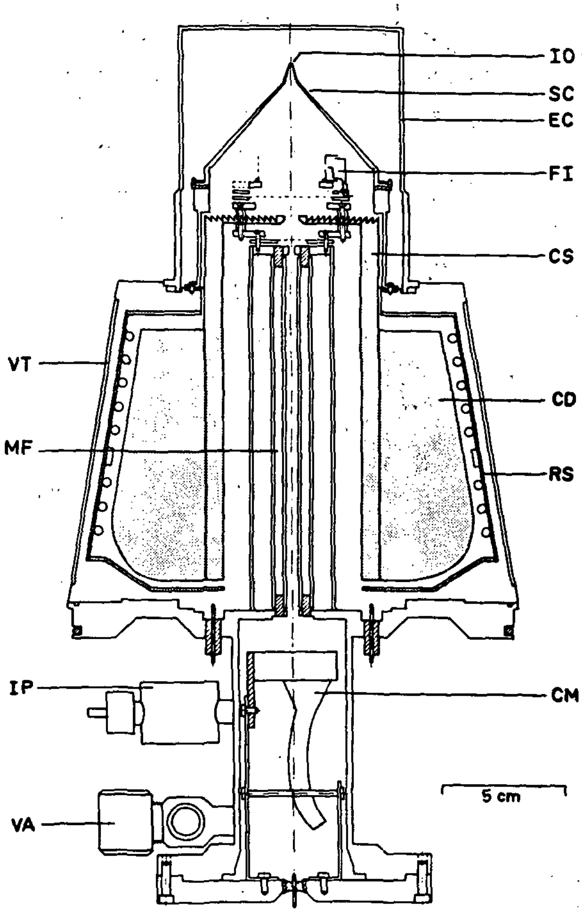

Figure 8. Combined positive ion, negative ion, and neutral gas composition mass spectrometer as used by the Max-Planck-Institut for Kernphysik, Heidelberg (from ARNOLD et al., 1977).

weights for liquid Ne and He being 1204 and 124.8 kg per cubic meter, the latent heat of vaporization for one liter of liquid neon is 105 kJ compared to 2.6 kJ for liquid helium. The standing time of the small neon pump is about 10 hours, which greatly relaxes preflight preparations and also offers an opportunity for measurements of stochastically occurring short term events like aurorae which require quick response times. Thus, the liquid neon-cooled condensation pump appears to be the most powerful high speed pump for applications towards rocket-borne ion mass spectrometry of the middle stratosphere.

3. MILESTONES IN INSTRUMENTAL DEVELOPMENTS AND RELATED PROGRESS IN ATMOSPHERIC ION COMPOSITION MEASUREMENTS

The first flight of a rocket-borne pumped ion mass spectrometer in the earth's atmosphere was carried out on October 31, 1963, by the AFGL group (NARCISI and BAILEY, 1965) and provided positive ion composition data at altitudes between 64 and 112 km. The instrument (Figure 6) was equipped with a

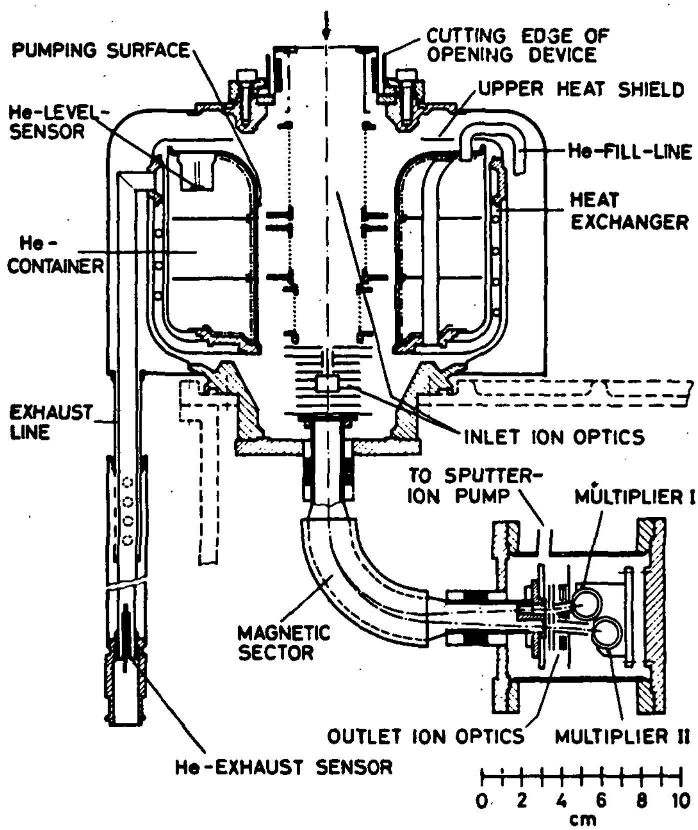

Figure 9. Positive ion single focussing magnetic sector mass spectrometer as used by the University of Bern (from ZBINDEN et al., 1975).

small commercial quadrupole mass filter developed and fabricated at the Bell and Howell Research Center and modified at AFGL. The pump used was a liquid nitrogen-cooled zeolithe cryo sorption pump which has been described in detail in the preceding section of this paper. Ion detection was accomplished using a ten-stage multiplier. The output current of which was measured with a logarithmic electrometer which had a response time of about 20 ms and a detection limit of approximately $5x10^{-16}$ A.

The small quadrupole (rod diameter: 0.1905 cm; rod length: 7.62 cm) was placed rather close to the planar sampling electrode which had an inlet hole with a diameter of 0.1 cm. A draw-in potential of -8 V was applied to the sampling electrode and after entering the instrument via the inlet hole, ions were attracted by a potential of -128 V applied to the quadrupole and quadrupole housing.

The small quadrupole offered a mass range from 1 to 46 amu and only a poor mass resolution $m/\Delta m$ of 16 corresponding to a peak width Δm of about 3 amu. The sensitivity for ion detection was roughly constant with height above approximately 80 km but decreased by about a factor of 100 below 80 km. Most likely, this dramatic loss of sensitivity below 80 km was due to the relatively inefficient pumping at these heights. Here, the higher ambient gas pressure gives rise to a stronger gas jet behind the inlet hole impinging directly onto

the unprotected quadrupole which was placed just behind the inlet hole. Thus, ion scattering reduces the transmission of the instrument.

The most striking result of this pioneering experiment was the discovery of atmospheric positive cluster ions. It was found (Figure 10) that below about 80 km ions with masses 19 (H_3O^+) and 37 ($H^+(H_2O)_2$) become more dominant than NO^+ (30), the dominant ion predicted by theory (NICOLET and AIKIN, 1960). It was also found that ions with masses larger than 45 are prominent below 75 km. At heights above 80 km, the dominant ions were NO^+ and O_2^+. Besides these, a layer of meteoric atomic metal ions, mostly Mg^+ (24, 25, 26) and Na^+ (23) with a peak at 95 km was also detected. However, possibly due to the poor mass resolution, several masses including 16, 17, 18 were found which could not be confirmed by later improved measurements.

During the following years, the AFGL group carried out a number of positive ion composition measurements under a variety of geophysical conditions including high latitudes, auroral energetic electron precipitation events, and sporadic E-layer events. For these studies, essentially the same type of instrument, with only minor modification, was used. Perhaps, the most important improvement was an extension of the mass range of the instrument to 86 amu which allowed the detection of Fe^+ (56) and $H^+(H_2O)_3$ (55). All these flights confirmed the existence of cluster ions $H^+(H_2O)_n$ (n = 1, 2, 3) below 85-80 km and of a meteoric metal atom layer peaking around 95 km and composed mostly of Mg^+ and Fe^+. Building on their laboratory studies of ion-molecule reactions, Ferguson and his colleagues at the NOAA Aeronomy Laboratory at Boulder (FERGUSON, 1971) proposed ion chemical schemes for the formation of the newly detected atmospheric $H^+(H_2O)_n$ clusters and meteoric metal atom ions. They suggested that the $H^+(H_2O)_n$ clusters are formed from NO^+ and O_2^+ by a chain of ion molecule reactions involving

POSITIVE IONS AT 64-112 KILOMETERS

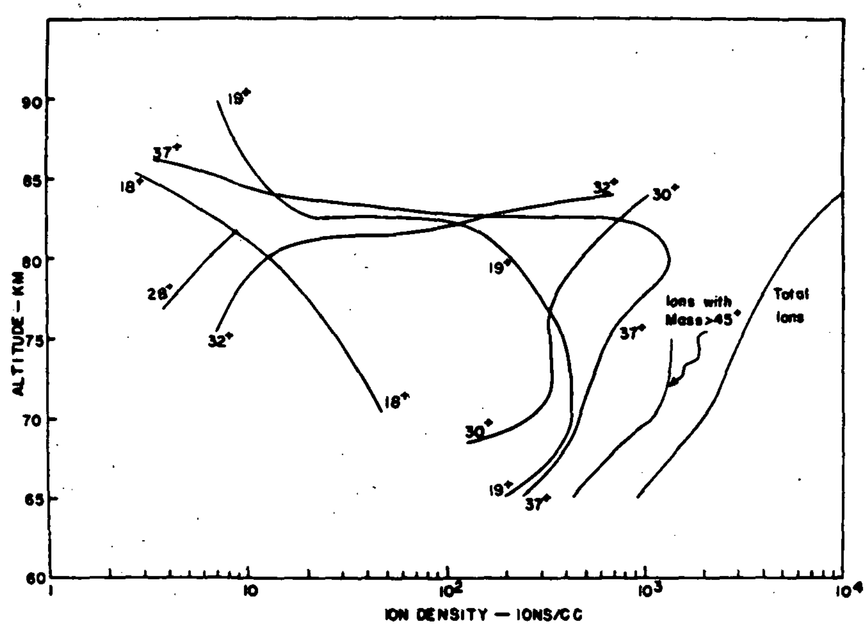

Figure 10. Positive cluster ion composition as obtained in the first flight of the AFGL group (from NARCISI and BAILEY, 1965).

atmospheric water vapor. Atomic metal ions, according to their scheme, are formed from neutral metal atoms resulting from meteor ablation. The most important formation mechanisms are photoionization and charge transfer from NO^+ and O_2^+ which is efficient due to very low ionization potentials of the metal atoms. Since atomic ions recombine only very slowly with electrons via radiative recombination, they are particularly long-lived and thereby can reach large fractional abundances despite the concentration of neutral metal atoms. Their long lifetime also allows atomic metal ions to be transported vertically by Lorentz forces when these ions are blown by horizontally directed winds across the earth's magnetic field lines. Wind shears may arrange the atomic metal ions in thin layers and thereby give rise to so-called sporadic E layers which influence radio wave propagation.

The next instrumental development was the NASA instrument flown for the first time on March 15, 1968 (GOLDBERG and BLUMLE, 1970). While the mass analyzer of this positive ion instrument was similar to the one used in the first AFGL flight of 1963, the high speed pumping system was entirely different (Figure 7). Instead of a zeolithe pump, a titanium sublimation pump combined with an ion getter pump was used (see preceding section of this paper). Also, the ion detection system involving a multiplier and current measurement was essentially similar to the one used by the AFGL group. The mass range was 13-49 amu and the mass resolution was about 1.5 amu (peak width at half amplitude). Like the AFGL instrument, the NASA instrument also employed a flat sampling electrode with an inlet hole of 0.075 cm in diameter and with the small quadrupole placed just behind the inlet hole. The draw-in potential applied to the sampling electrode was -10 V and the ion injection potential applied to the quadrupole rods and the entrance aperture of the quadrupole was -10 V. However, the apogee height of this first flight of the NASA-instrument was 303 km, far too high for a good middle atmosphere measurement. As a consequence, reasonable positive ion data could be obtained only down to a height of about 76 km below which the sensitivity of the instrument decreased dramatically. A somewhat improved version of this instrument with longer quadrupole rods (10 cm), a larger mass range (4 - 66 amu), and a smaller inlet hole (diameter: 0.05 cm) was flown twice in 1970, at the equator. Here apogee heights were only 101 and 122 km which allowed for reasonably good instrument performance in the upper part of the middle atmosphere. Positive ion composition data could be obtained above 60-65 km. The results are similar to the previous findings by the AFGL group confirming the existence of $H^+(H_2O)_n$ clusters (n = 1, 2, 3) below about 85 km and of the atomic metal ion layer around 95 km. However, in addition, some new and interesting information was also obtained on the equatorial atmosphere (Figure 11) and with these and later flights on metal ions (GOLDBERG and AIKIN, 1971; 1973).

The MPIK instrument came into use in 1969, and led to a major improvement in ion sampling. This instrument was developed and built in-house by the MPIK group based on the experience with their unpumped rocket-borne ion mass spectrometer and was for the first time successfully flown in 1967 (ARNOLD et al., 1969). This middle atmospheric instrument consisted of a large quadrupole mass filter (rod diameter: 0.9 cm; rod length: 20 cm) and a novel liquid helium-cooled cryo condensation pump (see preceding section). Furthermore, it was equipped with an ion detection system employing a channel electron multiplier (CEM) and single ion pulse counting. The sampling electrode was a planar circular plate (diameter: 6 cm) with a central inlet hole 0.1 cm in diameter. Draw-in potentials of ± 5 V and ± 10 V were applied to the sampling electrode. In constrast to previous designs, the quadrupole was positioned at a much larger distance (3 cm) from the inlet hole in order to allow for sufficient gas jet expansion before the jet impinged on the quadrupole. Another important feature of this instrument is a powerful RF-generator developed and built by the MPIK group which had an RF-amplitude V of 450 V and allows for a mass range of 1-130 amu despite the large quadrupole rod radius.

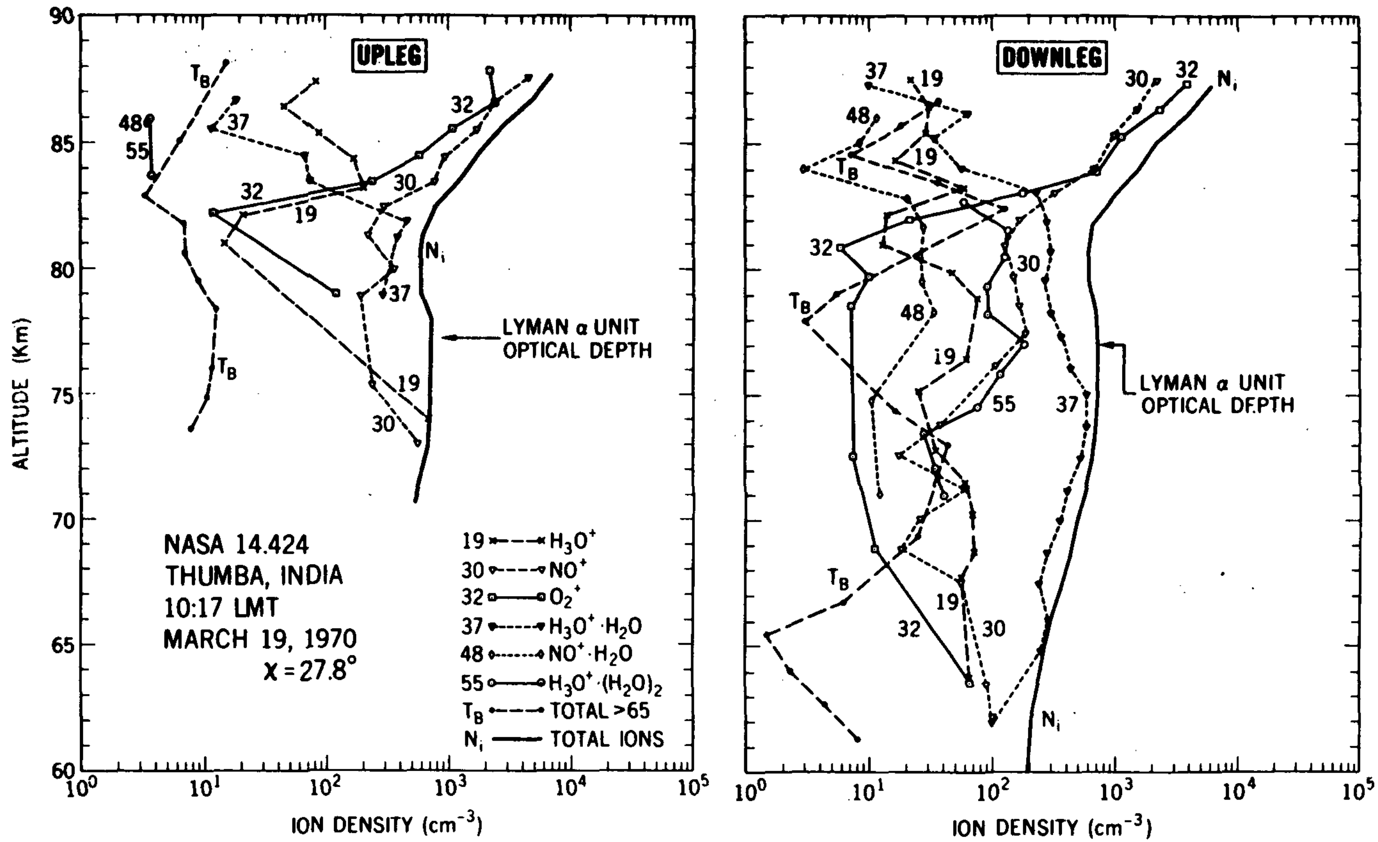

Figure 11. Positive ion composition as measured by the Nasa group in the equatorial ionosphere (from GOLDBERG, 1971).

The ion detection system, which involves single ion counting and a high voltage CEM-power supply with the capability to quickly switch the polarity of the high voltage (within 20 ms). This allows the measurements of positive and negative ions with one instrument.

The first successful flight of this combined positive and negative ion instrument, which provided near simultaneous positive and negative ion composition data, took place on March 22, 1970 (ARNOLD, 1971; ARNOLD et al., 1971). The negative ion data were the first high mass resolution negative ion data obtained in the earth's atmosphere. They also were the first negative ion data which yielded height profiles for individual negative ion species. Using their small modified quadrupole instrument, the AFGL group had also obtained negative ion data (NARCISI et al., 1971). But these suffered from poor mass resolution. In contrast, the MPIK measurement allowed separation of adjacent mass peaks. A total of 12 negative ion species was detected (Figure 12), most of which were present in large abundances only below 80 km. In this region, CO_3^- (60), Cl^- (35, 37) and HCO_3^- (61) were most prominent. Above 80 km, very massive species 111±1 and 125±1 were most prominent and O_2^- (32) was also present. It was proposed by ARNOLD et al. (1971) that the observed Cl^- is probably formed by ion-molecule reactions involving Cl-atoms or some atmospheric Cl-compound whose concentration was estimated to be about 10^5 cm^{-3} (ARNOLD, 1971; ARNOLD et al., 1971; ARNOLD and KRANKOWSKY, 1971). In the meantime interest in middle atmosphere chlorine has increased tremendously since it was recognized that Cl-atoms give rise to catalytic destruction of the ozone layer. Current theoretical model calculations of the mesosphere (c.f. BRASSEUR et al., 1983) predict a Cl atom concentration of about 10^5 cm^{-3} around 60 km which agrees well with the Cl abundance inferred by Arnold and his colleagues from their negative ion composition measurements already in 1971. This example demonstrates the enormous potential of atmospheric ion composition measurements as an analytical tool for neutral trace gas detection.

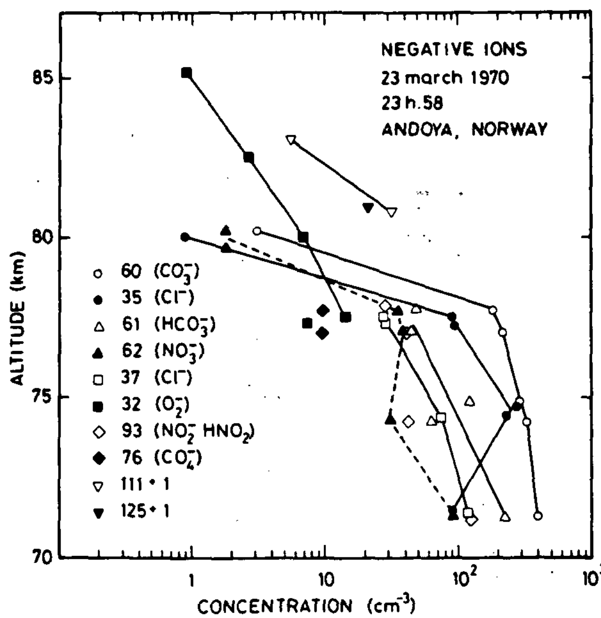

Figure 12. First high mass resolution measurements of atmospheric negative ions (from ARNOLD et al., 1971).

Other unexpected results of the MPIK flight were the presence of HCO_3^- which was later supported by laboratory studies of ion-molecule reactions (FERGUSON et al., 1979) and the predominance of CO_3^- instead of the expected NO_3^-. Also unexpected, were heavy ions at mass 111±1 and 125±1 which seem to be difficult to explain even by current atmospheric negative ion models. In contrast, most of the other observed ions can be explained by current models. Particularly, the sharp ledge of the regime of atomic and molecular negative ions observed around 78-80 km can be readily explained by associative detachment reactions of negative ions with oxygen atoms which at nighttime become abundant above these heights (c.f. ARNOLD and KRANKOWSKY, 1971).

As far as positive ions are concerned (ARNOLD, 1971; KRANKOWSKY et al., 1972a), the early MPIK measurements mostly confirmed the previous observations of the AFGL and NASA groups. However, due to the high mass resolution and sensitivity of the MPIK instruments, it was possible to better characterize the meteoric metal ion layer at 95 km. A total of 9 elements Na^+ (23), Mg^+ (24, 25, 26), Al^+ (27), K^+ (39, 41), Ca^+ (40, 42, 44), Cr^+ (52), Fe^+ (54, 56, 57), Ca^+ (59), and Ni^+ (58, 60) could be detected with fractional abundances being very similar to those of their parent elements in stony meteorites (chondrites) (ARNOLD, 1971; KRANKOWSKY et al., 1972b).

The next major step in instrumental developments was the single focussing magnetic sector instrument for positive ion detection by the UB group, which was first flown on December 14, 1971 (ZBINDEN et al., 1975). The instrument (Figure 9) was pumped by a liquid hellium-cooled cryo condensation pump (see preceding section of this paper) and employed conventional ion detection using a multiplier and current measurement. Like all previous instruments, it had a flat sampling electrode to which a draw-in potential of -5 V was applied and it used an inlet hole with a diameter of 0.2 cm. The mass range was 11-73 amu and the peak width was about 0.5 amu. Thus, the strength of this instrument was its high mass resolution power which was particularly well suited for isotopic studies.

Positive ion composition data were obtained between 75 and about 150 km. Besides confirming previous observations, the measurement provided additional new information, especially on meteoric ions (Figure 13). A total of 23 masses corresponding to 17 elements could be detected. As far as cluster ions are concerned, the measurements suffered from severe ion breakup which was partly due to the high apogee height (about 150 km).

A breakthrough in cluster ion composition measurements was achieved in 1972, when a new MPIK instrument especially designed for measurements below 85 km was flown (ARNOLD and KRANKOWSKY, 1974). This instrument was equipped with a conically shaped sampling electrode and a cold surface in front of the quadrupole mass filter. Apart from employing a larger quadrupole (rod diameter: 0.9 cm; rod length: 20 cm) and no electron impact ion source, it is essentially similar to the instrument shown in Figure 8. In contrast to previous measurements, a lower draw-in potential of only 2.5 V was applied in order to reduce electric field-induced cluster ion breakup. This was a consequence of laboratory simulation studies of cluster ion breakup carried out by the MPIK group which had clearly demonstrated that draw-in potentials as low as 5 V (the lowest value previously used) are sufficient to induce substantial collisional dissociation of weakly bonded cluster ions. The conically shaped (double cone with angles of 90° and 20°) was used to attach the shock wave and thereby sample ions from the undisturbed atmosphere. Thus, shock wave-induced cluster ions breakup should be reduced and furthermore, the ion sampling should efficiently be improved. The laminated cold surface placed in front of the quadrupole was introduced in order to freeze out the incoming

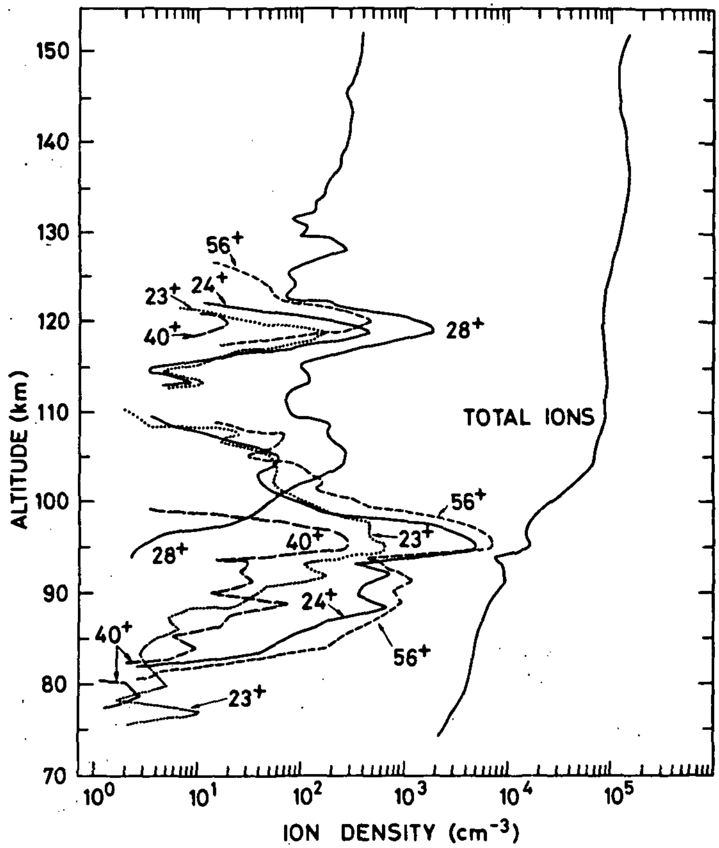

Figure 13. Atomic metal ion measurements as obtained by the high mass resolution magnetic sector mass spectrometer of the UB group (ZBINDEN et al., 1975).

gas jet. Thus, the transmission of the instrument, in particular at low heights, was markedly improved. Also, the risk of electric field-induced cluster ion breakup in front of the quadrupole was reduced.

The first flight of this new instrument in May 1972, provided the first positive ion composition measurements in the stratosphere (ARNOLD et al., 1977). It was found that cluster ions other than proton hydrates become prominent below about 40 km (Figure 14). Above 60 km, many new species were also detected. Numerous positive cluster ion species including weakly bonded ones like NO^+N_2 (bond energy: 0.22 eV) could be detected (Figures 15, 16, 17), many for the first time in the atmosphere, especially clusters with N_2, O_2, and CO_2 ligands. The discovery of these clusters had a major impact on our understanding of the D-region positive ion chemistry. It was recognized that cluster formation via N_2-, O_2-, and CO_2-clustering is important and accelerates the buildup and growth of clusters, especially at low mesospheric temperatures. It was recognized that D-region plasma densities must be rather temperature sensitive due to the strong temperature control of the conversion of molecular ions to cluster ions which recombine with electrons much faster than molecular ions (HUANG et al., 1978).

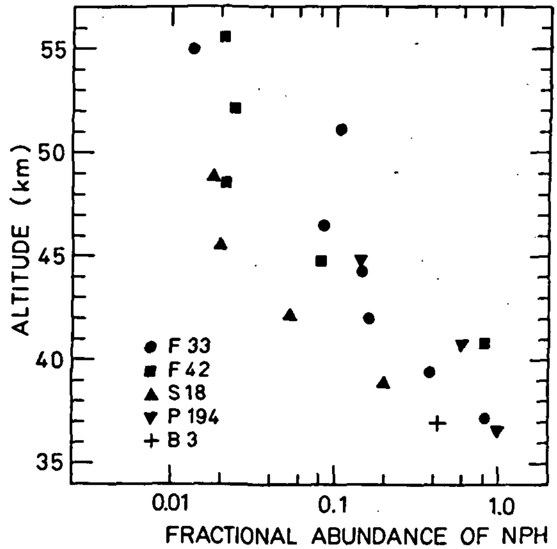

Figure 14. Measured profiles of positive ions (from ARNOLD et al., 1977).

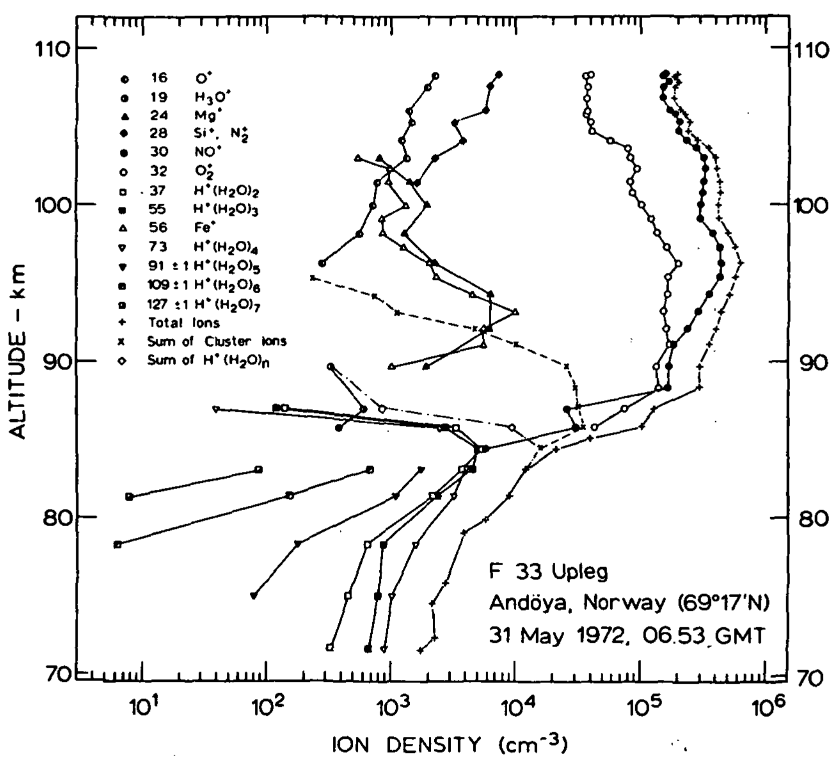

Figure 15. Positive cluster ion composition measurements obtained by using a sampling cone and a low draw-in potential (from ARNOLD and KRANKOWSKY, 1974).

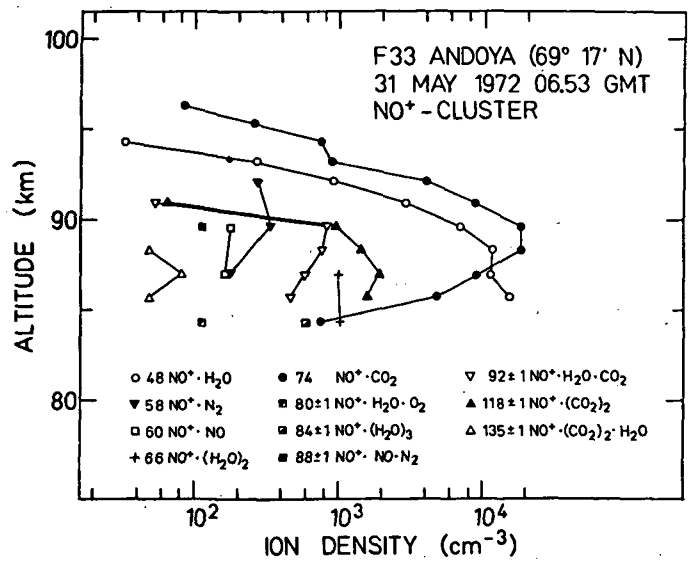

Figure 16. Positive cluster ion composition measurements obtained by using a sampling cone and a low draw-in potential (from ARNOLD and KRANKOWSKY, 1974).

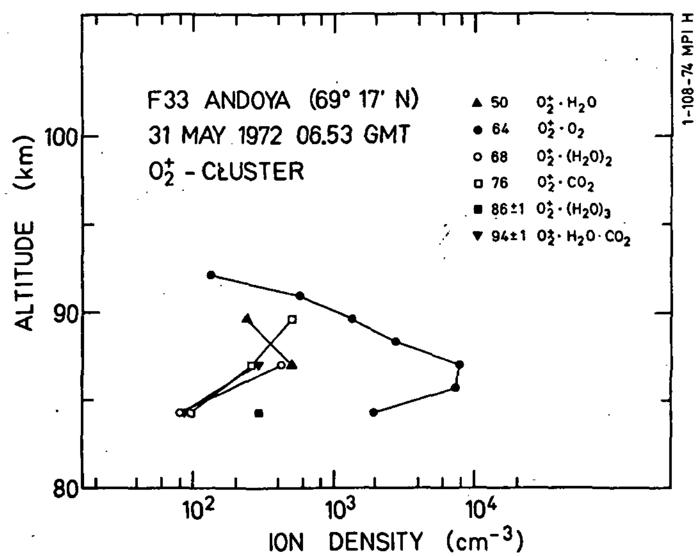

Figure 17. Positive cluster ion composition measurements obtained by using a sampling cone and a low draw-in potential (from ARNOLD and KRANKOWSKY, 1974).

Besides this information, the flight of May 1972, offered also other new insights regarding trace gas determination from ions. Thus, water vapor (Figure 18) (ARNOLD and KRANKOWSKY, 1977) and for the first time also H_2O_2 (Figure 19) (ARNOLD and KRANKOWSKY, 1974) could be inferred from the positive ion composition. The sampling cone techniques has now been adopted by all other groups.

The MPIK instrument was further modified. Use of a small quadrupole (rod diameter: 0.46 cm; rod length: 115 cm) and a lower RF-frequency w (1.4 MHz) allowed extension of the mass range up to 720 amu which has led to detection of particularly heavy ions (ARNOLD and JOOS, 1979). Furthermore, a fly-through electron impact ion source for combined ion and neutral gas composition measurements (Figure 8) was included. Thus, the concentration of oxygen atoms which are important for both the positive and negative ion chemistry could be measured nearly simultaneously with the ions (Figure 20) (ARNOLD et al., 1977).

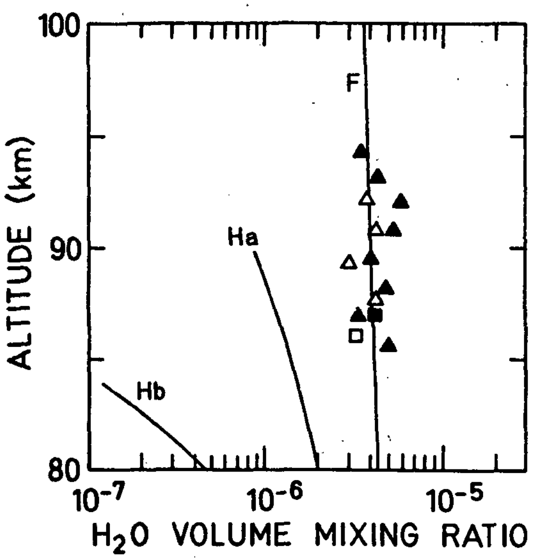

Figure 18. Water vapor abundances as inferred from positive ion composition measurements (ARNOLD and KRANKOWSKY, 1977).

The UB magnetic sector instrument has also been modified for negative ion measurements. Their first negative ion composition measurement which took place in 1979, provided high mass resolution negative ion data, which, however, are not yet published and therefore, cannot be discussed here.

Further progress in instrument development was made with the flight of an MPIK payload on August 13, 1978, specifically tailored for combined positive and negative ion composition studies in noctilucent clouds (BJORN and ARNOLD, 1981). The instrument was equipped with a liquid neon-cooled cryo condensation pump which, for purposes of a rocket measurement, offered practically the same pumping efficiency as the liquid helium-cooled pump, but had a standing time of about 10 hours. The latter was very helpful since some atmospheric phenomena such as noctilucent cloud events are rare and the rocket must be prepared for flight and remain in a standby position about 10 minutes prior to launch. Other interesting features of this instrument were a large mass range (1-720

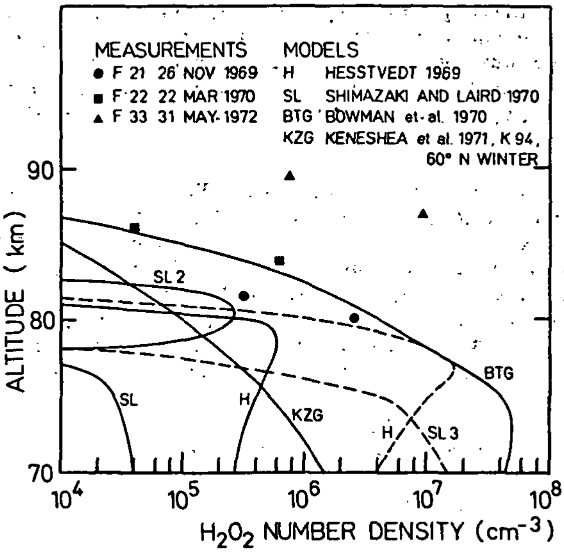

Figure 19. First hydrogen peroxide (H_2O_2) measurements in the atmosphere as obtained by passive chemical ionization mass spectrometry (ARNOLD and KRANKOWSKY, 1974).

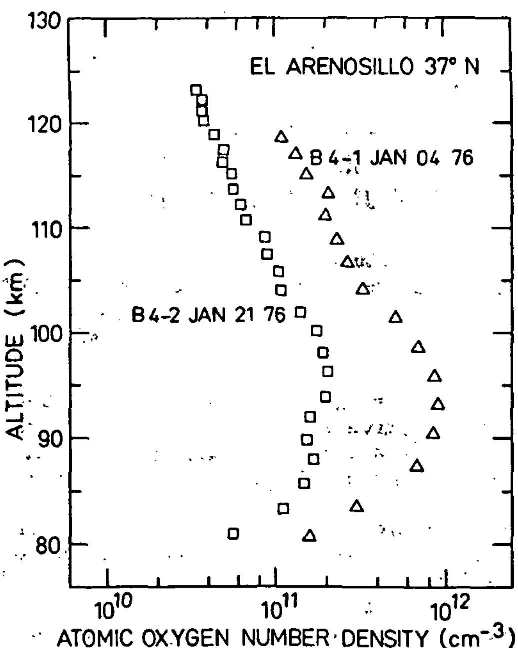

Figure 20. Atomic oxygen measurements as obtained by the combined ion and neutral gas composition mass spectrometer (from ARNOLD and KRANKOWSKY, 1977).

amu), a variable inlet hole (0.5 and 0.2 cm), and a very rapid scan (0.25 S for the entire mass range). The short scan time was used to achieve an altitude resolution of about 250 m. This is required to probe a noctilucent cloud layer which may have a thickness of only one kilometer. The change of the inlet hole was accomplished by using a movable sampling cone with an inlet hole of 0.2 cm sitting on top of a conical sampling electrode carrying an inlet hole of 0.5 cm. An O-ring seal was employed between the movable and the fixed cones. During ascent at 75 km, the movable cone was swung to the side thereby, exposing the 0.5 cm inlet hole. During descent at the same height, the operation was reversed. Thus, a large sensitivity at the lower heights where a smaller inlet hole is required to avoid ion scattering inside the mass analyzer.

In fact, a thin layer of very massive positive ions, mostly $H^+(H_2O)_n$ clusters with n up to 21, could be detected in the noctilucent cloud flight of August 13, 1978, around 90 km altitude (Figure 21) (BJORN and ARNOLD, 1981). Besides these, also very massive negative ions were detected. Even better heavy ion data, however, were obtained in the same year (1978) by the MPIK group using the same type of instrument (ARNOLD et al., 1982; ARNOLD and VIGGIANO, 1982). Interestingly, the noctilucent cloud experiment represented the first case of an almost simultaneous flight of the MPIK instrument and the UB magnetic sector instrument. The flight of the UB instrument which took place about 20 minutes after the MPIK flight provided high resolution data on positive ions allowing unambiguous identification of the ions in the heavy positive ions layer at 90 km as $H^+(H_2O)_n$ clusters. However, the sensitivity and the mass range of the UB instrument were lower than those of the MPIK instrument. Furthermore, the height resolution was also lower. Thus, the UB instrument was capable of detecting $H^+(H_2O)_n$ clusters only up to n = 12 (see Figure 21).

Further developments have included an ion mass spectrometer rocket payload which contained two ion mass spectrometers equipped with liquid neon-cooled cryopumps. This payload was used in a noctilucent cloud campaign on August 3,

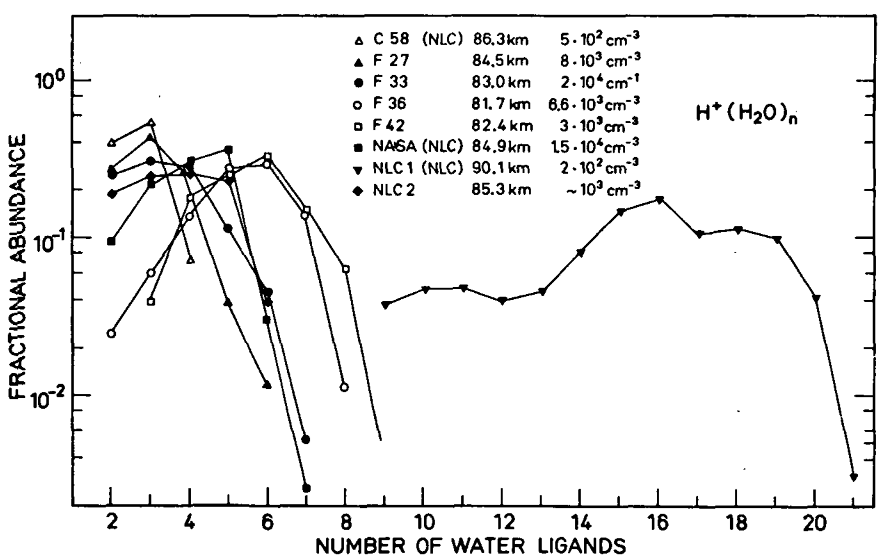

Figure 21. Detection of a thin layer of very massive cluster ions at the cold arctic mesopause during the 1978 noctilucent cloud campaign (from BJORN and ARNOLD, 1981).

1982 (SCHULTE and ARNOLD, 1985). The two instruments had different objectives and measuring programs. One measured negative ions with a very large mass range 1-800 amu and a high altitude resolution using the total throughput mode. In this mode, it was intended to achieve the maximum possible ion transmission of the instrument and thereby the maximum possible sensitivity, especially at higher masses. Furthermore, it was expected that a large variety of heavy negative ion species would be present, in which case partial concentrations of individual species would be rather small. Thus, many of these species may have fallen below the detection limit of the instrument. By integrating over all of these ion species (integral mode), however, many species may become detectable. The second instrument measured positive and negative ions using resolving modes so that actually simultaneous positive and negative ion composition measurements were made for the first time. A thin layer of very massive negative ions was detected around 82 km (Figure 22). It was suggested that these may represent negatively charged microclusters or microaerosols of meteoric origin formed by electron attachment to "meteor smoke" particles originally proposed by HUNTEN et al. (1980).

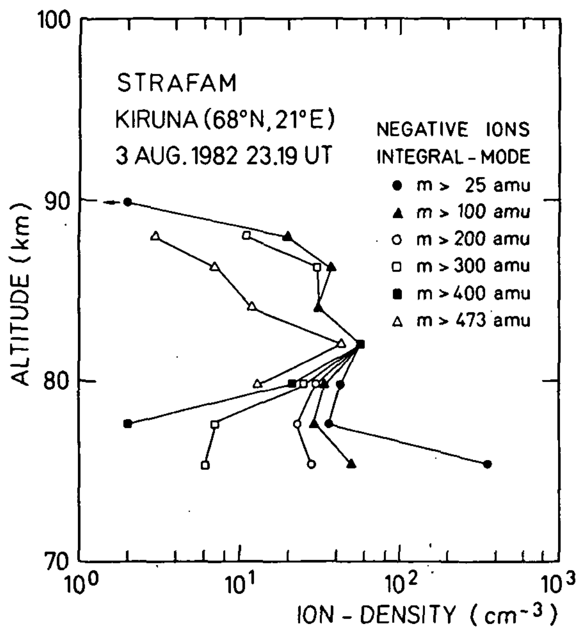

Figure 22. Detection of a layer of very massive negative ions around 90 km (from SCHULTZ and ARNOLD, 1985).

A new parachute-borne drop-sonde mass spectrometer payload (PFEILSTICKER and ARNOLD, 1984) has also been developed and was flown on January 31, 1984. The payload was equipped with two ion mass spectrometers and carried by a single-stage rocket to an altitude of 58 km. During ascent at 55 km, the parachute was deployed (Figure 23) and measurements commenced. Continuous measurements were made between 50 km on ascent to 35 km on descent. The angle of attack of the payload was mostly less than 30 degrees and the payload velocity was always subsonic during the measuring period. Ion composition data were obtained between 58 km and 35 km. These represent the first detailed ion composition data in the stratosphere region above balloon heights and below about 60 km. Most striking results are the high sensitivity for ion detection

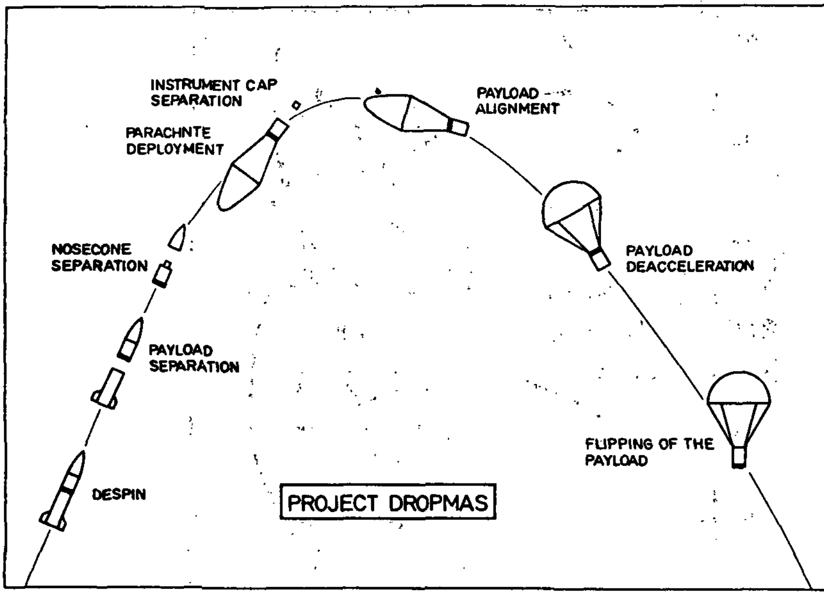

Figure 23. Schematic representation of the flight operations of the parachute-borne drop-sonde ion mass spectrometer payload (Project "DROPMAS") of the MPIK group (from PFEILSTICKER and ARNOLD, 1984).

(detection limit around 55 km: about 0.1 ions per cm^3) and the very weak cluster ion fragmentation. This is clearly demonstrated by Figure 24. Here the measured $H^+(H_2O)_n$ clusters are compared with equilibrium model calculations using actually measured temperatures. At heights below about 50 km, the most prominent proton hydrate observed is $H^+(H_2O)_4$, consistent with the model. Above 50 km, $H^+(H_2O)_3$ becomes most prominent which also agrees well with the model. However, lighter proton hydrates, in particular H_3O^+, are always overrepresented suggesting that some breakup is still occurring. However, this remaining breakup is not stronger than expected for balloon-borne measurements (ARNOLD et al., 1981).

Most recently, a second flight of the parachute-borne drop-sonde mass spectrometer payload equipped with a greatly improved quadrupole mass spectrometer providing much better mass resolution was carried out on May 14, 1985, over Kiruna. Again the measurements included both positive and negative ions but covered a larger altitude range (28 to 58 km). A typical positive ion mass spectrum as obtained between 37 and 43 km is shown in Figure 25. The width of a mass peak at half peak amplitude is about 1.5 amu which is comparable to the best spectra obtained by balloon-borne ion mass spectrometers (full scan mode). The ions detected include $H^+(H_2O)_n$ with n = (19), 2 (37), 3 (55), and 4 (73), as well as $H^+(CH_3CN)_1(H_2O)_m$ ions with 1 equal to 1 and m equal to 0 (42), 1 (60), 2 (78), and 3 (96). Besides these ions, clusters with 1 = 2 and m = 0 (83) and m = 1 (101) are also present.

The results of this flight are particularly encouraging since they prove that the new technique has the potential not only to complement but even to compete with balloon-borne ion composition measurements.

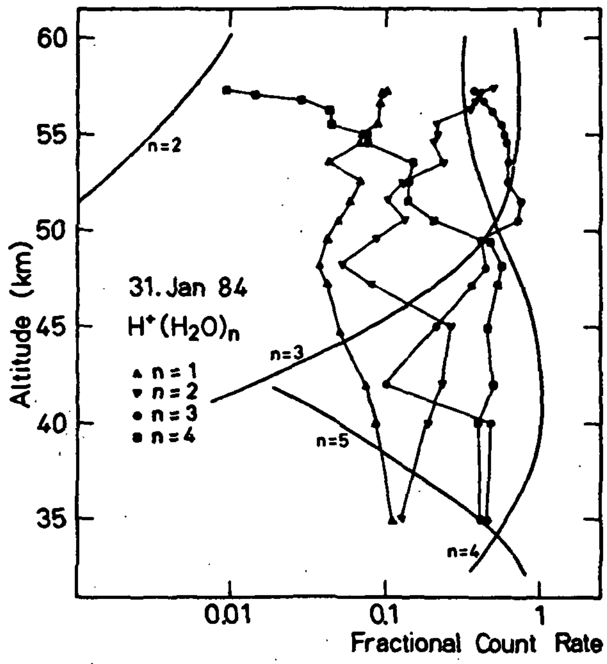

Figure 24. Stratospheric proton hydrates as measured during the first flight of the parachute-borne mass spectrometer ("DROPMAS") of the MPIK group (from PFEILSTICKER and ARNOLD, 1984).

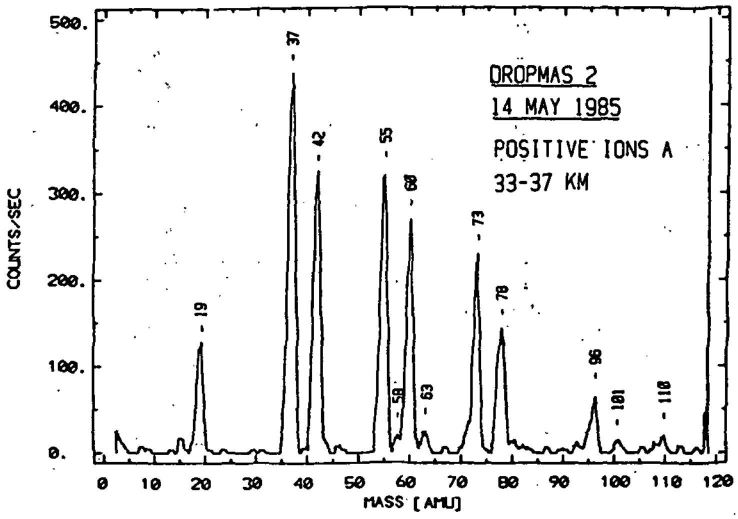

Figure 25. Positive ion mass spectrum as obtained on the second "DROPMAS" flight using a greatly improved mass spectrometer (MOHLER and ARNOLD, 1985).

4. SUMMARY AND OUTLOOK

During the last two decades, rocket-borne ion mass spectrometry has become a powerful tool for middle atmosphere ion composition studies and it has made a major contribution to our understanding not only of atmospheric ions but also of atmospheric trace gases and aerosols. An especially attractive aspect of this field of research appears to be analytical and diagnostic application of ion composition studies. Due to their close interaction with trace gases and aerosols, ions can serve as a powerful tool for probing trace gases and microaerosols in the middle atmosphere. This possibility is particularly attractive for species which cannot be detected by other methods, as for example, various metals, Cl-atoms, H_2O_2, mesospheric and lower thermospheric water vapor, H_2SO_4, upper stratospheric HNO_3, CH_3CN, meteor smoke microclusters, noctilucent cloud microclusters, and several other species.

By far, most of these measurements have covered only the altitude range above 70 km. Most of these were concerned with positive ions and only very few succeeded in providing negative ion composition data. Thus, our understanding of positive ions and their underlying processes at heights above 79 km is much better developed than that of negative ions. A major reason for the comparably poor knowledge of negative ions is that these are much more difficult to measure. First of all, they become prominent only at heights below about 80 km (night) to 70 km (day), where total ion concentrations usually become small (lower than 1000 cm^{-3}) and where the higher atmospheric gas pressures severely complicate mass spectrometer measurements. Another problem arises from the very large masses (several hundred amu) and the large variety of species of negative ions existing above 80 km, therefore, requiring particularly sensitive ion mass spectrometers with a very large mass range.

Below about 70 km and above about 33 km, the composition of both positive and negative ions to date is only poorly explored. The region above 33 km has not been accessible to most balloon-borne ion mass spectrometer measurements, and previous rocket-borne measurements using ballistic rockets have usually provided good data only above 70 km. Below this height, the rocket-borne measurements severely suffered from poor sensitivity and dramatic cluster ion breakup. Only very recently has it become possible to extend high quality ion mass spectrometer measurements into the region below 70 km using a unique parachute-borne drop-sonde ion mass spectrometer method. This method has opened a new altitude region and should, in the future, have the potential to explore the entire region between about 30 and 70 km.

As far as the altitude region above 70 km is concerned, future ion research should focus on negative ions, particularly on the heavy negative ion layer around 82 km. Here, improved instruments with high sensitivity, mass range, and altitude resolution are required. Certain aspects of positive ions above 70 km still are of great interest, especially positive ions containing meteoric species as for example, sodium. Another interesting field is positive ion clustering under conditions of low mesopause temperatures and the related question of ion-induced nucleation at the mesopause. Studies of these phenomena again require instruments with a large sensitivity, mass range, and altitude resolution.

In view of the above scientific objectives for rocket-borne ion composition studies in the middle atmosphere, the following future trends in instrumental development emerge: one line of action should be an extension of measurements towards altitudes below 70 km using parachute-borne drop-sonde ion mass spectrometers. Another trend should be the development of instruments for studies of minor ion species existing above 70 km. These should have an improved sensitivity, mass range and altitude resolution. To achieve a maximum height resolution, magnetic mass spectrometers equipped with a multiple

detector system, ideally a channelplate detector, would be suited since these allow to detect ion species of different mass simultaneously. However, the focussing efficiency of such instruments has to be improved to reach a higher sensitivity.

In summary, it therefore appears that a new era in middle atmosphere rocket-borne mass spectrometry has begun, and this field of research will remain exciting and productive during the years to come.

REFERENCES

Arijs, E., J. Ingels, and D. Nevejans (1978), Mass spectrometric measurement of the positive ion composition in the stratosphere, Nature, 271, 642.

Arnold, F. (1971), Mass spectrometric measurements of positive and negative ions in the lower ionosphere, Thesis, Universitat Heidelberg.

Arnold, F. (1980), Middle atmosphere ionized component. Proc. ESA-PAC Symposium on european rocket & balloon programmes and related research, Bournemouth, U.K., ESA SP-152, 479.

Arnold, F., W. Berthold, B. Betz, P. Lammerzahl, and J. Zahringer (1969), Mass spectrometer measurements of positive ions and neutral gases between 100 and 233 km above Andoya, Norway, Space Res., 9, 256.

Arnold, F., H. Bohringer, and G. Henschen (1978), Composition measurements of stratospheric positive ions, Geophys. Res. Lett., 5, 653.

Arnold, F., and R. Fabian (1980), First measurements of gas phase sulfuric acid in the stratosphere, Nature, 283, 55.

Arnold, F., R. Fabian, G. Henschen, and W. Joos (1980), Stratospheric trace gas analysis from ions: H_2O and HNO_3, Planet. Space Sci., 28, 681.

Arnold, F., and G. Henschen (1978), First mass analysis of stratospheric negative ions, Nature, 257, 521.

Arnold, F., G. Henschen, and E. E. Ferguson (1981), Mass spectrometric measurements of fractional ion abundances in the stratosphere - positive ions, Planet. Space Sci., 29, 185.

Arnold, F., and W. Joos (1979), Rapid growth of atmospheric cluster ions at the cold mesopause, Geophys. Res. Lett., 6, 763.

Arnold, F., J. Kissel, D. Krankowsky, H. Wieder, and J. Zahringer (1971), Negative ions in the lower ionosphere: a mass spectrometric measurement, J. Atmos. Terr. Phys., 33, 1169.

Arnold, F., and D. Krankowsky (1971), Negative ions in the lower ionosphere: a comparison of a model computation and a mass spectrometric measurement, J. Atmos. Terr. Phys., 33, 1693.

Arnold, F., and D. Krankowsky (1974), Measurements of $H_2O_2^{\ 2}$ in the D region and implications for mesospheric H_2O_2, Geophys. Res. Lett., 1, 243.

Arnold, F., and D. Krankowsky (1974), A new concept for the D-region ion chemistry as inferred from a mass spectrometer measurement, Proc. Int. Symp. on Solar-Terrestrial Physics, Cospar, 30.

Arnold, F., and D. Krankowsky (1977), Ion composition and ion-electron loss processes in the earth's atmosphere, in, Dynamic and Chemical Coupling of the Neutral and Ionized Atmosphere, edited by B. Grandal, J. A. Holtet, D. Reidel Dordrecht-Holland, 93-127.

Arnold, F., and D. Krankowsky (1977), Water vapor concentrations at the mesopause, Nature, 268, 218.

Arnold, F., D. Krankowsky, and K. H. Marien (1977), First mass spectrometric measurements of positive ions in the stratosphere, Nature, 267, 30.

Arnold, F., D. Krankowsky, K. H. Marien, and W. Joos (1977), A mass spectrometer probe for composition and structure analysis of the middle atmosphere plasma and neutral gas, J. Geophys., 44, 125.

Arnold, F., A. A. Viggiano, and E. E. Ferguson (1982), Combined mass spectrometric composition measurements of positive and negative ions in the lower ionosphere I. positive ions, Planet. Space. Sci., 30, 1295.

Arnold, F., A. A. Viggiano, and E. E. Ferguson (1982), Combined mass spectrometric composition measurements of positive and negative ions in the lower ionosphere II. Negative ions, Planet. Space. Sci., 30, 1307.

Bjorn, L., and F. Arnold (1981), Mass spectrometric detection of precondensation nuclei at the Arctic summer mesopause, Geophys. Res. Lett., 8, 1167.

Blewett, J. P. (1952), Radial focussing in the linear accelerator, Phys. Rev., 88, 1197.

Bohringer, H., and F. Arnold (1979), Collisional dissociation of proton hydrates induced by an electric field-simulation of atmospheric ion sampling, in, Scientific Ballooning, edited by W. Riedler, Pergamon Press, 33.

Brasseur, G., A. de Rudder, and P. C. Simon (1983), Implication for stratospheric composition of a reduced absorption cross section in the Herzburg continuum of molecular oxygen, Geophys. Res. Lett., 10, 20.

Courant, E. D., M. S. Livingston, and H. S. Snyder (1952), The strong-focussing synchroton - a new high energy accelerator, Phys. Rev., 88, 1190.

Ferguson, E. E. (1971), D-region ion chemistry, Rev. Geophys. Space. Phys., 9, 997.

Ferguson, E. E., F. C. Fehsenfeld, and D. L. Albritton (1979), in, Gas Phase Ion Chemistry, edited by M. Bowers, 1, Academic Press.

Goldberg, R. A., and A. C. Aikin (1971), Studies of positive ion composition in the equatorial D-region ionosphere, J. Geophys. Res., 76, 8352-8364.

Goldberg, R. A., and A. C. Aikin (1973), Comet Encke: meteor metallic ion identification by mass spectrometer, Science, 180, 294-296.

Goldberg, R. A., and L. J. Blumle (1970), Positive ion composition from a rocket-borne mass spectrometer, J. Geophys. Res., 75, 133-142.

Heitmann, H., and F. Arnold (1983), Composition measurements of tropospheric ions, Nature, 306, 747.

Huang, C. M., M. Whitaker, M. A. Biondi, and R. Johnson (1978), Electron-temperature dependence of recombination of electrons with $H_3O^+(H_2O)_n$ -series ions, Phys. Rev., A, 18, 64-67.

Krankowsky, D., F. Arnold, H. Wieder, J. Kissel, and J. Zahringer (1972a), Positive ion composition in the ionosphere, Radio Sci., 7, 93.

Krankowsky, D., F. Arnold, H. Wieder, and J. Kissel (1972b), The elemental and isotopic abundance of metallic ions in the lower E region as measured by a cryogenically pumped quadrupole mass spectrometer, Int. J. Mass Spectrom, Ion Phys., 8, 379-390.

Mohler, O., and F. Arnold (1985), High resolution composition measurements of positive and negative ions around the stratosphere, IAGA/IAMAP Conference, Prague, August 5-17.

Narcisi, R. S. (1973), Mass spectrometric measurements in the ionosphere, in, Physics and Chemistry of Upper Atmosphere, edited by B. M. McCormac, D. Reidel Pub. Co., 171-183.

Narcisi, R. S., and A. D. Bailey (1965), Mass spectrometric measurements of positive ions at altitudes from 64 to 112 kilometers, J. Geophys. Res., 70, 3687-3700.

Narcisi, R. S., A. D. Bailey, L. Della Luca, C. Sherman, and D. M. Thomas (1971), Mass spectrometric measurements of negative ions in the D- and lower F-regions, J. Atmos. Terr. Phys., 33, 1147-1159.

Nicolet, M., and A. C. Aikin (1960), The formation of the D region of the ionosphere, J. Geophys. Res., 65, 1464-1483.

Paul, W., and M. Raether (1955), Das elektrische massenfilter, Zeitschr. F. Physik, 140 262.

Paul, W., H. P. Reinhard, and U. von Zahn (1958), Das elektrische massenfilter als massenspektrometer und isotopentrenner, Z. Physik, 1952, 143-182.

Pfeilsticker, K., and F. Arnold (1984), Middle atmosphere ion composition measurements using a novel parachute-borne dropsonde mass spectrometer method, 7th ESA Symp. on European rocket and balloon programmes and related research, Loen, Norway, May 5-11.

Schulte, P., and F. Arnold (1985), Detection of a heavy negative ion layer at the mesopause, Nature (submitted).

Zbinden, P. A., M. A. Hidalgo, P. Eberhardt, and J. Geiss (1975), Mass spectrometer measurements of the positive ion composition in the D- and E-region of the ionosphere, Planet. Space. Sci., 23, 1621-1642.

138 D6-46

N86-26731

178

7614

6. DC-PROBE MEASUREMENTS IN THE MIDDLE ATMOSPHERE

E. V. Thrane

Norwegian Defence Research Establishment
P O Box 25, N-2007 Kjeller, Norway

N6894375

ABSTRACT

Rocket-borne dc probes ~~have been~~ were used extensively to study the weakly ionized plasma in the lower ionosphere and upper stratosphere. Although based upon the same basic principle, the probes ~~have been~~ were used in many different forms to measure both ion and electron densities, as well as electron temperature, and in some cases, ion composition. In recent years, probes have been used successfully to study turbulence in the middle atmosphere. ~~This paper reviews~~ the most important electrostatic probe techniques are reviewed and ~~discusses~~ discussed the accuracy and sensitivity of the different instruments are illustrated with sample measurements. The theory for the collection of ions or electrons by means of such probes in a collision-dominated regime is complex and not well developed. Some of the theoretical difficulties will be pointed out briefly.

1. INTRODUCTION

The middle atmosphere is weakly ionized. The ratio of the concentration of ions and electrons to the concentration of neutral atoms and molecules ranges from about 1.0E-14 at 30 km to 1.0E-7 near the 100 km level. All through this region, collisions between the ionized species and the neutrals are important, in fact, below 90 km, the behavior of the weakly ionized plasma is very strongly influenced by forces in the nonionized air, such as winds, waves and turbulence. Thermal equilibrium prevails here between all species. Above 90 to 95 km, the close coupling between ions, electrons and neutrals gradually weakens, and plasma phenomena become important. The use of rocket-borne plasma probes to study the middle atmosphere poses many problems, both of a theoretical and experimental nature. Very sensitive instruments are needed to collect the few charged particles along the rocket trajectory. Furthermore, the complex flow patterns near a space vehicle in a collision-dominated regime make the interpretation of the collected current in terms of ambient plasma parameters difficult.

There are two kinds of plasma probes, the dc or electrostatic probe, which uses the electrostatic properties of the plasma, and the radio frequency probe, which exploits the high frequency complex impedance of a plasma. In this article, we shall discuss the most important types of dc probes and their use for studies of the middle atmosphere. Specifically excluded from this review are Gerdien condenser probes, which will be described in a separate chapter. The original Gerdien probe was a dc probe formed as a hollow cylinder with a central electrode. Such probes have been proven very useful for certain applications, particularly in the lowest part of the ionosphere. They have, however, some limitations. The air flow through the cylinder is, for example, very sensitive to the aspect of the probe in relation to the probe velocity through the medium.

We shall first review briefly the basic principles of the dc probe, and discuss some of the limitations in the interpretation of the results, before giving a survey of the most important types of probes, illustrated with sample results.

2. PRINCIPLES OF THE DC PROBE

The dc probe is basically a very simple device, consisting of one or more electrodes inserted as diagnostic tools into the plasma to be studied. The electrode is given a potential relative to a reference, and the current flowing from the plasma to the electrode is measured. The term dc or electrostatic probe is normally used in a sufficiently broad sense to allow a slow variation (i.e., on time scales much larger than any plasma wave phenomena) of the probe potential. Unfortunately, the theory describing the current to the probe is far from simple, and in particular, the theory of dc probes on space vehicles moving through the upper atmosphere is beset with difficulties. In the brief article, it is impossible to give an exhaustive review of the subject. The literature is very extensive, and reviews have been given by CHUNG et al. (1975), FOLKESTAD (1970), and YORK et al. (1982). Here we shall have to be content with a mere mentioning of the most important topics.

2.1 The Sheath Region

When the probe is inserted in a plasma, the plasma will in general be perturbed, and a region of unequal concentrations of positive and negative charges will form close to the probe, with a corresponding change in electrostatic potential. The charge separation and associated electric field is created and maintained by the thermal energy of the plasma. The transition ozone is called the sheath region. The extent of this region is often described in terms of the Debye length:

$$\lambda_D = 6.9 \sqrt{T_e/N_e} \quad \text{(cm)} \tag{1}$$

where T_e is the electron temperature in Kelvin and N_e is the concentration of free electrons measured in cm(-3). In this simple expression, the effect of ions (which have small mobilities) has been ignored. The Debye length only gives a rough indication of the thickness of the sheath. In general, the structure of the disturbed region varies widely with the plasma parameters, as well as with the applied potential and geometric form of the electrode. Figure 1 illustrates schematically the charge density distribution near a negatively biased electrode. Far from the body, the plasma is almost neutral, the electric field is weak and the electrons and ions drift under the influence of ambipolar diffusion. At smaller distances, the imbalance between the ion and electron concentrations gradually builds up. Close to the surface of the probe, there may be an ion sheath, which is almost totally devoid of electrons.

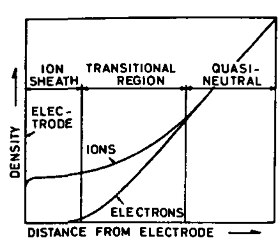

Figure 1. Schematic illustration of the charge density distribution near a negative electrode.

2.2 Equilibrium Potential of a Space Vehicle

In most applications of probes in the upper atmosphere, the space vehicle itself provides the return electrode in the probe circuitry. The impedance of the vehicle relative to the plasma will therefore influence the measurements. If the voltage of the probe varies slowly (in the sense discussed earlier), one

may assume that the spacecraft is at an equlibrium potential. This means that the current balance equation reads:

$$I_e + I_- + I_+ + I(\text{secondary}) = 0 \qquad (2)$$

where I_e, I_- and I_+ are currents due to electrons, negative and positive ions, respectively. There may also be a contribution I(secondary) due to secondary emissions of various types.

The current return problem becomes particularly important when the electrode potential is varied, and a constant reference potential is needed. This problem has been discussed in the literature by, for example, BOYD (1968) and WILLMORE (1965). A practical way to solve the problem is to construct electrodes with areas which are small compared to the surface area of the spacecraft. Required surface ratios are of the order of 10E-3 to 10E-4. It will be of interest for the subsequent discussions, to consider briefly the current-voltage characteristic of a probe, as shown schematically in Figure 2. The effective impedance of the plasma to the spacecraft is defined by the derivative of the current-voltage characteristic and depends upon how the equlibrium potential is established.

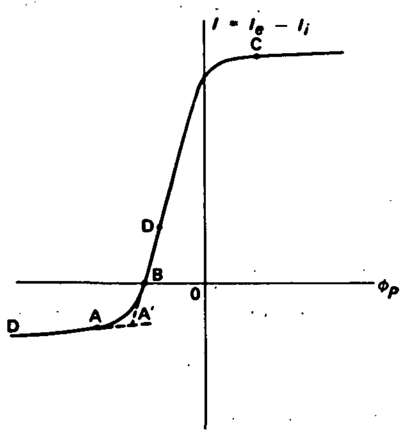

Figure 2. Typical current-voltage (CV) characteristic curve for single probe operation.

The qualitative behavior of the curve in Figure 2 may be explained as follows: for large negative values of the probe potential, all electrons in the vicinity of the probe are repelled from it, and the probe collects an ion current, determined by natural ion diffusion. When the voltage is made less negative, the most energetic electrons in the plasma will reach the probe and contribute to the current. At the point B, the electron and ion currents balance, and the net current is zero. This point is called the floating potential, and is negative with respect to the plasma. As the probe potential changes towards still smaller negative values, the probe attracts more electrons and the current rises sharply. If the electron energy distribution is Maxwellian, the rise will be exponential and the electron temperature may be derived from the slope of the curve. Finally, after the probe potential has become positive with respect to the plasma, the electron current will reach a saturation value Ies, determined by electron diffusion to the probe. The plasma potential is defined as the potential at which the current voltage characteristic has a kink, or a knee, at the top of the exponential part of the curve. In practice, the plasma potential is often difficult to determine because the measured transition from the steep slope to the saturation region is gradual.

The dc probes launched on sounding rockets may be operated at fixed or sweeping probe potentials, and the choice of fixed potential determines whether ion or electron current is measured. A sweeping probe can, when high time resolution is sacrificed, measure the current-voltage characteristic, so that in principle both ion and electron saturation currents, as well as electron temperatures, are measured. In the next section, we shall discuss some factors which determine the current collection efficiency of rocket-borne probes, with emphasis on problems encountered in the middle atmosphere.

2.3 Factors Influencing DC-Probe Measurements in the Middle Atmosphere

The environment encountered by a rocket-borne dc probe is very different from the idealized situation in which the probe is inserted into a stationary, homogeneous and isotropic plasma. Several factors have important consequences for the interpretation of the measurements:

During its flight, the probe may be exposed to electromagnetic and particle radiation which may cause secondary emission from the probe surface. Solar ultraviolet radiation with energies exceeding the work function of the probe surface material will thus cause emission of electrons from the surface. In order to minimize this effect, a material with a high work function, such as gold or nickel, is preferable, but other factors may determine the ultimate choice of material. The bombardment of the probe surface by precipitating energetic electrons and protons is particularly important in the auroral regions. The effect on the equilibrium potential is difficult to assess, but significant disturbances may occur during intense auroral events (FOLKESTAD, 1970).

One of the most vexing problems in probe application is the difficulty in ensuring that the probe has a clean uniformly conducting metallic surface. The surface may be easily contaminated, both before and during the flight, by oxidation or deposits of materials that may change the work function in an unpredictable manner. Such contamination may change completely the properties of the probe. A practical solution to this problem is to cover the probe surface with aquadag, an emulsion of carbon particles, which creates a uniformly conducting surface layer. In some experiments the probe surface is exposed to the air during the rocket launch, and the aerodynamic heating during the flight through the lower atmosphere can efficiently clean the surface. Another approach, used by ARNOLD et al. (1977) is to keep a carefully cleaned probe sealed in vacuum before and during launch, and to expose it to the atmosphere where the measurements start, near 60 km altitude. In general, there are no completely satisfactory solutions to the surface contamination problem.

For sounding rockets, the flight velocity V_r is always much smaller than the thermal velocity V_e of the electrons, so that the probe may, to a first approximation, be considered stationary with respect to the free electrons in the plasma. On the other hand, a sounding rocket moves faster than the thermal velocity V_i of the ions. A rocket with its apogee near 100 km, that is at the top of the middle atmosphere, will travel with a velocity which varies from a few times V_i to $V_r \sim V_i$ near apogee. As a consequence, the ion capture efficiency and the rocket equilibrium potential will depend upon the magnitude of the velocity vector, the geometry of the rocket, and its orientation.

The ionospheric plasma is anisotropic due to the earth's magnetic field. The fact that the charged particles spiral along the field lines will diminish the effective capture area of the probe for electrons, whereas the ion collection is not significantly impeded (WHIPPLE, 1965). In the middle atmosphere, where collisions between charged particles and neutrals are important, such effects are, in practice, of minor significance.

The middle atmosphere is weakly ionized and the motions of the charged particles will, through collisions, be determined by the motions of the neutral molecules. Only at the top from about 95 km, will the free electrons and ions gradually lose their strong coupling to the nonionized air. The mean free paths of the atmospheric constituents and their relations to the Debye length and the probe dimension are, therefore, important in determining the flow conditions near the probe. The Knudsen number, $Kn = \lambda/L$ where λ is the mean free path of a neutral particle and L is the probe dimension, has been used on an empirical basis to distinguish between three different kinds of flow:

a) For $Kn < 0.01$ the body is in a continuum regime and a hydrodynamic description applies.
b) For $Kn > 10$ the body is in a free molecular low regime and kinetic theory may be used to describe the particle motions.
c) In the intermediate range $0.01 < Kn < 10$ there is a transition regime where no adequate flow description is available.

Unfortunately, in the mesosphere the probe dimensions are often of the same magnitude as the mean free paths, so that adequate flow description is difficult. In the stratosphere case a) normally applies.

Theories for probes in free molecular flows commonly require that $\lambda/\lambda_D \gg 1$ implying that a particle does not collide in the region where it is under the influence of the probe potential. Again, this criterion is not in general fulfilled in the middle atmosphere.

Figure 3 summarizes the typical numerical values of the length parameters just discussed in the ionosphere and middle atmosphere (FOLKESTAD, 1970). Probe dimensions in sounding rockets are normally of the order of a few centimeters to 15 cm. The figure clearly illustrates the following important features:

a) The upper limit for the continuum regime, as defined by $Kn < 0.01$, is normally between 80 and 50 km.
b) The condition $\lambda_D \ll L$ cannot be fulfilled in the middle atmosphere, which implies that the complex sheath region extends far into the plasma.
c) The electron gyroradius is of the same order as the probe dimension L, whereas the ion gyroradius is significantly larger than L.

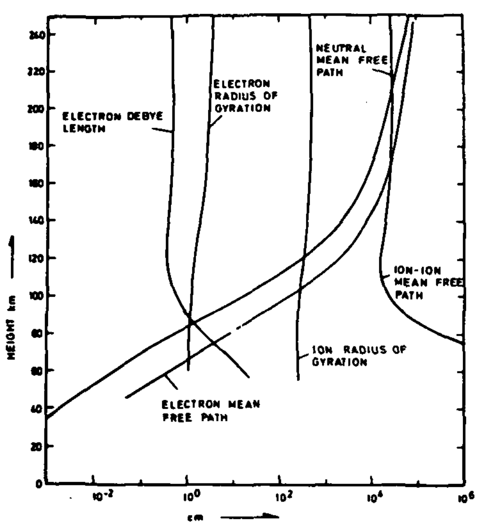

Figure 3. Typical numerical values of length parameters in the ionospheric plasma.

It is thus clear that a probe passing through the height region 30 to 100 km meets a variety of different operating conditions.

In addition to the factors discussed above, the aerodynamic effects add a new class of problems. A rocket reaching an altitude of 100 km or more travels at supersonic speed through most of the middle atmosphere. In the continuum regime, a shock front will form near the probe. From the previous discussions, we must expect that for a ballistic missile a shock front is unavoidable below 80 to 90 km. Behind the shock front, the air is compressed and heated, and due to the viscosity of the gas, large velocity gradients exist in a viscous boundary layer close to the probe surface. The form and extent of the shock region depend upon the geometry of the vehicle. A critical question is whether the ionization balance behind the shock is disturbed relative to the ambient plasma (see for example, the recent discussion by YORK et al., 1982). Typically, the pressure and temperature behind the shock may increase by factors of three to four, but the air will flow through the shock and pass the probe in a very short time interval, of the order of one millisecond. Nevertheless, it is possible that fragile species such as complex cluster ions may break up in the shock, and that this is a problem for mass spectrometry in the middle atmosphere. For measurements of total ion and electron density however, the assumption of "frozen chemistry" is believed to be a good approximation (SONIN, 1967). Parachute-borne probes have been successfully used to measure at subsonic velocities and thus avoid the shock effects. These probes will be discussed later.

From the above discussion, it should be obvious to the reader that the interpretation of middle atmosphere dc-probe measurements is not straightforward. Nevertheless, such techniques have yielded a great deal of very useful information which could not easily have been obtained by other means. Often, the difficulties may be solved by combining probe techniques with other types of measurements.

3. A SURVEY OF DC-PROBE TECHNIQUES

In this section, we shall discuss the most important probe techniques which have been used for middle atmosphere studies, illustrated with sample measurements.

3.1 The Langmuir Probe

The Langmuir probe technique measures the current-voltage characteristic of an electrode exposed to the plasma, by sweeping the voltage applied to the electrode. From each sweep of the type shown in Figure 2, the ion and electron saturation current as well as the electron temperature may, in principle, be derived. For a retarding potential, the electron current density, j, at the electrode is described by:

$$j = j_o \exp (eV/kT_e) \tag{3}$$

where V is the retarding potential. A semilogarithmic plot of j versus V will produce a curve where the slope in a certain interval is inversely proportional to electron temperature. With a positive (electron-accelerating) potential applied to the electrode, the current density to a small spherical electrode is given by:

$$j = j_o(1 + eV/kT_e) \tag{4}$$

When the probe is held at a constant positive potential, the current flowing to the electrode is proportional to the local electron density. It should be noted here that, because of all the complications described in the preceding

section, the constant of proportionality is difficult to determine in the middle atmosphere. It is therefore necessary to calibrate the probe measurements using other techniques, as discussed below.

The use of Langmuir probes in ionospheric rocket research dates back to the late 1940s (HOCK et al., 1953). A recent description of a modern probe of such a type is given by DURKIN and SMITH (1981). The basic block diagram of the system is given in Figure 4. Various types of electrodes have been used in practice, such as spherical and cylindrical probes mounted on booms or at the front of the rocket payload. A common configuration has been a conical electrode positioned at the tip of the rocket nose cone and insulated from the rocket body. ROSE and WIDDEL (1977) have flown "guard ring probes" of this type. SMITH (1969) has shown that the electron current collection efficiency of the conical electrode is sensitive to the orientation with respect to the earth's magnetic field. For the most recent probe DURKIN and SMITH have therefore chosen an ogival electrode, that is an electrode with a shape generated by a rotating circle segment. The probe voltage is swept from -1 V to +3 V, and the currents collected are in the range 1.0E-9 to 5.5E-5 Amps. These values are typical for Langmuir probes in the lower ionosphere. Durkin and Smith use different sweep modes during different parts of the rocket flight. Below 90 km, the probe voltage is held at a constant positive potential in order to achieve high resolution measurements of electron density, whereas a sweep rate of 10 Hz is used above 90 km to obtain electron temperature as well as electron density. The design of the electronic circuits is described in the report by Durkin and Smith. In general, electron temperatures in the middle atmosphere are too low to be measured accurately with this technique, and only density measurements are discussed in the present article. Figure 5 shows an example of electron-density profiles measured by the Langmuir-probe technique. It is common practice to combine the probe measurements with simultaneous measurements of Faraday rotation and differential absorption. The latter experiments provide absolute values of electron density and can resolve height structures of scales of the order of kilometers, that is with fairly poor height resolution. The probe on the other hand, can yield high resolution measurements and resolve scales of a few meters using the reasonable assumption that probe current is proportional to electron density over small height intervals (for example, 1-2 km). Such techniques have been employed by a number of authors (see for example: MECHTLY et al., 1972; MECHTLY and SMITH, 1970; FOLKESTAD, 1972; BENNETT et al., 1972; HALL, 1973). The accuracy of the electron densities obtained with the combined techniques has been discussed by THRANE (1974) and by MECHTLY (1974).

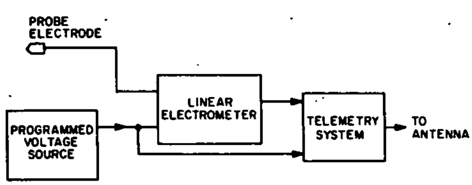

Figure 4. Block diagram for a Langmuir probe.

3.2 Screened Electrostatic Probes

The dc probes, with one or more grids between the plasma and the current collecting electrode, have been used to study both electron and ion densities in the lower ionosphere. The grids may serve several purposes, such as rejection of unwanted ambient particles, reduction of the effects of secondary emissions, and to make possible an analysis of the energy distribution of the constituents of the plasma.

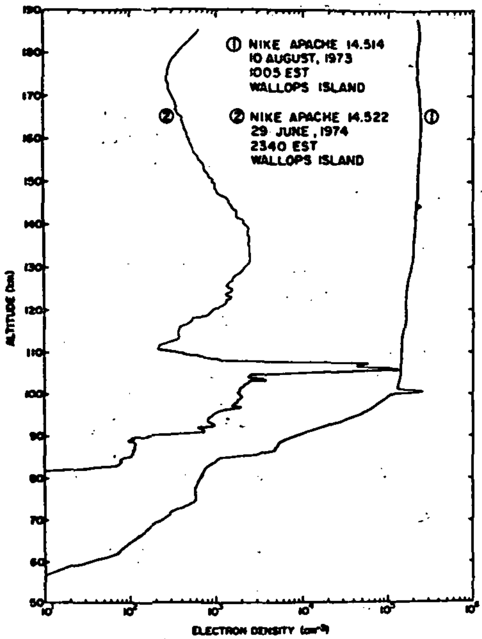

Figure 5. Electron-density profiles obtained with the Langmuir probe technique.

Plane-gridded analyzers have been described in the literature by, for example, WHIPPLE and PARKER (1969) and reviewed by BOYD (1968). Here we shall briefly discuss an experiment developed by SPENNER et al. (1977). Their instrument consisted of two retarding potential analyzers (RPA) mounted on double booms in sounding rockets launched during the European Winter Anomaly Campaign in 1975 (OFFERMANN, 1977). Figure 6 shows schematically the design of their probe, which has altogether 5 grids in front of a small plane collector. The large first grid and the guard ring surrounding the collector provide radially uniform particle flux about the sensor axis. The collector samples only electrons or ions from this uniform central region. With suitable potentials applied to the 5 grids, different kinds of charged particles can be sampled and analyzed. The experiment works in three different modes: a "temperature mode" which provides the electron temperature and the relative electron density, an "ion mode" providing the ion density, and a "photoelectron mode" which yields the energy distribution of suprathermal electrons. The experiment gave useful information on ion and electron density in the middle atmosphere down to about 90 km, although it was primarily designed for E-region studies.

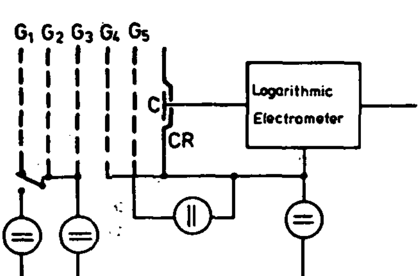

Figure 6. Schematic illustration of the design of a planar retarding potential analyzer (RPA).

Single grid spherical sensors have been used successfully both to measure ion and electron densities below 100 km. Figure 7 shows a schematic diagram of this type of probe. Because of its simple geometry, the theory is better developed than for many other configurations (SAGALYN et al., 1963; FOLKESTAD, 1970). The sensor is normally operated under saturation conditions, that is, the collector bias is sufficiently large (positive or negative) so that all particles of the wanted polarity passing through the grid are drawn to the collector, and charges of the opposite polarity are all rejected. A simple probe of this type, designed to measure positive ion density in the D region, has been described by FRIEDRICH et al. (1977). They use a negative bias voltage on the collector of -22.5 V, whereas the grid is at rocket body potential. The block diagram for the instrument is shown in Figure 8. A multirange electrometer measures currents in the range 2E-10 to 2E-7 A. The ion current is a function of the rocket velocity, the ion temperature and the effective cross section of the probe.

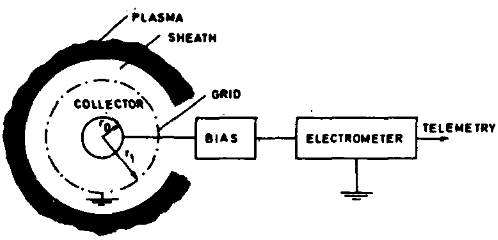

Figure 7. Single grid spherical probe.

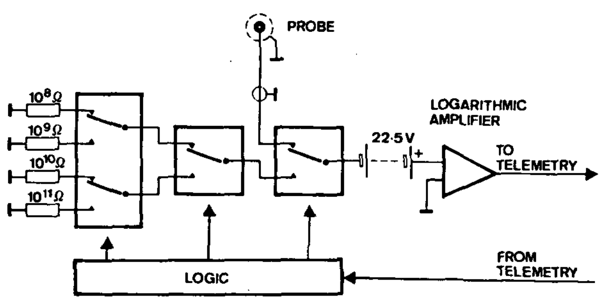

Figure 8. Block diagram of constant voltage positive ion probe (FRIEDRICH et al., 1977).

Figure 9 shows an example of measured nighttime ion densities, normalized to the absolute values of electron density at heights above 80 km. The height variation of N_i from the probe and N_e from the Faraday rotation measurements are very similar above 80 km, justifying the normalization. The discrepancy below 80 km is, at least partly, due to the presence of negative ions. Such a procedure is commonly used to derive $\lambda = N_-/N_e$, where N_- is the concentration of negative ions formed by attachment of electrons to neutral molecules (see for example, BJORN et al., 1979). Bearing in mind the problems discussed in Section 2.3, the values of N_- derived in this manner should be regarded with caution.

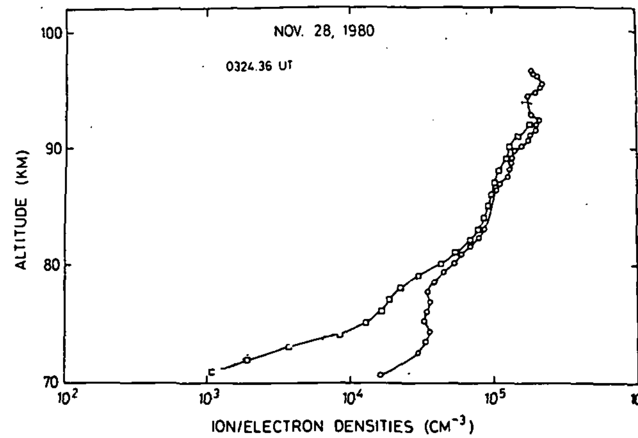

Figure 9. Nighttime positive ion and electron densities measured in the auroral zone, at Andoya Rocket Range.
o--o--o positive ion densities measured by a dc probe.
-- -- electron densities measured by the Faraday rotation and differential absorption technique.
The probe results have been normalized to the electron density at heights above 80 km (BREKKE et al., 1984).

3.3 Blunt Probes

During normal ionospheric conditions, the rocket techniques described above yield information about ion or electron densities down to altitudes of about 60 km. The ionospheric D region and the very interesting and photochemically complex region below 60 km, have been explored by means of "blunt probes" and by Gerdien probes. These probes are equipped with parachutes, and are released from sounding rockets in the upper D region. They fall at subsonic speeds through the lower D region (mesosphere) and stratosphere, thus avoiding the complicated effects associated with a shock front.

The blunt probe is a two-electrode instrument for measuring the bipolar conductivity of a weakly ionized plasma. The original instrument was designed at The Pennsylvania State University and is described by HALE et al. (1966). Figure 10 shows the instrument as deployed during flight (HALE, 1974). The collector is an aluminum disk surrounded by a guard ring held at the same potential as the collector, and the return electrode is the housing for the electronics and power supply. The configuration is insensitive to the angle of attack of the flow and to secondary emission from the collector due to solar ultraviolet radiation. The electronic circuits of the instrument have been described by MITCHELL (1973). A sweep voltage generator applies a known waveform between the two electrodes, and a sensitive electrometer measures the collected current. In this way, the conductivity of the surrounding plasma may be measured.

In a recent article, YORK et al. (1982) have discussed the ion and electron collection by blunt probes in the middle atmosphere. They conclude that blunt probes may be used with confidence to measure conductivities, but that there are difficult outstanding questions regarding the relationship of conductivity to charged particle concentrations. For ions, the question is whether fragile ion clusters exist which may break up in the vicinity of the

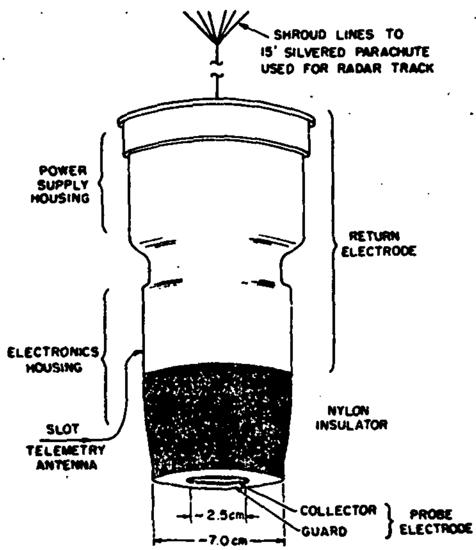

Figure 10. Parachute-borne blunt probe (HALE, 1974).

probe, thus altering the ion composition. If the collection process does not affect the ion composition, the positive ion density may be expressed as:

$$N_i = (\sigma_+/e\mu_{+o})\ (T_o\ p/T\ p_o) \tag{6}$$

where μ_{+o}, T_o and p_o are the mobility, temperature and pressure, respectively, reduced to sea level standard conditions. The conductivity is derived from the measurements as:

$$\sigma_+ = (R/2r_{col}{}^2)\ |dI_+/dV\ | \tag{7}$$

where R is the outer radius of the guard ring and r_{col} is the radius of the collector.

For electrons, the scaling is quite different, since the electrons have much higher drift velocities than the ions. Using a height dependent scaling, YORK et al. (1982) found reasonable agreement between the electron densities from the blunt probe and electron densities derived form Faraday rotation measurements and ground-based partial-reflection measurements. The comparison was possible for heights between 60 and 80 km; below 60 km, independent checks of the blunt probe electron densities are still missing. Figure 11 shows a set of measured conductivities, and Figure 12 shows a comparison between electron densities obtained by different methods. Note that the electron density derived from the blunt probe data is fairly constant between 70 and 50 km and then decreases with decreasing height.

3.4 Measurements of Turbulence in the Middle Atmosphere

In recent years, dc probes have proven useful in studies of fine structure and turbulence in the lower ionosphere. The role of neutral air turbulence in the energy budget of the middle atmosphere is not well known, and there is an urgent need to map the small-scale dynamical features in order to understand how heat and minor atmospheric constituents are transported. In the weakly ionized air below about 100 km, the lifetime of an ion against recombination is long compared to the lifetime of a turbulent eddy, and the ions may be used as

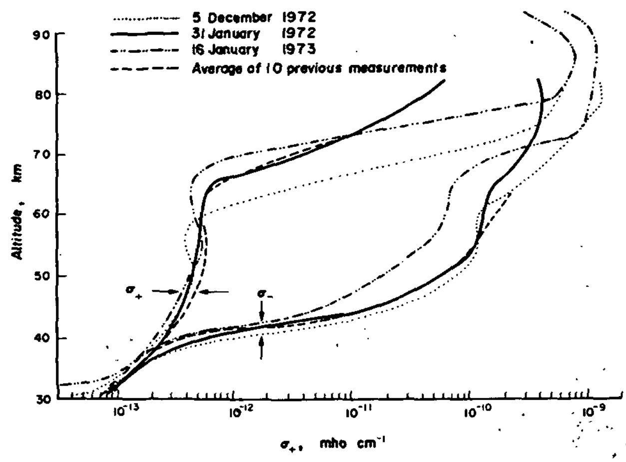

Figure 11. Variation of blunt probe conductivity measurements during winter conditions (YORK et al., 1972).

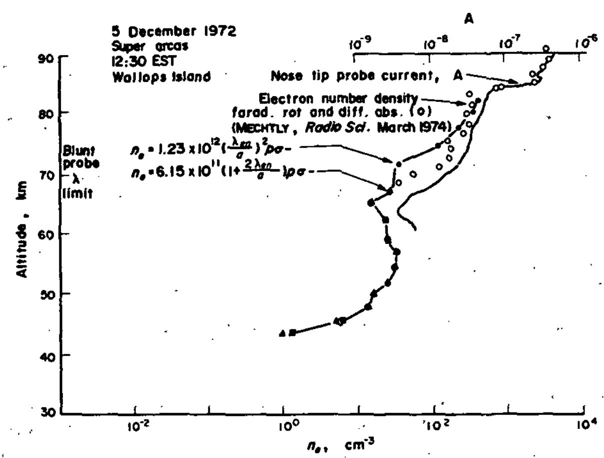

Figure 12. Comparison of height variations of electron density predicted from blunt probe measurements with electron densities from other techniques (YORK et al., 1982). The formulae indicated in the figure give the expressions used to derive electron densities from measured conductivities in different height ranges.

passive tracers for small-scale irregularities in the neutral gas. A rocket-borne dc probe, with its capability for high sampling rate of ion or electron current, therefore, offers unique opportunities for studies of such irregularities. Theoretical aspects of fluctuations in D-region ionization due to turbulence have been discussed in detail by HILL and BOWHILL (1976).

THRANE and GRANDAL (1981) and THRANE et al. (1985) have measured the fine scale structure of positive ion density with spherical, gridded dc probes. The instruments have been described by GRANDAL et al. (1981), and the electronics

by CHRISTENSEN (1981). The probe consisted of an inner spherical collector with diameter 11 cm, and an outer concentric spherical grid with diameter 12 cm (see Figure 13). The collector housed the 7 decade electrometer, power supply, PCM encoder and VHF telemetry transmitter. The collector was biased with -7 V with respect to the outer grid. The current was sampled every 0.5 ms and the measured value telemetered to the ground as 12-bit words.

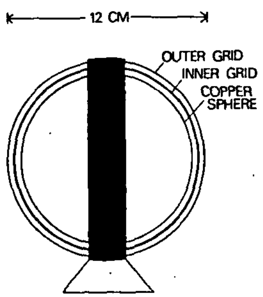

Figure 13. The mechanical design of the electrostatic probe used by THRANE et al. (1985). The inner grid serves as a collector and is biased by -7 V relative to the outer grid. The inner sphere houses the electronics. The two halves of the sphere are held together by a metal belt which is mounted on a base at the top of payload E4. For the rocket E1, the two free-flying probes have telemetry antennas mounted on the belt. (See text.)

Such probes were used in an experiment designed to measure the ion density at three points in space simultaneously (THRANE et al., 1985). This was achieved in the following way: Two rockets, code-named E1 and E4, were launched simultaneously. Rocket E4 carried a dc probe mounted at the top of the payload, and rocket E1 carried two probes which were released as dropsondes from the main E1 payload during the upleg part of the rocket trajectory. The two E1 dropsondes contained their own telemetry, but were otherwise identical to the E4 probe. The E1 probes were released sideways from the main payload near a height of 65 km and moved slowly away from the main payload during the rest of the flight. At the same time, the E4 payload followed a parallel trajectory a few km away in the horizontal direction. The three probes thus followed closely adjacent trajectories through the lower ionosphere, and at each height independent measurements of ion density were obtained at three points in space. The observations can be used to provide information about the horizontal as well as the vertical structure of irregularities in ion density. A detailed study of the cross correlation between the data from the three probes is in progress (T. Blix, private communication). Figure 14 shows an example of ion currents measured near 75 km with three probes.

Using the assumption of "frozen chemistry" and the fact that the probes moved through the medium at three times the thermal speed of the ions, a spectrum of spatial irregularities along the probe trajectory may be derived for each probe, for selected height intervals. The relation between probe current I and ion density N_i may be written:

$$I = e\, N_i\, \sigma_{eff} V_r \tag{8}$$

where e is the ionic charge, σ_{eff} is the effective probe cross section and V_r is the probe velocity. The difficulties in determining the effective current collection cross section may be overcome by considering not the absolute currents, but the fluctuations relative to a reference, for example a running mean. By differentiating (8) and assuming that σ_{eff} and V_r vary slowly with height, one obtains:

$$\Delta I/\langle I\rangle = \Delta N_i/\langle N_i\rangle \tag{9}$$

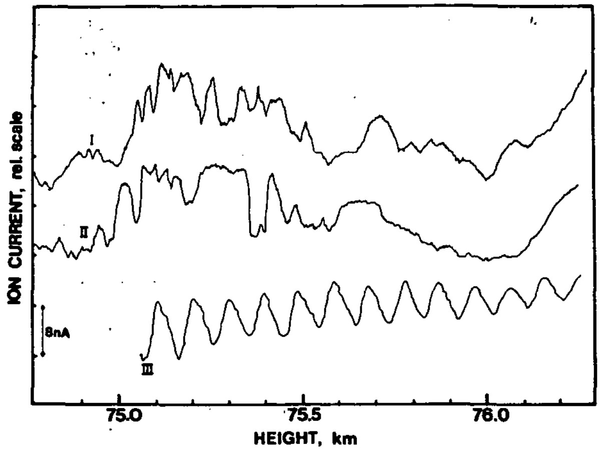

Figure 14. Example of simultaneous measurements of D-region fine structure in positive ion current by means of three probes (GRANDAL et al., 1981). The curves labelled I and II refer to dropsondes which are about 40 meters apart in the horizontal plane. The curve labelled III refer to a probe mounted on a rocket payload flying at a distance of 3.7 km from the two other probes. The regular oscillations observed by probe III are due to a spin modulation. The current values are relative, and the curves have been shifted along the vertical axis to keep them apart.

THRANE and GRANDAL (1981) have shown that for small height intervals, the fluctuation in neutral density is:

$$\Delta n/\langle n\rangle = F\ (\Delta N_i/\langle N_i\rangle \tag{10}$$

where the constant F is determined from the mean height variations of neutral gas density and temperature. Once the neutral density fluctuation intensity is known, information about the neutral air turbulence, such as eddy diffusion and energy dissipation rates, may be derived (THRANE et al., 1985). Figure 15 shows an example of the results of a Fourier analysis of probe data from a height interval of about 1 km (2048 data points). The basis for the spectrum is the curve labelled I in Figure 14. The dotted line in Figure 15 represents the slope of the spectrum, in this case represented with a spectral index of -2.5. The spectral index expected from theories describing isotropic and homogeneous turbulence is -5/3. Note that the spectral power is given as a function of frequency. Using the known probe velocity, the frequency scale may be translated into spatial scales of the irregularities, as indicated in the figure.

Several attempts have been made recently to study mesospheric irregularities with rocket-borne probes and ground-based radars simultaneously (THRANE et al., 1981; HOCKING and VINCENT, 1982; ROYRVIK and SMITH, 1984). The results are suggestive and interesting, and on the whole the use of dc probes for in situ studies of small-scale irregularities opens up a promising line of research, that yields information which is otherwise difficult to obtain.

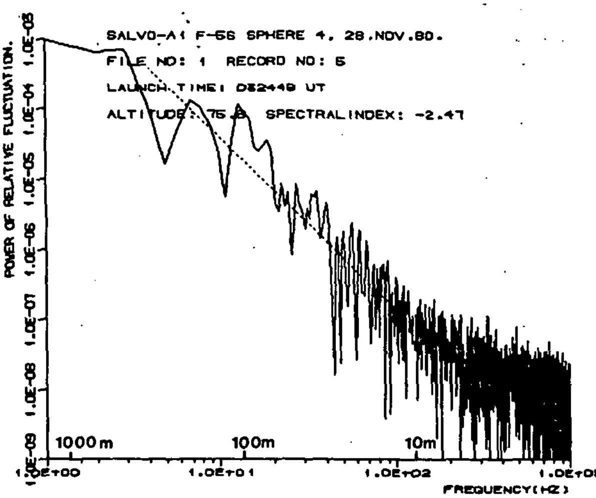

Figure 15. Power spectrum of ion density fluctuations derived from the curve labelled I in Figure 13. The spectrum is based on 2048 data points centered at 75.8 km. The frequency scale is obtained when the data string is regarded as a time series. Using the known probe velocity through the medium, the length scales may be derived (THRANE et al., 1984).

4. CONCLUSION

The aim of this review has been to demonstrate the versatility and usefulness, and also the limitations of electrostatic probes in middle atmosphere research. The main advantage of the dc probes is the simple experimental technique that allows the instruments to be launched on fairly small, inexpensive rockets. The disadvantages lie in the complex interpretation of the results and the present lack of adequate theories which can link the measured currents and conductivities to plasma densities. Both theoretical and experimental work are needed to solve the important outstanding problems. In particular, more information is needed about the very weakly ionized plasma in the stratosphere. Of the techniques discussed above, only the blunt probe and the Gerdien probe have provided data about ion and electron densities below 60 km, and these results need confirmation from independent experiments. From the point of view of synoptic studies, the presently available information about the middle atmosphere is scarce. Future developments of electrostatic probe theory and technique offer opportunities for filling some gaps in our knowledge of this interesting part of the earth's atmosphere.

Finally, it should be pointed out that the literature on probe theory and application is vast, and this brief review makes no claim to completeness or to do justice to all the important work which has been done. It is hoped, however, that the examples and references given here can provide a basis for further study for those not familiar with the field.

REFERENCES

Arnold, F., D. Krankowsky, K. H. Marien, and W. Joss (1977), A mass spectrometer probe for composition and structure analysis of the middle atmosphere plasma and neutral gas, J. Geophys., 44.

Bennett, F. D. G., J. E. Hall, and P. H. G. Dickinson (1972), D-region electron densities and collision frequencies from Faraday rotation and differential absorption measurements, J. Atmos. Terr. Phys., 34, 1321-1335.

Bjorn, L. B., F. Arnold, D. Krankowsky, B. Grandal, O. Hagen, and E. V. Thrane (1979), Lower ionosphere ion production, density and composition in an auroral absorption event, J. Atmos. Terr. Phys., 41, 1184-1194.

Boyd, R. L. F. (1968), Plasma Diagnostics, edited by W. Lochte-Holtgreven, North-Holland Publ. Co., Amsterdam, 732.

Brekke, A., O. Holt, P. H. G. Dickinson, M. Freidrich, T. Hansen, P. Stauning, and E. V. Thrane (1984), Development of D-region electron and ion densities under various auroral conditions during the energy budget campaign, J. Atmos. Terr. Phys., in press.

Christensen, R. (1981), A seven decade multirange electrometer for fine scale ion current measurements in the lower ionosphere, FFI/RAPPORT-81/7003, Norwegian Defence Research Establishment, Kjeller, Norway.

Chung, P. M., L. Talbot, and K. J. Touryan (1975), Electric probes, in Stationary and flowing plasmas: Theory and Application, Springer - Verlag, Berlin.

Durkin, C., and L. G. Smith (1981), A rocket-borne Langmuir probe for high-resolution measurement of the ionospheric electron temperature profile, Aeron. Rep.No. 95, Univ. Ill., Urbana.

Folkestad, K. (1970), Ionospheric studies by in situ measurements in sounding rockets, NDRE Rep. No. 59, Norwegian Defence Research Establishment, Kjeller, Norway.

Folkestad, K. (1972), Probe measurements of positive ions and electron temperatures in high latitude rocket flights, J. Atmos. Terr. Phys., 34, 1935-1939.

Friedrich, M., K. Torkar, and S. Ulrich (1977), A rocket borne experiment to measure plasma densities in the D-region, J. Geophys., 44, 91-98.

Grandal, B., R. Christensen, and E. V. Thrane (1981), An experiment designed to measure fine scale structure in the mesosphere and lower thermosphere, in, Sounding Rocket Program Aeronomy Project: Energy Budget Campaign 1980, Experiment Summary, edited by D. Offermann and E. V. Thrane, Forschungsbericht W 81-052, DFULR, Bundesministerium for Forschung and Technologie.

Hale, L. C. (1974), Positive ions in the mesosphere, in, Methods of Measurements and Results of Lower Ionosphere Structure, edited by K. Rawer, Akademie-Verlag, Berlin, 219-235.

Hale, L. C., D. P. Hoult, and R. G. Willis (1966), Preliminary results of rocket measurements of D-region ion density, in, Electron Density Profiles in Ionosphere and Exosphere, edited by J. Frihagen, North-Holland Publ. Co., Amsterdam, 108-115.

Hall, J. E. (1973), Lower ionosphere electron densities from rocket measurements employing LF radio propagation and dc probe techniques, Planet. Space. Sci., 21, 119-131.

Hill, R. J., and S. A. Bowhill (1976), Small-scale fluctuations in D-region ionization due to hydrodynamic turbulence, Aeron. Rep. No. 75, Univ. Ill., Urbana.

Hocking, W. K., and R. A. Vincent, A comparison between HF partial reflection profiles from the D-region and simultaneous Langmuir probe electron density measurements, J. Atmos. Terr. Phys., 44, 843-854.

Hok, G., N. W. Spencer, and W. G. Dow (1953), Dynamic probe measurements in the ionosphere, J. Geophys. Res., 58, 235-242.

Mechtly, E. A. (1974), Accuracy of rocket measurements of lower ionosphere electron concentrations, Radio Science, 9, 373-378.

Mechtly, E. A., S. A. Bowhill, L. G. Smith, and H. W. Knoebel (1967), Lower ionosphere electron concentration and collision frequency from rocket measurements of Faraday rotation, differential absorption, and probe current, J. Geophys. Res., 72, 5239-5245.

Mechtly, E. A., and L. G. Smith (1970), Changes of lower electron densities with solar zenith angle, Radio Science, 5, 1407-1412.

Mitchell, J. D. (1973), An experimental investigation of mesospheric ionization, Ionospheric Research, Scientific Report 416, The Pennsylvania State University.

Offermann, D. (1977), A study of the D-region winter anomaly in Western Europe, 1975/76, J. Geophys., 44, 1-13.

Rose, G., and H. U. Widdel (1977), Payload BI: a compact and economic D-region experiment package for use on small sounding rockets, J. Geophys., 44, 65-79.

Royrvik, O., and L. G. Smith (1984), Comparison of mesospheric VHF radar echoes and rocket-probe electron-concentration measurements, J. Geophys. Res., in press.

Sagalyn, R. C., M. Smiddy, and J. Wisnia (1963), Measurement and interpretation of ion density distribution in the daytime F region, J. Geophys. Res., 68, 199-211.

Smith, L. G. (1969), Langmuir probes in the ionosphere, in, Small Rocket Instrumentation Technique, edited by K. Rawer, North-Holland Publ. Co., Amsterdam, 1-15.

Sonin, A. A. (1967), Theory of ion collection by a supersonic atmospheric sounding rocket, J. Geophys. Res., 72, 4547-4557.

Spenner, K., W. Ott, and H. J. Bradenstein (1977), Plasma measurements during the western european winter anomaly campaign, J. Geophys., 44, 81-90.

Thrane, E. V. (1974), Ionospheric profiles up to 160 km: a review of techniques and profiles, in, Method of Measurements and Results of Lower Ionosphere Structure, edited by K. Rawer, Akademie-Verlag, Berlin, 1-21.

Thrane, E. V., O. Andreassen, T. Blix, A. Brekke, F. J. Schmidlin, H. U. Widdel, and U. von Zahn (1985), Neutral air turbulence in the upper atmosphere observed during the energy budget campaign, J. Atmos. Terr. Phys., in press.

Thrane, E. V., B. Grandal, T. Fla, and A. Brekke (1981), Fine structure in the ionospheric D-region, Nature, 292, 221-223.

Thrane, E. V., and B. Grandal (1981), Observations of fine scale structure in the mesosphere and lower thermosphere, J. Atmos. Terr. Phys., 43, 179-189.

Whipple Jr., E. C. (1965), NASA Report X-615-65-296, Goddard Space Flight Center.

Whipple Jr., E. C., and L. W. Parker (1969), Theory of an electron trap on a charged spacecraft, J. Geophys. Res., 74, 2962-2971.

Willmore, A. P., (1965), Probe techniques, in, High Latitude Particles and the Ionosphere, edited by B. Maehlum, Logos Press Lim, 21.

York, T. M., R. O. Olsen, J. D. Mitchell, and D. L. Mott (1982), Evaluation of electron and ion densities in the middle atmosphere from rocket-borne blunt probes, J. Atmos. Terr. Phys., 44, 257-266.

N86-26732 D7-46 188

7. ROCKET PROBE TECHNIQUES FOR MEASURING BULK ION PROPERTIES

J. D. Mitchell

Communications and Space Science Laboratory
The Pennsylvania State University
University Park, PA 16802

7615 P5478704

ABSTRACT

An overview of rocket probe techniques for measuring middle atmosphere ion properties is presented ~~in this paper~~. The measured parameters include conductivity, ion mobility and number density, all of which characterize the region's electrical structure. Particular consideration is given to the Gerdien condenser because of its capability to measure all three of these ion quantities. This probe ~~has been~~ was adapted for flight operation while either attached to a rocket or, more often, descending on a parachute. The use of a parachute potentially enhances the probe's measurement capabilities and also it lessens detrimental flow effects on ion collection.

From the brief presentation of measurement results, it is demonstrated that a variety of presently flown probe systems, both supersonic and subsonic, show general consistency in measuring conductivity; and, in fact, they occasionally have been combined to enhance overall investigations. Also, it is observed that electrical conductivity is the most variable of the three parameters, having a strong dependence on temperature, solar conditions, and local ionization sources.

A comparison of positive ion mobility measurements obtained by different Gerdien condensers also demonstrates generally good agreement between the various supersonic and subsonic probe systems. Of particular interest are the very small-valued positive ion mobilities, observed by several different experimental groups, which are thought to indicate the presence of charged particulates in the middle atmosphere. The Gerdien condenser is important for the measurement of these charged species which appear too large for identification by presently flown ion mass spectrometers. The density of these very large positive ions is approximately $10^8\ m^{-3}$ below 65 km, which is somewhat smaller than the concentration of light ions; and then it appears to increase at higher altitudes, although such observations are more limited. Opportunities for comparing different ion density probe techniques are limited; however, one example showing general measurement consistency is presented for supersonic electrostatic ion probes and parachute-borne Gerdien condensers.

INTRODUCTION

Rocket probe techniques for measuring middle atmospheric bulk ion properties, specifically electrical conductivity, ion mobility and charge number density, are considered in this paper. Some of these probe systems are designed to operate supersonically while either attached to or after ejection from the rocket; other payloads are flown on a parachute after separation from the rocket near its apogee. In some cases, the same basic probe has been adapted for different flight configurations.

Measurements of middle atmospheric electrical structure are important to studies of electrodynamic processes and to ionization investigations in the region. Specifically, the mapping of electric fields and the resultant charged particle currents are affected by the region's electrical conductivity (MAYNARD et al., 1984; CROSKEY et al., 1985). Also, the parameters of global electrical circuit models (HAYS and ROBLE, 1979) and their associated electrical response characteristics (HALE, 1984; HOLZWORTH et al., 1985) are dependent on atmospheric electrical conductivity.

The characterization of ions by their mobility values and the determination of their associated number densities are important to the understanding of middle atmospheric ion processes. Relatively small-valued positive ion mobility measurements, as first obtained by ROSE and WIDDEL (1972), are believed to indicate the presence of charged particulates in the middle atmosphere. Ion species of such large mass sizes (in the range of 10^3 to 10^4 AMU) have heretofore been unmeasurable in situ by quadrupole mass spectrometers. These observations, although relatively limited in number, have been reported by several different experimental groups for a variety of geophysical conditions (CROSKEY et al., 1977; CONLEY et al., 1983; MITCHELL, 1985). The significance of these ion species to middle atmospheric electrodynamics is currently under investigation.

An overview of probe techniques with regard to the different ion parameter measurements (electrical conductivity, ion mobility, and charge density) is now presented. While some probes, by virtue of their particular collector geometry, measure specifically one or possibly two of these bulk ion properties, the Gerdien condenser's electrode configuration is suitable for measuring all three of them. Hence, primary consideration will be given to the development of this particular probe technique. Also, a brief review of measurement results is included as a basis for probe intercomparisons and to illustrate nominal ion parameter values.

ELECTRICAL CONDUCTIVITY

The positive and negative components of electrical conductivity are each proportional to the summation of products formed by multiplying all respective charge densities of like polarity by their associated mobility values. A variety of probe configurations designed to operate either supersonically or subsonically have demonstrated generally good consistency in their measurement of this parameter. The two most frequently used parachute-borne probe techniques have been the blunt probe (HALE et al., 1966) and the Gerdien condenser (PEDERSEN, 1964; CONLEY, 1974; MITCHELL et al., 1982). An illustration of one kind of blunt probe in flight is shown in Figure 1. This particular miniaturized version can be flown on the small Super-Loki rocket, which makes it a payload suitable for launching at most meteorological rocket facilities. The relatively small collecting electrode, oriented downward in flight, consists of

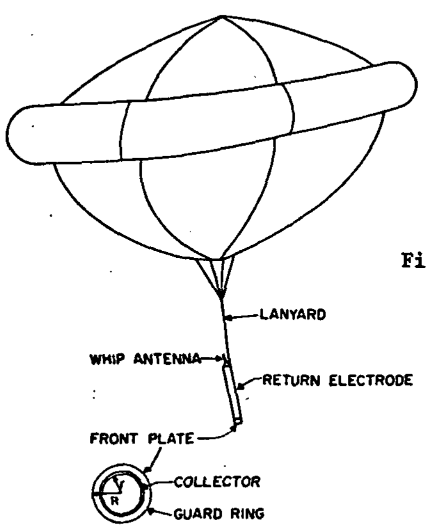

Figure 1. Parachute-borne blunt probe (launched using a Super-Loki rocket).

a disk-shaped collector and a concentric, annular guard ring. The larger cylindrical return electrode provides a low impedance path to the surrounding plasma and it also shields the electronics housed inside. A positive ion current is measured at the collector when it is biased negative with respect to the return electrode; and conversely, a positive voltage applied to the collecting electrode results in the collection of negatively charged species. In practice, a known voltage waveform swept through both polarities results in the alternate collection of positively and negatively charged species, and hence both polar components of electrical conductivity are measured.

The theory for charged particle collection by the blunt probe, developed by HOULT (1965) and SONIN (1967), yields the following current-voltage relation applicable for evaluating electrical conductivity:

$$I_{\pm} = \frac{2r^2}{R}\,\sigma_{\pm}\,V \tag{1}$$

In this equation, $I_{\pm}$ and, correspondingly, $\sigma_{\pm}$ represent either polar component of charged particle current and electrical conductivity, respectively. The radius of the collector disk is r, and the guard ring's outer radius is R. Finally, the collecting electrode's potential with reference to the plasma is V. In measuring conductivity, the blunt probe has negligible angle-of-attack dependence to flow which makes it well suited for flights where parachute swing might be a problem. This was one reason for the preferential use of blunt probes up through the early 1970s. The particular electrical parameters measurable with this planar collector surface openly exposed to the plasma generally have been limited to the two polar components of conductivity, although some recent theories have considered the application of this probe technique to measuring electron density (YORK et al., 1982).

The Gerdien condenser has a concentric cylindrical electrode geometry, with charged particle collection occurring from the axially directed air flowing between the two electrodes. A particular parachute-borne Gerdien condenser, included with deployable probes for measuring atmospheric electric fields (CROSKEY et al., 1985), is shown in Figure 2. This payload would be launched using a Super-Arcas rocket. The inner electrode, not visible in this picture, consists of a collector and a guard cylinder virtually at the same voltage to reduce fringing field effects on charged particle collection. Any fringing field effects at the probe's orifice are designed to be minimal. The outer return electrode shields the inner electrode from the environment, and ideally it and the payload skin are both "locked" to the plasma's potential.

The electrode configuration for this instrument, including its inner collector and guard electrode and the outer return electrode, is drawn in Figure 3. A negative probe voltage applied to the inner electrode, with reference to the outer return, will result in the collection of positive ions as illustrated in this figure. Likewise, a positive voltage on the collecting electrode, with reference to the return, would result in the collection of negatively charged species. An idealized Gerdien condenser current-voltage characteristic is shown in Figure 4 for the particular case of charged particle collection involving: two different positive ion mobility groups, electrons, and a single mobility group of negative ions. The solid curve for positive current corresponds to the collection of positive ions including both ion mobility groups; each of their current components is shown by dashed lines. Likewise, the two mobility groups of collected negatively charged particles are each represented by dashed lines, and the total negative current is shown as a solid curve.

The linear region of operation for the Gerdien condenser occurs at probe voltages sufficiently small such that no mobility group is completely collected from the air sample. Specifically, the linear region for positive ion current

ORIGINAL PAGE IS
OF POOR QUALITY

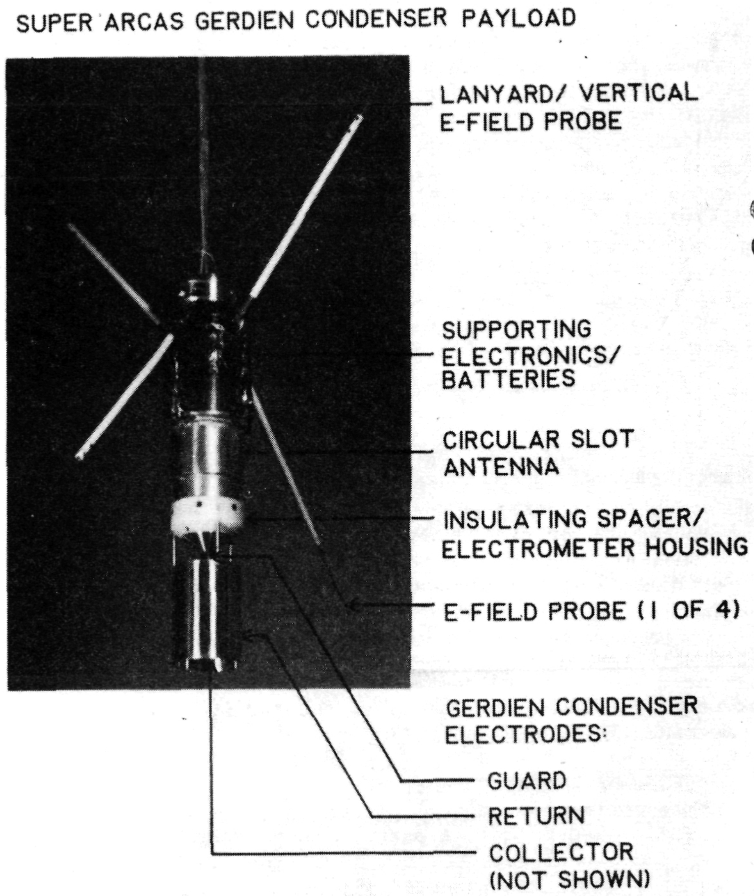

ORIGINAL PAGE IS
OF POOR QUALITY

Figure 2. Parachute-borne Gerdien condenser
(launched using a Super-Arcas rocket).

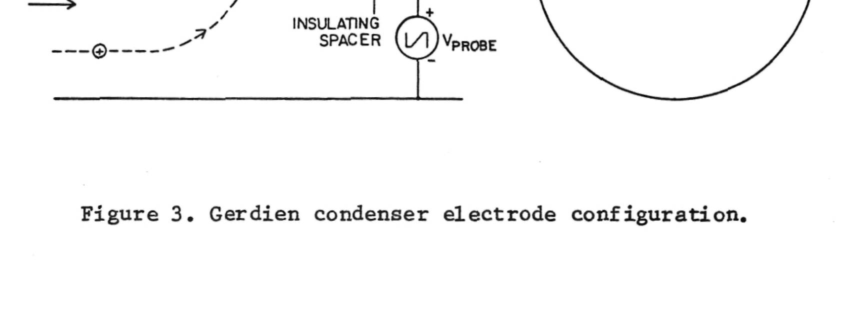

Figure 3. Gerdien condenser electrode configuration.

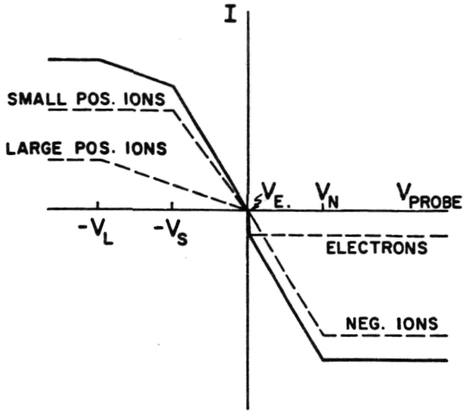

Figure 4. Idealized Gerdien condenser current-voltage characteristic including two positive ion mobility groups, electrons and one negative ion mobility group.

in Figure 4 corresponds to negative probe voltages having magnitudes smaller that V_S. The linear region for negatively charged particle collection is confined to a much smaller range of positive voltages (less than V_E) where the electron current component varies linearly with voltage. The operation of the probe in the linear region enables one to determine the polar components of conductivity as described by the equation:

$$I_{\pm} = \frac{2\pi l}{\ln(r_o/r_i)} \sigma_{\pm} V \tag{2}$$

In this generalized expression, $I_{\pm}$ represents either polar component of collected charged particle current, which is measured to determine the corresponding polar conductivity value $\sigma_{\pm}$. The probe's geometric constants are: r_i, the collector's radius; r_o, the return electrode's inner radius; and l, the collector's length. These geometric parameters are identified in Figure 3. Finally, V is the negative value of the probe voltage shown as V_{PROBE} in Figure 3. In practice, a periodic swept voltage waveform often is used for V_{PROBE}, thus making it possible to evaluate $\sigma_{\pm}$ by measuring $dI_{\pm}/dV$.

Finally, one observes from the sample I-V characteristic in Figure 4 that the slope of the negative current response in its linear region is much steeper, which is attributable to the presence of free electrons with their very large mobility values. In fact, the number of free electrons may be small when compared to that for negative ions, and yet their much larger mobilities often will have the dominant effect on the value of negative conductivity. Also, any possible problems with fringing fields on charged particle collection appear particularly susceptible to free electrons are present in the air sample is often more difficult than the determination of positive ion conductivity.

Since charged particle collection ideally is limited to the air core within the aspirator, a sufficiently large negative probe voltage will result in the collection of all positive ion species from the air sample. This current limiting condition is called "saturation". The saturation condition for all positive ions occurs in Figure 4 at negative probe voltages having magnitudes larger than or equal to V_L. Actually, if there are positive ion species in the air sample having distinctly different mobility values, the more mobile charged carriers become completely collected at a smaller probe voltage magnitude resulting in an apparent partial saturation condition for the probe's current response. As will be developed later in this chapter, the measurement of the probe voltages and currents where the different ion mobility groups become completely collected from the air sample leads, in turn, to the determination of their particular mobility and density values. Likewise, measuring

the negative ion mobility and density values for an air sample requires biasing the collector with a sufficient positive voltage; however, such measurements again are inherently more difficult if free electrons are present. Thus, the Gerdien condenser's electrode geometry, designed to collect charged species from a finite volume of air, has expanded measurement capabilities which include the determination of ion mobility and density values.

The Gerdien condenser also has been used to measure ion parameters under supersonic flow conditions. Specifically, the probe system of CONLEY (1974) and CONLEY et al. (1983) remains attached to the rocket, thus providing ion measurements during both the ascent and descent of the rocket. Other forms of supersonic conductivity probes having collectors openly exposed to the plasma include: a nose tip probe, which is a hemispheric electrode positioned at the tip of the rocket's nose cone as shown in Figure 5 (HALE et al., 1972; NGO, 1984); and a circular patch probe, similar to the blunt probe's collecting electrode, which is oriented downward on the surface of a gyro-stabilized, ballistic sphere (see Figure 6) that is ejected from a rocket (MAYNARD et al., 1981). The detrimental effects of supersonic flow on ion collection, particularly the alteration of ion properties through the shock layer, are a serious problem to such measurements. Also, the measurement period is relatively more limited than that for a parachute-borne probe. Supersonic probe systems have the advantage that measurements generally can be made to higher altitudes where parachutes are no longer effective as decelerators.

Of the parameters to be considered in this paper, electrical conductivity, with its dependency on both ion mobility and density, demonstrates the largest variability with respect to changes in geophysical conditions. This is particularly the case for the negative component of conductivity which relates to both free electron and negative ion properties. Representative examples showing the range of conductivity values measured at mid- and high latitudes are presented in Figures 7 and 8, respectively.

At midlatitudes, probe measurements have demonstrated appreciable variability for both polar components of conductivity (see Figure 7). The diurnal variations are largest for negative conductivity when free electrons

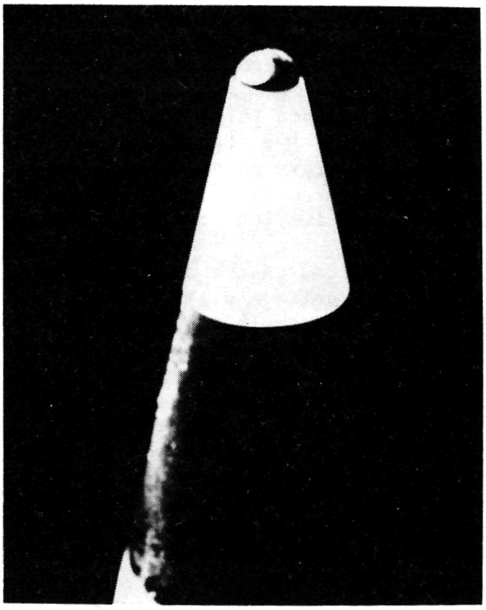

Figure 5. Nose tip probe for measuring conductivity during rocket ascent.

ORIGINAL PAGE IS
OF POOR QUALITY

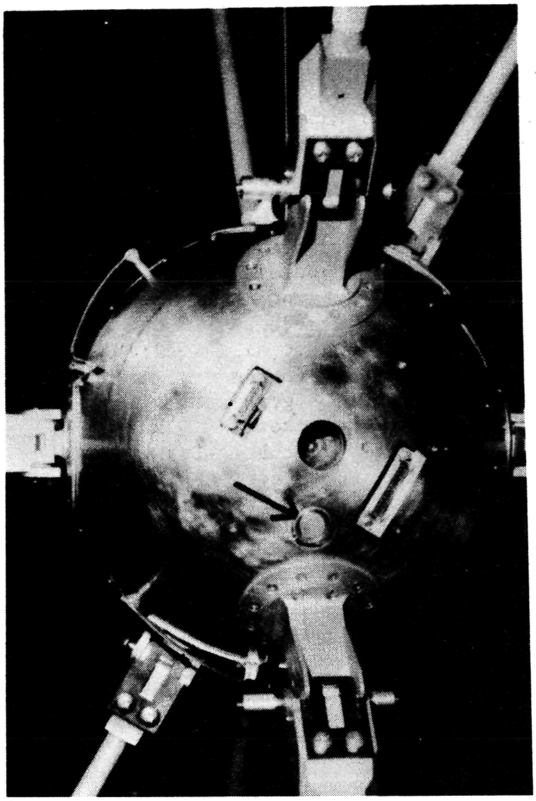

Figure 6. Patch probe for measuring conductivity from a gyro-stabilized, ballistic sphere.

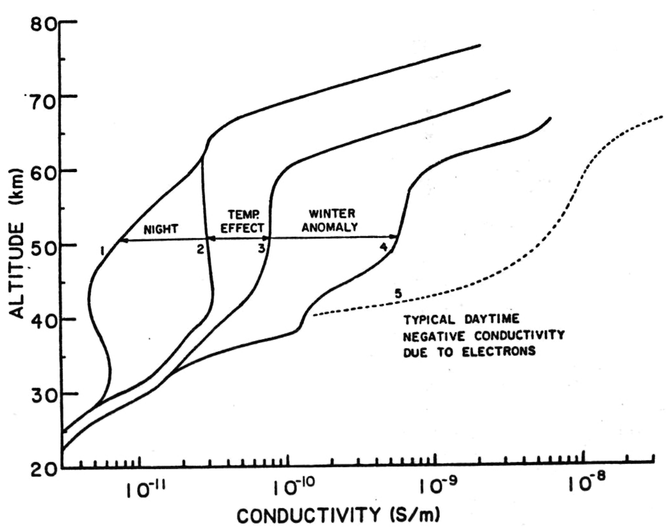

Figure 7. Midlatitude positive conductivity (1-4) and negative conductivity (5) values for different geophysical conditions.

ORIGINAL PAGE IS
OF POOR QUALITY

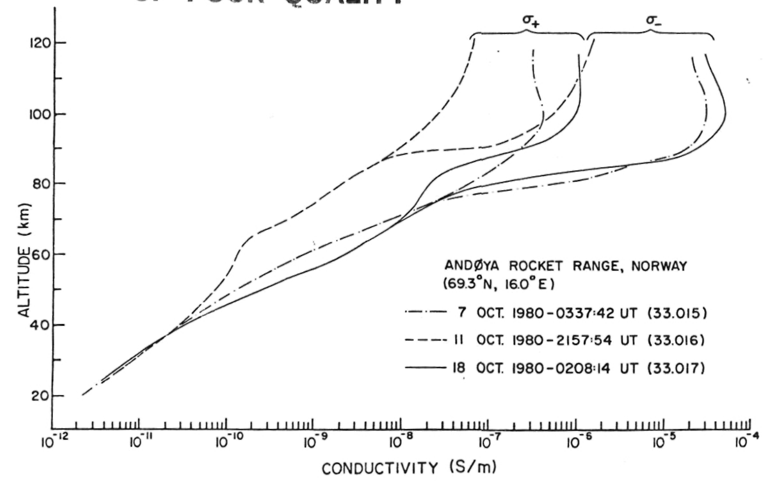

Figure 8. Electrical conductivity profiles measured by patch probes (at higher altitudes) and parachute-borne Gerdien condensers (at lower altitudes).

cause orders of magnitude enhancement in the daytime values (curve 5). At night, the two polar components of conductivity are generally comparable in value at these altitudes. The largest diurnal effects on positive conductivity have been observed at sunrise, as demonstrated by curves 1 and 2 (MITCHELL et al., 1977). This conductivity buildup appears to be attributed to the photodissociation of larger ions at sunrise.

A temperature dependence for positive conductivity also has been observed with the range of values represented by curves 2 and 3 (CIPRIANO et al., 1972). The associated temperature coefficient of about 4%/°K, which is considered too large for simple molecular ions, is believed to suggest the presence of charged particulates in the middle atmosphere (CHESWORTH and HALE, 1974). Finally, increased positive conductivity values (curve 4) also have been measured during winter periods of enhanced HF radio wave absorption -- the so-called "winter anomaly" (HALE, 1984).

Appreciable variability in electrical conductivity also has been measured at high latitudes during periods of auroral activity. The smoothed profiles for conductivity in Figure 8 were obtained from rocket flights in Norway on three different nights; two of them (7 and 18 October 1980) were geomagnetically disturbed and the other (11 October 1980) was relatively quiet. These particular probe measurements, which range over eight decades in the 20 to 120 km altitude region, were obtained for each night using two rockets flown almost simultaneously. Specifically, measurements down to 65 km obtained by previously described circular patch probes flown on gyro-stabilized ballistic spheres were combined with parachute-borne Gerdien condenser conductivity measurements obtained below 80 km. In the altitude regions where the data overlapped, the measurement intercomparisons between the different probe systems showed very good agreement (NGO, 1984), and hence a single smoothed profile was developed for each nighttime series.

Electrical conductivity is very responsive to local auroral energy deposition which is demonstrated for altitudes above 40 km. For these particular data, the variations in conductivity exceed an order of magnitude at all alti-

tudes above 60 km. The two auroral ionization sources observed in this region are a bremsstrahlung X-ray component dominating at the lower heights and relativistic electrons primarily at the higher altitudes (GOLDBERG et al., 1984). The conductivity profiles for the two geomagnetically disturbed nights display somewhat distinct characteristics, thus suggesting relatively different levels in auroral ionization over the altitude region. In particular, for the measurement period of 18 October, a stronger bremsstrahlung component is indicated by larger conductivity values in the 40 to 70 km altitude region, while electron energy deposition was relatively weaker in the 70 to 90 km region. At even higher altitudes where the energy deposition is associated with precipitating electrons of lower energy levels, the ionization effects for 18 October were stronger, which is consistent with the bremsstrahlung effects observed at lower altitudes. These observations are supported by available X-ray energy deposition data obtained from the same rocket flights.

The observed splitting of the two polar conductivity components at higher altitudes, with the negative conductivity values being relatively larger, is attributed to the presence of free electrons. The high-altitude negative conductivity values agree well with the relative concentrations of free electrons and also their altitude structure as measured by both rocket-borne instruments and ground-based experiments operated in conjunction with these particular probe flights.

These two figures for electrical conductivity present only a brief overview of this parameter as measured by rocket probes. In fact, of the parameters considered in this chapter, it probably is the one which has been most frequently measured and also for the most diverse set of geophysical conditions.

ION MOBILITY

The Gerdien condenser's confined collecting electrode geometry is capable of measuring ion mobility and charge density in addition to electrical conductivity. Referring again to the ideal Gerdien condenser I-V characteristic in Figure 4, a breakpoint in the linear positive ion current response occurs at a negative probe voltage of magnitude V_S. This breakpoint indicates the voltage and current levels at which a particular ion mobility group -- notably, the larger valued one associated with the small, light positive ions -- is completely collected from the air sample flowing through the condenser. The current response at more negative voltages continues to display a linear characteristic having a smaller slope attributed to the further collection of low-mobility ions, until a voltage of magnitude V_L is reached where these ions also are completely collected from the air sample. The flat current response for voltages more negative than $(-V_L)$ corresponds to the region of positive ion saturation for the Gerdien condenser.

The determination of mobility values for the two positive ion groups involves measuring the voltages associated with the two breakpoints of the piecewise linear ion current response. These voltage values are combined with information about the air flow through the condenser in the following equation:

$$k_{n+} = \frac{v\,(r_o^2 - r_i^2)\,\ln(r_o/r_i)}{2\,(lV_n)} \tag{3}$$

In this generalized expression, k_{n+} represents the positive ion mobility value for the nth mobility group, which is inversely proportional to the magnitude of the probe voltage V_n at the corresponding breakpoint. In Figure 4, the voltage V_n would be either V_S or V_L. The flow velocity through the condenser, assumed uniform, is v; and r_i, r_o, and l are the probe's geometric constants described earlier.

The determination of the ion density values for these two indicated mobility groups involves scaling slopes of the current waveforms between successive breakpoints to obtain partial ion conductivity values. In Figure 4, if the current-voltage waveform between voltages ($-V_S$) and ($-V_L$) is scaled, a partial conductivity value, σ_{L+}, may be determined by applying Equation 2 (with $\sigma = \sigma_{L+}$). This partial conductivity term includes only those positive ions having mobility values smaller than k_{S+}, and it follows that the positive small-ion density is obtained from the expression:

$$N_{S+} = \frac{\sigma_+ - \sigma_{L+}}{ek_{S+}} \tag{4}$$

For probe voltages more negative than the value at breakpoint L, the slope of the current waveform is zero and hence the saturation condition, i.e., the complete collection of all positive ion species flowing through the condenser, has been met. The associated partial conductivity in this saturation region is zero in value, and thus, the simplified expression for calculating the concentration of positive large ions is:

$$N_{L+} = \frac{\sigma_{L+}}{ek_{L+}} \tag{5}$$

It should be noted that the general procedure of evaluating probe voltages at breakpoints to determine mobility values, and then determining appropriate partial conductivity values to solve for ion concentrations, may be extended in a similar fashion to the current-voltage characteristics for negatively charged species and also for current waveforms displaying even more structure. Some evidence for additional positive ion mobility groups, in fact approximating a mobility continuum, have been reported by CROSKEY et al. (1977) and CONLEY et al. (1983).

Actual in-flight waveforms for measured probe current I in response to a known collection voltage V_{PROBE} are shown in Figure 9 for a particular parachute-borne Gerdien condenser flight. The probe voltage was swept between limits of -25.7 V and +19.2 V with the alternate application of negative and positive voltages resulting in the collection of positively and negatively charged species, respectively. In Figure 9, the linear region for positive ion collection occurs at positive current levels below the breakpoint marked "S". The scaling of the current-voltage characteristics in this region enables one to evaluate the positive component of conductivity by using Equation 2 described earlier.

The magnitude of V_{PROBE} corresponding to breakpoint S is used in Equation 3 to evaluate the positive small-ion mobility. Likewise, the breakpoint marked "L" signifies the complete collection of less mobile, larger positive ions from the air sample; and the measurement of this voltage level results in the evaluation of their associated mobility.

As noted from Equations 3 to 5, the measurements of ion mobility and density are dependent on air flow. The determination of air flow velocity usually is calculated from trajectory data for the probe. This approach is supported by earlier Gerdien condenser flights (ROSE and WIDDEL, 1972; WIDDEL et al., 1977) having flow meters which demonstrated good consistency between measured air flow values and those calculated from the probe's velocities (WIDDEL, 1976). Of course, the probe's orientation must be known for the calculation of air flow; this can be determined if an attitude sensor such as a magnetometer is included with the payload. Calculations for ion collection under nonuniform flow conditions have been considered by CHANG and YORK (1980). It will be demonstrated later that measurements of ion mobility appear generally consistent for a variety of Gerdien condenser payloads, flown either sub-

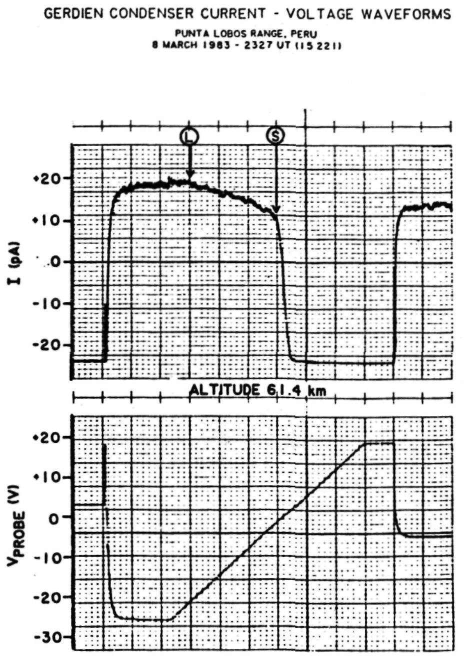

ORIGINAL PAGE IS
OF POOR QUALITY

Figure 9. Gerdien condenser probe current and voltage waveforms.

sonically or supersonically, and thus flow-associated effects on ion collection do not seem to have caused serious discrepancies in the presented measurements of this parameter.

Gerdien condenser measurements of positive ion mobility are shown in Figure 10 for the flight which included the I-V waveforms in Figure 9. The "+"s represent mobilities for the small, light ions; and the "x"s are values for the less mobile large, heavy ions. The two ion mobility groups become further separated at higher altitudes which would indicate correspondingly larger differences in their ion masses. Calculations of reduced mobility for the two ion groups, in fact, suggest that their differences largely result from increases in mass for the large ions at higher altitudes. These general features have been repeatedly observed in the equatorial middle atmosphere (FUENTES, 1984; MITCHELL, 1985).

The dashed line in Figure 10 represents the lower measurement limit for positive ion mobility, i.e., ions having mobility values smaller than those associated with the dashed line would not be identifiable by this particular Gerdien condenser. The values for this curve were calculated by using Equation 3 with V_n set equal to the positive ion collection voltage limit, which in this case was 25.7 V in magnitude. Such a measurement limit exists for every Gerdien condenser; it is dependent on probe geometry, flow conditions and size of collection voltage. For a fixed collecting electrode configuration, the extension of this lower measurement limit is attainable by reducing the flow velocity and/or increasing the collection voltage. Obviously, flow velocity reduction is achieved by flying the Gerdien condenser on a parachute. Extending the range of collection voltage must always be weighed against the possibility of ion breakup, and hence the alteration of ion mobility is some critical value of electric field is exceeded. Presently, probe voltage magnitudes up to 38 V have been used with our parachute-borne Gerdien condensers. Measurement checks, which involve the alternate use of large and small collec-

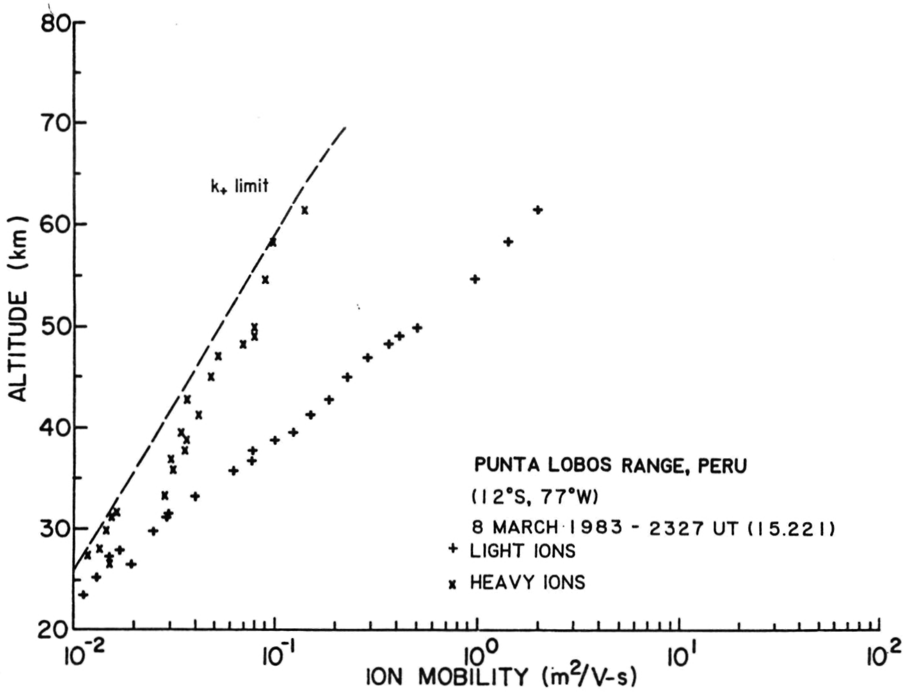

Figure 10. Gerdien condenser positive ion mobility measurements.

tion voltage ranges, produce repeatable ion values which would indicate that no such breakup effects on ions have occurred.

An overview of recent positive ion mobility measurements obtained by different Gerdien condenser systems is presented in Figure 11. The low-altitude mobility values of WIDDEL, et al. (1977) and HALE and CROSKEY (1978) were obtained by parachute-borne Gerdien condensers, while the values of REIKERT (1971) and ROSEN and HOFMANN (1981) resulted from balloon-borne probes. The ion mobility values of Rosen and Hofmann actually were calculated from measurements of conductivity and small-ion total density, and their numbers represent "averaged" small-ion mobility values for the stratosphere. The disparity in values at these low altitudes, if interpreted as differences in ion mass, would correspond to a large range of ion sizes (KILPATRICK, 1971). Two factors which may contribute to measurement discrepancies are electric field induced ion breakup (MEYEROTT et al., 1980) and flow restriction in the aspirator (CHANG and YORK, 1980).

One observes an even larger range of values at higher altitudes where additional positive ion mobility groups have been measured; however, all Gerdien condensers flown either subsonically or supersonically demonstrated good consistency in measuring the larger valued mobilities associated with small ions. This group of small-ion mobility values appears bracketed over most of the high-altitude region by the curves of CONLEY (1974) and MITCHELL et al. (1983). The additionally measured, smaller values at high altitudes, first reported by ROSE and WIDDEL (1972), have particularly interesting implications. The overall spread in ion mobility at the higher altitudes is in excess of an order of magnitude which corresponds to even larger differences in ion mass size (KILPATRICK, 1971). The smallest reduced mobility values calculated from

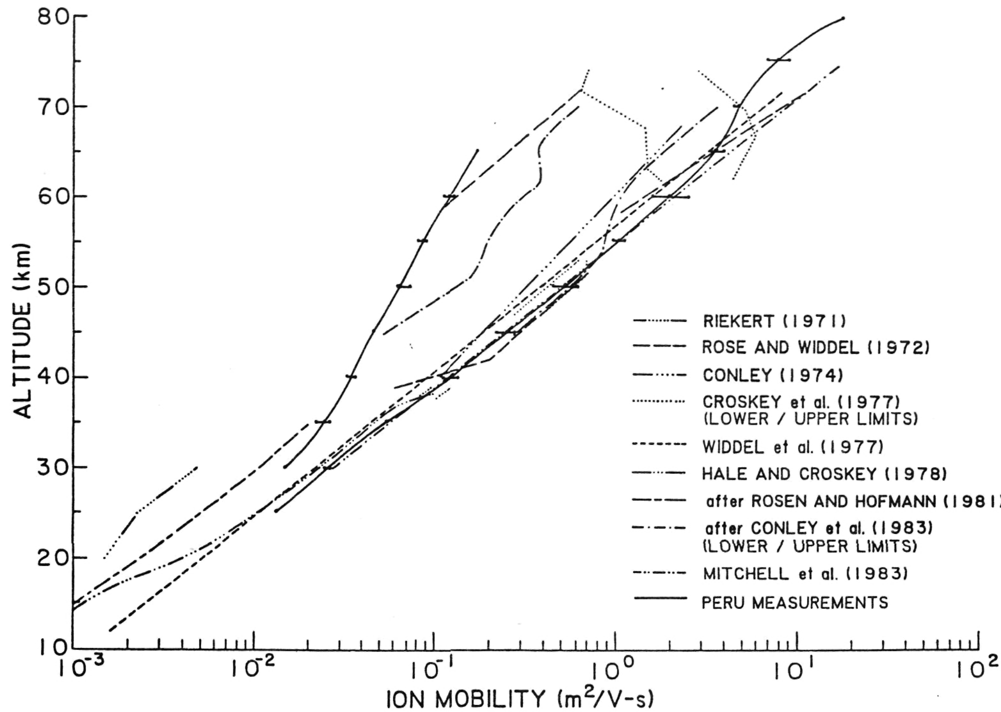

Figure 11. A composite of Gerdien condenser positive ion mobility measurements.

these measurements are on the order of 0.1 cm^2/V-s, suggestive of ion mass sizes approaching 10^4 AMU which are far in excess of any present species identifiable by quadrupole mass spectrometers.

The ion mobility measurements of CROSKEY et al. (1977) and CONLEY et al. (1983) show a range of values between their lower and upper limits drawn in Figure 11 which would indicate a larger variety of ion mass sizes than just two distinct groups. In fact, a certain degree of curvature appears in the current response waveform of Figure 9 between breakpoints S and L which also could suggest the presence of additional mobility groups.

Finally, the two solid curves for ion mobility in Figure 11, obtained from a series of eight parachute-borne Gerdien condenser flights (FUENTES,1984), demonstrate the transition of ion mobility from higher altitudes where separate groups are observed to lower altitudes where generally only small ions are measured. Again, this ion mobility transition shown for the Peru measurements suggests a change in large-ion mass size to increasing values at higher altitudes.

In summary, the curves in Figure 11 for higher altitudes demonstrate consistency in the measurement of positive light-ion mobilities. This good agreement occurred between Gerdien condensers flown under both supersonic and subsonic flow conditions and during a variety of geophysical conditions. The low-mobility ion values, indicative of very large positive ions, show more disparity and were obtained less frequently. The inherent instrumental con-

straints on the ion mobility measurement range would help explain the relative infrequency of such measurement results. Also, it is possible that such ion species are not always present, although the data set presented in Figure 11 does include a variety of geophysical conditions.

ION DENSITY

The ion density probe techniques to be considered all involve the simultaneous measurement of the collected ion current to a biased probe in conjunction with the probe's velocity. Such probe systems flown supersonically while attached to the rocket include: the nose tip probe (ROSE and WIDDEL, 1972); the electrostatic (ion trap) probe (FRIEDRICH et al., 1977); and the Gerdien condenser (CONLEY, 1974; CONLEY et al., 1983). This latter instrument can measure component ion density values associated with the different ion mobility groups, while the other two probe systems measure total ion density. Most Gerdien condensers, however, have been designed to measure ion density under reduced flow conditions obtainable with a parachute. Such ion density measurements have been reported by ROSE and WIDDEL (1972), CORSKEY et al. (1977), WIDDEL et al. (1977), MITCHELL et al. (1983), FUENTES (1984) and MITCHELL (1985) for a variety of geophysical conditions.

In reviewing supersonic probe techniques, the nose tip probe of ROSE and WIDDEL (1972), which is similar to a Langmuir probe, uses the tip of the rocket as the collecting electrode. A section of the nose cone adjacent to the collector is used as a guard electrode to reduce possible fringing field effects on ion collection. This section also serves as the driven electrode with reference to the rest of the rocket's metallic skin. The collection voltage used was a $\pm$ 3 V triangular waveform which resulted in the alternate collection of both polar current components. The positive ion current measurements were not converted to density values but showed similar altitude features when compared to the parachute-borne Gerdien condenser ion density values obtained from the same rocket flight.

The electrostatic probe, also designed for supersonic flight (FRIEDRICH et al., 1977), consists of a concentric spherical collecting electrode enclosed within a grid held at the rocket's potential. The collector is biased at a fixed voltage for charged particle collection. For positive ion collection, a negative voltage biases the inner collector that is sufficient in size to repel negatively charged species, but not of such a large magnitude as to cause secondary emission from the collecting surface. A value of -22.5 V was applied to the collector with reference to the rocket body. The measured positive ion current is primarily a ram current component which is not considered to be seriously affected by uncertainty in kinetic ion temperature or ion mass size. The determination of absolute ion density from the probe current measurements has required normalizing the density values to electron density measurements from a wave propagation experiment flown aboard the same rocket. The resulting ion density values for both upleg and downleg parts of the rocket flight have shown good consistency.

The Gerdien condenser, with its ion collection ideally from a confined air sample, directly measures ion density without a need for calibration with another in situ measurement. The use of a swept collection voltage waveform to distinguish different ion mobility groups also enables one to determine the corresponding component ion density values. A sufficiently large voltage applied to the collector, such that all ions of a particular polarity are collected from the air sample within the aspirator, achieves the saturation condition necessary for determining total ion density. The presence of low-mobility ions, as recently observed, necessitates the use of relatively large collection voltages to ensure saturation. Also, the use of a parachute to reduce the air flow makes attainment of the saturation condition more realizable,

and it reduces shock-induced ion breakup and other possible flow-related effects on the measurement of ion mobility. While both rocket-attached and parachute-borne Gerdien condensers have been flown to measure ion density, the latter approach has been the one more frequently used to date.

The parachute-borne Gerdien condenser measurements of positive ion density, presented in Figure 12, are from the same flight as were the ion mobility values in Figure 10. Consistent notation has been used with the dots included to represent total positive ion density values. Our measurements for the equatorial middle atmosphere show that the concentration of low-mobility positive ions is typically 10^8 m^{-3} in the region below 65 km. The large-ion concentration displays less altitude dependence and smaller values than what are generally observed for small ions in this region. The limited data available for higher altitudes would indicate that the concentration of positive large ions increases above 65 km in the daytime and that these ion species appear to dominate for some of the available measurements (MITCHELL, 1985). The earlier measurements of ROSE and WIDDEL (1972) showed the positive large-ion concentrations dominating over the entire region in which they were measured, from 57 to 74 km.

Finally, a comparison of positive ion density measurements obtained by two different probes flown on the same rocket, an electrostatic probe and a parachute-borne Gerdien condenser, is demonstrated in Figure 13. The rocket flights used to obtain these data were some of the same ones used to measure the conductivity values in Figure 8. The electrostatic ion probe measurements (TORKAR and FRIEDRICH, 1984) occurred after the payload separated from the rocket until the parachute was deployed. The Gerdien condenser measured ion parameters at lower altitudes following parachute deployment. Thus, the ion

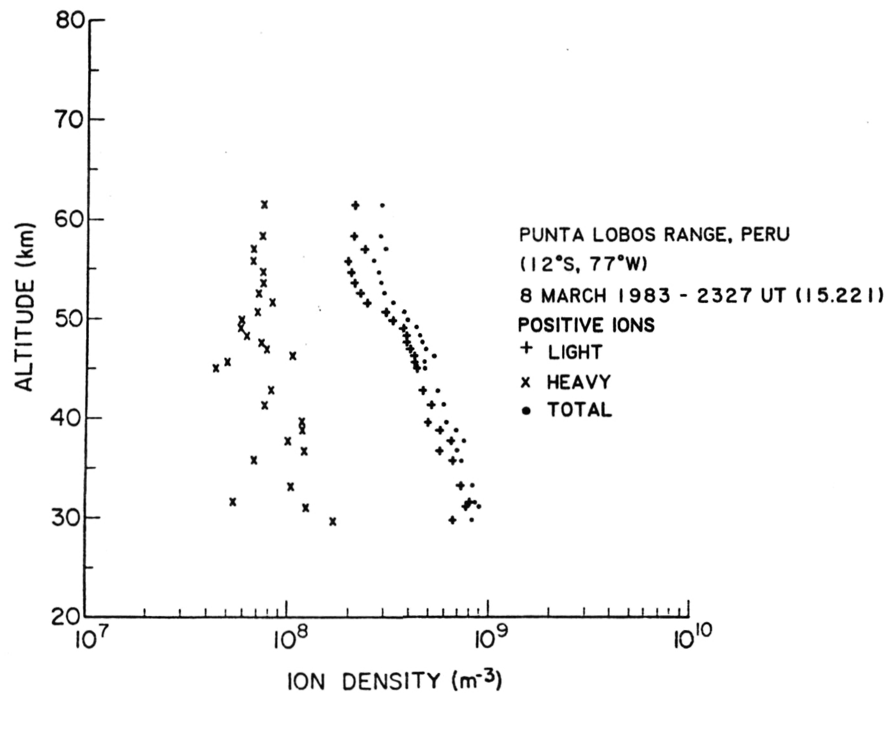

Figure 12. Gerdien condenser positive ion density measurements.

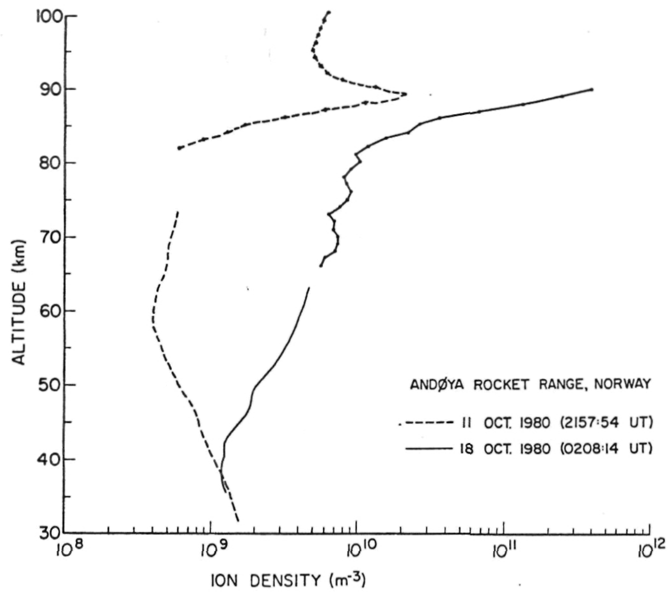

Figure 13. Positive ion density profiles measured by electrostatic ion probes (at higher altitudes) and parachute-borne Gerdien condensers (at lower altitudes).

density measurements for the two probes did not overlap in altitude; however, the pair of profiles obtained for each rocket flight appear to fit nicely, which would suggest good consistency between the two probe techniques.

As noted earlier, the measurement period on 18 October 1980, occurred during aurorally active conditions, which caused enhancements in ion density above 40 km when compared to the geomagnetically quiet day of 11 October 1980. The level of enhancement for ion density between these two flights is of the same order as that which was observed in Figure 8 between the respective positive conductivity values. In general, opportunities such as these for comparing different ion probes on the same rocket have been generally scarce, and further such investigations are important for the understanding and evaluation of these different measurement techniques.

CONCLUSIONS

In reviewing the various probe techniques for measuring bulk ion properties, one basis for evaluation involves comparing the measurement results from the different instruments. A number of conductivity measurement intercomparisons have been conducted by the Penn State group (HALE et al., 1972; MITCHELL et al., 1982; NGO, 1984), with one such study resulting in the profiles shown in Figure 8. From such investigations, it would appear that the different probe techniques considered in this paper, both supersonic and subsonic, are capable of obtaining generally consistent measurements of electrical conductivity.

The only probe considered for measuring positive ion mobility was the Gerdien condenser. This instrument is particularly important in the measurement of very low-mobility ion species which are indicative of charged particulates too large for identification by presently flown quadrupole ion mass spec-

trometers. An overview of recent ion mobility measurements was presented in Figure 11. The particular probe dimensions and flight conditions under which these mobility values were obtained were quite variable, and yet in most cases there appeared to be general consistency between measurements by the different Gerdien condensers. Such agreement is particularly encouraging since ion mobility is a parameter which is dependent on flow geometry.

Opportunities for intercomparing different probe measurements of ion density appear generally scarce. The dependence of this parameter on geophysical conditions makes it necessary for such comparisons to involve measurements done closely in time and location. Although an intercomparison of ion density between high-altitude electrostatic probes and parachute-borne Gerdien condensers was attempted and shown to display general agreement (see Figure 13), it is apparent that further studies of this kind are important for assessing the validity of these different probe techniques.

REFERENCES

Chang, S. K., and T. M. York (1980), Numerical analysis of flow in Gerdien condenser probes with applications to lower ionosphere composition data, AIAA Paper, 80-1387.

Chesworth, E. T., and L. C. Hale (1974), Ice particulates in the mesosphere, Geophys. Res. Lett., 1, 347-350.

Cipriano, J. P., L. C. Hale, and J. D. Mitchell (1974), Relations among low ionosphere parameters and A3 radio wave absorption, J. Geophys. Res., 79, 2260-2265.

Conley, T. D. (1974), Mesospheric positive ion concentrations, mobilities and loss rates obtained from rocket-borne Gerdien condenser measurements, Radio Sci., 9, 575-592.

Conley, T. D., E. R. Hegblom, and R. S. Narcisi (1983), D-region positive and negative concentration and mobilities during the February 1979 eclipse, J. Atmos. Terr. Phys., 45, 449-513.

Croskey, C. L., L. C. Hale, and S. C. Leiden (1977), Results of ionization measurements in the middle atmosphere, COSPAR Space Research XVIII, edited by M. J. Rycroft and A. C. Stickland, Pergamon, Oxford and New York.

Croskey, C. L., L. C. Hale, J. D. Mitchell, D. Muha, and N. C. Maynard (1985), A diurnal study of the electrical structure of the equatorial middle atmosphere, J. Atmos. Terr. Phys., in press.

Friedrich, M., K. Torkar, and S. Ulrich (1977), A rocket borne experiment to measure plasma densities in the D-region, J. Geophys., 44, 91-98.

Fuentes, J. R. (1984), Electrical parameters of the middle atmosphere, M. S. Thesis, The Pennsylvania State University.

Goldberg, R. A., C. H. Jackman, J. R. Barcus, and F. Soraas (1984), Nighttime auroral energy deposition in the middle atmosphere, J. Geophys. Res., 89, 5581-5596.

Hale, L. C. (1984), Middle atmosphere electrical structure, dynamics and coupling, Adv. Space Res., 4, 175-186.

Hale, L. C., and C. L. Croskey (1978), Electrical structure and ionizable constituent measurement, Stratcom-VIII, NASA Conf. Pub. CP-2043, edited by E. I. Reed.

Hays, P. B., and R. G. Roble (1979), A quasi-static model of global atmospheric electricity: 1. The lower atmosphere, J. Geophys. Res., 84, 3291-3305.

Holzworth, R. H., M. C. Kelley, C. L. Siefring, L. C. Hale, and J. D. Mitchell (1985), Electrical measurements in the atmosphere and the ionosphere over an active thunderstorm: 2. DC electric fields and conductivity, J. Geophys. Res., in press.

Hoult, D. P. (1965), D-region probe theory, J. Geophys. Res., 70, 3183-3187.

Widdel, H. U., G. Rose, and R. Borchers (1976), Experimental results on the variation of electric conductivity and ion mobility in the mesosphere, J. Geophys. Res., 81, 6217-6220.

Widdel, H. U., G. Rose, and R. Borchers (1977), Payload B III--an instrument package for the measurement of conductivity, concentration and mobility of positive and negative ions in the mesosphere, J. Geophys., 44, 179-188.

York, T. M., R. O. Olsen, J. D. Mitchell, and D. L. Mott (1982), Evaluation of electron and ion densities in the middle atmosphere from rocket-borne blunt probes, J. Atmos. Terr. Phys., 44, 257-266.

Kilpatrick, W. D. (1971), An experimental mass-mobility relation for ions in air at atmospheric pressure, Proceedings of the 19th Annual Conference on Mass Spectrometry, Atlanta, GA.

Maynard, N. C., L. C. Hale, J. D. Mitchell, F. J. Schmidlin, R. A. Goldberg, J. R. Barcus, F. Soraas, and C. L. Croskey (1984), Electrical structure in the high-latitude middle atmosphere, J. Atmos. Terr. Phys., 46, 807-817.

Meyerott, R. E., J. B. Reagan, and R. G. Joiner (1980), The mobility and concentration of ions and the ionic conductivity in the lower stratosphere, J. Geophys. Res., 85, 1273-1278.

Mitchell, J. D. (1985), Middle-atmosphere positive ion measurements during solar eclipses, Annales Geophysicae, 3, 95-102.

Mitchell, J. D., L. C. Hale, C. L. Croskey, and R. O. Olsen (1983), Eclipse-related measurements of middle-atmosphere electrical parameters, J. Atmos. Terr. Phys., 45, 515-525.

Mitchell, J. D., D. C. Schroder, K. J. Ho, K. Domagalski, and R. O. Olsen (1982), Subsonic probe measurements of middle-atmosphere electrical parameters, AIAA Journal, 20, 503-508.

Mitchell, J. D., R. S. Sagar, and R. O. Olsen (1977), Positive ions in the middle atmosphere during sunrise conditions, Space Res. XVII, edited by M. J. Rycroft and A. C. Stickland, Pergamon, Oxford, 199-204.

Ngo, Q. V. (1984), Supersonic and subsonic probes measurements of middle-atmosphere electrical conductivity, M. S. Thesis, The Pennsylvania State University.

Pedersen, A. (1964), Measurements of ion concentrations in the D-region of the ionosphere with a Gerdien condenser rocket probe, Research Institute of National Defence Rept. A607.

Riekert, H. (1971), Untersuchungen zur beweglichkeit der Kleinionen in der freien Atmosphare, Ph. D. dissertation, Eberhard-Karls-Universitat, Tubingen, Federal Republic of Germany.

Rose, G., and H. U. Widdel (1972), Results of concentration and mobility measurements for positively and negatively charged particles taken between 85 and 22 km in sounding rocket experiments, Radio Sci., 7, 81-87.

Rosen, J. M., and D. J. Hofmann (1981), Balloon-borne measurements of electrical conductivity, mobility, and the recombination coefficient, J. Geophys. Res., 86, 7406-7410.

Sonin, A. A. (1967), Theory of ion collection by a supersonic atmospheric sounding rocket, J. Geophys. Res., 72, 4547-4557.

Torkar, K. M., and M. Friedrich (1984), Up-dated collection of D- and E-region plasma density profiles processed at the Technical University Graz, Space Research Institute of the Austrian Academy of Sciences, Report No. IWF 8404.

Widdel, H. U. (1976), Private communication.

N86-26733 D8-46 15P

8. ELECTRON DENSITY MEASUREMENTS IN THE MIDDLE ATMOSPHERE BY RADIO PROPAGATION TECHNIQUES

L. G. Smith

Department of Electrical and Computer Engineering
University of Illinois
Urbana, Il 61801

7616
IB641432

ABSTRACT

Radio propagation between a ground-based transmitter and a rocket-borne receiver provides a useful method of obtaining the electron density structure of the middle atmosphere. The basis of the experiment is contained in magnetoionic theory. The implementation of the experiment takes the form of Faraday rotation and differential absorption; the two techniques are often combined into a single system.

INTRODUCTION

The application of radio propagation techniques for rocket experiments was first demonstrated by SEDDON (1953). The use of radio propagation experiments on rockets to study the D region and lower E region of the ionosphere has continued to the present day and, stimulated by competition from *in situ* probes on rockets and from ground-based radio techniques, is likely to continue.

The changes in amplitude, in phase and in polarization of a radio wave propagating in the ionosphere can be used separately or together to obtain electron density and, sometimes, electron collision frequency. The principal advantage of the radio propagation experiment is the freedom from the effects of local perturbation of the ionosphere by the rocket. The main disadvantage is the implicit assumption of a horizontally stratified ionosphere.

Most of the following discussion is concerned with the observation of the normal midlatitude ionosphere during the daytime (when some absorption is present) and during the night (when absorption is negligible). Two other special situations are treated briefly. One is the high latitude ionosphere under conditions of high absorption; the other is the equatorial situation (where the characteristic modes are linear).

No attempt has been made to give a comprehensive bibliography of the results obtained by radio propagation experiments on rockets but, it is hoped, major descriptions of experimental techniques in books and journals are referenced.

Rocket experiments using LF and VLF propagation to study the D region are excluded from the present discussion. Descriptions of these have been given by CARTWRIGHT (1964), KIMURA and HIRAO (1971) and HALL (1973).

MAGNETOIONIC THEORY

The propagation of a radio wave through the ionosphere is described by magnetoionic theory. The theory as developed by Appleton and Hartree applies to a partially ionized gas containing free electrons, positive ions and neutral atoms and molecules. A uniform magnetic field is present and the electrons are considered to be monoenergetic. This last condition leads to serious error below about 80 km in the earth's ionosphere and the theory must be modified.

A comprehensive discussion of the unmodified Appleton-Hartree theory has been given by RATCLIFFE (1962) and here we summarize some of the relevant relations. The theory starts with two of Maxwell's equations, namely:

$$\text{curl}\ \underline{H} = \varepsilon_o \dot{\underline{E}} + 4\pi\dot{\underline{P}}$$

and

$$\text{curl}\ \underline{E} = -\mu_o\dot{\underline{H}}$$

where $\underline{H}$ is the magnetic wave field, $\underline{E}$ is the electric wave field and $\dot{\underline{P}}$ is the volume polarization of the medium; ε_o and μ_o are, respectively, the electric and magnetic permittivity of free space. These are combined with the equation of motion for an electron:

$$m\dot{\underline{v}} = -m\nu\underline{v} + q\underline{E} + q\ \underline{v} \times \underline{B}$$

where m is the mass of the electron, $\underline{v}$ its velocity and q the magnitude of the electronic charge; $\underline{B}$ is the magnetic field and ν is the electron collision frequency. The manner in which the effect of collisions is introduced into the equation of motion is empirical and may not be correct. This is of no practical consequence except, perhaps, at the lowest altitudes where the collision term dominates.

Two useful quantities which characterize the medium through which the wave is propagating are the gyrofrequency, given by

$$\omega_B = qB/m$$

and the plasma frequency, given by

$$\omega_N = (Nq^2/\varepsilon_o m)^{1/2}$$

where numerical values are (in SI units)

$$q = 1.602 \times 10^{-19}\ \text{C}$$

$$\varepsilon_o = 8.854 \times 10^{-12}\ \text{F/m}$$

and, for electrons,

$$m = 9.110 \times 10^{-31}\ \text{kg.}$$

For a wave of angular frequency ω propagating in a medium where the electron density is N, the magnitude of the magnetic field is B and the angle between the wave normal and the magnetic field is θ, these equations can be solved for the polarization (R) and the complex refractive index (n):

$$R = \frac{-i}{Y_L}\left\{\frac{\frac{1}{2}Y_T^2}{1 - X - jZ} \mp \left(\frac{\frac{1}{4}Y_T^4}{(1 - X - jZ)^2} + Y_L^2\right)^{1/2}\right\}$$

and

$$n^2 = 1 - \frac{X}{1 - jZ - \frac{1}{2}Y_T^2/(1 - X - jZ) \pm \left[\frac{1}{4}Y_T^4/(1 - X - jZ)^2 + Y_L^2\right]^{1/2}}$$

where $X = \omega_N^{\,2}/\omega^2$

$Y_L = \omega_L/\omega = (\omega_B \cos\theta)/\omega$

$Y_T = \omega_T/\omega = (\omega_B \sin\theta)/\omega$

$Z = \nu/\omega$

Another, sometimes useful, relation is

$$n^2 = 1 - X/(1 - jZ - jY_L R).$$

The $\pm$ sign in the equation for R (and, consequently, for n^2) indicate that there are two characteristic waves which can each propagate through the medium with their polarization unchanged.

The two characteristic waves are referred to as the "ordinary" and "extraordinary" waves (or O-mode and X-mode, respectively). In practical terms, the ordinary wave is affected to a lesser extent and the extraordinary wave to a greater extent by the presence of the magnetic field. Also, when collisions are significant, the extraordinary wave suffers greater attenuation than does the ordinary wave. (These statements may not be true for the lowest altitudes of the D region.)

Two limiting cases will be noted. For longitudinal propagation ($\theta = 0°$, giving $Y_T = 0$):

$$R_o = +j \text{ and } R_x = -j$$

indicating that the two characteristic waves are circularly polarized, in opposite senses (right-handed and left-handed). For transverse propagation ($\theta = 90°$, giving $Y_L = 0$):

$$R_o = \infty \text{ and } R_x = 0$$

so that the two characteristic waves are linearly polarized, with electric vectors parallel and perpendicular to the magnetic field, respectively. At propagation angles between 0° and 90° the characteristic waves are elliptically polarized.

The complex refractive index (n) can be expressed as real and imaginary parts:

$$n = \mu - j\chi$$

The meaning of μ and χ can be understood by considering a wave (propagating in the z direction):

$$E = E_o \exp[j\omega(t - nz/c)]$$

Thus

$$E = E_o \exp(-\omega\chi z/c) \exp[j\omega(t - \mu z/c)]$$

or

$$E = E_o \exp(-kz) \exp[j\omega(t - z/v)].$$

The first exponential term represents attenuation (absorption) of the wave so that χ is the absorption index, more practically expressed by the absorption coefficient $k = \omega\chi/c$. The second exponential term shows that the phase velocity of the wave in the medium is $v = c/\mu$ and μ is the refractive index.

The rocket experiments described here are based on the measurement of the absorption coefficient (k) or the refractive index (μ). Earlier experiments favored the measurement at two frequencies, harmonically related but well separated. More recent experiments have tended toward the measurement of the differential properties of two characteristic waves having the same frequency.

It has already been noted that the treatment of electron collisions is the weak point of magnetoionic theory. PFISTER (1954), in a theoretical study, and KANE (1961), working with data from a rocket experiment, pointed out the serious error of assuming monoenergetic electrons. The theory of Appleton and Hartree was revised by SEN and WYLLER (1960; with correction by MANCHESTER, 1965) to properly include the statistics of the collision process. Their analysis has been confirmed by BUDDEN (1965).

The practical effect of the generalization of the Appleton-Hartree by Sen and Wyller has tended to be exaggerated. Within the limits of experimental error, the simpler formulation of the Appleton-Hartree theory can be used with an effective electron collision frequency (ν_{eff}) which is numerically equal to 2.5 ν_m, where ν_m is the monoenergetic collision frequency calculated from the properties of the neutral gas.

The role of collision frequency in rocket radio-propagation experiments is well illustrated in some calculations of BENNETT et al. (1972) shown in Figure 1. The Sen-Wyller equations are used. In Figure 1(a) the specific differential refractive index is plotted as a function of monoenergetic electron collision frequency (using the Sen-Wyller equations). The radio frequency is 2.29 MHz and the propagation angle is 27°. The magnitude of the earth's magnetic field is 0.47 μT. Notice that the differential refractive index ($\mu_o - \mu_x$) is roughly proportional to electron density. Also note that collisions can be neglected for $\nu_m < 10^5\ s^{-1}$, which corresponds to altitudes > 90 km. For $\nu_m > 10^6\ s^{-1}$ (altitudes below about 80 km), $\mu_o - \mu_x$ decreases rapidly, changing sign at $\nu_m \approx 10^7\ s^{-1}$ (about 63 km). This reversal has been observed (in a Faraday rotation experiment) by AIKEN et al. (1964) and provided what was probably the first direct measurement of electron collision frequency in the ionosphere.

Figure 1(b) shows the specific differential absorption, for the same conditions of frequency, propagation angle and magnetic field, plotted over a range of monoenergetic collision frequency. Again the quantity of interest, differential absorption coefficient ($\chi_x - \chi_o$), is roughly proportional to electron density. The maximum values occur for $\nu_m \approx 2 \times 10^6\ s^{-1}$ (about 75 km). The decrease as ν_m becomes smaller (at greater altitudes) would be expected but the decrease at low altitudes is not physically obvious.

The effect of changing the angle of propagation on specific differential refractive index is shown in Figure 2. The Sen-Wyller equations are again used. The wave frequency is 2.2 MHz, the gyrofrequency is 1.4 MHz (appropriate for Wallops Island, Virginia) and the electron density is $10^2\ cm^{-3}$. As has been noted in connection with Figure 1, there is little change for electron densities up to $10^4\ cm^{-3}$. The altitude scale is added using the collision frequency model to be discussed later. The propagation angles are 0°, 30°, 60° and 90°. Clearly, an experiment which measures ($\mu_o - \mu_x$) has reduced sensitivity as the propagation angle increases. It is also interesting to note that the change

(a)

(b)

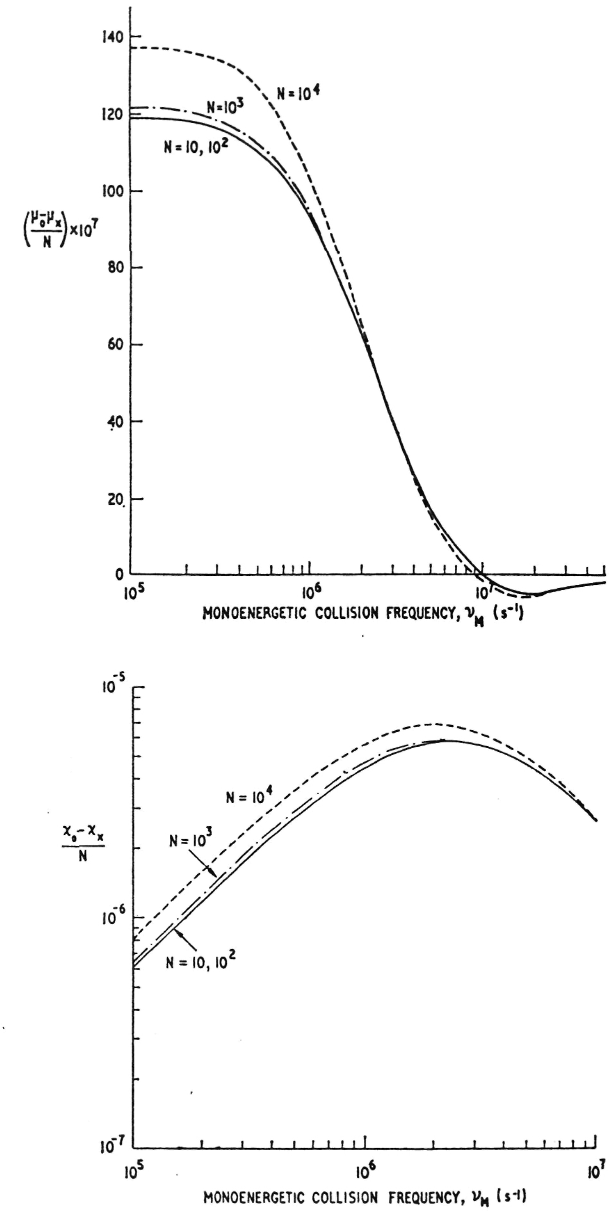

Figure 1. Variation of (a) specific differential refractive index and (b) specific differential absorption index with monoenergetic electron collision frequency (BENNETT et al., 1972).

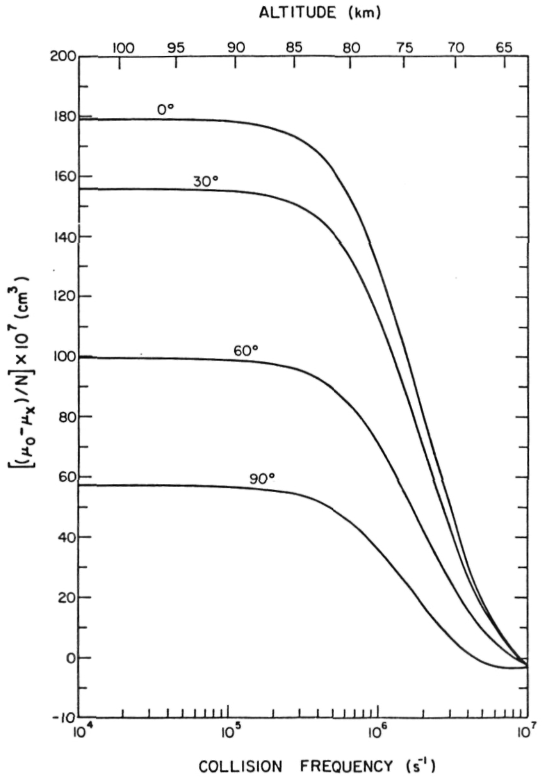

Figure 2. The variation of specific differential refractive index with monoenergetic electron collision frequency for four propagation angles.

of sign of (μ_o - μ_x) is confirmed for all propagation angles, although the altitude of this change is about 5 km greater for 90° propagation than it is for 0°, 30° and 60°.

The specific differential absorption also changes with the propagation angle, as shown in Figure 3. This is calculated for the same values of wave frequency, gyrofrequency and electron density as were used for Figure 2. As the propagation angle increases, the differential absorption decreases, reducing the sensitivity of an experiment.

The specific absorption values implicit in Figure 3 are shown separately in Figure 4 for the two characteristic modes for propagation angles of 0° and 90° (longitudinal and transverse propagation, respectively). The extraordinary wave has the greater absorption, the ordinary wave the lesser absorption in each pair. It is interesting to note that the absorption of the ordinary mode increases as the angle of propagation increases.

This figure also illustrates an important point in connection with the computation of μ and χ, whether from the Appleton-Hartree or (as here) from the Sen-Wyller formulas. It concerns the terms "ordinary" and "extraordinary". In the equations for R and n^2 the upper sign (of the $\mp$ or $\pm$) gives the ordinary wave properties while the lower sign gives the extraordinary wave properties.

ORIGINAL PAGE IS
OF POOR QUALITY

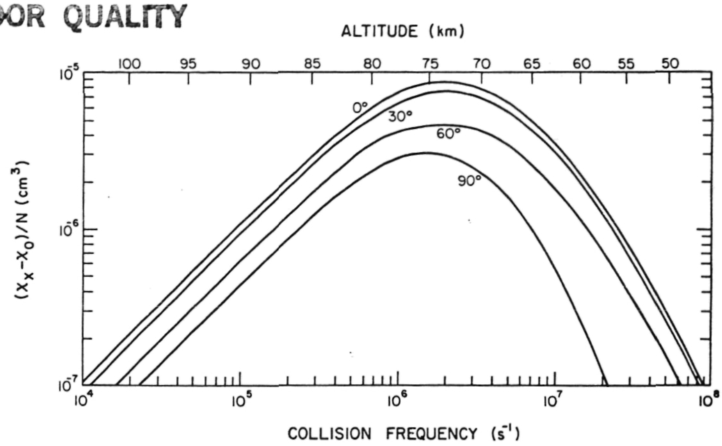

Figure 3. The variation of specific differential absorption index with monoenergetic electron collision frequency for four propagation angles.

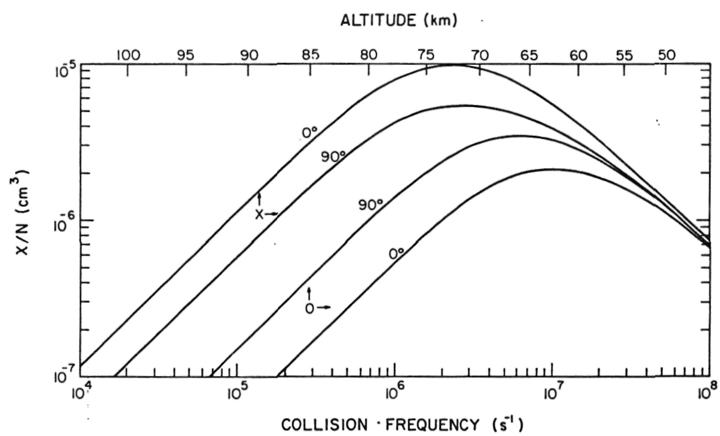

Figure 4. The variation of specific absorption index with monoenergetic electron collision frequency for the two characteristic modes (O and X) of longitudinal (0°) and transverse (90°) propagation.

However this is true only down to a certain altitude, indicated by the short vertical lines in Figure 4. At altitudes below about 68 km (for 90°) or 64 km (for 0°) the situation changes and the upper sign gives the extraordinary wave properties, the lower sign the ordinary wave properties. This has produced some confusion in the literature where it has been implied that the differential absorption changes sign at low altitudes. There is experimental evidence for a change of sign at low altitudes but it is not contained in magnetoionic theory, in either the Appleton-Hartree or Sen-Wyller formulations.

The preceding figures have been calculated for a particular frequency. The effect of changing frequency is illustrated in Figure 5 from JACOBSEN and FRIEDRICH (1979). The data are presented for a realistic electron density

profile (in part represented by the line labelled "plasma frequency"). Figure 5(a) is a Faraday rotation experiment measuring a quantity (deg/km) proportional to ($\mu_o - \mu_x$). Taking 0.5°/km as a practical lower limit of detection and signal loss at −20 dB (relative to 50 km) shows that a low frequency (about 1 MHz) would allow the measurement of electron density between about 58 and 67 km. Increasing the frequency to 10 MHz would change the range of altitude so that the lower limit is about 65 km and the upper limit is above 80 km.

Figure 5(b) illustrates the corresponding situation for an experiment measuring differential absorption. Here, a frequency near 2 MHz would allow a useful measurement of electron density to the lowest possible altitude, about 62 km. The upper limit would be 80 km. A frequency 5 MHz (or more) would raise the altitude range of the measurements.

The data of Figure 5 show clearly why a single-frequency experiment is of limited value in the real ionosphere. This restriction has lead most experimenters to use two or more frequencies.

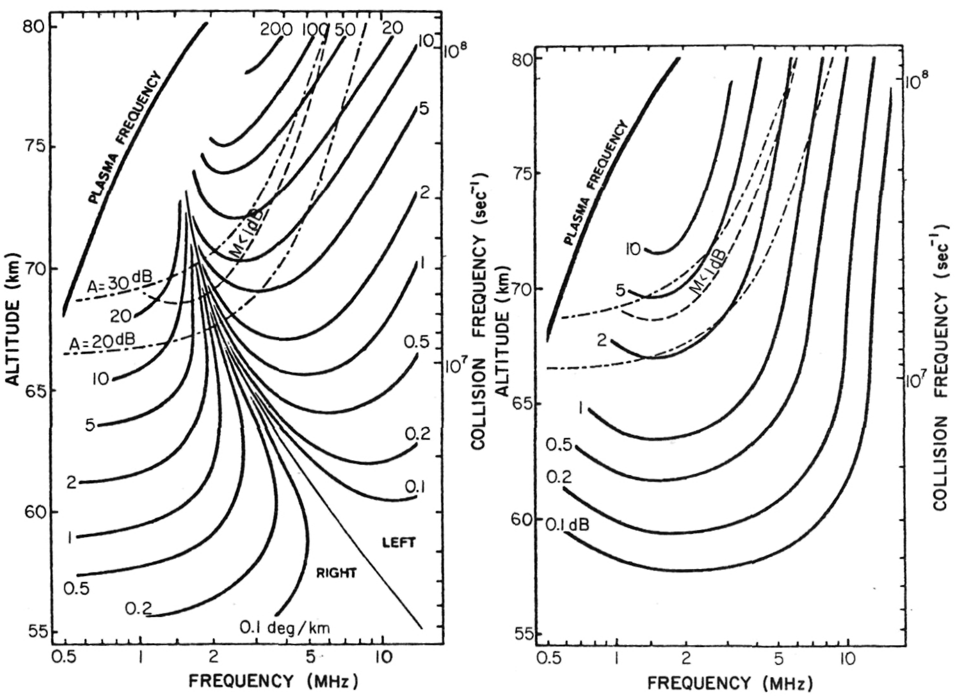

Figure 5. Contours of constant Faraday rotation (a) and differential absorption (b) for a high density summer profile in deg/km and dB/km, respectively. A value of 0.5 deg/km and 0.5 dB/km may be considered as the detection limit for good measurements. The upper height limitation is either determined by signal loss, indicated by A = −20 or 30 dB relative to the value at 50 km, or by loss of detectable double spin modulation, M, e.g. M < 1 dB (differential absorption > 25 dB) (JACOBSEN and FRIEDRICH, 1979).

EXPERIMENTS FOR SOUNDING ROCKETS

The first successful rocket-borne CW propagation experiment was developed by SEDDON (1953). This was the dispersive Doppler technique in which signals at two harmonically related frequencies (24.53 and 73.60 MHz, in the early experiments) were transmitted from the rocket to a receiving system on the ground. The higher frequency also served as the carrier of FM/FM telemetry. One major problem, antenna breakdown in the altitude range 60 to 100 km, was solved by reducing the transmitted power in the early part of the flight.

Modern experiments using CW propagation make two major changes from that of Seddon. First, the transmitter is located on the ground and the receiving system in the rocket payload. This eliminates the antenna breakdown problem and simplifies the payload construction (receivers are smaller and use less power than do transmitters). It does, however, require that the payload have a separate telemetry system.

The second, perhaps more fundamental change, is the use of the two characteristic modes at the same frequency (or, in one version, separated by 500 Hz) rather than harmonically related frequencies. This approach is particularly attractive for the D region where differential absorption can be used in addition to differential phase. (Note that differential phase is a general term: it includes both the dispersive Doppler and Faraday rotation experiments.)

In a typical experiment a 100 W CW signal is radiated from a simple dipole antenna near the ground-based transmitter. The frequency is generally within the range of 2 to 10 MHz. Several, independent systems having different frequencies are generally required to obtain a complete electron density profile in the D and E regions.

The sounding rocket is launched on a trajectory that makes the line-of-sight from the transmitting antenna as near vertical as possible. (Safety considerations are usually the limiting factor.) The rocket payload contains receiving systems, usually one for each frequency being used. The receiving antennas may be inside the payload (if the payload shell is nonmetallic) or maybe external.

A sounding rocket is usually spin stabilized. The spin frequency is 3 to 10 Hz, depending on the type of rocket being used, unless a de-spin system is included to reduce the spin. In CW propagation experiments the highest possible spin frequency is desired. As the receiving antenna spins with the rocket the signal fed to the receiver is modulated sinusoidally: maximum amplitude occurs when the transmitting and receiving antennas are parallel, minimum (initially zero) amplitude occurs when they are perpendicular.

The linearly polarized transmitted signal can be considered to be decomposed into the two circularly polarized characteristic modes. (In the special case of equatorial experiments, transverse propagation leads to characteristic modes which are linear.) In the ionosphere, the difference in refractive index of the two modes produces a phase difference which appears to the receiving antenna as a rotation of the plane of polarization (Faraday rotation). A spatial phase reference is accomplished by inclusion in the payload of a magnetic aspect sensor in the payload. (Other systems, such as solar sensors or a VHF radio signal, have also been used.)

The quantity measured in this experiment is the Faraday rotation rate, the rate of change of phase of the envelope of the received signal, relative to that of the spatially fixed reference. This measurement can be made very accurately:

a phase-locked loop is effective in minimizing the effect of atmospheric noise, the most significant natural limit on accuracy.

Once the Faraday rate has been obtained it can be converted to electron density. This involves additional information: the trajectory of the rocket (position and velocity as a function of time), a model for the geomagnetic field and a model for electron collision frequency. The latter is not so important for the Faraday rotation experiment as it is for the differential absorption experiment.

Radio wave absorption provides an alternative to phase as a method of measuring electron density. As with the phase experiment the differential behavior of the two characteristic modes is used. Considering the same instrumentation as used for the Faraday rotation experiment, the effect of the difference in absorption coefficient of the two characteristic modes is to change the polarization from linear to circular (when the extraordinary mode has been totally absorbed). Thus, the effect on the modulation of the signal received at the spinning rocket is a reduction in the depth of modulation. This effect occurs concurrently with the phase shift of the Faraday rotation and the modulation changes in the manner shown in Figure 6, from BENNETT et al. (1972). (The reference, in this instance, is a VHF signal which experiences neither Faraday rotation nor differential absorption.)

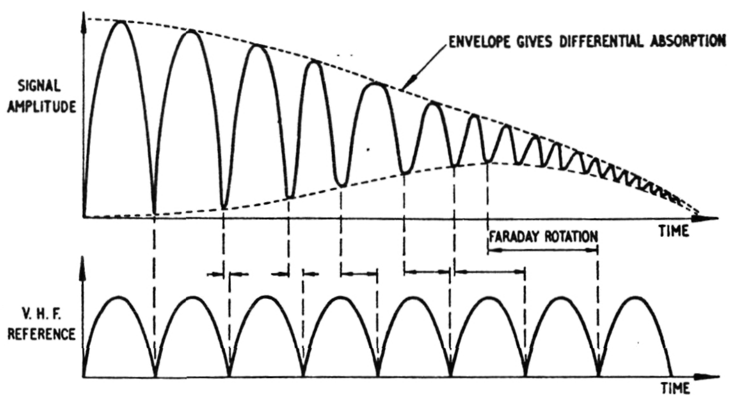

Figure 6. Simplified form of received rocket signal illustrating the measurement of Faraday rotation and differential absorption (BENNETT et al., 1972).

If the angle between the receiving antenna and the major axis of the polarization ellipse is θ then the amplitude of the signal (the modulation) is given by

$$y = \sqrt{P + Q \cos 2\theta}$$

where P and Q are constants which define the shape of the ellipse. BENNETT et al. (1972) use the two extrema ($y_{max} = \sqrt{P + Q}$ and $y_{min} = \sqrt{P - Q}$) to calculate the differential absorption:

$$A = 20 \log_{10} \left(\frac{y_{max} - y_{min}}{y_{max} + y_{min}} \right)$$

C-3

Torkar and Friedrich (quoted in JACOBSEN and FRIEDRICH, 1979) use a least-squares fit to the waveform to achieve greater accuracy (particularly in the presence of noise).

A different approach is used by MECHTLY et al. (1969) and MECHTLY (1974). The two characteristic modes are separately generated using two transmitters each feeding a circularly polarized antenna. The two transmitters are separated in frequency by 500 Hz which causes the polarization ellipse to rotate. The essence of the experiment is that a fixed depth of modulation is introduced by making the power of the transmitter for the O-mode 10 dB greater than that of the transmitter for the X-mode. As the X-mode is absorbed, the power of that transmitter is increased so that the depth of modulation is maintained.

The differential absorption (in dB) is immediately obtained from the change in transmitted power, which is recorded during the flight. This has proved to be a very sensitive measurement, allowing 0.1 dB accuracy (the simpler systems give about 0.5 dB). Another advantage is that the sign of the differential absorption is retained; the simpler systems must assume that the X-mode experiences greater absorption than does the O-mode. This refinement has allowed SMITH et al. (1983) to show that, at altitudes below about 56 km the O-mode is, unexpectedly, subject to greater absorption than is the X-mode.

The design of the transmitter and antenna for the ground-based part of the experiment is straightforward. At least one launch site (Kiruna, Sweden) has permanently installed facilities for the CW propagation experiment.

The payload instrumentation comprises the receiving system (antenna and receiver) together with a spin-reference system and telemetry. The antenna may be an electric dipole external to the payload (as in JACOBSEN and FRIEDRICH, 1979) or a magnetic dipole contained within a nonmetallic section of the payload (as in MECHTLY et al., 1967).

The received signal has a narrow bandwidth so that, to minimize the effect of atmospheric noise, the receiver should also have a narrow bandwidth. The only major design decision concerns the receiver AGC time constant. The effect of a short time constant (1 s) is illustrated in the upper part of Figure 7. The rocket spin rate is 6 Hz and there is distortion of the modulation due to insufficient filtering of the AGC voltage. Increasing the time constant to 10 s (as in the lower part of Figure 7) gives a satisfactory waveform.

An alternative approach (as in JACOBSEN and FRIEDRICH, 1979) is to use a very short time constant so that the AGC voltage contains the modulation information. A careful calibration of the receiver is needed because of the nonlinearity of the AGC characteristic.

In most instances the modulation of the received signal is telemetered and recorded for subsequent processing. Sometimes (as in FRANCE and WILLIAMS, 1976) the data are partially processed (in this case a phase measurement) before transmission.

The differential absorption experiment is not useful in the midlatitude nighttime ionosphere. The Faraday rotation experiment can be used but the small values of electron density and increased atmospheric noise make it difficult to achieve the accuracy (100 cm^{-3}) of daytime experiments. The sources of error and comparisons of several versions of the Faraday rotation experiment have been discussed by SMITH and GILCHRIST (1984). Since that publication, further experiments with phase-locked loops have shown that atmospheric noise can be much reduced, leaving the phase reference (in their experiment a magnetic aspect sensor) as the most important source of error.

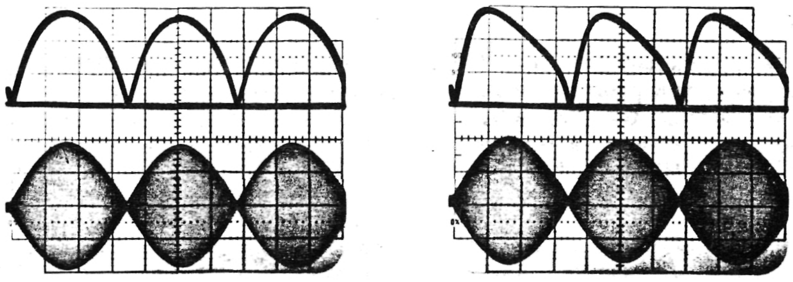

Figure 7. Receiver outputs with AGC time constants of (a) one second and (b) ten seconds.

Experiments at the magnetic equator must be considered separately because the characteristic modes are linear. No Faraday rotation takes place: the polarization ellipse does not rotate but changes its ellipticity. For this reason, the successful experiments have been restricted to absorption measurements (KANE, 1974; SOMAYAJULU et al., 1971). Typically the two modes are separately transmitted from ground-based dipole antennas; the O-mode from a N-S dipole, the X-mode from an E-W dipole (magnetic coordinates). A single transmitter is switched between these two antennas. The difference in absorption of the two modes appears as a square-wave modulation at the receiver in the rocket payload.

A differential phase experiment for the equatorial ionosphere was demonstrated during the CONDOR campaign in Peru in 1983 (SMITH and HALPERN, unpublished). The data are satisfactory to an altitude of about 105 km. The scattering of the radio wave by the electrojet prevents the determination of phase at greater altitudes. At present it appears that propagation experiments are not practical for the upper E region at the equator.

The model for the earth's magnetic field that has been most widely used is that of CAIN et al. (1967). A newer model is IGRF 80 (PEDDIE, 1982), which is recommended for current use. The difference between the two models is probably insignificant except for transverse propagation (as at the equator) where the two models may lead to propagation angles differing by 1°.

The model for electron collision frequency has been discussed in SMITH et al. (1978). They recommend

$$\nu_M = 6.3 \times 10^5 \ p$$

where p is the pressure (in N m^{-2}) from CIRA 1972. It is interesting to note, from Figure 3, that electron densities determined from the differential absorption experiment are insensitive to the value of collision frequency at altitudes near 75 km.

The height resolution is ultimately limited by the spin rate and velocity of the rocket. In practice, a time interval of 1 sec is needed to obtain a value of electron density. This limits the altitude resolution (in the D region) to about 1 km. The data from the propagation experiment can be effectively combined with data from a probe (in the same rocket payload) to

obtain an electron density profile of good absolute accuracy and good height resolution.

The probe experiment has been described by SMITH (1969). Theory and experiment support the proportionality of probe current (I), measured at a fixed positive voltage (usually 4 V), and electron density (N). The procedures for combining the two data sets have been described in MECHTLY et al. (1967) and by SMITH and GILCHRIST (1984). The ratio N/I is calculated for averages of each quantity obtained from a 1-second interval of data. A semi-log plot is then made of the (N/I) average value as a function of altitude. In general the ratio may not be constant; any change, however, is expected to be slowly varying with altitude. In this way, a calibration factor (the best estimate of N/I) as a function of altitude is obtained which can then be used to multiply individual values of probe current (measured at 0.1-second intervals) to obtain the final profile. Examples of electron density profiles illustrating the variability of electron density in the wintertime midlatitude D region are shown in Figure 8, from SMITH et al. (1978).

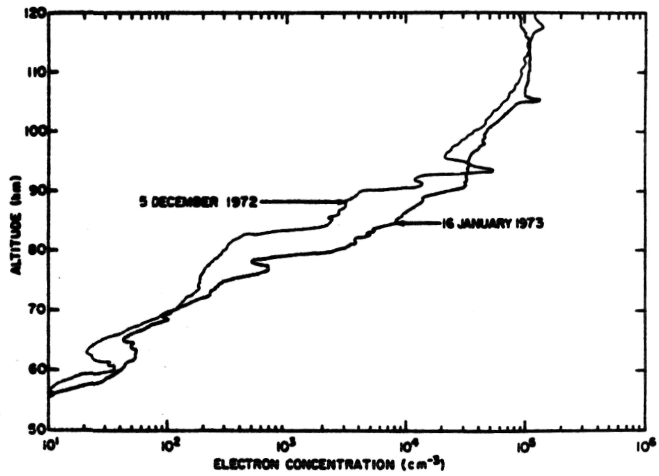

Figure 8. Electron density profiles for 5 December 1972 and 16 January 1973. These were, respectively, days of low and high absorption at 1.8 MHz.

The details of the implementation of the propagation experiment of the University of Illinois are contained in Aeronomy Reports, available on request from the Aeronomy Laboratory, Department of Electrical and Computer Engineering, 1406 West Green Street, Urbana, Illinois 61801, U.S.A. These are:

Aeronomy Report No. 14. J. E. Salah and S. A. Bowhill, Collision frequencies and electron temperatures in the lower ionosphere, August 1966.

Aeronomy Report No. 20. M. M. Rao, Studies of the equatorial ionosphere using rockets, July 1967.

Aeronomy Report No. 30. R. C. Condon, K. Seino and E. A. Mechtly, Part 1, Design of polarization adjustment instrumentation for a rocket propagation experiment, Part 2, Analysis of a rocket experiment to measure ionospheric electron density, December 1968.

Aeronomy Report No. 35. A. G. Slekys and E. A. Mechtly, Aeronomy Laboratory system for digital processing of rocket telemetry tapes, March 1970.

Aeronomy Report No. 37. E. A. Mechtly, P. E. Monro, N. Golshan and R. S. Sastry, FORTRAN programs for calculating lower ionosphere electron densities and collision frequencies from rocket data, July 1970.

Aeronomy Report No. 45. R. F. Lodato and E. A. Mechtly, Rocket measurements of electron collision frequency, September 1971.

Aeronomy Report No. 64. J. C. Ginther and L. G. Smith, Studies of the differential absorption experiment, December 1974.

Aeronomy Report No. 73. R. W. Fillinger, Jr., E. A. Mechtly and E. K. Walton, Analysis of sounding rocket data from Punta Chilca, Peru, July 1976.

Aeronomy Report No. 85. B. E. Gilchrist and L. G. Smith, Rocket measurement of electron density in the nighttime ionosphere, April 1979.

Aeronomy Report No. 101. L. Dean and L. G. Smith, An improved pulse-height analyzer for energetic particle measurements in the upper atmosphere.

Aeronomy Report No. 113. M. K. McInerney and L. G. Smith, Rocket observations of the ionosphere during the eclipse of 26 February 1979, May 1984.

ACKNOWLEDGEMENT: The preparation of this report was supported by the National Aeronautics and Space Administration under grant NGR 14-005-181.

REFERENCES

Aiken, A. C., J. A. Kane, and J. Troim (1964), Some results of rocket experiments in the quiet D region, J. Geophys. Res., 69, 4621.

Bennett, F. D. G., J. E. Hall, and P. H. G. Dickinson (1972), D-region electron densities and collision frequencies from Faraday rotation and differential absorption measurements, J. Atmos. Terr. Phys., 34, 1321.

Budden, K. G. (1965), Effect of electron collisions on the formulas of magneto-ionic theory, Radio Sci., 69D, 191.

Cain, J. C., S. J. Hendricks, R. A. Langel, and W. V. Hudson (1967), A proposed model for the international geomagnetic reference field 1965, J. Geomagn. Geoelect., 19, 335.

Cartwright, D. G. (1964), A 10-kilocycle per second Doppler observation of the intermediate layer of the nighttime ionosphere, J. Geophys. Res., 69, 4031.

France, L. A., and E. R. Williams (1976), An improved Faraday rotation experiment for rocket measurements of lower ionosphere electron concentrations, J. Atmos. Terr. Phys., 38, 957.

Hall, J. E. (1973), Lower ionosphere electron densities from rocket measurements employing LF radio propagation and dc probe techniques, Planet. Space Sci., 21, 119.

Jacobsen, T. A., and M. Friedrich (1979), Electron density measurements in the lower D-region, J. Atmos. Terr. Phys., 41, 1195.

Kane, J. A. (1961), Re-evaluation of ionospheric electron densities and collision frequencies derived from rocket measurements of refractive index and attenuation, J. Atmos. Terr. Phys., 23, 338.

Kane, J. A. (1974), Rocket-borne radio measurements of D- and lower E-region electron density profiles at the magnetic equator, Ind. J. Radio Space Phys., 3, 99.

Kimura, I., and K. Hirao (1971), Rocket experiment of electron density measurement by VLF Doppler and probe methods, Rep. Iono. Space Res. Japan, 25, 59.

Manchester, R. N. (1965), Correction to paper by H. K. Sen and A. A. Wyller, J. Geophys. Res., 70, 4995.

Mechtly, E. A. (1974), Accuracy of rocket measurements of lower ionosphere electron concentrations, Radio Sci., 9, 373.

Mechtly, E. A., S. A. Bowhill, L. G. Smith, and H. W. Knoebel (1967), Lower ionosphere electron density and collision frequency from rocket measurements of Faraday rotation, differential absorption and probe current, J. Geophys. Res., 72, 5239.

Peddie, N. W. (1982), International geomagnetic reference field: the third generation, J. Geomag. Geoelect., 34, 309.

Pfister, W. (1954), Studies of the refractive index of the ionosphere: the effect of the collision frequency and of ions, The Physics of the Ionosphere, Cambridge, 394.

Ratcliffe, J. A. (1962), The Magneto-Ionic Theory and its Application to the Ionosphere, Cambridge.

Seddon, J. C. (1953), Propagation measurements in the ionosphere with the aid of rockets, J. Geophys. Res., 58, 323.

Sen, H. K., and A. A. Wyller (1960), On the generalization of the Appleton-Hartree magnetoionic formulas, J. Geophys. Res., 65, 3931.

Smith, L. G. (1969), Langmuir probes in the ionosphere, in Small Rocket Instrumentation Techniques, edited by K. I. Maeda, 1-15, North-Holland, Amsterdam.

Smith, L. G., and B. E. Gilchrist (1984), Rocket observations of electron density in the nighttime E region using Faraday rotation, Radio Sci., 19, 913.

Smith, L. G., M. K. McInerney, and H. D. Voss (1983), Electron density and energetic particle precipitation observed during the eclipse of 26 February 1979, J. Atmos. Terr. Phys., 45, 427.

Smith, L. G., E. K. Walton, and E. A. Mechtly (1978), Vertical incidence absorption calculated using electron density profiles from rocket experiments and comparison with observations during the winter anomaly, J. Atmos. Terr. Phys., 40, 1185.

Somayajulu, Y. V., M. B. Avadhanulu, K. S. Zalpuri, and S. C. Garg (1971), Some preliminary results of rocket sounding of the D region at the geomagnetic equator, Space Res., 11, 1131.

Dq-46

N86-26734

158

7617

NC999967

9. MEASUREMENT TECHNIQUES FOR MIDDLE ATMOSPHERE ELECTRIC FIELDS

N. C. Maynard*

Laboratory for Extraterrestrial Physics
Goddard Space Flight Center
Greenbelt, Maryland 20771

ABSTRACT

Both the difficulty of access to the region and the difficulty of measurement techniques has caused the middle atmosphere to be one of the last near-earth regions to be explored electrodynamically. Recent improvements in measurement techniques spurred by the apparent discovery of large V/m electric fields have resulted in new thrusts into this previously neglected field. Both double probe techniques and field mills ~~have been~~ were adapted for middle atmosphere measurements. A brief description of each technique is given along with some of the pitfalls and difficulties associated with middle atmosphere electric field measurements. Measurement of mV/m level electric fields is now possible in the D region. The detection of V/m level fields in the lower ionosphere remains controversial; however, increasing evidence is accumulating for their existence.

I. INTRODUCTION

The difficulty of access to most of the middle atmosphere, the region between the tropopause and the mesopause, has in the past limited attempts to measure electric fields (see review by MAYNARD, 1980). In addition, measurement techniques which work in the ionosphere or which are useful in the troposphere require adaptation to the weakly ionized environment of the stratosphere and mesosphere. Some of these adaptations have met with limited to good success; others have failed.

The first electric field measurements in the middle atmosphere were made in the lower stratosphere by adapting the double floating probe technique (see Section II for a discussion of techniques) to fly on balloons (MOZER and SERLIN, 1969). These measurements were primarily attempted in order to study the projection down equipotential magnetic field lines of magnetospherically and ionospherically generated electric fields. Thus, primary attention was paid to the horizontal components. In an average sense many of the features of the magnetospheric convection pattern were reproduced (see MOZER and LUCHT, 1974). Differences have been explained away as thunderstorm effects or the difference between an average measurement and a point measurement (KELLEY and MOZER, 1975).

The first measurements in the upper stratosphere and lower mesosphere were made by BRAGIN et al. (1974) and TYUTIN (1976) using a field mill on a rocket. Their apparent observations of large V/m vertical electric fields near 60 km has been greeted with some skepticism (see BERING et al., 1980). Similar reaction was given to HALE and CROSKEY'S (1979) measurement of V/m electric fields in the same region using asymmetric double probes. Other attempts at measurements of electric fields in the mesosphere by BERING et al (1977) and KELLEY et al. (1983) using double probes have admittedly resulted in measurements of artifacts created by the presence of the rocket payload. However, a

* Present address: Air Force Geophysics Laboratory, Hanscom AFB, MA 01731

payload designed to emphasize symmetry has been successful in measuring mV/m electric fields in the D region (MAYNARD et al., 1984) and has detected evidence of V/m electric fields similar to those observed by Hale and Croskey in the lower mesosphere (MAYNARD et al., 1981). The large electric fields are seen under some conditions but not others (see also HALE et al., 1981), and are seen far less often than would be necessary for the constant layer inferred by TYUTIN (1976).

This paper will briefly review the basic measurement techniques and explore the problems in applying these techniques to the middle atmosphere regions.

II. BASIC TECHNIQUES FOR ELECTRIC FIELD MEASUREMENTS

Field Mills

Field mills operate on the principles of electrostatic induction rather than electrical conduction. A field mill consists of a test plate that is alternately exposed to and shielded from the lines of force of the electric field by a grounded cover (see CHALMERS, 1967; MAPLE and WHITLOCK, 1955). The induced surface charge on the plate is a function of the electric fields exposed to the plate and becomes a function of time as the plate is alternatively exposed and shielded.

$$Q(t) = - \varepsilon_o EA(t)$$

where Q is the surface charge, ε_o is the free space dielectric constant, E is the electric field and A is the exposed area. The displacement current is the derivative of the surface charge while the conduction current is proportional to Q. DETTRO and SMITH (1982) have shown that by letting the exposed area vary in a sinusoidal fashion (proportional to $(1 + \sin \omega t)$) the amplitude and phase of the resulting ac component of the total current are easily related to the displacement and conduction currents and thence to the electric field (E) and polar conductivity (λp) for positive or negative ions.

If $\quad i_{ac} = M \cos (\omega t - \phi)$

then $\quad E = - \dfrac{M \cos \phi}{\varepsilon_o A_o \omega}$

and $\quad \lambda p = \dfrac{M \sin \phi}{EA_o} = \varepsilon_o \omega \tan \phi$

where A_o is the maximum area exposed, ω is the rotation frequency of the mill, and M and ϕ are the amplitude and phase of the signal. Since the electric field is a vector quantity, more than one of these devices is necessary to define the vector. Dettro and Smith suggest one at the front end and one on the side of the payload. The resulting payload is expected to detect electric fields down to 0.1 V/m and will soon be tested. Figure 1 shows a photo of the Dettro and Smith detector. TYUTIN'S (1976) sensor was similar in principle but less sophisticated.

Factors which make the measurement difficult include (1) the very small current levels (picoamps) of the desired signal which makes the device sensitive to leakage currents and sources of noise in the system, (2) the need for a uniform work function over the sensor surface, and (3) photoemission currents in daylight. A question not addressed by TYUTIN (1976) is whether the signals measured could be influenced by charges on the payload or by the sheaths resulting from the presence of the payload in the plasma.

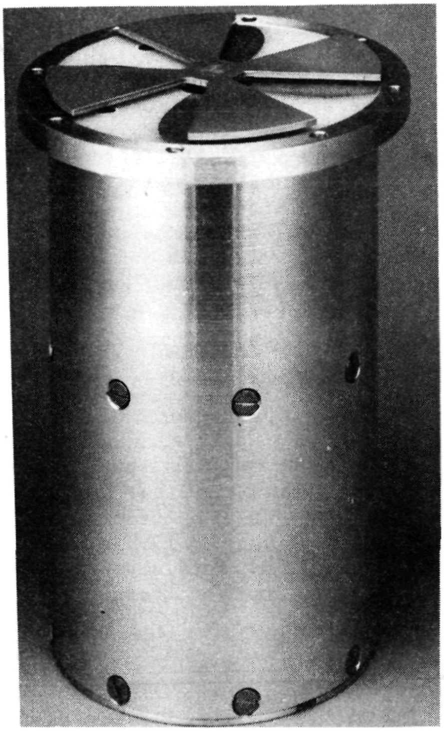

ORIGINAL PAGE IS
OF POOR QUALITY

Figure 1. Photo of the field mill instrument of DETTRO and SMITH (1982) for making electric field measurements from a rocket. The rotor and stator (underneath) can be seen at the top of the instrument.

This technique is commonly used for ground-based measurements and has been used on airplanes (see KASEMIR, 1965). Its applications aboard rockets for use in a partially ionized gas such as the mesosphere is currently limited to the measurements of TYUTIN (1976). It is hoped that the proposed measurements of DETTRO and SMITH (1982) will either confirm Tyutin's results or establish where and over what range valid middle atmosphere electric field measurements can be made with the field mill.

Passive Double Probes

The double floating probe technique for electric field measurements in a plasma was developed for space use by AGGSON (1969) and FAHLESON (1967). The technique is now commonly used in the ionosphere on both sounding rockets and satellites and has been adapted for use in the low density plasmas in the magnetosphere and beyond (see MAYNARD et al., 1983; and PEDERSEN et al., 1984).

The basic technique utilizes two floating Langmuir probes. Any body immersed in an ionized medium will float at a potential relative to the medium such that the net current to that body is zero. In the ionosphere, the basic balance is reached between currents from electron collection and positive currents from ion collection and photoemission. If two probes have symmetry with respect to their axis and to the supporting spacecraft body, then each floating potential will be the same if no electric fields exist. A difference in potential in the medium from electric fields, either ambient or generated from the motion of the sensor system across magnetic field lines ($\underline{v} \times \underline{B}$), will be reflected in the relative floating potentials of each sensor. Measurement of each of these potentials relative to the payload or spacecraft and their differential subtraction leads to a measurement of the electric field

$$(V_1-V_s) - (V_2-V_s) = V_1-V_2 = (\underline{E} + \underline{v} \times \underline{B}) \cdot \underline{d}$$

where V_1, V_2 and V_s are the potentials of each sensor and the spacecraft, $\underline{d}$ is the vector separation distance between the sensors, $\underline{v}$ is the spacecraft velocity and $\underline{B}$ is the magnetic field. Both spherical and cylindrical sensors have been used.

Sources of error include asymmetries in photoemission and contact potentials, current drawn by the voltmeter, wakes generated by the central body, and inaccurate knowledge of both attitude and B which are necessary to do the $\underline{v} \times \underline{B}$ subtraction. In low density plasmas, photoemission currents from the central body and support structures can be collected by the sensor and become a significant fraction of the total current collected. Symmetry of the system configuration helps to reduce problems from several of the above error sources. Measurements at the mV/m level are achievable.

If less accuracy is required, it is possible to make a double probe measurement using asymmetric probes (see HALE et al., 1981). In this case, the potential difference is partially related to the ambient density since some of the error currents do not change. As the collection of current from the medium changes, the potential of each probe must react differently in affecting a net current balance. In this case, where accuracies are in the fraction of a V/m range, the subtraction of $\underline{v} \times \underline{B}$ (a few 10's of mV/m) becomes insignificant. An asymmetric measurement in the vertical direction is very easy on small parachuted payloads by measuring the difference in potential between an electrode on the parachute lanyard and the conducting payload.

Figure 2 shows a payload configuration that has been successful in the D region at the mV/m level by emphasizing symmetry. Section III will discuss problems relative to the application of the double probe technique for measurements in the middle atmosphere.

Active Double Probes

A variation on the double probe technique in weakly ionized cases is to create ionization in the vicinity of the probes using a radioactive source (see STERGIS et al., 1957; MARKSON, 1976). This technique has been successfully used in the troposphere on airplanes. The balloon measurements of the vertical electric field by Stergis et al. seem to give higher values than other measurements (e.g., KASEMIR, 1977). The radioactive source enhances the currents available for collection making the system less susceptible to noise. Since this technique has not been used above balloon altitudes, it will not be discussed further.

III. PROBLEMS RELATIVE TO DOUBLE PROBE MEASUREMENTS IN THE MIDDLE ATMOSPHERE

Upper Mesosphere Measurements

Several attempts at electric field measurements in the D region have suffered from wake effects which have prevented useful ambient measurements (see BERING et al., 1977; and KELLEY et al., 1983). In each case, symmetric probes attached to a large cylindrical central body payload were used. Kelley et al. found V/m signals which were not of natural origin in their data at mesospheric altitudes. In the denser plasmas of the E and F region, this arrangement makes acceptable measurements, although it should be noted that BERING (1983) has identified magnetic wake effects in data from some configurations of double probes in the lower ionosphere.

In order to better understand some of these effects it is instructive to look at data taken in the mesosphere by a symmetric payload similar to that used by MAYNARD et al. (1981) (see Figure 2). Figure 3 shows a schematic of

ORIGINAL PAGE IS
OF POOR QUALITY

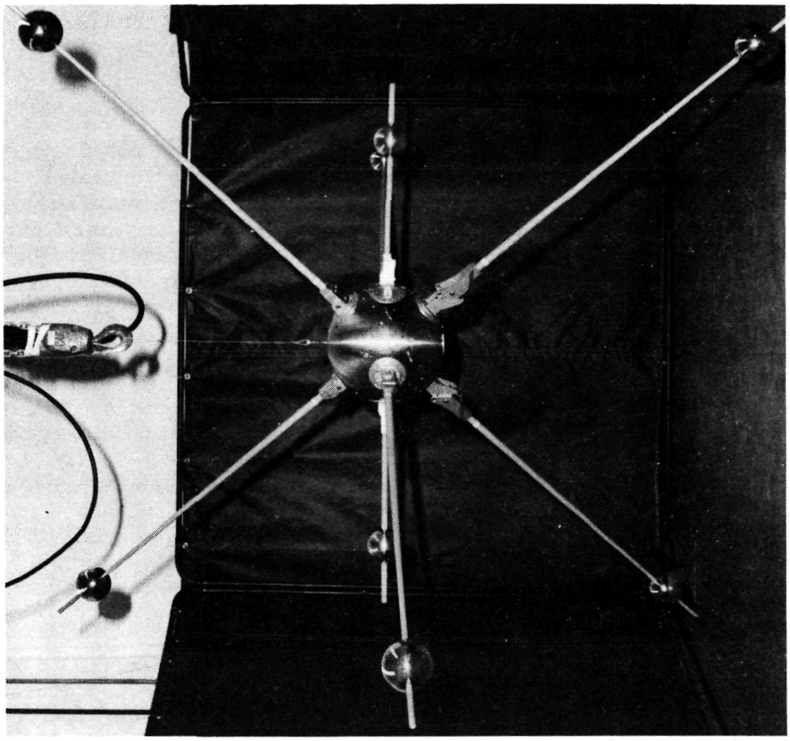

Figure 2. Photo of a symmetric, small central body payload for making double probe electric field measurements while free-falling through the middle atmosphere (see also MAYNARD et al., 1981).

this payload with all the booms rotated into the plane of the paper in order to compare antenna lengths. The spherical payload is shown attached to the rocket motor. The presence of this large object in the plasma can disturb measurements in its vicinity from wake effects. Note that in the horizontal direction, the inertia booms (instrumented for the most recent flights), the projections of the X and Y axes (located at 45° to the spin axis) into the spin plane, and the Z axis which is nominally in the spin plane, provide measurements at three different baselines (1.04 m, 1.72 m, 2.30 m, respectively). As the payload spins, a sinusoidal waveform is generated on each of these axes which should be proportional according to the ratios of the effective baselines. The X and Y axes have the same measurement baseline as the Z axis, but the effective baseline for the sine wave is reduced by the cosine of the angle of the axis (45°) to the spin plane.

From Figure 3, it is clear that the conditions before payload ejection are drastically different from that of the symmetric conditions after the separation. Figure 4 shows raw data from each axis both before and after separation. Both sets of data were taken above 92 km in the daytime (early morning). Several features are prominent. After separation, all axes show a small sinusoidal signal from the combination of the ambient electric field and $\underline{v} \times \underline{B}$. The I axis also has spike-like features which are due to the shadowing of each sensor by the central body. This reduction in photoemission causes the sensor to seek a new floating potential and symmetry is lost. Data during shadowing

ORIGINAL PAGE IS
OF POOR QUALITY

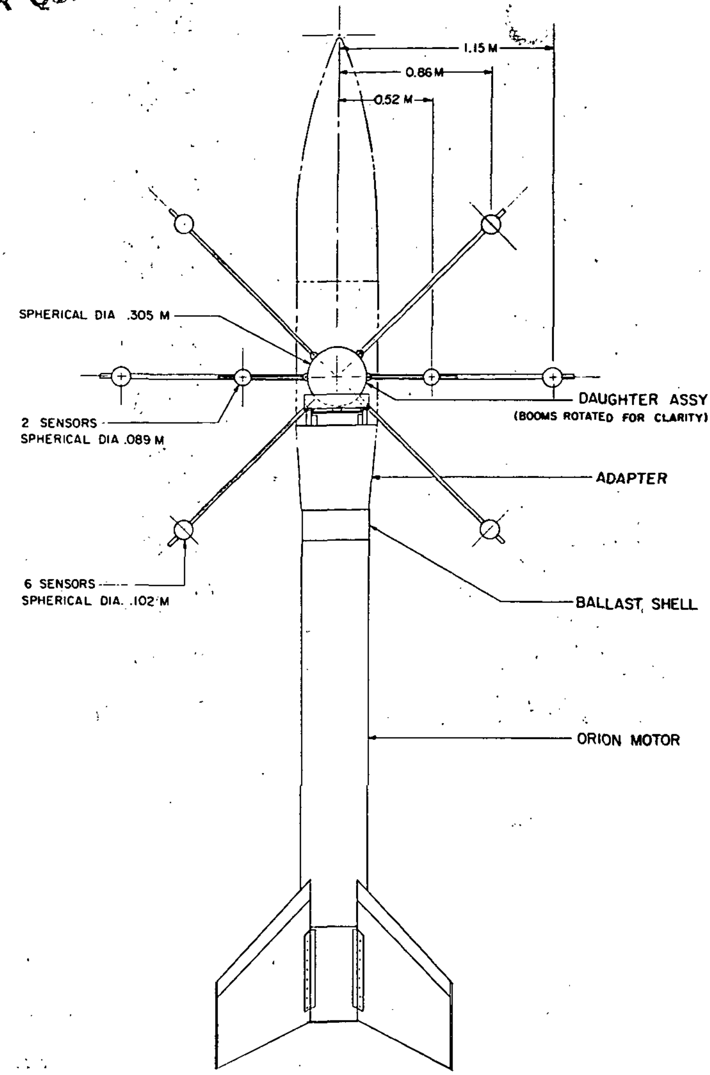

Figure 3. Schematic representation of the payload shown in Figure 2 while still attached to the rocket motor. All booms have been rotated into the plane of the paper for ease in comparing baselines. The envelope of the nose cone is also shown. The baseline dimensions are those that relate the amplitude of the resultant sine waves from the payload spinning through a horizontal electric field. The X and Y axes are at 45° to the spin axis. The Z axis is in the spin plane completing the orthogonal system. The I axis is the short axis which is also in the spin plane and is located 15° from the X Y plane.

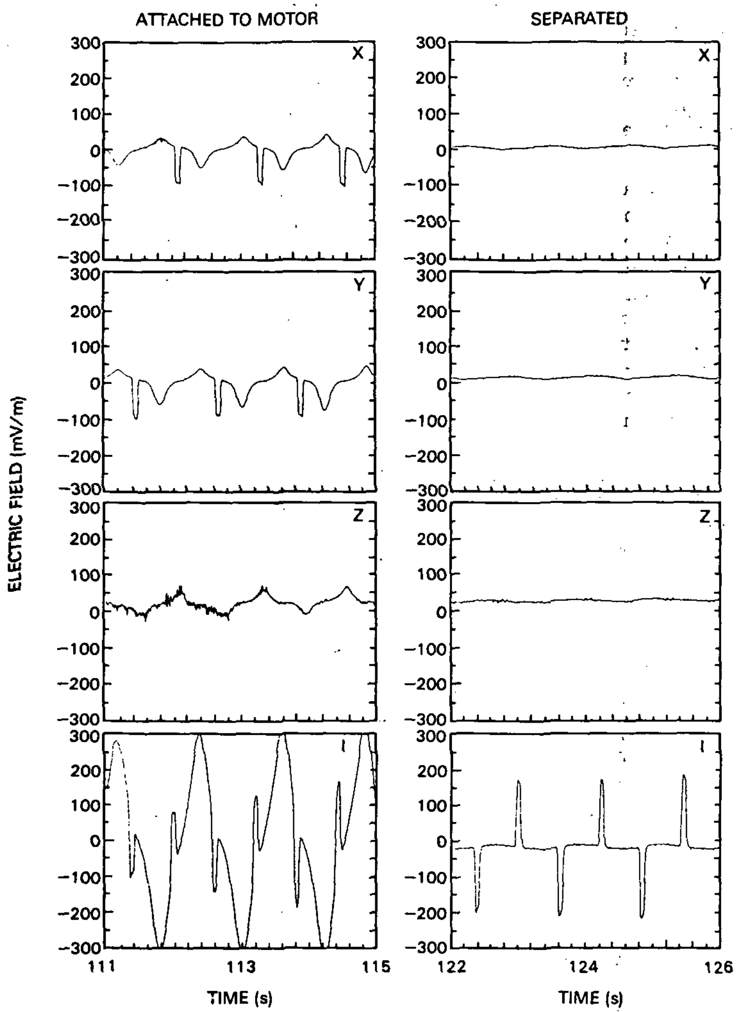

Figure 4. Raw data from each of the four axes on the symmetric double probe payload. The left panels show data while the payload is still attached to the rocket motor, while the right panels show data taken after the payload was separated. The sharp spike-like pulses in several of the panels result when one of the sensors is shadowed by the main body. All data were taken between 90 and 95 km.

must be culled before analysis can be done on the remainder of each spin cycle. Before separation much larger signals which are not real electric fields were seen on all of the axes. The signal is larger on the shorter I axis than on the longer Z axis: similar to the effect reported by KELLEY et al. (1983) (see their Figure 5). The origin of these fields is not clear, but they are clearly artifacts from the presence of the large asymmetric central body. The shadow pulses are seen in the I axis data and from the lower spheres in the X and Y axis data. The Z axis sensors do not get shadowed.

In order to understand where the accuracy breaks down in the highly asymmetric case, Figures 5 and 6 show ratios and differences of the amplitudes from the least squares fits to the data from each of the various length axes for two different flights. All data have been adjusted by their respective baselines so that a ratio of 1 would be expected if no errors exist, as would a difference of zero. Only downleg data are displayed since deployment of the antennas occurred above 90 km. Both flights were from Wallops Island; 31.039 (Figure 5) was just prior to dawn, while 31.038 (Figure 6) was shortly after dawn in sunlight. Comparison of panels C and F each figure shows that the short axis develops error signals just below 100 km on both flights. The ratios and differences show that the other three axes were consistent down to 75 km in darkness (Figure 5) and down to 85 km in sunlight (Figure 6). These altitudes have meaning only for these particular flights. However, several definite conclusions can be inferred from the above discussions relative to accurate mesospheric measurements at the mV/m level:

a. Symmetry must be maintained.
b. The size of the central body should be minimized and a spherical shape is preferred.
c. Separations of the sensors from the body should be greater than 0.5 m and preferably greater than $\sim$5 times the maximum body radius. (This criteria obviously is at best qualitative. The actual requirements will be a function of the plasma density and temperature, body photoemission, probe velocity, and the geometry.)
d. Photoemission from the sensors and the central body should be minimized.

At first glance the daytime measurement appears more difficult because of photoemission. However, low ionization levels also limit the accuracy, especially at low latitudes where nighttime D-region ionization levels can be very low. The problem with photoemission arises when photoelectrons emitted from the main body are collected by the sensor and vice versa. These error currents will not be symmetrical and will therefore affect the floating potential balance. Photoemission is asymmetrical by nature from the directionality of the sun and from variations in surface properties including fingerprints, etc. If it can be minimized, then the daytime errors can be reduced. Metals in general are high photoemitters. Graphite coatings can be used to reduce the photoemission significantly.

Since the $\underline{v} \times \underline{B}$ electric field from the rocket motion is indistinguishable from the ambient electric field by the instrument, it must be vectorially subtracted from the measured electric field. The $\underline{v} \times \underline{B}$ field is calculated using the payload velocity and the spherical harmonic model magnetic field. To make the subtraction it must be transformed to the rocket system using an accurate attitude solution. The payload discussed above uses a gyroscopic reference platform to determine the attitude. Attitude accuracy of 1 to 2° is needed to maintain mV/m accuracy in the final results.

Uniformity of surface properties affects current collection by the sensors. A contact potential between the sensors and the plasma will always

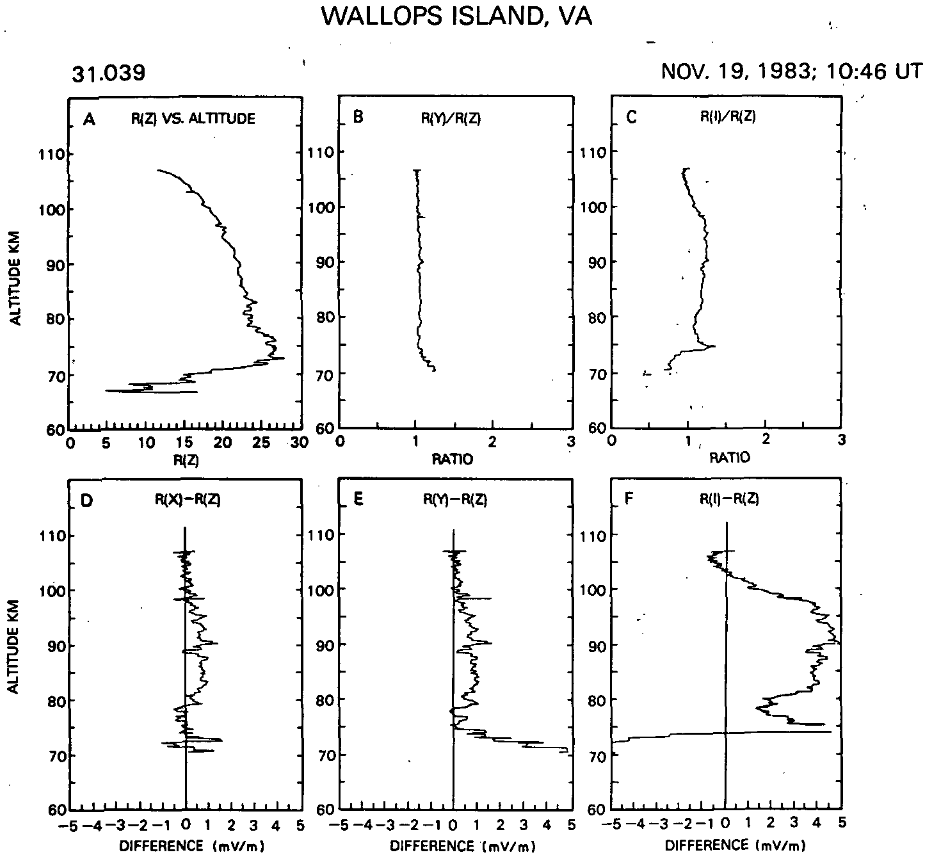

Figure 5. Comparisons of the amplitudes of the least squares fits from each of the axes. The upper panels show the amplitude in the horizontal plane and the ratios of axes (see Figure 3 for axis identification). All data have been normalized so that the expected ratio should be one if no errors exist. The bottom panels show the difference between the shorter axis amplitudes and the long spin plane axis data. A zero difference would be errorless. This flight was in darkness just prior to dawn.

exist. Small variations in surface properties change the effective coupling to the plasma of the sensors and therefore change the contact potential. The contact potential difference between the sensors is an error voltage. This will appear as a dc offset to the signal and must be subtracted from the data. For an axis in the spin plane where the expected signal is a pure sinusoid — the contact potential is just the dc offset. For axes that are at an angle to the spin plane, an electric field along the spin axis will also appear as a dc offset. Contact potentials must be determined by comparison of the data from other axes, and can be checked in most D- and E-region locations where $\underline{E}$ is perpendicular to $\underline{B}$ by satisfying the equation

$$\underline{E} \cdot \underline{B} = 0.$$

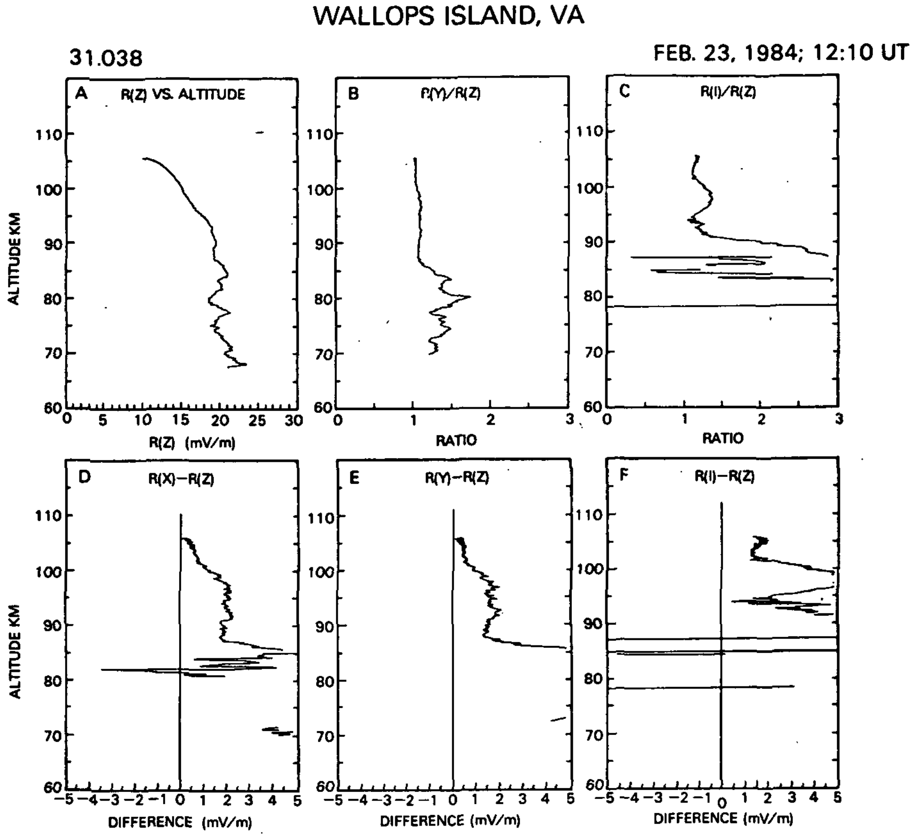

Figure 6. Similar to Figure 5 but for a flight into sunlight shortly after dawn.

Nonconformity to this equation defines the contact potential error. Note that this assumption breaks down in the presence of space charges. Contact potentials do not have a chance to completely settle down on a short rocket flight as surface properties change with outgassing. Some variability over the flight is generally encountered. The assumption is generally made that the variation is relatively small and also slow compared to spin or precession times.

The above discussion emphasizes the difficulties of the measurement in the upper mesosphere. However, mV/m level measurements are possible (see MAYNARD et al., 1984) down to near 70 km where the disappearance of free electrons makes the current balance more difficult and amplifies the effects of some of the above errors. Measurement accuracy is not always good to 70 km. Figure 7 shows the reduced electric field data from one of the flights discussed above. The variations below 85 km on this particular flight are not real as revealed by the difference plots in Figure 6.

Lower Mesosphere and Upper Stratosphere

As we descend in altitude, the conductivity decreases and the measurement becomes more difficult. Positive and negative ion ram currents dominate. The effective collection area for these currents is modified by the flow passing by the sensor. Eventually as free electrons disappear the floating potential de-

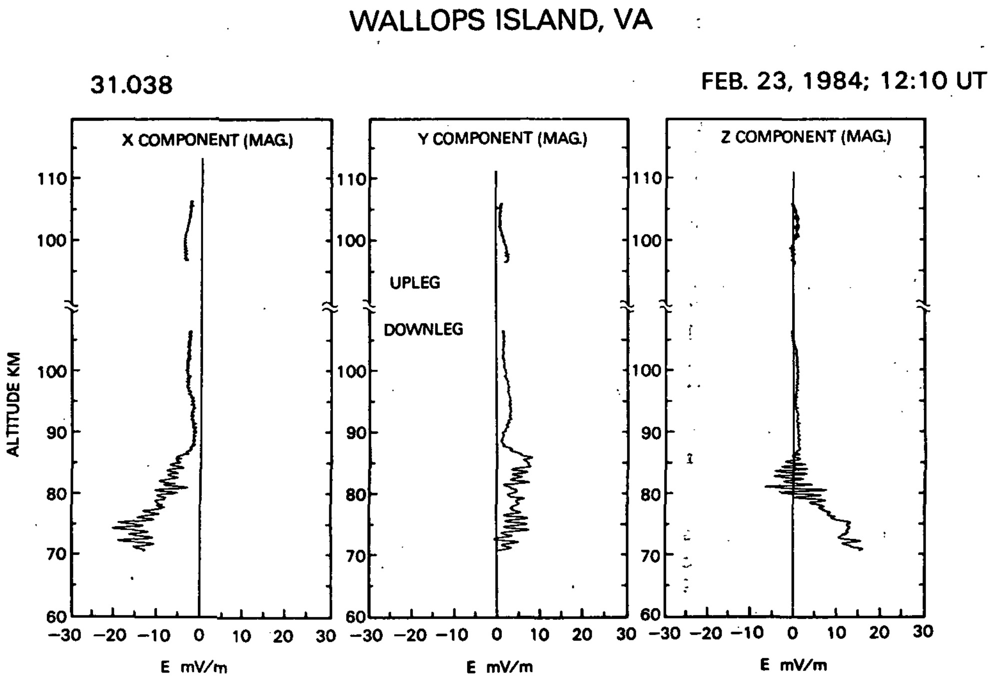

Figure 7. Reduced electric field data from the flight displayed in Figure 6. The data are in a magnetically orientated coordinate system in which Z is along B, X is nearly north and perpendicular to B in the plane containing B and the local vertical, and Y is nearly east and perpendicular to B. The accuracy decreases in this flight below 85 km as shown by the data in Figure 6.

pends on a micro-balance of these ram currents (and photoemission if in sunlight). It is no longer possible to conduct mV/m level measurements from a free-falling payload. Wake effects can become important in a payload moving at supersonic speed.

In the region below 75 km, two double probe techniques have been used to measure middle atmosphere electric fields. Both instruments, the asymmetric double probe of HALE and CROSKEY (1979) and the symmetric double probe of MAYNARD et al. (1981) have, on occasion, detected signals indicating V/m electric fields. Both have considerably reduced accuracy (of the order of ± 0.5 V/m) from the measurements discussed in the previous sections. The free-falling symmetric probe is unable to make any measurements below 45 km because of the high velocities. The parachuted probe such as that of Hale and Croskey is better suited to this region because the velocity can be kept subsonic.

Traveling at supersonic speeds, the free-falling payload suffers from wake effects in this region. Ram currents are higher and more variable because of the high speed. The wake further complicates the current balance. Any increase in central body size obviously has to affect the measurements. Variations that appear to be real from the individual sensors are less inside the

wake. Wake-induced error signals appear to be enhanced by photoemission by the sensors. A graphite coating to limit photoemission acts in reducing wake effects.

Even at subsonic velocities wake effects can be important. This was illustrated when the Hale asymmetric probe measurement was attempted from a large diameter payload instead of the usual small diameter payload. The resulting attenuated signals were thought to have been affected by the wake of the large payload (MAYNARD et al., 1981).

The asymmetric probe has been shown to repeatedly reproduce the fair weather electric field profile in the troposphere. However, during the complete descent, an offset has been often seen (see HALE et al., 1981). Figure 8, taken from Hale et al., shows a number of such profiles. This offset may partially be a form of "contact potential" difference from the asymmetries of the system. HALE (1985) has shown that it is primarily related to the separation between the sensor and the main body, hence a sheath overlap effect. Recent flights with larger electrode separation do not have the offset in the data (see Figure 9).

The obvious questions in light of the above problems are: Are any of the V/m observations real? Several observations argue strongly for a physical cause. MAYNARD et al. (1984) point out that the V/m class fields have been observed only when the conductivity is of the order of 10^{-10} S/m or less.

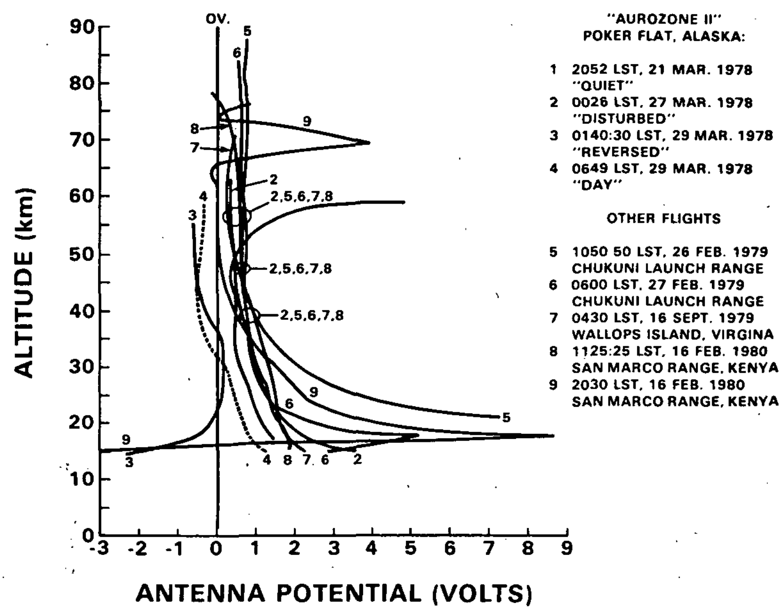

Figure 8. Electric field data profiles using asymmetric probes from HALE et al. (1981). The fair weather electric field increase at lower altitudes is evident. The offset from zero at higher altitudes appears to be an artifact from contact potential differences and from too close spacing between the lanyard electrode and the payload body.

The large electric fields occur only a small fraction of the time, and may not occur even though the conductivity criteria is met. Horizontal components have no relationship to the rocket velocity, but may be anticorrelated with the neutral wind. The large electric field observed by the free-falling payload (MAYNARD et al., 1981) created signals on the three axes that displayed internal consistency. HALE (1985) has seen large vertical electrical fields from the same payload using two radically different sensor configurations. Figure 9 shows data from two flights in which V/m class electric fields were seen on both configurations. The evidence points to a real physical effect. It is not clear whether all possible interactions of the instrument with the medium are understood well enough to be quantitatively sure of error estimate.

Lower Stratosphere and Below

The asymmetric double probe measurements using the parachuted payload has been shown to provide an effective measurement of the vertical profile of the

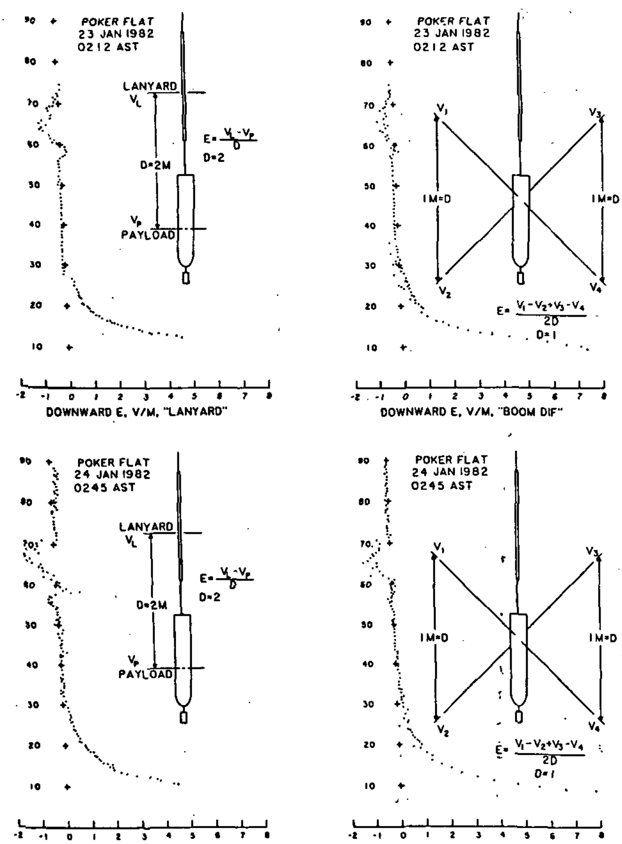

Figure 9. Data from HALE (1985) in which the same large electric fields are measured by two very different configurations (see the insert of the sensors for each panel). Note also that the offset seen in the data on Figure 8 is not present with the larger spacing between the electrode and central body.

fair weather electric field (HALE and MARKSON, 1984). However, ice clouds can create significant deviation from the normal curve. These are yet to be evaluated.

The largest source of data in the lower stratosphere is from balloon measurements using double probes. Millivolt/meter horizontal electric fields in the high latitude stratosphere in the presence of V/m vertical electric fields have been related to magnetospheric convection electric fields (MOZER and LUCHT, 1974). The balloon technique has been described by MOZER (1972) and will not be further discussed here.

CONCLUSION

Electric field measurements in the middle atmosphere are in their infancy. The last several years have resulted in significant advances in understanding how to perform double probe measurements. The new measurements have answered some questions and raised others. It is hoped that the new field mill instrument will provide complementary data to help resolve the new questions.

Measurements of mV/m level electric field are now possible in the D region. The detection of V/m fields in the lower mesosphere remains controversial. However, our understanding of when and where these electric fields exist is increasing. The questions of how and why remain unanswered.

ACKNOWLEDGEMENTS

Thanks are due to Drs. T. L. Aggson, R. A. Goldberg, and L. C. Hale for helpful comments and encouragement over the last few years as mesospheric double probe techniques were being developed.

REFERENCES

Aggson, T. L. (1969), Measurements of electric fields in space, in, Atmospheric Emissions, edited by B. M. McCormac and A. Omholt, 305, Van Norstrand Reinhold (New York).

Bering, E. A. (1983), A sounding rocket observation of an apparent wake generated parallel electric field, J. Geophys. Res., 88, 961.

Bering, E. A., J. R. Benbrook, and W. R. Sheldon (1977), Investigations of the electric field below 80 km from parachute-deployed payload, J. Geophys. Res., 82, 1925.

Bering, E. A., J. R. Benbrook, and W. R. Sheldon (1980), Problems with mesospheric electric field measurements, Nature, 283, 695.

Bragin, Yu. A., A. A. Tyutin, A. A. Kochee, and A. A. Tyutin (1974), Direct measurement of the atmosphere's vertical electric field intensity up to 80 km, Cosmic Res., 12, 279.

Chalmers, J. A. (1967), Atmospheric Electricity, 2nd edition, Pergamon Press (New York).

Dettro, G. J., and L. G. Smith (1982), A rocket-borne electric field meter for the middle atmosphere, Aeronomy Report 105, Univ. of Illinois, Urbana.

Fahleson, U. V. (1967), Theory of electric field measurements conducted in the magnetosphere with electric probes, Space Sci. Rev., 7, 238.

Hale, L. C. (1985), Middle atmosphere electrical structure, dynamics, and coupling, in press, Space Research.

Hale, L. C., and C. L. Croskey (1979), An auroral effect on the fair weather electric field, Nature, 278, 239.

Hale, L. C., C. L. Croskey, and J. D. Mitchell (1981), Measurements of middle atmosphere electric fields and associated electrical conductivities, Geophys. Res. Lett., 8, 927.

Kasemir, H. W. (1977), Theoretical problems of the global atmospheric electrical circuit, in, Electrical Processes in Atmosphere, edited by H. Dolezalik and R. Reiter, 423, Steinkopff Verlag (Darmstadt).

Kelley, M. C., and F. S. Mozer (1975), Simultaneous measurements of the horizontal components of the earth's electric field in the atmosphere and in the ionosphere, J. Geophys. Res., 80, 3275.

Kelley, M. C., C. L. Siefring, and R. F. Pfaff, Jr. (1983), Large amplitude middle atmospheric electric fields: Fact or Fiction?, Geophys. Res. Lett., 10, 733.

Mapleson, W. W., and W. S. Whitlock (1955), Apparatus, for accurate and continuous measurement of the earth's electric field, J. Atmos. Terr. Phys., 7, 61.

Markson, R. (1976), Ionospheric potential variations obtained from aircraft measurements of potential gradient, J. Geophys. Res., 81, 1980.

Maynard, N. C. (1980), Middle atmosphere electric fields, Proc. Vth ESA-PAC Symposium on European Rocket and Balloon Programs and Related Research, edited by T. Guyenne, 105, ESA SP-152.

Maynard, N. C., C. L. Croskey, J. D. Mitchell, and L. C. Hale (1981), Measurement of volt/meter vertical electric fields in the middle atmosphere, Geophys. Res. Lett., 8, 923.

Maynard, N. C., T. L. Aggson, and J. P. Heppner (1983), The plasmaspheric electric field as measured by ISEE-1, J. Geophys. Res., 88, 3991.

Maynard, N. C., L. C. Hale, J. D. Mitchell, F. J. Schmidlin, R. A. Goldberg, J. Barcus, F. Soraas, and C. L. Croskey (1984), Electrical structure in the high-latitude middle atmosphere, J. Atmos. Terr. Phys., 46, 807.

Mozer, F. S. (1971), Balloon measurements of vertical and horizontal electric fields, Pure and Appl. Geophys., 84, 32.

Mozer, F. S., and R. Serlin (1969), Magnetosphere electric field measurements with balloons, J. Geophys. Res., 74, 4739.

Mozer, F. S. and P. Lucht (1974), The average auroral zone electric field, J. Geophys. Res., 79, 1001.

Pedersen, A., C. A. Cattell, C.-G. Falthammar, V. Formisano, P.-A. Lindqvist, F. Mozer, and R. Torbert (1984), Quasistatic electric field measurements with spherical double probes on the GEOS and ISEE satellites, Space Sci. Rev., 11, 77.

Stergis, C. G., G. C. Rein, and T. Kangas (1957), Electric field measurements in the stratosphere, J. Atmos. Terr. Phys., 11, 77.

☆U.S. GOVERNMENT PRINTING OFFICE: 1986—156—000—50198

CUMULATIVE LISTING FOR THE MAP HANDBOOK

Volume	Contents	Date of Publication
1	National Plans, PMP-1 Report, PMP-2 Report, PMP-3 Report, Approved MAP Projects	June 1981
2	Symposium on Middle Atmosphere Dynamics and Transport (Extended Abstracts)	June 1981
3	PMP-5 Report, MSG-1 Report, MSG-2 Report, MSG-3 Report, Antarctic Middle Atmosphere Project (AMA), EXOS-C Scientific Observations, WMO Report No. 5, Updated Chapter 2 of MAP Planning Document, Condensed Minutes of MAPSC Meetings	November 1981
4	Proceedings of MAP Assembly held in Edinburgh, 14-15 August 1981, Condensed Minutes of MAP Steering Committee Meetings held in Edinburgh, Proceedings of MAP Open Meeting held in Hamburg, 19 August 1981	April 1982
5	A Catalogue of Dynamic Parameters Describing the Variability of the Middle Stratosphere during the Northern Winters	May 1982
6	MAP Directory	November 1982
7	Acronyms, Condensed Minutes of MAP Steering Committee Meetings, Ottawa, May 1982, MAP Project Reports, National Reports, Committee Reports, PMP and MSG Reports, Workshop Reports, Announcements and Corrigendum	December 1982
8	MAP Project Reports: DYNAMICS, GLOBUS, and SSIM, MSG-7 Report, National Reports: Czechoslovakia, USA	July 1983
9	Papers presented at the URSI/SCOSTEP Workshop on Technical Aspects of MST Radar, May 23-27, 1983, Urbana	December 1983
10	Papers presented at the International Symposium on Ground-Based Studies of the Middle Atmosphere, May 9-13, 1983, Schwerin, German Democratic Republic	May 1984
11	Condensed Miuntes of the MAP Steering Committee Meetings held in Hamburg 13-14 August 1983, Research Recommendations for Increased US Participation in the Middle Atmosphere Program, GRATMAP Project Report, MAP Study Group MSG-7 Report	June 1984
12	Coordinated Study of the Behavior of the Middle Atmosphere in Winter (PMP-1) Workshops	July 1984
13	Ground-Based Techniques	November 1984
14	Papers presented at the URSI/SCOSTEP Workshop on Technical Aspects of MST Radar, May 22-25, 1984, Urbana	December 1984
15	Balloon Techniques	June 1985
16	Atmospheric Structure and its Variation in the Region 20 to 120 km: Draft of a New Reference Middle Atmosphere	July 1985
17	Condensed Minutes of MAP Steering Committee Meeting, Condensed Miuntes of MAP Assembly, MAP Projects and Study Group Reports, National Reports	August 1985
18	Papers presented at MAP Symposium, November 26-30, 1984, Kyoto (Extended Abstracts)	December 1985
19	Rocket Techniques	March 1986

ROCKET TECHNIQUES

TABLE OF CONTENTS